Doctoral Thesis

OXIDATION OF MICROCYSTINS BY PERMANGANATE, OZONE AND FERRYL-TETRAPOLYPHOSPHATE COMPLEX: KINETICS AND MECHANISM

Min Sik Kim

Department of Urban and Environmental Engineering
(Environmental Science and Engineering)

Graduate School of UNIST

2018

OXIDATION OF MICROCYSTINS BY PERMANGANATE, OZONE AND FERRYL-TETRAPOLYPHOSPHATE COMPLEX: KINETICS AND MECHANISM

Min Sik Kim

Department of Urban and Environmental Engineering
(Environmental Science and Engineering)

Graduate School of UNIST

Oxidation of microcystins by permanganate, ozone and ferryl-tetrapolyphosphate: kinetics and mechanism

A dissertation
submitted to the Graduate School of UNIST
in partial fulfillment of the
requirements for the degree of
Doctor of Philosophy

Min Sik Kim

6. 22. 2018 of submission
Approved by

Advisor
Changha Lee

Oxidation of microcystins by permanganate, ozone and ferryl-tetrapolyphosphate: kinetics and mechanism

Min Sik Kim

This certifies that the dissertation of Min Sik Kim is approved.

6. 22. 2018 of submission

Advisor: Changha Lee

Jaeweon Cho

Young-Nam Kwon

Jaesang Lee

Kangwoo Cho

ABSTRACT

Microcystins (MCs) are the most common cyanotoxins (known as potent hepatotoxins and tumor promoters), and express their toxicity by inhibiting protein phosphatases activity. Because of their highly acute toxicity, the World Health Organization has set a provisional drinking water guideline value of 1 μg L^{-1} for MC-LR. Previous studies have shown that physical water treatment methods are not sufficient to control the dissolved MCs. Chemical oxidation has been suggested as a promising alternative to treat the dissolved MCs and has been extensively studied. In this dissertation, three different oxidation systems including potassium permanganate ($KMnO_4$; Mn(VII)), ozone (O_3) and Fenton reaction using ferrous ion coupled with tetrapolyphosphate in the presence of oxygen and hydrogen peroxide (i.e., Fe(II)-TPP/O_2 and Fe(II)-TPP/H_2O_2 systems) were investigated for the effective control of MCs in terms of kinetics and mechanism.

Firstly, oxidation of six common MCs (MC-RR, -LR, -YR, -LF, -LW and -LA) by Mn(VII) was studied, focusing on the pH- and temperature-dependent reaction kinetics, the effect of dissolved organic matter (DOM), and the oxidation mechanisms. Second-order rate constants for the reactions of the six MCs with Mn(VII) ($k_{Mn(VII),MC}$) were determined at pH 7.2 and 21°C. Their pH- and temperature-dependency was also investigated. The degradation of MCs in natural waters was modeled using a kinetic model composed of Mn(VII) exposure ($\int$[Mn(VII)]dt) values. The correlation analysis between various characteristics of DOM in natural waters and $\int$[Mn(VII)]dt was investigated to improve the practical applicability of the kinetic prediction model for the removal efficiency of MCs by Mn(VII). In addition, a thorough product study of MC-LR oxidation by Mn(VII) was performed using liquid chromatography-mass spectrometry (LC/MS). Based on the identified 17 products, oxidation pathways are proposed. New oxidation products (primary products from the oxidation of alkene groups, and secondary products, possibly from the hydrolysis of amide groups) were identified.

Secondly, the oxidative degradation by O_3 and $^{\bullet}OH$ of the above-mentioned MCs was investigated, focusing on the pH- and temperature-dependent reaction kinetics. Second-order rate constants for the reactions of the six MCs with O_3 and $^{\bullet}OH$ ($k_{O3,MC}$ and $k_{^{\bullet}OH,MC}$) were determined at pH 6−9 and 5−33°C via the competition kinetic method using cinnamic acid (CA, for O_3) and *para*-chlorobenzoic acid (for $^{\bullet}OH$), respectively. Since the second-order rate constants of CA with O_3 ($k_{O3,CA}$) reported in the literature are different from each other, the $k_{O3,CA}$ values at various pH and temperature conditions were directly determined using stopped-flow spectrometry. In order to verify the determined kinetic values, the oxidation of MCs in two natural waters was predicted by the kinetic model using O_3 and $^{\bullet}OH$ exposure values.

Lastly, Fe(II)-TPP/O_2 and Fe(II)-TPP/H_2O_2 systems were assessed for the oxidative degradation of MC-LR. The degradation of MC-LR by Fe(II)-TPP/O_2 and H_2O_2 systems was optimized by varying the molar ratio of TPP:Fe(II) and H_2O_2 concentration. The degradation of MC-LR was also examined by varying the pH from 3 to 11 in the Fe(II)-TPP/O_2 and Fe(II)-TPP/H_2O_2 systems. The results exhibited two pH optima for MC-LR degradation ie, ~ 7 and 9, which can be attributed to pH-dependent reactivity changes of the resultant oxidants (most likely the ferryl-tetrapolyphostate complex, Fe(IV)-TPP complex). LC/MS identified 22 products of MC-LR by the oxidation of Fe(IV)-TPP complex, including four primary oxidation products. One of the primary products, in particular, was formed via oxidative cleavage of the alkene group in the Mdha moiety of MC-LR. This compound and its secondary oxidation products are rarely found when MC-LR is transformed by other oxidants, which is believed to reflect a unique reaction pathway involving Fe(IV)-TPP complex. The reduction of the hepatotoxicity of the reaction solution during the Fe(IV)-TPP oxidation was confirmed by a decrease in MC-LR concentration.

CONTENTS

Abstract i

Contents iii

List of Figures vi

List of Tables xv

Chanper 1. Introduction 1

1.1. Research bacground 1

1.1.1. Environmental issues of microcystins 1

1.1.2. MCs in drinking water treatment plant 1

1.1.3. Chemical oxidation of MCs 2

1.2. Limitations of the previous works 4

1.2.1. Overview 4

1.2.2. Oxidation of MCs by Mn(VII) 5

1.2.3. Oxidation of MCs by O_3 6

1.2.4. Oxidation of MCs by Fe(IV)-TPP complex 7

1.3. Objectives of the study 8

Chanper 2. Materials and Methods 9

2.1. Oxidation of MCs by Mn(VII) 9

2.1.1. Reagents 9

2.1.2. Determination of rate constants 9

2.1.3. Natural water samples 11

2.1.4. Analysis of MCs and oxidation products of MC-LR 11

2.1.5. Analysis of Mn(VII) in natural waters 12

2.1.6. DOM characterization 14

2.1.7. Computational pK_a prediction for MCs 14

2.2. Oxidation of MCs by O_3 17

2.2.1. Reagents 17

2.2.2. Determination of rate constants 17

2.2.3. Natural water samples 25

2.2.4. Analysis of O_3 in natural waters 26

2.2.5. Analytical methods 27

2.3. Oxidation of MC-LR by Fe(IV)-TPP complex 28

2.3.1. Reagents 28

2.3.2. Experimental procedure 28

2.3.3. Experimental design for RSM analysis 28

2.3.4. Analytical methods 29

Chanper 3. Results and Discussion 30

3.1 . Oxidation of MCs by Mn(VII) 30

3.1.1. Kinetics for the reactions of MCs with Mn(VII) 30

3.1.2. Oxidative degradation of MCs in natural waters 39

3.1.3. Effects of DOM characteristics on $\int$[Mn(VII)]dt 41

3.1.4. Oxidation products and pathways 47

3.2 . Oxidation of MCs by O_3 61

3.2.1. Kinetics for the reactions of MCs with O_3 61

3.2.2. Kinetics for the reactions of MCs with $^{\bullet}OH$ 67

3.2.3. Oxidation of MCs by O_3 in natural waters 70

3.3 . Oxidation of MC-LR by Fe(IV)-TPP complex 72

3.3.1. MC-LR degradation by the Fe(II)/O_2 and Fe(II)/H_2O_2 systems in the presence of ligands 72

3.3.2. Optimization of Fe(II), TPP, and H_2O_2 doses 74

3.3.3. Effect of pH 79

3.3.4. Oxidation products and pathways 83

3.3.5. Hepatotoxicity test 99

Chanper 4. Conclusions 100

References 102

감사의 글 113

List of Figures

Figure 1.1. Inflow of cyanobacteria and extracellular MCs into water treatment plant..... 1

Figure 1.2. Limitation of physical treatment methods according to the literature..... 2

Figure 1.3. (a) MC structure, and (b) L-amino acids located in the X and Y positions for the six MCs (MC-RR, -LR, -YR, -LF, -LW and -LA). Possible protonation sites are highlighted with grey circles. 4

Figure 2.1. Example of the determination of $k_{Mn(II),MC}$. (a) Time-dependent profiles of ln([MC-LR])$_0$/[MC-LR]) at different Mn(VII) doses, and (b) plot of k_{obs} as a function of Mn(VII) concentration ([MC-LR]$_0$ = 0.1 μM, [Mn(VII)]$_0$ = 2.5 μM, pH = 7.2, temperature = 21 ± 1°C). 10

Figure 2.2. Experimental setups for the temperature control. 11

Figure 2.3. Example of measurement of Mn(VII) concentration in natural water. (a) Absorbance spectra during the decomposition of Mn(VII) in Maegok water. Red dotted lines represent the locations of 418 and 525 nm. The lightest lines are the final spectra obtained at the depletion point of Mn(VII). (b) Decomposition of Mn(VII) in Maegok water ([Mn(VII)]$_0$ = 2.5 μM, temperature = 21 ± 1°C). 13

Figure 2.4. Calculated speciation of MCs based on the computational predicted pK_a values..... 16

Figure 2.5. Example of the determination of $k_{O3,MC}$. CK plot of ln([MC-LR]$_0$/[MC-LR]) versus ln([CA]$_0$/[CA]) at different O_3 doses ([MC-LR]$_0$ = 0.1 μM, [CA]$_0$ = 0.1 μM, [O_3]$_0$ = 0.02-0.2 μM, [*t*-BuOH]$_0$ = 5 mM, temperature = 20 ± 1°C, pH = 7.2, used $k_{O3,CA} = 7.80\times10^5$ M^{-1} s^{-1})..... 18

Figure 2.6. Example of measurement of CA concentration. (a) Absorbance at 280 nm during CA oxidation by excess O_3. Red and bule dotted lines represent fits of the absorbance regarding whole examined reaction time and stationary phases (from 0.2 to 0.5 s), respectively. (b) Calculated CA from the subtraction of blue dotted line from red line in (a) ([CA]$_0$ = 5 μM, [O_3]$_0$ = 83.1 μM, [*t*-BuOH]$_0$ = 5 mM, pH = 7.2, temperature = 20 ± 1°C)..... 20

Figure 2.7. pH-dependent molar absorption coefficient of CA at 280 nm. 21

Figure 2.8. (a) Quartz photoreactor with UV illumination, (b) actual photon flow considered by shielding effect of H_2O_2 and the acutual optical pathlength, and (c) the optical pathlength variation by different incidence angle of photon and reactor shape. 21

Figure 2.9. Reduction of ferrioxalate (Fe(III)-Oxalate) by UV as a function of illumination time ([Fe(III)]$_0$ = 0.1 mM; [Oxalate]$_0$ = 0.6 mM, temperature = 20 ± 1°C). 22

Figure 2.10. Time-dependent profiles of (a) MC-LR and (b) ln([MC-LR]$_0$/[MC-LR]) in UV system with/without H_2O_2 ([MC-LR]$_0$ = 0.1 μM, [*p*CBA]$_0$ = 0.1 μM, [H_2O_2]$_0$ = 1 mM). 23

Figure 2.11. Time-dependent profile of ln([H_2O_2]$_0$/[H_2O_2]) during UV illumination ([H_2O_2]$_0$ = 0.1 mM, [*t*-BuOH]$_0$ = 10 mM, [PBS] = 10 mM, pH = 7.2, temperature = 21 ± 1°C). 25

Figure 2.12. Example of measurement of CA concentration. (a) Absorbance at 258 nm during O_3 decomposition in Gamak natural water. Red and bule dotted lines represent fits of the absorbance regarding whole examined reaction time and stationary phases (from 2 to 3 s), respectively. (b) Calculated O_3 from the subtraction of blue dotted line from red line in (a) ([O_3]$_0$ = 0.35 mg L^{-1}, pH = 7.95, temperature = 20 ± 1°C)..... 26

Figure 3.1. (a) Plots of k_{obs} as a function of Mn(VII) concentration, and (b) Arrhenius plots of $k_{Mn(VII),MC}$ ([MCs]$_0$ = 0.1 μM, pH = 7.2 for (a) and (b); temperature = 21 ± 1°C for (a)). 32

Figure 3.2. Time-dependent profiles of ln([MC]$_0$/[MC]) at different Mn(VII) doses ([MC-RR]$_0$ = [MC-YR]$_0$ = [MC-LR]$_0$ = [MC-LW]$_0$ = [MC-LF]$_0$ = [MC-LA]$_0$ = 0.1 μM, pH 7.2, temperature = 21 ± 1°C). 32

Figure 3.3. Oxidation of L-amino acids by Mn(VII) ([L-Ala]$_0$ = [L-Arg]$_0$ = [L-Leu]$_0$ = [L-Phe]$_0$ = [L-Trp]$_0$ = [L-Tyr]$_0$ = 0.1 μM, [Mn(VII)]$_0$ = 5 μM, pH 7.2, temperature = 21 ± 1°C). 33

Figure 3.4. Electronic effect of the amino acids located in the X and Y positions in MC structure on the reactivities of alkene groups with Mn(VII)..... 33

Figure 3.5. Time-dependent profiles of ln([MC]$_0$/[MC]) at different temperatures ([MC-RR]$_0$ = [MC-YR]$_0$ = [MC-LR]$_0$ = [MC-LW]$_0$ = [MC-LF]$_0$ =[MC-LA]$_0$ = 0.1 μM, [Mn(VII)]$_0$ = 2.5 μM, pH 7.2). 34

Figure 3.6. Effect of pH on the $k_{Mn(VII),MC}$ values for the six selected MCs. Symbols represent experimental data, and lines represent model predictions of $k_{Mn(VII),MC}$ (solid) and $k_{Mn(VII),MC,i}$ α_i (dashed) ([MCs]$_0$ = 0.1 μM, [Mn(VII)]$_0$ = 2.5 μM, temperature = 21 ± 1°C)..... 37

Figure 3.7. Time-dependent profiles of ln([MC]$_0$/[MC]) at different pH values ([MC-RR]$_0$ = [MC-YR]$_0$ = [MC-LR]$_0$ = [MC-LW]$_0$ = [MC-LF]$_0$ =[MC-LA]$_0$ = 0.1 μM, [Mn(VII)]$_0$ = 2.5 μM, temperature = 21 ± 1°C). 38

Figure 3.8. Oxidation of MCs in natural waters. Symbols represent experimental data, and solid lines represent model predictions using Equation 3.2 with the measured ∫[Mn(VII)]dt ([MCs]$_0$ = 10 nM, [Mn(VII)]$_0$ = 2.5 μM, temperature = 21 ± 1°C). 39

Figure 3.9. Absorbance spectra during the decomposition of Mn(VII) in natural waters. The lightest

lines are the final spectra ([Mn(VII)]$_0$ = 2.5 μM, temperature = 21 ± 1°C)..... 40

Figure 3.10. Decomposition of Mn(VII) in natural waters. The ∫[Mn(VII)]dt value was calculated for each graph ([Mn(VII)]$_0$ = 2.5 μM, temperature = 21 ± 1°C). 40

Figure 3.11. Effects of various water quality parameters on the oxidation of MC-LR by Mn(VII) ([MC-LR]$_0$ = 0.1 μM, [Mn(VII)]$_0$ = 2.5 μM, temperature = 21 ± 1°C; (b) counter anion: Cl^-; (c) counter cation: Na^+). 41

Figure 3.12. FTIR spectra of different DOM fractions. 42

Figure 3.13. (a)–(e) Fluorescence excitation-emission matrix (EEM) spectra measured for the five natural waters, and (f) a reference indicating four regions in the EEM spectra. 43

Figure 3.14. Correlation between ∫[Mn(VII)]dt and DOM characteristics ((a) DOM concentration, (b) UV_{254}, (c) $SUVA_{254}$, (d)–(g) average fluorescence intensity in five EEM regions, and (h)–(i) peak fluorescence intensity in Region II and IV) for natural waters ((1) Maegok, (2) Cheonsang, (3) Hoeya, (4) Gamak, and (5) Taehwa) ([Mn(VII)]$_0$ = 2.5 μM, temperature = 21 ± 1°C)..... 44

Figure 3.15. Experimental and predicted removal efficiency of MCs in natural waters. Lines represent the obtained linear regression model (solid) and the 95% prediction interval (dashed). ([MCs]$_0$ = 10 nM, [Mn(VII)]$_0$ = 2.5 μM, reaction time = 1 h, temperature = 21 ± 1°C). 46

Figure 3.16. Experimental and predicted removal efficiency of MC-LR in three natural water samples (sample 1, 2, and 3) from different sites of the Nakdong river in Korea ([MC-LR]$_0$ = 10 nM, [Mn(VII)]$_0$ = 2.5 μM, reaction time = 1 h, temperature = 21 ± 1°C). 46

Figure 3.17. Oxidation pathways of MC-LR by Mn(VII) proposed by Jeong et al.[44]: (a) diene oxidation products, (b) aromatic ring oxidation products, and (c) amide bond hydrolysis products. “Not detected” indicates the product noted as not detected by Jeong et al.’s study. “Not clarified” indicates the product of which detection was not clearly stated in Jeong et al.’s study. The comments on each product are in blue text. 48

Figure 3.18. Mechanism of alkene oxidation by Mn(VII) at alkaline pH conditions. 49

Figure 3.19. LC/MS identification of MC-LR ([M+H] + = 995.5560). The chromatogram at 0 min with mass spectra (left) and time-dependent chromatograms (right) of MC-LR. 51

Figure 3.20. LC/MS identification of P_{795} ($[M+H]^+$ = 795.3995). The chromatogram at 15 min with mass spectra (left) and time-dependent chromatograms (right) of P_{795} 51

Figure 3.21. LC/MS identification of P_{797} ($[M+H]^+$ = 797.3788). The chromatogram at 60 min with mass spectra (left) and time-dependent chromatograms (right) of P_{797}. 51

Figure 3.22. LC/MS identification of P_{811} ($[M+H]^+$ = 811.3944). The chromatogram at 15 min with mass spectra (left) and time-dependent chromatograms (right) of P_{811}. 52

Figure 3.23. LC/MS identification of P_{813} ($[M+H]^+$ = 813.3737). The chromatogram at 60 min with mass spectra (left) and time-dependent chromatograms (right) of P_{813}. 52

Figure 3.24. LC/MS identification of P_{815} ($[M+H]^+$ = 815.3893). The chromatogram at 60 min with mass spectra (left) and time-dependent chromatograms (right) of P_{815}. 52

Figure 3.25. LC/MS identification of P_{827} ($[M+H]^+$ = 827.3893). The chromatogram at 60 min with mass spectra (left) and time-dependent chromatograms (right) of P_{827}. 53

Figure 3.26. LC/MS identification of P_{843} ($[M+H]^+$ = 843.3842). The chromatogram at 60 min with mass spectra (left) and time-dependent chromatograms (right) of P_{843}. 53

Figure 3.27. LC/MS identification of P_{845} ($[M+H]^+$ = 845.3999). The chromatogram at 60 min with mass spectra (left) and time-dependent chromatograms (right) of P_{845}. 53

Figure 3.28. LC/MS identification of P_{997} ($[M+H]^+$ = 997.5353). The chromatogram at 15 min with mass spectra (left) and time-dependent chromatograms (right) of P_{997}. 54

Figure 3.29. LC/MS identification of P_{1015} ($[M+H]^+$ = 1015.5458). The chromatogram at 60 min with mass spectra (left) and time-dependent chromatograms (right) of P_{1015}. 54

Figure 3.30. LC/MS identification of P_{1027} ($[M+H]^+$ = 1027.5458). The chromatogram at 15 min with mass spectra (left) and time-dependent chromatograms (right) of P_{1027}. 54

Figure 3.31. LC/MS identification of P_{1029} ($[M+H]^+$ = 1029.5251). The chromatogram at 60 min with mass spectra (left) and time-dependent chromatograms (right) of P_{1029}. 55

Figure 3.32. LC/MS identification of P_{1045} ($[M+H]^+$ = 1045.5564). The chromatogram at 15 min with mass spectra (left) and time-dependent chromatograms (right) of P_{1045}. 55

Figure 3.33. LC/MS identification of P_{1047} ($[M+H]^+$ = 1047.5357). The chromatogram at 60 min with mass spectra (left) and time-dependent chromatograms (right) of P_{1047}. 56

Figure 3.34. LC/MS identification of P_{1059} ($[M+H]^+$ = 1059.5357). The chromatogram at 60 min with mass spectra (left) and time-dependent chromatograms (right) of P_{1059}. 56

Figure 3.35. LC/MS identification of P_{1077} ($[M+H]^+$ = 1077.5462). The chromatogram at 60 min with

mass spectra (left) and time-dependent chromatograms of P_{1077} (right). 57

Figure 3.36. LC/MS identification of P_{1091} ($[M+H]^+$ = 1091.5255). The chromatogram at 60 min with mass spectra (left) and time-dependent chromatograms of P_{1091} (right). 57

Figure 3.37. Proposed pathways for the oxidation of MC-LR by Mn(VII). 58

Figure 3.38. Various reaction mechanisms applied in the reaction of MC-LR with Mn(VII). B indicates base. 60

Figure 3.39. Variations of $\ln([MC]_0/[MC])$ as a function of corresponding $\ln([CA]_0/[CA])$ during the ozonation at different pH values ($[MC]_0$ = 0.1 μM, $[CA]_0$ = 0.1 μM, $[O_3]_0$ = 0.025–0.25 μM, $[t\text{-BuOH}]_0$ = 5 mM, temperature = 20 ± 1°C). 61

Figure 3.40. Variations of $\ln([MC]_0/[MC])$ as a function of corresponding $\ln([CA]_0/[CA])$ during the ozonation at temperatures ($[MC]_0$ = 0.1 μM, $[CA]_0$ = 0.1 μM, $[O_3]_0$ = 0.025–0.25 μM, $[t\text{-BuOH}]_0$ = 5 mM, pH = 7.2). 62

Figure 3.41. Plot of k_{obs} as a function of O_3 concentration at different (a) pH values and (b) temperatures ($[CA]_0$ = 5 μM, $[t\text{-BuOH}]_0$ = 5 mM, temperature = 20 ± 1°C for (a) and (b); temperature = 20 ± 1°C for (a), pH = 7.2 for (b)). 63

Figure 3.42. (a) pH-dependence of $k_{O3,CA}$, and (b) Arrhenius plot of $k_{O3,CA}$. Symbols and lines in (a) represent experimental data, model prediction of $k_{O3,CA}$ (solid) and $k_{O3,CAi}\alpha_i$ (dashed), respectively ($[CA]_0$ = 5 μM, $[O_3]_0$ = 28.7–118.4 μM, $[t\text{-BuOH}]_0$ = 5 mM for (a) and (b); temperature = 20 ± 1°C for (a), pH = 7.2 for (b)). 64

Figure 3.43. (a) pH-dependence of $k_{O3,MC}$ and (b) Arrhenius plots of $k_{O3,MC}$ (temperature = 20 ± 1°C for (a), pH = 7.2 for (b)). 64

Figure 3.44. Variations of $\ln([MC]_0/[MC])$ as a function of corresponding $\ln([p\text{CBA}]_0/[p\text{CBA}])$ during the oxidation reaction in UV/H_2O_2 system at different pH values ($[MC]_0$ = 0.1 μM, $[CA]_0$ = 0.1 μM, $[H_2O_2]_0$ = 1 mM, temperature = 20 ± 1°C). 67

Figure 3.45. Variations of $\ln([MC]_0/[MC])$ as a function of corresponding $\ln([p\text{CBA}]_0/[p\text{CBA}])$ during the oxidation reaction in UV/H_2O_2 system at different temperatures ($[MC]_0$ = 0.1 μM, $[CA]_0$ = 0.1 μM, $[H_2O_2]_0$ = 1 mM, temperature = 20 ± 1°C). 68

Figure 3.46. (a) Variations of $\ln([p\text{CBA}]_0/[p\text{CBA}])$ as a function of corresponding $\ln([HCHO]_0/[HCHO])$ during the oxidation reaction in UV/H_2O_2 system at different temperatures, and (b) Arrhenius plot of $k_{\bullet OH,p\text{CBA}}$ ($[HCHO]_0$ = 10 μM, $[p\text{CBA}]_0$ = 0.1 μM, pH = 7.2, $[H_2O_2]_0$ = 1 mM).

..... 69

Figure 3.47. (a) pH-dependence of $k_{\bullet OH,MC}$ and (b) Arrhenius plots of $k_{\bullet OH,MC}$ (temperature = 20 ± 1°C for (a), pH = 7.2 for (b)). 69

Figure 3.48. Oxidation of MCs as a function of O_3 concentration in Maegok and Gamak natural waters. Symbols and lines represent experimental data and prediction model using Equation 3.3 ($[MCs]_0$ = 0.1 μM, temperature = 20 ± 1°C). 70

Figure 3.49. $\int[O_3]dt$ and (b) $\int[^{\bullet}OH]dt$ as a function of O_3 concentration. Symbols and lines represent experimental data and prediction model, respectively. 71

Figure 3.50. Degradation of MC-LR by (a) Fe(II)/O_2 and (b) Fe(II)/H_2O_2 systems with various ligands ($[MC\text{-}LR]_0$ = 0.2 μM, $[Fe(II)]_0$ = 100 μM, $[EDTA]_0$ = $[Oxalate]_0$ = $[TPP]_0$ = 500 μM, $[H_2O_2]_0$ = 250 μM, pH = 7). 72

Figure 3.51. (a) Degradation of MC-LR by Fe(II)-TPP/O_2 system with different Fe(II) and TPP concentrations, and (b) degradation of MC-LR by Fe(II)-TPP/H_2O_2 system with different TPP:Fe(II) ratios and H_2O_2 concentration. Refer to Table 2.4 for detailed conditions ($[MC\text{-}LR]_0$ = 0.2 μM, $[Fe(II)]_0$ = 5, 100, 195 μM, $[TPP]_0$ = 10, 500 and 990 μM, $[H_2O_2]_0$ = 0, 250 and 500 μM, pH = 7). 74

Figure 3.52. Effects of Fe(II), TPP, and H_2O_2 doses on the degradation efficiency of MC-LR by Fe(II)-TPP/O_2 (a) and Fe(II)-TPP/H_2O_2 systems ($[MC\text{-}LR]_0$ = 0.201 mg/L (0.2 μM), pH = 7, $[Fe(II)]_0$ = 100 μM for (b), reaction time = 60 min for (a) and 10 min for (b)). 75

Figure 3.53. Normal probability plot of residuals for the model of MC-LR degradation efficiency by (a) the Fe(II)-TPP/O_2 system and (b) the Fe(II)-TPP/O_2. 76

Figure 3.54. Degradation efficiency of MC-LR by (a) Fe(II)-TPP/O_2 and (b)Fe(II)-TPP/H_2O_2 systems as a function of pH. Red open circles in (b) represent the fraction of residual H_2O_2 ($[MC\text{-}LR]_0$ = 0.2 μM, $[Fe(II)]_0$ = 100 μM, $[TPP]_0$ = 500 μM, $[H_2O_2]_0$ = 250 μM for (b), reaction time = 60 min). 79

Figure 3.55. Degradation of MC-LR by Fe(II)-TPP/O_2 (a) and Fe(II)-TPP/H_2O_2 (b) systems at different pH values ($[MC\text{-}LR]_0$ = 0.201 mg/L (0.2 μM); $[Fe(II)]_0$ = 100 μM; $[TPP]_0$ = 500 μM; $[H_2O_2]_0$ = 250 μM). 80

Figure 3.56. Degradation efficiency of different MC congeners by the Fe(II)-TPP/O_2 system ($[MC\text{-}LF]_0$ = $[MC\text{-}YR]_0$ = $[MC\text{-}LW]_0$ = $[MC\text{-}LR]_0$ = $[MC\text{-}RR]_0$ = $[MC\text{-}LA]_0$ = 0.2 μM, $[Fe(II)]_0$ = 100 μM, $[TPP]_0$ = 500 μM, pH = 7, reaction time = 60 min). 81

Figure 3.57. Degradation of six MC congeners by Fe(II)-TPP/O_2 system at pH (a) 7 and (b) 8 ([MC-

LF]$_0$ = [MC-YR]$_0$ = [MC-LW]$_0$ = [MC-LR]$_0$ = [MC-RR]$_0$ = [MC-LA]$_0$ = 0.2 μM, [Fe(II)]$_0$ = 100 μM, [TPP]$_0$ = 500 μM). 81

Figure 3.58. LC/MS identification of MC-LR ([M+H]$^+$ = 995.5560). The chromatogram at 20 min with mass spectra (left) and time-dependent chromatograms of MC-LR (right). 84

Figure 3.59. LC/MS identification of P_{783} ([M+H]$^+$ = 783.3995). The chromatogram at 20 min with mass spectra (left) and time-dependent chromatograms of P_{783} (right). 84

Figure 3.60. LC/MS identification of P_{785} ([M+H]$^+$ = 785.3788). The chromatogram at 20 min with mass spectra (left) and time-dependent chromatograms of P_{785} (right). 84

Figure 3.61. LC/MS identification of P_{795} ([M+H]$^+$ = 795.3788). The chromatogram at 20 min with mass spectra (left) and time-dependent chromatograms of P795.3788 (right). 85

Figure 3.62. LC/MS identification of P_{797} ([M+H]$^+$ = 797.3788). The chromatogram at 20 min with mass spectra (left) and time-dependent chromatograms of P_{797} (right). **Note: The peak filled in white was excluded because it overlapped with P_{795}.* 85

Figure 3.63. LC/MS identification of P_{811} ([M+H]$^+$ = 811.3944). The chromatogram at 20 min with mass spectra (left) and time-dependent chromatograms of P_{811} (right). 85

Figure 3.64. LC/MS identification of P_{813} ([M+H]$^+$ = 813.3740). The chromatogram at 20 min with mass spectra (left) and time-dependent chromatograms of P_{813} (right). **Note: The peak filled in white was excluded because it overlapped with P_{811}.* 86

Figure 3.65. LC/MS identification of P_{835} ([M+H]$^+$ = 835.4308). The chromatogram at 20 min with mass spectra (left) and time-dependent chromatograms of P_{835} (right). 86

Figure 3.66. LC/MS identification of P_{837} ([M+H]$^+$ = 837.4101). The chromatogram at 20 min with mass spectra (left) and time-dependent chromatograms of P_{837} (right). 86

Figure 3.67. LC/MS identification of P_{851} ([M+H]$^+$ = 851.4257). The chromatogram at 20 min with mass spectra (left) and time-dependent chromatograms of P_{851} (right). 87

Figure 3.68. LC/MS identification of P_{853} ([M+H]$^+$ = 853.4050). The chromatogram at 20 min with mass spectra (left) and time-dependent chromatograms of P_{853} (right). 87

Figure 3.69. LC/MS identification of P_{855} ([M+H]$^+$ = 855.4206). The chromatogram at 20 min with mass spectra (left) and time-dependent chromatograms of P_{855} (right). 87

Figure 3.70. LC/MS identification of P_{997} ([M+H]$^+$ = 997.5353). The chromatogram at 20 min with

mass spectra (left) and time-dependent chromatograms of P_{997} (right). 88

Figure 3.71. LC/MS identification of P_{1009} ($[M+H]^+$ = 1009.5353). The chromatogram at 20 min with mass spectra (left) and time-dependent chromatograms of P_{1009} (right). **Note: The white peaks were excluded because the mass tolerances (for the monoisotopic mass) were over 10 ppm.*..... 88

Figure 3.72. LC/MS identification of P_{1011} ($[M+H]^+$ = 1011.5509). The chromatogram at 20 min with mass spectra (left) and time-dependent chromatograms of P_{1011} (right). 88

Figure 3.73. LC/MS identification of P_{855} ($[M+H]^+$ = 1013.5302). The chromatogram at 20 min with mass spectra (left) and time-dependent chromatograms of P_{1013} (right). 89

Figure 3.74. LC/MS identification of P_{1015} ($[M+H]^+$ = 1015.5458). The chromatogram at 20 min with mass spectra (left) and time-dependent chromatograms of P_{1015} (right). 89

Figure 3.75. LC/MS identification of P_{1027} ($[M+H]^+$ = 1027.5458). The chromatogram at 20 min with mass spectra (left) and time-dependent chromatograms of P_{1027} (right). 89

Figure 3.76. LC/MS identification of P_{1029} ($[M+H]^+$ = 1029.5251). The chromatogram at 20 min with mass spectra (left) and time-dependent chromatograms of P_{1029} (right). 90

Figure 3.77. LC/MS identification of P_{1031} ($[M+H]^+$ = 1031.5408). The chromatogram at 20 min with mass spectra (left) and time-dependent chromatograms of P_{855} (right). 90

Figure 3.78. LC/MS identification of P_{1043} ($[M+H]^+$ = 1043.5308). The chromatogram at 20 min with mass spectra (left) and time-dependent chromatograms of P_{1043} (right). 90

Figure 3.79. LC/MS identification of P_{1045} ($[M+H]^+$ = 1045.5200). The chromatogram at 20 min with mass spectra (left) and time-dependent chromatograms of P_{1045} (right). 91

Figure 3.80. LC/MS identification of P_{1047} ($[M+H]^+$ = 1047.5357). The chromatogram at 20 min with mass spectra (left) and time-dependent chromatograms of P_{1047} (right). 91

Figure 3.81. The structure of MC-LR and its primary oxidation sites (A–D). 91

Figure 3.82. Proposed pathways for oxidative degradation of MC-LR by the Fe(II)-TPP/O_2 system. 93

Figure 3.83. Proposed pathways for oxidative degradation of P_{997} by the Fe(II)-TPP/O_2 system..... 94

Figure 3.84. Proposed reaction pathway for the production of P_{997}..... 95

Figure 3.85. Production of (a) P_{997} (relative to P_{1011}) and (b) HCHO during the MC-LR degradation by

Fe(II)-TPP/O_2 and UV/H_2O_2 systems ([MC-LR]$_0$ = 2 μM, pH = 7, [Fe(II)]$_0$ = 100 μM and [TPP]$_0$ = 500 μM for the Fe(II)-TPP/O_2 system, [H_2O_2]$_0$ = 250 μM)..... 96

Figure 3.86. LC/MS identification of MC-LR ([M+H]$^+$ = 995.5560). The chromatogram at 20 min with mass spectra (left) and time-dependent chromatograms of MC-LR (right). 96

Figure 3.87. LC/MS identification of P_{997} ([M+H]$^+$ = 997.5353). The chromatogram at 20 min with mass spectra (left) and time-dependent chromatograms of P_{997} (right). 97

Figure 3.88. LC/MS identification of P_{1011} ([M+H]$^+$ = 1011.5509). The chromatogram at 20 min with mass spectra (left) and time-dependent chromatograms of P_{1011} (right). 97

Figure 3.89. LC/MS identification of DNPH-derivatized HCHO (HCHO-2,4-DNPH; [M-H]$^-$ = 209.0316) produced from MC-LR oxidation by the Fe(II)-TPP/O_2 system: time-dependent chromatograms of HCHO-2,4-DNPH (left) and the chromatogram at 20 min with mass spectra (right). 98

Figure 3.90. LC/MS identification of DNPH-derivatized HCHO (HCHO-2,4-DNPH; [M-H]$^-$ = 209.0316) produced from MC-LR oxidation by the UV/H_2O_2 system: time-dependent chromatograms of HCHO-2,4-DNPH (left) and the chromatogram at 20 min with mass spectra (right). 98

Figure 3.91. Variations of MC-LR concentration and hepatotoxicity during the degradation of MC-LR at different initial concentrations by the Fe(II)-TPP/O_2 system ([Fe(II)]$_0$ = 100 μM; [TPP]$_0$ = 500 μM; pH = 7)..... 99

List of Tables

Table 1.1. Summary of literature for the control of MCs using several oxidation systems 3

Table 1.2. Summary of kinetics for the reactions of six MCs with Mn(VII), O_3, and $^{\bullet}OH$..... 5

Table 2.1. Characterization of natural waters 11

Table 2.2. Summary of computationally predicted pKa values (macroconstants) for the six MCs..... 16

Table 2.3. Characterization of natural waters 25

Table 2.4. Experimental design for RSM..... 29

Table 3.1. Summary of $k_{Mn(VII),MC}$ and E_a values 31

Table 3.2. Summary of the activation enthalpy ($\Delta H^{\ddagger}$) and activation entropy ($\Delta S^{\ddagger}$) for the Mn(VII) reactions of different compounds having alkene groups (the values for MCs determined in this study, and those for other compounds reported in the literature)..... 35

Table 3.3. Summary of the species-specific second-order rate constants for the reactions of MCs with Mn(VII) ($k_{Mn(VII),MCi}$, M^{-1} s^{-1}), determined in this study 38

Table 3.4. Summary of the predicted ∫[Mn(VII)]dt values for natural waters..... 45

Table 3.5. Oxidation products of MC-LR identified by LC/MS..... 50

Table 3.6. Summary of $k_{O3,MC}$ and $k_{\bullet OH,MC}$, and their temperature dependencies 65

Table 3.7. ANOVA for the regression model of degradation efficiency of MC-LR (Y_1) as functions of Fe(II) (X_1) and TPP concentrations (X_2) (for Figure 3.52a) 76

Table 3.8. ANOVA for the regression model of degradation efficiency of MC-LR (Y_2) as functions of [TPP]/[Fe(II)] (X_3) and H_2O_2 concentration (X_4) (for Figure 3.52b) 78

Table 3.9. Oxidation products of MC-LR identified by LC/MS..... 83

Chapter 1. Introduction

1.1. Research background

1.1.1. Environmental issues of microcystins. Global warming and eutrophication deduced by human activities (e.g., sewer runoff and overuse of fertilizers) have resulted in harmful cyanobacterial algal blooms in natural water bodies.[1] The cyanobacterial algal blooms have raised a public concern regarding the safety of drinking water resources since their occurrence not only leads to taste and odor issues but also poses health risks by the generation of cyanotoxins.[2–4] One of the most common cyanotoxins is microcystins (MCs) known as potent hepatotoxins by inhibiting protein phosphatases activity.[5, 6] The mouse LD_{50} of MC-LR (the most abundant MC, occupying 45.5–99.8wt% of the total MCs in natural samples[7]) was determined to be 50 μg kg^{-1},[8] exhibiting higher lethality than the cobra venom ($LD_{50,cobra}$ = 282.8 μg kg^{-1} [9]). Historically, a number of cases for human poisonings by MCs have been reported. Among them, two of the most serious cases with human fatalities took place in Brazil: i) in the area of the Itaparica Dam in 1988, 88 human fatalities (mostly children) over a 42-day period were found to be caused by drinking water contaminated by MCs,[10] ii) in Caruaru in 1996, 60 patients died during the hemodialysis with reservoir water contaminated by MCs.[11, 12] Due to their highly lethal toxicity, the World Health Organization has set a provisional drinking water guideline value of 1 μg L^{-1} for MC-LR in 1998.[13]

1.1.2. MCs in drinking water treatment plant. The intracellular MCs are generally produced by numerous cyanobacterial genera, including *Microcystis*, *Anabaena*, *Oscillatoria*, *Nostoc*, *Anabaenopsis* and *Aphanocapsa*,[8] and are excreted to aquatic environments through cell metabolic reactions or released after cell lysis (in this case, extracellular MCs).[14] These intracellular and extracellular MCs can be introduced into the drinking water treatment plant via a raw water intake (Figure 1.1).

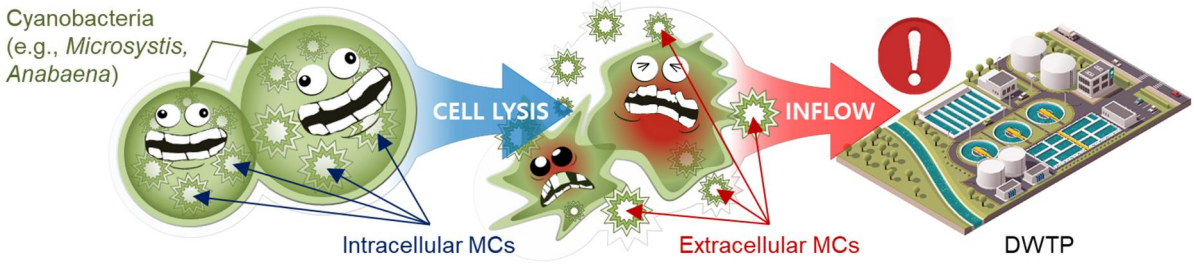

Figure 1.1. Inflow of cyanobacteria and extracellular MCs into water treatment plant.

Some of studies have tested the treatment performance of both types of MCs in natural waters by conventional water treatment methods in a pilot scale.[15–17] Their studies have commonly concluded that the physical water treatment methods (e.g., coagulation/flocculation and sand filtration) are effective in

removal of the intracellular MCs, but are not sufficient to eliminate the intracellular MCs, and may even accelerate the release of MCs through the destruction of cells by a mechanical pressure (e.g., turbulences in pipes and pressure gradients during filtration) (Figure 1.2).[15–19]

	Targets	RW	AF	ASF
Initial cells	*M. aeruginosa* *A. circinalis*	54,000 151,000	570 2300	165 2
Removal (%)	*M. aeruginosa* *A. Circinalis*	- -	98.9 98.5	99.7 99.9
Toxin (ng/L)	MCs	820±160	470±150	310±35
Removal (%)	MCs	-	42.5	61.9
Dissolved toxin (%)	MCs	17.5	97.9	97.9
Dissolved toxin (ng/L)	MCs	143	460	303.5

**RW: raw water, AF: after flocculation, ASF: after sand filtration and flocculation*

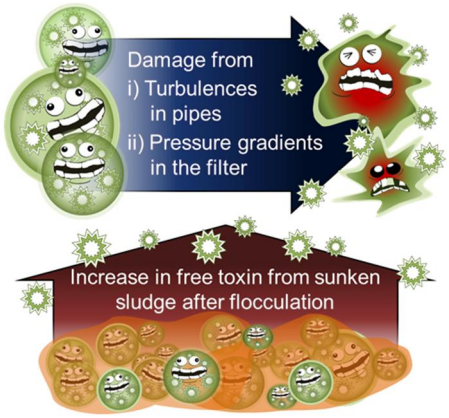

Figure 1.2. Limitation of physical treatment methods according to the literature.[15]

On the other hand, chemical oxidation has been suggested as a promising alternative to remove the dissolved MCs because of toxicity reduction through destruction of the parent MCs, and potential for complete mineralization.[20, 21] For the reliable and effective control of the dissolved MCs by the chemical oxidation, the following information is essential: i) kinetics (second-order rate constant and its pH- and temperature-dependencies), ii) effects of organic and inorganic substances (this concept accompanies natural water experiment), iii) oxidation mechanism, and iv) toxicity change.

1.1.3. Chemical oxidation of MCs. Chemical oxidation of MCs has been extensively studied in terms of the considerations described above. The degradation of MCs by conventional oxidants including chlorine (Cl_2, HOCl/OCl^-),[22–30] chlorine dioxide (ClO_2),[25, 31–33] ozone (O_3),[25,34–41] and potassium permanganate ($KMnO_4$; Mn(VII))[25, 26–28, 30, 42–44] has been reported (Table 1.1). Many of other oxidation processes using hydroxyl radical ($^{\bullet}OH$) have also been suggested as options to treat MCs; the UV/H_2O_2 process,[45–47] TiO_2 photocatalysis,[48–53] and the Fenton processes[54–57] have been tested. Sulfate radical ($SO_4^{\bullet-}$)-based oxidation technologies have also previously been reported for the oxidation of MC-LR[58, 59] (refer to Table 1.1).

Table 1.1. Summary of literature for the control of MCs using several oxidation systems

Systems	Contents and target MCs	References
Chlorination ($HOCl/OCl^-$)	i) Kinetics (second-order rate constant): MC-RR, -LR, -YR, -LF, -LW and -LA i-i) pH-Dependence of i): MC-RR, -LR, -YR and -LA i-ii) Temperature-dependence of i): MC-RR and -LR	23–25, 30
	ii) Modeling of MC-LR degradation in natural waters	23, 24, 27
	iii) Oxidation mechanism of MC-LR	22, 28, 29
	iv) Toxicity change during MC-RR and -LR oxidation	22, 26
Chlorination (ClO_2)	i) Kinetics (second-order rate constants): MC-LR i-i) pH-Dependence of i): MC-RR and -LR i-ii) Temperature-dependence of i): MC-RR	25, 31, 33
	ii) Modeling of MC-LR degradation in natural waters	25, 32
	iii) Oxidation mechanism of MC-RR and -LR	31, 33
	iv) Toxicity change during MC-LR oxidation	31
Ozonation (O_3, $^{\bullet}OH$)	i) Kinetics (second-order rate constants for O_3): MC-RR and -LR i-i) pH-Dependence of i): MC-RR and -LR i-ii) Temperature-dependence of i): MC-RR and -LR	36, 38, 39
	ii) Degradation of MC-LR and -LA in natural waters	25, 34–38
	iii) Oxidation mechanism of MC-RR and -LR	39–41
	vi) Toxicity changes during MC-RR, -LR and -LA oxidation	37, 39, 40
Permanganate oxidation (Mn(VII))	i) Kinetics (second-order rate constants): MC-RR, -LR, -YR, -LF, -LW and -LA i-i) pH-Dependence of i): MC-RR and -LR i-ii) Temperature-dependence of i): MC-RR and -LR	25, 30, 42, 43, 44
	ii) Modeling of MC-LR degradation in natural waters	25, 27, 43, 44
	iii) Oxidation mechanism of MC-LR	28, 44
	iv) Toxicity changes during MC-RR and -LR oxidation	26
UV/H_2O_2 (UV-C, $^{\bullet}OH$)	i) Kinetics (second-order rate constants for $^{\bullet}OH$): MC-RR, -LR, -YR, and -LA ii) Effects of pH, alkalinity and DOM on MC-LR degradation; natural water experiments iii) Oxidation mechanism of MC-LR iv) Toxicity changes during MC-RR, -LR, -YR and -LA oxidation	45–47
TiO_2 based photocatalysis (UV-C, $^{\bullet}OH$, h^+)	ii) Effect of pH on MC-LR degradation and adsorption by TiO_2 iii) Oxidation mechanism of MC-LR	48–53
Fenton (-photo) ($^{\bullet}OH$)	• Assessment of the potential of Fenton and photo-Fenton systems	54–57
Persulfates oxidation ($S_2O_8^{2-}$, HSO_5^-, $SO_4^{\bullet-}$, $^{\bullet}OH$)	• Comparison and evaluation of metal-persulfates systems for MC-LR degradation iii) Oxidation mechanism of MC-LR	58, 59

1.2. Limitations of the previous works

1.2.1. Overview. Most of the above-mentioned studies are mainly performed on MC-RR and -LR, despite of the fact that there are many kinds of MCs. MCs cab be characterized as monocyclic heptapeptides, including a unique β-amino acid known as Adda ((2*S*,3*S*,8*S*,9*S*)-3-amino-9-methoxy-2,6,8-trimethyl-10-phenyldeca-4,6-dienoic acid), D-glutamic acid (D-Glu), *N*-methyldehydroalanine (Mdha), D-alanine (D-Ala), D-erythro-β-methylaspartic acid (D-MeAsp), and two variable L-amino acids (X and Y) (refer to Figure 1.3).[60]

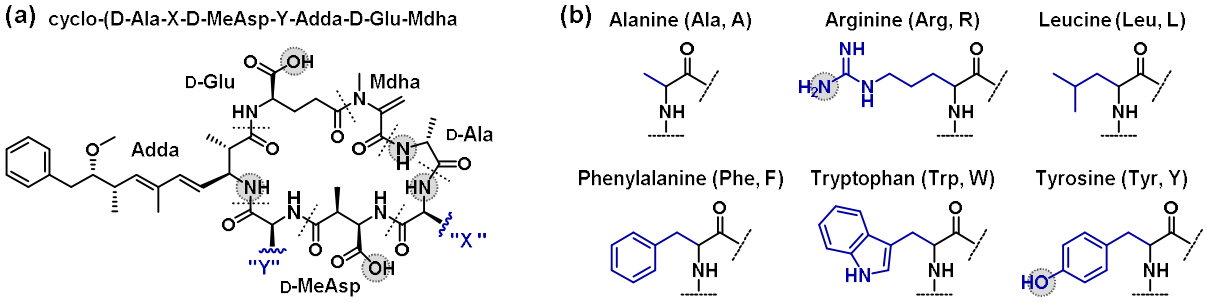

Figure 1.3. (a) MC structure, and (b) L-amino acids located in the X and Y positions for the six MCs (MC-RR, -LR, -YR, -LF, -LW and -LA). Possible protonation sites are highlighted with grey circles.

Various MC congeners (although a few MCs have structural variations in MeAsp and Mdha) are determined by the L-amino acids combinations in the X and Y positions,[61] and more than 100 different MC congeners have been identified to date.[62] Among them, the most frequently observed MC congeners in the environment are MC-RR, -LR, -YR, -LF, -LW and -LA,[21, 63] which have the combinations of the following L-amino acids located in the X and Y positions of MC structure: Ala (A), phenylalanine (Phe, F), leucine (Leu, L), arginine (Arg, R), tyrosine (Tyr, Y), and tryptophan (Trp, W). It can be easily anticipated that the reactivity of MCs with an oxidant can vary depending on the combination of amino acids, however, the kinetics for the reaction of those six MCs with representative oxidants still remain unknown (refer to Table 1.2). With respect to the three representative oxidants (i.e., Mn(VII), O_3 and $^{\bullet}OH$), many of second-order rate constants and their activation energy (E_a) values are missing. Especially, none of the E_a values for the reaction of six MCs with $^{\bullet}OH$ have not been determined. In the case of O_3, the kinetics related to the only MC-LR were investigated. In addition, among the determined kinetic values, some of them exhibited very big difference depending on each study: the determined second-order rate constants for the reaction of MC-LR with O_3 differ more than 10 times depending on the literature (refer to Table 1.2). Therefore, further investigation regarding a comprehensive and reliable kinetic database for the oxidation of major six MCs by the representative oxidants is required for the effective control of those MCs.

Table 1.2. Summary of kinetics for the reactions of six MCs with Mn(VII), O_3 and $^{\bullet}OH$

MCs	Mn(VII)		O_3		$^{\bullet}OH$	
	k (M^{-1} s^{-1})	E_a (kJ mol^{-1})	k (M^{-1} s^{-1})	E_a (kJ mol^{-1})	k (M^{-1} s^{-1})	E_a (kJ mol^{-1})
MC-RR	469 ± 37 [42] 418 [43] 470 [30]	18.9 [42]	ND	ND	1.5×10^{10} [47]	ND
MC-LR	357.2 ± 12.5 [43] 408 [30] 289.9 [44]	ND	3.8×10^{4} [21] 4.1×10^{5} [38]	29.3	1.1×10^{10} [38] 2.3×10^{10} [64] 1.1×10^{10} [47]	ND
MC-YR	405.9 [43] 396 [30]	ND	ND	ND	1.6×10^{10} [47]	ND
MC-LF	246 [30]	ND	ND	ND	ND	ND
MC-LW	273 [30]	ND	ND	ND	ND	ND
MC-LA	170 [30]	ND	ND	ND	1.1×10^{10} [47]	ND

ND is not determined.

Meanwhile, recently, numerous oxidation systems have been newly developed and examined for the control of MCs. Most of their systems are based on the photocatalyst: N-F codoped TiO_2,[65] BiOBr, [66] graphene oxide-TiO_2,[67] maghemite-vis,[68] nanodiamond-TiO_2,[69] SnP-silica,[70] etc. However, their systems are far from the filed applications by the following limitations: poor production yields of their photocatalyst, high cost, and difficulty of operation. For the purpose of the MCs treatment, the newly developed systems should be more likely to be applicable to the real conditions and also should be low cost. From these perspectives, ferrous coupled with tetrapolyphosphate (TPP, an inorganic iron-chelating agent), which can activate oxygen into reactive oxidants capable of degrade organic compounds (i.e., the Fe(II)-TPP/O_2 system) under the neutral pH conditions[71], can be an excellent option for the removal of MCs.

In this study, two conventional oxidants, i.e., Mn(VII) and O_3, and a promising oxidation system using Fe(II)-TPP complex in the presence of O_2 were selected for the oxidation of MCs, and their specific literature reviews are described as follows.

1.2.2. Oxidation of MCs by Mn(VII). Mn(VII) is an oxidant utilized for the treatment of organic pollutants, and offers several advantages that contain wide workable pH conditions, ease to control, relatively low oxidant demand, low cost, and no production of harmful byproducts (unlike O_3 and Cl_2).[42, 72, 73] The degradation of MCs by Mn(VII) has been extensively investigated from various aspects, including the kinetics, effects of treatment conditions and water quality parameters, mechanism of MC

oxidation, and toxicity changes. Many of the previous studies have determined second-order rate constants for the reactions of representative MCs with Mn(VII) ($k_{Mn(VII),MC}$).[42–44] Oxidation mechanism of MC-LR has also been investigated: dihydroxylation of alkene groups in Adda and Mdha moieties of MC-LR (refer to Figure 1.3) was suggested as a primary oxidation mechanism,[21, 43, 74] which was further supported by LC/MS.[28, 44] In addition, it has been demonstrated that the hepatotoxicity of MCs is effectively reduced by Mn(VII) oxidation.[26] The effects of various water quality parameters, such as pH, temperature, and organic and inorganic matters, have also been tested, exhibiting that the dissolved organic matter (DOM) is a primary factor that can affect the MC-LR degradation by Mn(VII).[27, 43, 44]

Despite of the abovementioned studies, some of important subjects on the oxidation of MCs by Mn(VII) remain unknown, and in part, misinterpreted. First, limited information is available for the pH- and temperature-dependencies of MC degradation by Mn(VII); specific second-order rate constants regarding the pH-dependent species of MCs have not been determined, and E_a for the reactions of several major MCs are not determined. Second, little is known about the effects of different DOM characteristics on MC degradation by Mn(VII). Finally, the oxidation mechanism of MC-LR by Mn(VII) that has been suggested in previous studies[28, 44] are questionable, since they are not consistent with the chemistry commonly known for alkene oxidation by Mn(VII).[75–77]

1.2.3. Oxidation of MCs by O_3. Ozonation has been widely applied in many drinking water treatment plants for the oxidation of the refractory micropollutants and disinfection, because O_3 is a highly reactive oxidant ($E^0(O_3, 2H^+/O_2, H_2O)$ = 2.076 V_{NHE}[78]). O_3 can either directly react with organic pollutants or decompose to a highly reactive and nonselective $^{\bullet}OH$ ($E^0(^{\bullet}OH, H^+/H_2O)$ = 2.813 V_{NHE}[78]) which also react with the target pollutants.[79] In particular, ozonation has been estimated to be the most potent option for the removal of MCs,[20, 31, 35] because alkene groups of MC structure are highly vulnerable to attack by O_3 and $^{\bullet}OH$ (refer to Figure 1.3): most of organic compounds containing alkenes usually exhibit high second-order rate constant values with O_3 ($\geq 10^5$ M^{-1} s^{-1}) and $^{\bullet}OH$ ($\geq 10^{10}$ M^{-1} s^{-1}).[80] The oxidation of MCs by O_3 has been investigated concerning several aspects, such as the kinetics, effects of treatment conditions and water quality parameters, mechanism of MCs oxidation, and toxicity changes. The literature has reported second-order rate constants for the reaction of representative MCs with O_3 and $^{\bullet}OH$ ($k_{O3,MC}$[36, 38, 39] and $k_{\bullet OH,MC}$[38, 45, 64]). Oxidation mechanisms have been also studied: hydroxylation of phenyl group, and dihydroxylation and cleavage of alkene groups were postulated as a primary oxidation mechanisms by the mass spectrometric evidences.[39, 40, 41] In addition, it has been demonstrated that the hepatotoxicity of MCs decreased concurrently with a decrease on the concentration of MCs during the ozonation.[37, 39, 40] The influences of water quality parameters, such as pH, alkalinity, temperature, and type and concentration of DOM, have also been tested, concluding that most of parameters affects the oxidation of MCs by O_3, and the most influential factor is DOM concentration.[25, 34–39]

Despite of the abovementioned studies, several important subjects on the oxidation of MCs by O_3 remain unknown, and in part, unclear. First, limited information is available for $k_{O3,MC}$ and $k_{\bullet OH,MC}$ values and their pH- and temperature-dependencies: i) second-order rate constants of O_3 were determined for only two MCs (i.e., MC-RR and MC-LR), and only one E_a for MC-LR was provided, ii) second-order rate constants of $^{\bullet}OH$ for MC-RR, -LR, -YR and -LA are available (from 1.1×10^{10} to 1.6×10^{10} M^{-1} s^{-1} [38, 45, 64]), however, their E_a values have not been reported at all. Second, there is a significant difference in the determined $k_{O3,MC\text{-}LR}$ values (from 3.8×10^{4} to 4.1×10^{5} M^{-1} s^{-1} [36, 38, 39]) depending on each study. Moreover, to the best of author's knowledge, those kinetics have not been verified by the prediction of MCs oxidation in natural waters through the kinetic model using O_3 and $^{\bullet}OH$ exposure values.

1.2.4. Oxidation of MCs by Fe(IV)-TPP complex. The reaction of Fe(II) with O_2 is known to produce reactive oxidants under the neutral pH conditions, leading to the oxidation of organic pollutants.[81, 82] However, a major drawback of the Fe(II)/O_2 system was the low yield of reactive oxidants due to the iron precipitation at the neutral pH range; the oxidant yield was only less than 10% with respect to Fe(II) added.[83] To enhance the oxidant production of Fe(II)/O_2 system by increasing the iron solubility, various organic iron-chelating agents such as oxalate, ethylenediaminetetraacetic acid (EDTA), and nitrilotriacetic acid have been applied.[84, 85] However, the use of organic ligands is problematic with water treatment applications because they scavenge the produced oxidants and subsequently undergo self-destruction by oxidation. Recently, it was reported that TPP, a stable inorganic iron-chelating agent, improves oxidant production of Fe(II)/O_2 system under the neutral pH conditions.[71] Fe(II)-TPP complexes transform O_2 into hydrogen peroxide (H_2O_2), which is subsequently used to produce reactive oxidants via the Fenton-like reaction (the reaction of Fe(II)-TPP with H_2O_2). A recent study has proposed that ferryl complexes (most likely Fe(IV)-TPP complexes) rather than $^{\bullet}OH$ are dominantly produced by the Fe(II)-TPP/O_2 system.[86] A few studies have demonstrated that Fe(II)-TPP/O_2 and its related systems are able to effectively oxidize recalcitrant organic pollutants such as pesticides (atrazine and pentachlorophenol),[71, 86–88] pigments (reactive black 5 and rhodamine B), [86, 89] and pharmaceutical compounds (acetaminophen, carbamazepine, and cimetidine).[86]

Besides of the above-mentioned studies, limited information is available for the potential of the Fe(II)-TPP/O_2 system to oxidize various organic pollutants. The Fe(II)-TPP/O_2 system has not been investigated for the oxidation of MCs. Plus, the effect of externally-supplied H_2O_2 (i.e., the Fe(II)-TPP/H_2O_2 system) has not been investigated, even if the Fe(II)-TPP/H_2O_2 system is expected to significantly accelerate the generation of reactive oxidants compared to the Fe(II)-TPP/O_2 system.

1.3. Objectives of the study

This study is divided into the following three parts: 1) oxidation of MCs by Mn(VII), 2) oxidation of MCs by O_3, and 3) oxidation of MC-LR by Fe(IV)-TPP complex. The objective of each part is as follows:

1) The objectives of the first part are i) to obtain kinetic data for the reactions of the six MCs with Mn(VII) in a wide range of pH and temperature conditions, ii) to quantify the effects of DOM on MC oxidation by Mn(VII) in natural waters, and iii) to revisit the oxidation mechanism of MC-LR by Mn(VII).
   For these purposes, species-specific second-order rate constants and E_a for the reactions of the six MCs with Mn(VII) were determined. The quantitative correlation analysis between various DOM characteristics and $\int$[Mn(VII)]dt was performed in five natural waters. In addition, the detailed product study on the MC-LR oxidation by Mn(VII) was carried out using liquid chromatography-mass spectrometry (LC/MS).

2) The objective of the second part is to obtain comprehensive and reliable kinetic data for the reaction of MCs with O_3 and $^{\bullet}OH$ in a circumneutral pH range and a wide temperature condition. For this purpose, second-order rate constants and E_a for the reactions of six MCs with O_3 and $^{\bullet}OH$ were determined using competition kinetics. The validity of the established kinetic values was verified by the prediction of removal efficiencies of the six MCs in two natural water samples using kinetic model.

3) This objective of the last part is to assess the potential of Fe(II)-TPP/O_2 and Fe(II)-TPP/H_2O_2 systems to control MC-LR by investigating the kinetics and mechanism of MC-LR degradation. For this purpose, MC-LR degradation was examined and optimized by varying the doses of Fe(II), TPP, and H_2O_2, and the pH of the solution. The oxidation products of MC-LR were identified by liquid chromatography-mass spectrometry (LC/MS), and the transformation pathways were elucidated based on the identified products.

Chapter 2. Materials and Methods

2.1. Oxidation of MCs by Mn(VII)

2.1.1. Reagents. All chemicals were of reagent grade, and were used without further purification. The chemicals used in this study are as follows: $KMnO_4$ (≥99%, Sigma-Aldrich), sodium thiosulfate pentahydrate ($Na_2S_2O_3$•$5H_2O$, ≥99.5%, Sigma-Aldrich), potassium phosphate monobasic (KH_2PO_4, ≥99%, Sigma-Aldrich), potassium phosphate dibasic (K_2HPO_4, ≥98%, Sigma-Aldrich), sodium carbonate (≥99%, Sigma-Aldrich), sodium bicarbonate (≥99.5%, Sigma-Aldrich), sodium chloride (≥99%, Sigma-Aldrich), sodium bromide (≥99%, Sigma-Aldrich), sodium nitrate (≥99%, Sigma-Aldrich), sodium sulfate (≥99%, Sigma-Aldrich), potassium chloride (≥99%, Sigma-Aldrich), calcium chloride (≥96%, Sigma-Aldrich), ammonium chloride (≥99.5%, Sigma-Aldrich), magnesium chloride (≥98%, Sigma-Aldrich), sodium hydroxide (NaOH, ≥98%, Sigma-Aldrich), perchloric acid ($HClO_4$, 70%, Sigma-Aldrich), phosphoric acid (85 wt.%, Aldrich), L-alanine (L-Ala, ≥98%, Sigma-Aldrich), L-arginine (L-Arg, ≥98%, Sigma-Aldrich), L-leucine (L-Leu, ≥98%, Sigma), L-phenylalanine (L-Phe, ≥98%, Sigma-Aldrich), L-tryptophan (L-Trp, ≥98%, Sigma-Aldrich), L-tyrosine (L-Tyr, ≥98%, Sigma-Aldrich), humic acid sodium salt (NaHA, *no information on purity*, Aldrich), Suwanee river humic acid (SRHA, *no information on purity*, International Humic Substances Society), Suwanee river fluvic acid (SRFA, *no information on purity*, International Humic Substances Society), MC-RR (≥99%, Enzo Life Science Inc.), MC-LR (≥95%, Enzo Life Science Inc.), MC-YR (≥95%, Enzo Life Science Inc.), MC-LF (≥95%, Enzo Life Science Inc.), MC-LW (≥95%, Enzo Life Science Inc.), MC-LA (≥95%, Enzo Life Science Inc.), 0.1% formic acid (v/v) in water (0.095-0.105%, Thermo Fisher Scientific), and methanol (>99.99%, Honeywell). All solutions were prepared using deionized water (>18.2 MΩ cm, Millipore Co., USA). The Mn(VII) stock solution (4 mM) was prepared and stored in the dark at 4 °C, until use.

2.1.2. Determination of rate constants. The literature has demonstrated that the reactions of various organic compounds (including MCs) with Mn(VII) follow second-order kinetics.[42, 43, 72, 73] The $k_{Mn(VII),MC}$ values were determined by measuring the decrease in concentration of the target MC in the presence of excess Mn(VII). The reactions of MCs with Mn(VII) are first-order with respect to each reactant, and can be described by Equation 1.1:

$$-d[MC]/dt = k_{Mn(VII),MC}\,[Mn(VII)]\,[MC] \quad (1.1)$$

where, [Mn(VII)] and [MC] represent the concentrations of Mn(VII) and the target MC, respectively. Equation 1.1 can be simplified to Equation 1.2 in the presence of excess Mn(VII) (i.e., [Mn(VII)] >> [MC]):

$$-d[MC]/dt = k_{obs}[MC] \quad (1.2)$$

$$k_{obs} = k_{Mn(VII),MC}[Mn(VII)] \quad (1.3)$$

where, k_{obs} is the observed pseudo-first-order rate constant for the reactions of MCs with Mn(VII) (s^{-1}), which can be obtained by measuring the decrease of the target MC concentration as a function of time. In all experiments, the concentration of MCs followed a pseudo-first-order decay (Figure 2.1a). Using Equation 1.3, $k_{Mn(VII),MC}$ values were obtained from the slopes of plots of k_{obs} versus [Mn(VII)] (Figure 2.1b).

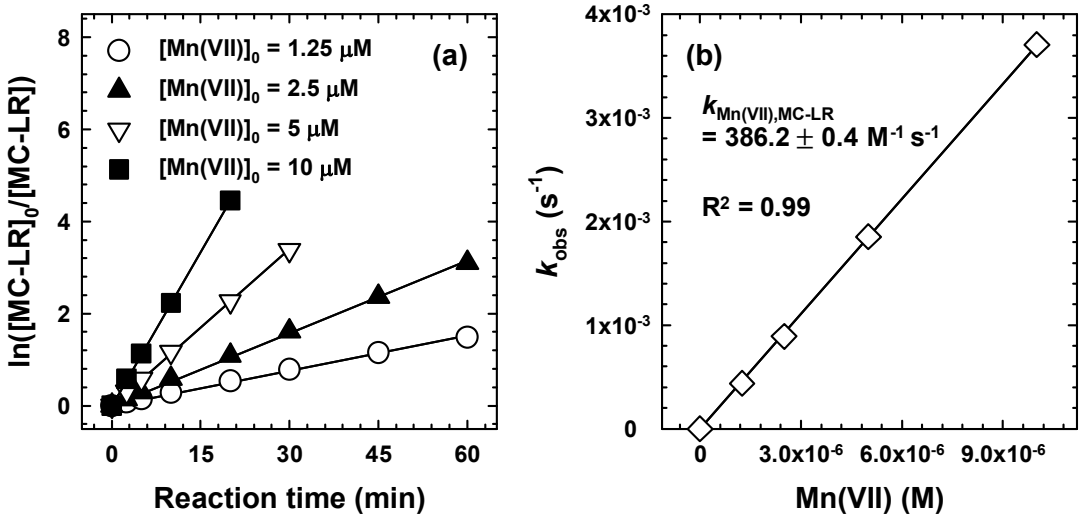

Figure 2.1. Example of the determination of $k_{Mn(II),MC}$. (a) Time-dependent profiles of ln([MC-LR])$_0$/[MC-LR]) at different Mn(VII) doses, and (b) plot of k_{obs} as a function of Mn(VII) concentration ([MC-LR]$_0$ = 0.1 μM, [Mn(VII)]$_0$ = 2.5 μM, pH = 7.2, temperature = 21 ± 1°C).

All kinetic experiments were performed with 20 mL solutions in a 25 mL-beaker open to the atmosphere. The reaction temperature was adjusted to the aimed value, and controlled to be stable during the reaction by water circulation systems coupled with a probe type chiller (TC®45E-F, Huber Co., Germany) (for 5–21°C) and a water bath heater (for 30°C) (Figure 2.2). The solution pH was adjusted by 10 mM phosphate (for pH 5–7) and carbonate buffers (for pH 8–11). No pH buffers were used for experiments at pH 2–4; the pH changes during the reactions were less than 0.2 units. The reaction was initiated by the injection of an aliquot of Mn(VII) stock solution into preequilibrated reaction solutions containing the target MC (0.1 μM). Samples (1 mL) were withdrawn at predetermined time intervals, and were immediately quenched by the addition of 20 μL sodium thiosulfate solution (10 mM). All experiments were conducted at least in duplicate, and the average values with standard deviations were provided.

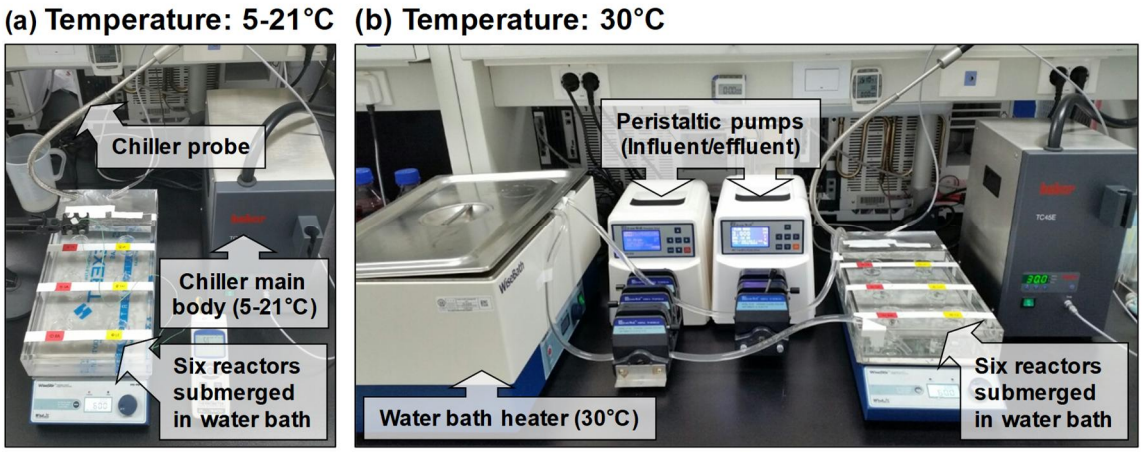

Figure 2.2. Experimental setups for the temperature control.

2.1.3. Natural water samples. Five different natural waters were sampled from the intakes of three drinking water treatment plants located in Ulsan and Daegu cities (Maegok, Cheonsang, and Hoeya), and from raw waters of Gamak lake and Taehwa river in Ulsan city, Republic of Korea. The natural water samples were filtered using a 0.45 μm filter within 24 h after sampling, and stored at 4°C until use. The water quality parameters of the five natural waters are presented in Table 2.1.

Table 2.1. Characterization of natural waters

Parameters	Natural waters				
	Maegok	Cheonsang	Hoeya	Gamak	Taehwa
DOC (mgC L^{-1})	3.55 ± 0.05	3.06 ± 0.02	2.32 ± 0.01	1.80 ± 0.06	0.79 ± 0.02
DTN (mgN L^{-1})	2.88 ± 0.01	1.11 ± 0.01	1.21 ± 0.01	0.59 ± 0.01	3.03 ± 0.01
UV_{254}	0.103	0.070	0.039	0.029	0.011
$SUVA_{254}$ (L mgC^{-1} m^{-1})	2.90 ± 0.04	2.30 ± 0.02	1.70 ± 0.01	1.60 ± 0.05	1.50 ± 0.04
pH	7.85	7.76	7.77	8.19	7.87
Alkalinity (mg L^{-1} as $CaCO_3$)	40.0 ± 2.0	34.4 ± 1.1	31.3 ± 1.0	83 ± 1.0	49.0 ± 1.0

2.1.4. Analysis of MCs and oxidation products of MC-LR. *Quantification of MCs.* The concentration of MCs was measured by Q Exactive™ quadrupole-Orbitrap mass spectrometry (Thermo Fisher Scietific Inc., USA) coupled with rapid separation liquid chromatography (RSLC, UltiMate 3000, Dionex Co., USA), without pre-concentration step for all samples. The chromatographic separation was performed on Acclaim™ C18 column (2.1 mm × 50 mm, 2.2 μm, 120 Å; Thermo Fisher Scientific Inc., USA), and the mobile phase was an isocratic mixture of 0.1 % formic acid and methanol at a flow

rate of 0.3 mL min^{-1}. The methanol content in the mobile phase was 60 % for MC-RR, -LR, and -YR, and 70 % for MC-LF, -LW and -LA. The heated electrospray ionization source interface was operated in the positive ionization mode under the following conditions: spray voltage was +3.5 kV, sheath gas was 40 arbitrary units, auxiliary gas was 10 arbitrary units, no sweep gas, capillary and vaporized temperature were 320˚C and 350˚C, respectively. The mass spectra were obtained in full scanning mode from 750 to 1200 m/z at a resolution of 35000. To achieve high mass accuracy, LC/MS calibration was performed before the analysis using Pierce™ ESI positive ion calibration solution. All data acquisition and its processing were performed using Xcalibur 3.0.2 software (Thermo Fisher Scientific Inc., USA).

Identification of MC-LR and its products. In order to clearly identify the oxidation products, a relatively high concentration of MC-LR (1 μM) was used as the initial concentration. The chromatographic separation was extended by using a relatively long analytic column (Acclaim™ 120 C18 column; 2.1 mm × 150 mm, 5 μm, 120 Å; Thermo Fisher Scientific Inc., USA), and reduced methanol content (55 %) in the mobile phase. The other operating conditions are the same as above. From the LC/MS data, the products were chosen through the scanning of the peak intensity of total ion current chromatography, and were identified by finding the best match with the exact mass values of the anticipated products (within 5 ppm of mass tolerance). In this study, only monoisotopic mass with hydrogen adduct (i.e., $[M+H]^+$) was considered.

2.1.5. Analysis of Mn(VII) in natural waters. The Mn(VII) decrease during the natural water experiments was measured by the Lee and Perez-Benito method using a UV/vis spectrometer (S-3100, Scinco Co., Korea),[90] and the detailed information is described as follows.

Difficulties in the analysis of Mn(VII). Mn(VII) concentration can be determined by the direct measurement of visible light absorbance at 525 nm ($\varepsilon^{525}_{Mn(VII)}$ = 2440–2460 M^{-1} cm^{-1} [72, 91]), or by an indirect spectrophotometric method using *N*,*N*-dimethyl phenylendiamine (DPD) colored at 551 nm (usually for measuring low concentrations of Mn(VII)). However, when using these methods, the interferences of colloidal manganese dioxide (MnO_2), the oxidation product of Mn(VII), should be minimized; MnO_2 has light absorption at 525 nm,[92]92 and reacts with DPD reagent. Moreover, the interference in absorbance can vary, depending on the size distribution of the produced colloidal MnO_2 particles (which is affected by the rate of Mn(VII) reduction).[72] In some previous studies,[25, 27, 43] Mn(VII) was analyzed by the DPD method, after filtering MnO_2 in a sample through a 0.22 μm pore size filter, to avoid the interferences by MnO_2. However, this method fails to completely remove MnO_2 particles of which the size is less than 0.22 μm. Crimi and Ko[93] demonstrated that non-filterable MnO_2 (< 0.1 μm) can be produced during the decomposition of Mn(VII).

The Lee and Perez-Benito method. A method suggested by Lee and Perez-Benito[90] can minimize the MnO_2 interferences by monitoring 418 and 525 nm simultaneously, until the depletion of Mn(VII) (note that only MnO_2 has absorbance at 418 nm). Accurate Mn(VII) concentrations can be measured by Equation 1.7 derived from Equations 1.4–1.6:

$$A_t^{525} = [Mn(VII)]_t\, \varepsilon_{Mn(VII)}^{525} + [MnO_2]_t\, \varepsilon_{MnO_2}^{525} \quad (1.4)$$

$$[Mn(VII)]_t = \left(A_t^{525} - \varepsilon_{MnO_2}^{525}[MnO_2]_t\right)/\varepsilon_{Mn(VII)}^{525} \quad (1.5)$$

$$[Mn(VII)]_t = \left(A_t^{525} - \varepsilon_{MnO_2}^{525}\, A_t^{418}/\varepsilon_{MnO_2}^{418}\right)/\left(A_i^{525}/[Mn(VII)]_i\right) \quad (1.6)$$

$$[Mn(VII)]_t = \left(A_t^{525} - A_f^{525}\, A_t^{418}/A_f^{418}\right)/\left(A_i^{525}/[Mn(VII)]_i\right) \quad (1.7)$$

where, A is the absorbance, the superscript indicates wavelength, and the subscripts i, f, and t represent initial, final, and variable time, respectively. UV/vis spectrophotometery (S-3100, Sinco Co., Korea) and a 10 cm path length quartz cuvette were used to acquire the absorbance values at 418 and 525 nm. The example of the measured absorbance and the calculated Mn(VII) during the reaction of Mn(VII) in Maegok water is presented in Figure 2.3.

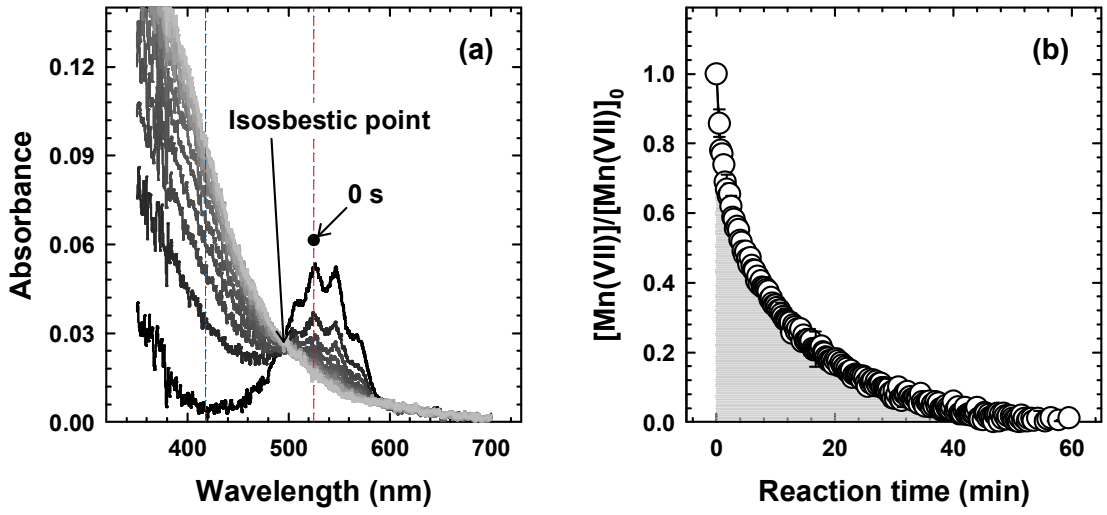

Figure 2.3. Example of measurement of Mn(VII) concentration in natural water. (a) Absorbance spectra during the decomposition of Mn(VII) in Maegok water. Red dotted lines represent the locations of 418 and 525 nm. The lightest lines are the final spectra obtained at the depletion point of Mn(VII). (b) Decomposition of Mn(VII) in Maegok water ($[Mn(VII)]_0$ = 2.5 μM, temperature = 21 ± 1°C).

2.1.6. DOM characterization. The excitation-emission matrix (EEM) fluorescence spectroscopy was utilized to characterize the DOM in natural water samples. EEM fluorescence spectra were monitored by using a fluorescence spectrophotometer (F-4500, Hitachi Co., Japan). The emission (Em) intensity was measured in the wavelength range from 285 to 545 nm at 2 nm increments with varying the excitation (Ex) wavelength from 200 to 400 nm at 5 nm increments. Ex and Em slits were set to a 10 nm band pass, and the scanning speed was set to 1200 nm min^{-1}. Contour maps of EEM spectra were plotted using OriginPro 8.5 software (OriginLab Co., USA).

The functional groups of commercial natural organic matters (i.e., Suwanee river humic acid, Suwanee river fluvic, and humic acid sodium salts) were characterized by using a Fourier-transform infrared (FTIR) spectrometer (Nicolet 6700, Thermo Scientific Inc., USA) equipped with a flat plate germanium attenuated total reflectance crystal. The FTIR spectra were collected from 1300 to 4000 cm^{-1} at 4 cm^{-1} resolution under a moisture-free environment (continuously purged with N_2 gas).

The dissolved organic carbon (DOC) concentration and total dissolved nitrogen were analyzed by TOC/TN analyzer (TOC-V_{CPH}, Shimadzu Co., Japan).

2.1.7. Computational pK_a prediction for MCs. pK_a values of MCs were calculated using the ACD/Percepta 2017.1.1 software (Advanced Chemistry Development Inc., Canada) based on the empirical prediction method, under 25°C and zero ionic strength in aqueous solution conditions. The detailed information is described as follows.

Difficulties of the experimental determination of the pK_a *values of MCs.* Despite numerous studies related to MCs during the last couple of decades, information on the pK_a values of MCs is very limited, probably due to the following reasons: i) structural complexity, including multiple protonation sites; ii) chromophore (i.e., diene moiety of Adda side chain in MC structure) is located far from protonation sites (making it hard to use the spectrophotometric method); iii) high cost (the minimum required concentration for the pK_a determination is about 0.1 mM). Only one study has reported pK_a values of MC-RR, -LR, and -YR for their carboxylic moieties (3.4 ± 0.2 for MC-RR and -YR, and 3.3 ± 0.2 for MC-LR), which were determined using an HPLC technique.[94]

Structural complexity of MCs as polyprotic compounds. Since MCs are polyprotic compounds, they possess many pK_a values at both the macroscopic and microscopic points of view.[95] For example, consider diprotic acid H_2A; this can lose each proton to give HA^- or AH^- (depending on the deprotonation sites), and then further lose a proton to give A_2^- (Equations 1.8–1.10):

$$H_2A \overset{K_a}{\leftrightarrow} HA^- \overset{K_c}{\leftrightarrow} A^{2-} \quad (1.8)$$

$$H_2A \overset{K_b}{\leftrightarrow} AH^- \overset{K_d}{\leftrightarrow} A^{2-} \quad (1.9)$$

$$\text{Overall: } H_2A \overset{K_1}{\leftrightarrow} [HA^- \text{ and } AH^-] \overset{K_2}{\leftrightarrow} A^{2-} \quad (1.10)$$

In this case, there are two macroscopic dissociation constants, K_1 and K_2, and four microscopic dissociation constants (so-called microconstants), K_a, K_b, K_c, and K_d. The K_1 and K_2 are related to the four microconstants by Equations 1.11–1.13:

$$K_1 = K_a + K_b \quad (1.11)$$

$$1/K_2 = 1/K_c + 1/K_d \quad (1.12)$$

$$K_1K_2 = K_bK_c = K_aK_d \quad (1.13)$$

As the number of protonation sites increases, the number of microconstants greatly expands. MCs generally possess more than five protonation sites, and thus they demonstrate higher structural complexity.

Computational pK_a *prediction for MCs using ACD/Percepta.* A computational approach is very useful for the pK_a prediction of unknown macromolecular organic compounds like MCs. Most of the computational pK_a predictors are based on empirical database, and the prediction accuracy is continuously being improved, along with the accumulation of database and the advancement of calculation algorithms. In this study, the author analyzed the pK_a values of six MCs using ACD/Percepta 2017.1.1 software (Advanced Chemistry Development Inc., Canada), which has demonstrated more accurate predictive results compared to the other software tools.[96, 97] ACD/Percepta provides two different predictive algorithms: (i) Classic algorithm based on Hammet-type equations and electronic substituent constants for ionizable groups; (ii) GALAS (global, adjusted locally according to similarity) algorithm based on a multistep procedure considering the microconstants for all possible ionization centers in the hypothetical state of an uncharged molecule.[98] In this study, Table 2.2 presents the predicted macroscopic pK_a values of the six MCs from the GALAS algorithm, which is more suitable for the analysis of polyprotic compounds. Figure 2.4. presents the speciation of each MC congener, on the basis of the predicted pK_a.

Table 2.2. Summary of computationally predicted pK_a values (macroconstants) for the six MCs

MCs	pK_{a1}	pK_{a2}	pK_{a3}	pK_{a4}	pK_{a5}	pK_{a6}
MC-RR	2.6 ± 0.4	3.4 ± 0.4	10.9 ± 1.1	12.5 ± 1.0	13.5 ± 0.5	14.1 ± 0.4
MC-LR	2.7 ± 0.4	3.4 ± 0.4	11.1 ± 1.1	12.4 ± 1.0	13.0 ± 0.9	13.9 ± 0.5
MC-YR	2.7 ± 0.4	3.4 ± 0.4	9.9 ± 0.4	11.5 ± 1.0	12.6 ± 0.9	13.9 ± 0.5
MC-LF	2.7 ± 0.4	3.4 ± 0.4	11.1 ± 1.1	12.4 ± 1.0	13.0 ± 1.0	-
MC-LW	2.7 ± 0.4	3.4 ± 0.4	11.1 ± 1.1	12.5 ± 1.0	13.2 ± 1.0	-
MC-LA	2.7 ± 0.4	3.4 ± 0.4	11.1 ± 1.1	12.5 ± 1.0	13.2 ± 1.0	-

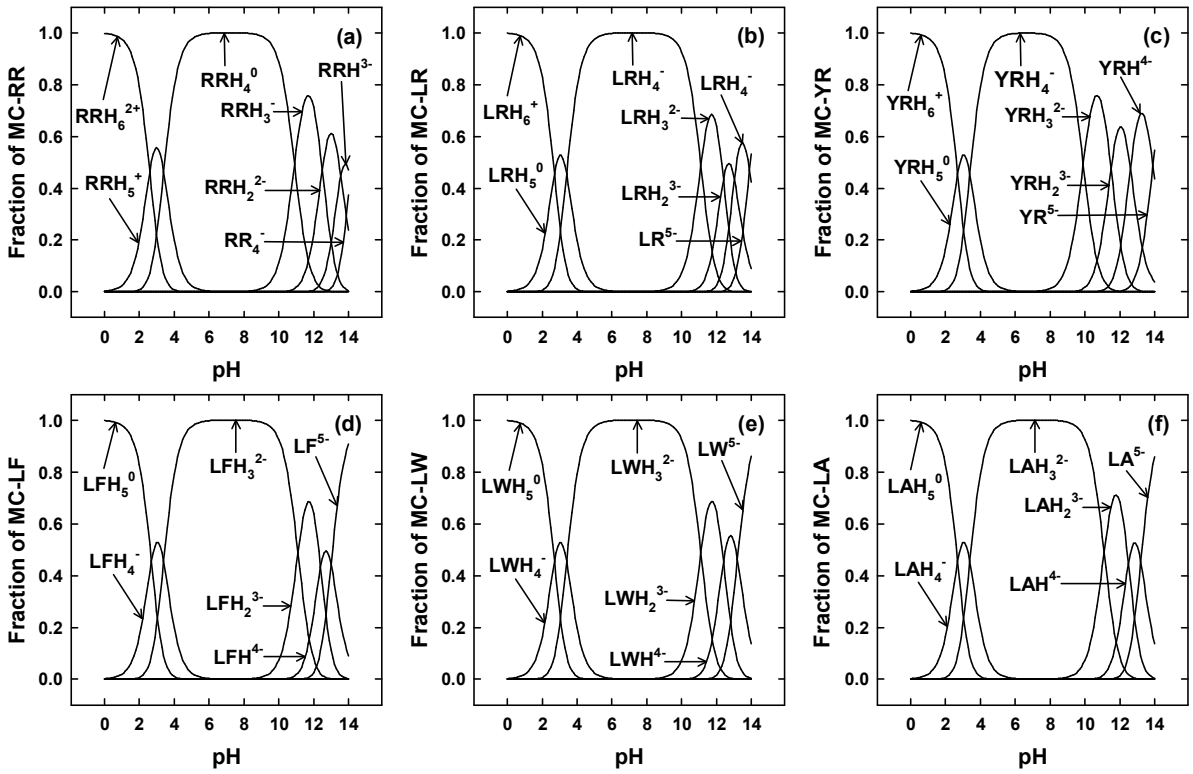

Figure 2.4. Calculated speciation of MCs based on the computational predicted pK_a values.

2.2. Oxidation of MCs by O_3

2.2.1. Reagents. All chemicals were of reagent grade, and were used without further purification, except for 2,4-dinitrophenyl hydrazine (DNPH). DNPH was recrystallized three times using acetonitrile. The chemicals used in this study are as follows: *trans*-cinnamic acid (CA, ≥99%, Sigma-Aldrich), *para*-chlorobenzoic acid (*p*CBA, 99%, Sigma-Aldrich), *tert*-butanol (t-BuOH, ≥99.5%, Sigma-Aldrich), formaldehyde solution (HCHO, 37 wt. % in H_2O, Sigma-Aldrich), iron(III) perchlorate hydrate ($Fe(ClO_4)_3 \cdot xH_2O$, crystalline, Sigma), sodium tetraborate decahydrate (≥99.5%, Sigma-Aldrich), boric acid (≥99.5, Sigma), H_2O_2 (30 wt. % in H_2O, Sigma-Aldrich), potassium oxalate monohydrate ($K_2C_2O_4 \cdot H_2O$, 99%, Sigma-Aldrich), trifluoroacetic acid (TFA, >99%, Sigma-Aldrich), and acetonitrile (>99.99%, Honeywell). KH_2PO_4, K_2HPO_4, phosphoric acid, NaOH, $HClO_4$, six MCs (MC-RR, -LR, -YR, -LF, -LW, and -LA), 0.1% formic acid (v/v) in water, and methanol were same as that of section 2.1.1. All solutions were prepared using deionized water (>18.2 MΩ cm, Millipore Co., USA). O_3 stock solutions (≈30 mg L^{-1}) were produced by sparging O_3-containing O_2 (generated by an ozone generator, Lab-II, Ozonetech Co., Korea) through deionized water in an ice bath.

2.2.2. Determination of rate constants. According to the literature, the $k_{O3,MC}$ and $k_{\bullet OH,MC}$ values were estimated to be roughly > 10^4 and > 10^9 M^{-1} s^{-1}, respectively. [36, 38, 39, 45, 64] In the case of rapid kinetics above 10^3 M^{-1} s^{-1}, it is impossible to measure the rate constant with manual sampling in seconds. There are two ways that can directly and indirectly determine fast kinetics, that is, stopped-flow spectrophotometry (SFS) and competition kinetics (CK), respectively. SFS is a direct method to obtain the most accurate kinetic information by monitoring the behavior of target compounds during the reaction in milliseconds through UV/vis absorbance. However, for the successful SFS experiments, the following condition is required; a sufficient concentration of target compound or its high molar absorption coefficient for meaningful UV/vis absorbance analysis. Although MCs have relatively large molar absorption coefficients in 210–250 nm wavelengths (e.g., $\varepsilon_{238,MC\text{-}LR}$ = 36500–39800 M^{-1} cm^{-1} [99]), significant observations of their UV absorbance are difficult due to the lack of usable MC concentration. CK could be an appropriate alternative for the determination of $k_{O3,MC}$ and $k_{\bullet OH,MC}$, because it can be performed at micromolar concentrations of reactants, allowing the use of MCs to be minimized.[38] CK utilizes the ratio of each residue concentration when the target compound and competitor are simultaneously decomposed by an oxidant, and can be described by the following Equation 2.1:

$$\ln\left(\frac{[T(0)]}{[T(n)]}\right)/\ln\left(\frac{[C(0)]}{[C(n)]}\right) = k_T/k_C \quad (2.1)$$

Where T is the target compound, C is the competitor whose second-order rate constants are known, n is the specific oxidant dose, k_T is the second-order rate constant for the reaction of target compound

with oxidant, and k_C is the second-order rate constant for the reaction of competitor with oxidant. The k_T can be calculated from the slope of the plot of ln([T(n)]/[T(0)]) versus ln([C(n)]/[C(0)]) with dividing k_C.

Determination of $k_{O3,MC}$. The $k_{O3,MC}$ values were determined by CK experiments. The chosen competitor was CA, and the second-order rate constant for its reaction with O_3 was directly determined in this study using SFS (the detailed procedure is described in the following section). All kinetic experiments for $k_{O3,MC}$ were carried out with 10 mL solutions in a 25 mL-beaker open to the atmosphere. The reaction temperature was adjusted to the desired value, and controlled to be constant during the reaction by water circulation systems equipped with a probe type chiller (TC®45E-F, Huber Co., Germany) (for 4–20°C) and a water bath heater (for 25–33°C) (refer to Figure 2.2). The solution pH was controlled using 10 mM phosphate (for pH 6.2–8.1) and 10 mM borate buffer (for pH 9). The reaction was initiated by the injection of an aliquot of O_3 stock solution into preequilibrated reaction solutions containing the equimolar concentrations of target MC (0.1 μM) and CA (0.1 μM), and 5mM of *t*-BuOH as an •OH radical scavenger. After the ozonation, the residual concentrations of the target MC and CA were determined by RSLC. For a $k_{O3,MC}$ value calculated from a slope of the CK plot, CK batch experiments were conducted at least five times by varying the dose of O_3 (0.02–0.2 μM). The average and standard deviation of $k_{O3,MC}$ values were calculated by the linear regression analysis of the data in each CK plot (refer to Figure 2.5).

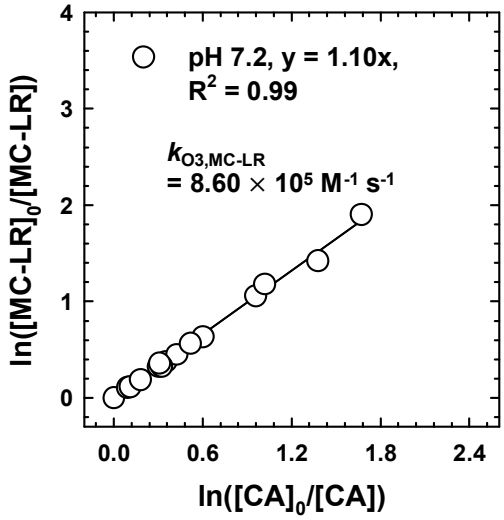

Figure 2.5. Example of the determination of $k_{O3,MC}$. CK plot of ln([MC-LR]$_0$/[MC-LR]) versus ln([CA]$_0$/[CA]) at different O_3 doses ([MC-LR]$_0$ = 0.1 μM, [CA]$_0$ = 0.1 μM, [O_3]$_0$ = 0.02-0.2 μM, [*t*-BuOH]$_0$ = 5 mM, temperature = 20 ± 1°C, pH = 7.2, used $k_{O3,CA} = 7.80\times10^5$ M^{-1} s^{-1}).

Determination of $k_{O3,CA}$. The $k_{O3,CA}$ values were determined by measuring the decrease in the concentration of CA in the presence of excess O_3; it is much more advantageous in the measurement to monitor the absorbance of CA than O_3, because the molar absorption coefficient of CA is much larger than O_3 in 250–300 nm wavelength ($\varepsilon_{280,CA}$ = 16890 M^{-1} cm^{-1} [100] > $\varepsilon_{258,O3}$ = 3000 M^{-1} cm^{-1} [101]). The reactions of CA with O_3 are first-order with respect to each reactant, and can be described by Equation 2.2:

$$-d[CA]/dt = k_{O3,CA}[O_3][CA] \quad (2.2)$$

where, $[O_3]$ and [MC] represent the concentrations of O_3 and CA, respectively. Equation 2.2 can be simplified to Equation 2.3 in the presence of excess O_3 (i.e., $[O_3] >> [CA]$):

$$-d[CA]/dt = k_{obs}[MC] \quad (2.3)$$

$$k_{obs} = k_{O3,CA}[O_3] \quad (2.4)$$

where, k_{obs} is the observed pseudo-first-order rate constant for the reactions of CA with O_3 (s^{-1}), which can be obtained by measuring the decrease of CA concentration as a function of time.

The time-dependent profile of CA was measured using a SFS system (SFM-4000, Biologic Science Instruments, France) equipped with a UV/vis fiber light source (L10290, Hamamatsu photonics K. K., Japan), a diode array detector (TIDS S 300K, J & M Analytik AG, Germany), and thermostated water. The SFS system worked with two 10 mL syringes, each filled with O_3 and CA solution (including *t*-BuOH and buffer). For each measurement, 201 μL of each reagent in the syringes was injected with a mixing ration of 1:1 and a flow rate of 6 mL s^{-1} per syringe. The calculated deadtime was 2.5 ms based on the total flow rate (12 mL s^{-1}) and the dead volume (30.2 μL) between rapid mixer and quartz cuvette (1 cm pathlength). The acquisition of the absorbance data at 280 nm was performed every millisecond until the CA was completely degraded. It is important to note that the blank absorbance by O_3 should be considered during data processing. To calculate the actual concentration of CA, the absorbance by O_3 was compensated for by the following data fitting process: i) two fit lines are obtained for the two phases (i.e., decreasing and stationary phases) using OriginPro 8.5 software (OrginLab Co., USA) (Figure 2.6a), ii) after subtracting the two fit lines from each other, the actual CA concentrations were calculated using the molar absorption coefficients of CA (Figure 2.6b). In all experiments, the concentration of CA followed a pseudo-first-order decay. Using Equation 2.4, $k_{O3,CA}$ values were calculated from the slopes of plots of k_{obs} versus $[O_3]$.

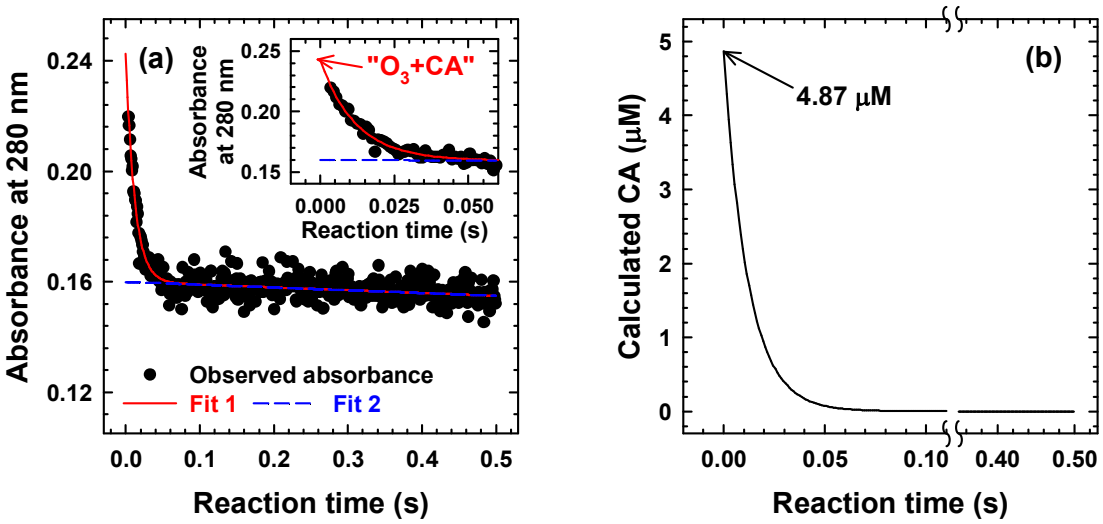

Figure 2.6. Example of measurement of CA concentration. (a) Absorbance at 280 nm during CA oxidation by excess O_3. Red and bule dotted lines represent fits of the absorbance regarding whole examined reaction time and stationary phases (from 0.2 to 0.5 s), respectively. (b) Calculated CA from the subtraction of blue dotted line from red line in (a) ($[CA]_0$ = 5 μM, $[O_3]_0$ = 83.1 μM, $[t\text{-BuOH}]_0$ = 5 mM, pH = 7.2, temperature = 20 ± 1°C).

The effect of pH on $k_{O3,CA}$ was examined by varying pH 2–9. Considering the pH-dependent species of CA (pK_a of CA = 4.4[102]), $k_{O3,CA}$ can be expressed by Equation 2.5:

$$k_{O3,CA} = k_{O3,CA1}\,\alpha_1 + k_{O3,CA2}\,\alpha_2 \quad (2.5)$$

where, $k_{O3,CAi}$ and α_i represent the species-specific second-order rate constant and the molar fraction of MC_i, respectively. The $k_{O3,CAi}$ values were determined by fitting the experimental data of $k_{O3,CA}$ into Equation 2.5, using the least-squares regression function of Microsoft Excel 2016 software (Microsoft Co., USA). Note that CA concentration at different pH ranges was calculated using pH-dependent $\varepsilon_{280,CA}$ values (Figure 2.7). The effect of temperature on $k_{O3,CA}$ was also examined by varying 4–33°C. The reaction temperature was adjusted to the desired value by thermostat (Polystat 36, Fisher Scientific, France) connected to the SFS system. All experiments were carried out at least duplicate, and the average values with standard deviations are presented.

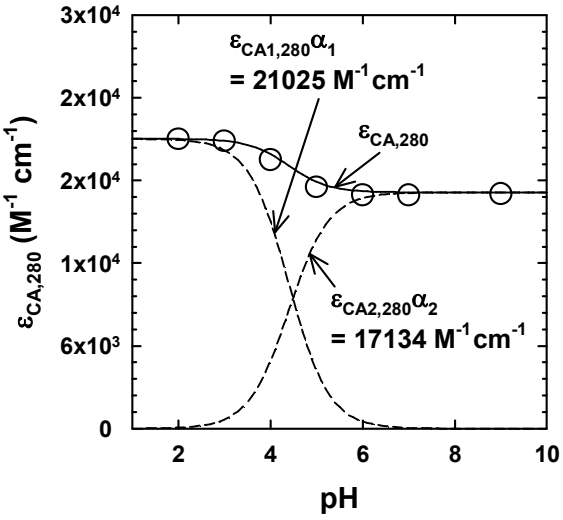

Figure 2.7. pH-dependent molar absorption coefficient of CA at 280 nm.

Determination of $k_{\bullet OH,MC}$. The $k_{\bullet OH,MC}$ values were determined by CK experiments. The chosen competitor was *p*CBA (second-order rate constant for the reaction of *p*CBA and OH, $k_{\bullet OH,pCBA} = 5.0\times10^9$ M^{-1} s^{-1} at pH 6–9.4[103]). UV/H_2O_2 system was employed to generate •OH. All kinetic experiments for $k_{\bullet OH,MC}$ were performed with 20 mL solutions in a 30 mL quartz reactor placed in a dark chamber equipped with 4 W low-pressure mercury lamps (λ_{max} = 254 nm, Philips Co., USA) (Figure 2.8a). The incident light intensity of this setup was determined to be 1.27×10^{-6} Einstein s^{-1} L^{-1} by ferrioxalate actinometry (Figure 2.9).[104]

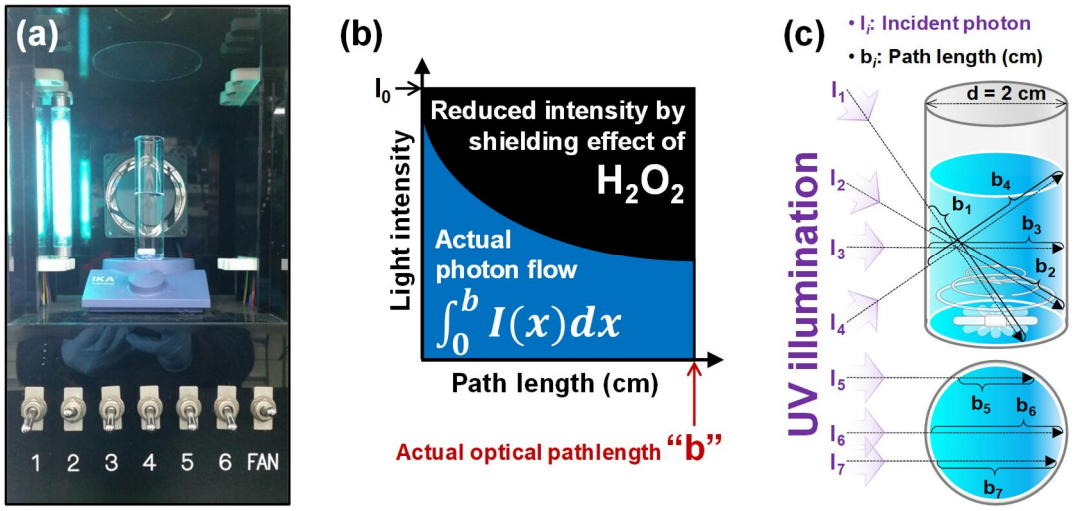

Figure 2.8. (a) Quartz photoreactor with UV illumination, (b) actual photon flow considered by shielding effect of H_2O_2 and the acutual optical pathlength, and (c) the optical pathlength variation by different incidence angle of photon and reactor shape.

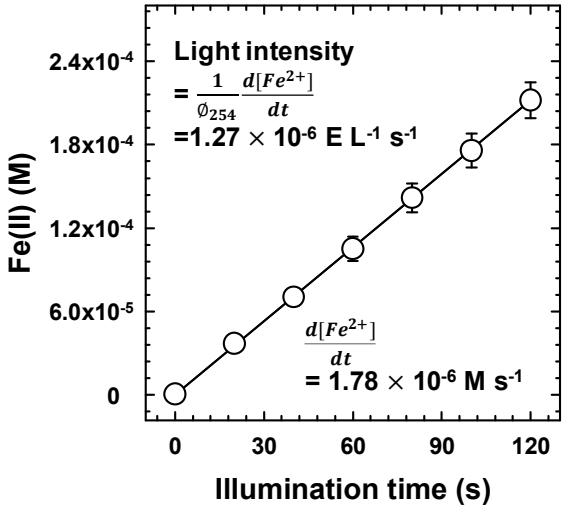

Figure 2.9. Reduction of ferrioxalate (Fe(III)-Oxalate) by UV as a function of illumination time ($[Fe(III)]_0$ = 0.1 mM; $[Oxalate]_0$ = 0.6 mM, temperature = 20 ± 1°C).

The reaction solution contains the target MC (0.1 μM), *p*CBA (0.1 μM), buffer (10 mM), and H_2O_2 (1 mM). The solution pH was controlled by 10 mM phosphate (for pH 6.2–8.1) and 10 mM borate buffer (for pH 9). The reaction temperature was adjusted in advance to the desired temperature before starting the experiment. The reaction was initiated by UV illumination. No temperature control was performed after the start of the reactions, and the temperature variation during the reactions was less than 1.5°C due to the short reaction time (70 s). In order to minimize the loss of total reaction volume, 250 μL of samples were withdrawn every 10 s, and were immediately placed in amber vial with insert (inner volume: 475 μL). Each sample was analyzed for the target MC and *p*CBA using RSLC.

It should be noted that the target MC is degraded not only by •OH but also direct UV photolysis (the degradation of *p*CBA by UV photolysis was negligible within 70 s). In order to compensate for the direct UV photolysis, the control experiments in the absence of H_2O_2 were carried out (i.e., UV system). The portion of direct UV photolysis was corrected by subtracting photolysis rate of the target MC in the UV system from the degradation rate of the target MC in the UV/H_2O_2 system. The detailed procedure is as follows.

The degradation of the target MC in UV and UV/H_2O_2 systems can be described by Equations 2.6 and 2.7, respectively:

$$\left.\frac{\mathrm{d[MC]}}{\mathrm{dt}}\right|_{\mathrm{UV}} = -I_0\left(1-10^{-\varepsilon_{\mathrm{MC}}\mathrm{b[MC]}}\right)\emptyset_{\mathrm{MC}} \tag{2.6}$$

$$\left.\frac{\mathrm{d[MC]}}{\mathrm{dt}}\right|_{\mathrm{UV/H_2O_2}} = -I_0\left(1-10^{-\varepsilon_{\mathrm{MC}}\mathrm{b[MC]}}\right)\emptyset_{\mathrm{MC}} - k_{\cdot\mathrm{OH,MC}}[\cdot\mathrm{OH}]_{\mathrm{ss}}[\mathrm{MC}] \tag{2.7}$$

where, I_0 is the incident photon flow (Einstein s^{-1} L^{-1}), ε_{MC} is the molar absorption coefficient of the target MC (M^{-1} cm^{-1}), b is the optical pathlength of the quartz photoreactor (cm), [MC] is the concentration of the target MC, $\emptyset_{MC}$ is the quantum yield of photolysis of the target MC, and $[^{\bullet}OH]_{ss}$ is the $^{\bullet}OH$ concentration at steady state. Equations 2.6 and 2.7 can be simplified to Equations 2.8 and 2.9 when the absorbance of reaction solution of the control experiment is less than 0.1 (i.e., ε_{MC} b [MC] << 0.1):

$$\left.\frac{d[MC]}{dt}\right|_{UV} \approx -2.303 I_0 \varepsilon_{MC} b \, \emptyset_{MC}[MC] = -k_{obs}[MC], \; (k_{obs}=2.303 I_0 \varepsilon_{MC} b \emptyset_{MC}) \quad (2.8)$$

$$\left.\frac{d[MC]}{dt}\right|_{UV/H_2O_2} = -k_{obs}[MC] - k^*_{obs}[MC], \; (k^*_{obs} = k_{\cdot OH,MC}[\cdot OH]_{ss}) \quad (2.9)$$

where, k_{obs} and k^*_{obs} are the pseudo-first order rate constant of degradation of the target MC by UV and $^{\bullet}OH$, respectively, which can be obtained by measuring the decrease of the target MC concentrations as a function of time in UV and UV/H_2O_2 systems (Equations 2.10 and 2.11; refer to Figure 2.10).

$$\ln\left(\frac{[MC]_0}{[MC]}\right)_{UV} = k_{obs} t \quad (2.10)$$

$$\ln\left(\frac{[MC]_0}{[MC]}\right)_{UV/H_2O_2} = (k_{obs} + k^*_{obs}) t \quad (2.11)$$

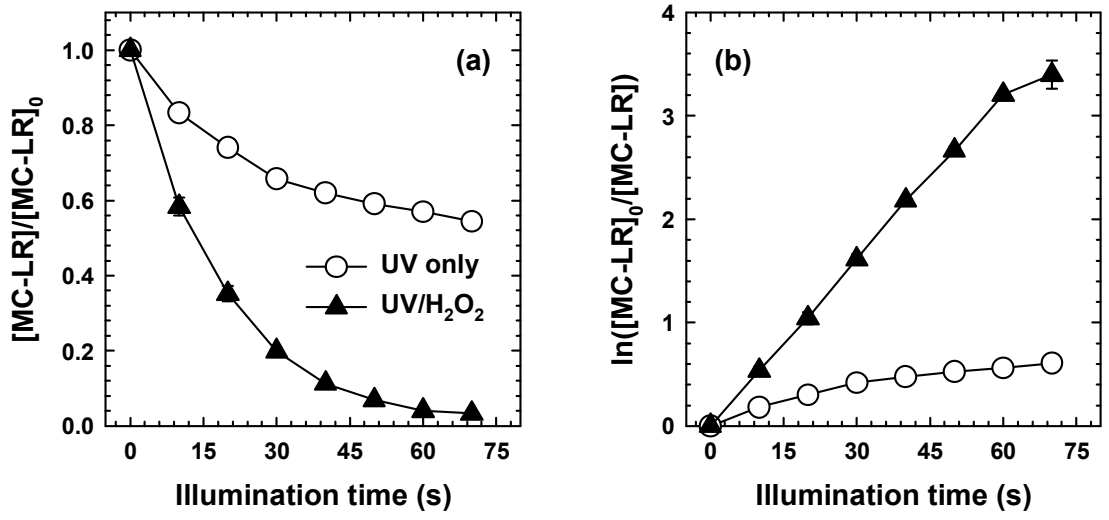

Figure 2.10. Time-dependent profiles of (a) MC-LR and (b) ln([MC-LR]$_0$/[MC-LR]) in UV system with/without H_2O_2 ([MC-LR]$_0$ = 0.1 μM, [*p*CBA]$_0$ = 0.1 μM, [H_2O_2]$_0$ = 1 mM).

Therefore, the degradation rate of the target MC by $^{\bullet}OH$ can be given by Equation 2.12 by subtracting Equation 2.10 from Equation 2.11:

$$\ln\left(\frac{[MC]_0}{[MC]}\right)_{\cdot OH} = \ln\left(\frac{[MC]_0}{[MC]}\right)_{UV/H_2O_2} - \ln\left(\frac{[MC]_0}{[MC]}\right)_{UV} = k^*_{obs}t \quad (2.12)$$

However, before the calculation of Equation 2.12, there is still a point to be considered, which is the shielding effect of H_2O_2. Since the control experiments (UV system) do not reflect the UV shielding effect of H_2O_2 in UV/H_2O_2 experiments, it is necessary to compensate for the overestimated MC degradation by multiplying a correction coefficient reflecting actual incident photon flow when H_2O_2 is present. Because the photon flow value is exponentially reduced as it passes through the optical pathlength of the photoreactor (Figure 2.8b), Equation 2.13 was integrated as a function of the optical pathlength "x" as follows:

$$\left.\frac{d[MC]}{dt}\right|_{UV} = -\int_0^b I_x\left(10^{-\varepsilon_{MC}[MC]dx}\right)\emptyset_{MC} = -2.303\varepsilon_{MC}[MC]\,\emptyset_{MC}\int_0^b I_x\,dx \quad (2.13)$$

where I_x represents the incident photon flow at the optical pathlength x cm in the presence of H_2O_2 ($I_x = I_0 10^{-\varepsilon_{H_2O_2}x[H_2O_2]}$). Equation 2.13 can be simplified as Equation 2.14.

$$\begin{aligned}\left.\frac{d[MC]}{dt}\right|_{UV} &= -2.303\varepsilon_{MC}[MC]\emptyset_{MC}I_0\left[\frac{10^{-\varepsilon_{H_2O_2}x[H_2O_2]}}{2.303\varepsilon_{H_2O_2}[H_2O_2]}\right]_0^b \\ &= -2.303\varepsilon_{MC}[MC]\emptyset_{MC}I_0\left(\frac{1-10^{-\varepsilon_{H_2O_2}b[H_2O_2]}}{2.303\varepsilon_{H_2O_2}[H_2O_2]}\right) \\ &= -2.303\varepsilon_{MC}[MC]\emptyset_{MC}I_0 b\left(\frac{1-10^{-\varepsilon_{H_2O_2}b[H_2O_2]}}{2.303\varepsilon_{H_2O_2}b[H_2O_2]}\right) = -2.303I_0\varepsilon_{MC}b\emptyset_{MC}\alpha[MC]\end{aligned} \quad (2.14)$$

where α represents the correction coefficient for the control experiment $\left(\alpha = \frac{1-10^{-\varepsilon_{H_2O_2}b[H_2O_2]}}{2.303\varepsilon_{H_2O_2}b[H_2O_2]}\right)$. Meanwhile, the b value is not the same as the diameter of the cylindrical photo reactor (2 cm) due to the shape of the photoreactor and the angle of the incident photon (Figure 2.8c). For this reason, the b value was thereby chemically determined by the photolysis kinetics of H_2O_2 using Equations 2.15–2.16.

$$\left.\frac{d[H_2O_2]}{dt}\right|_{UV} = -2.303I_0\varepsilon_{254,H_2O_2}b\emptyset_{254,H_2O_2}[H_2O_2] \quad (2.15)$$

$$\ln\left(\frac{[H_2O_2]_0}{[H_2O_2]}\right)_{UV} = 2.303I_0\varepsilon_{254,H_2O_2}b\emptyset_{254,H_2O_2}t = k_{obs,H_2O_2}t \quad (2.16)$$

where ε_{254,H_2O_2} is the molar absorption coefficient of H_2O_2 at 254 nm (19.6 M^{-1} cm^{-1} [105]), $\emptyset_{254,H_2O_2}$ is the quantum yield of H_2O_2 at 254 nm (0.5 mol $photon^{-1}$ [105]), k_{obs,H_2O_2} is the observed pseudo-first-order rate constant for the photolysis of H_2O_2 and were calculated to be 6.8×10^{-5} s^{-1} (Figure 2.11). Using

Equation 2.16, the determined b was 2.37 cm, which was applied into Equation 2.14. The finally determined α value was 0.94, and the shielding effect of H_2O_2 was corrected by multiplying the term of the UV system in Equation 2.12 by 0.94. All CK experiments for $k_{\bullet OH,MC}$ were conducted at least in duplicate, and the average values with standard deviations were presented.

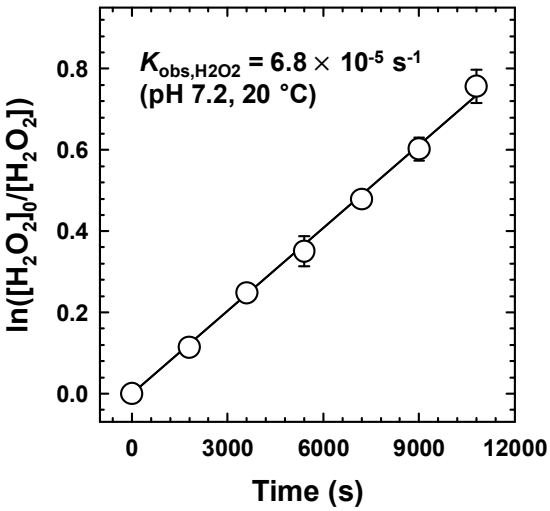

Figure 2.11. Time-dependent profile of $\ln([H_2O_2]_0/[H_2O_2])$ during UV illumination ($[H_2O_2]_0$ = 0.1 mM, $[t\text{-BuOH}]_0$ = 10 mM, [PBS] = 10 mM, pH = 7.2, temperature = 21 ± 1°C).

2.2.3. Natural water samples. Two natural water samples were obtained from two sites in the Republic of Korea: the intakes of the Maegok drinking water treatment plant in Daegu, and from the raw waters of Gamak lake in Ulsan city. The natural waters were filtered with a 0.45 μm filter within 24 h after sampling. The two natural waters were gently concentrated at 40°C overnight for the SFS experiments which accompany the dilution of the samples, then were stored at 4°C until use. Table 2.3 summarizes the water quality parameters of the natural waters used in the actual experiments (i.e., the diluted state).

Table 2.3. Characterization of natural waters

Parameters	Natural waters	
	Maegok	Cheonsang
DOC (mgC L^{-1})	5.06 ± 0.12	2.66 ± 0.06
pH	7.65	7.95

2.2.4. Analysis of O_3 in natural waters. The decrease of O_3 during the natural water tests was measured by SFS. The SFS system worked with two 10 mL syringes, each filled with O_3 and natural water samples. The operation conditions of SFS for the natural water experiments was the same as that of the *Determination of* $k_{O3,MC}$ in section 2.2.2. The acquisition of the absorbance data at 258 nm was performed every millisecond until the O_3 was completely decomposed. It is important to note that the blank absorbance by the natural water sample should be considered during data processing. To calculate the actual concentration of O_3, the absorbance by natural water sample was compensated for by the following data fitting process: i) two fit lines are obtained for the two phases (i.e., decreasing and stationary phases) using OriginPro 8.5 software (OrginLab Co., USA) (Figure 2.12a), ii) after subtracting the two fit lines from each other, the actual O_3 concentrations were calculated using the molar absorption coefficients of O_3 (Figure 2.12b). All experiments were carried out at least in duplicate, and the average values with standard deviations were presented.

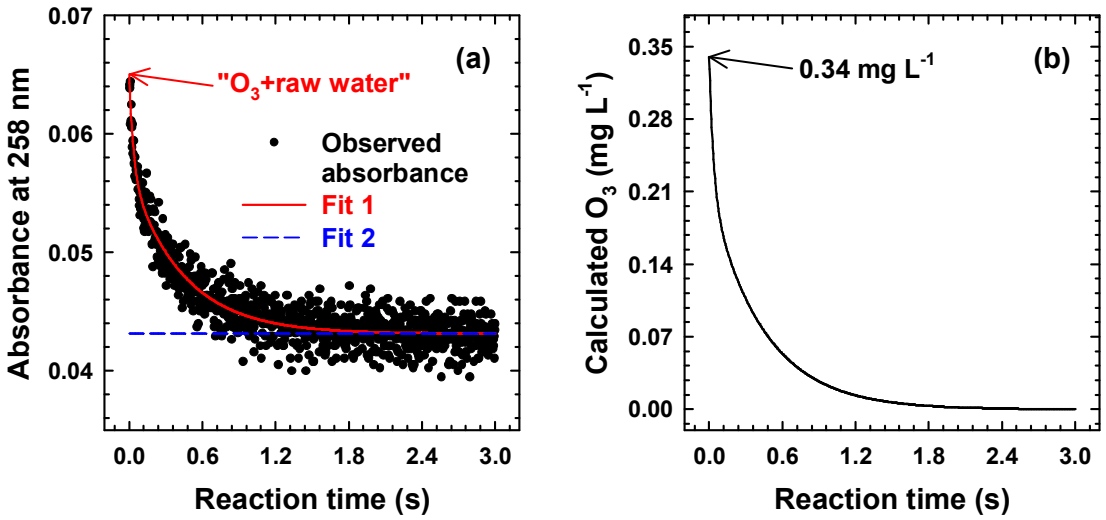

Figure 2.12. Example of measurement of CA concentration. (a) Absorbance at 258 nm during O_3 decomposition in Gamak natural water. Red and bule dotted lines represent fits of the absorbance regarding whole examined reaction time and stationary phases (from 2 to 3 s), respectively. (b) Calculated O_3 from the subtraction of blue dotted line from red line in (a) ($[O_3]_0$ = 0.35 mg L^{-1}, pH = 7.95, temperature = 20 ± 1°C).

2.2.5. Analytical methods. MCs were measured using RSLC (UltiMate 3000, Dionex Co., USA) system with UV absorbance detection at 222 nm (for MC-LF) and 238 nm (for other MCs). The chromatographic separation was performed on an Acclaim^{TM} C18 column (2.1 mm × 50 mm, 2.2 μm, 120 Å; Thermo Fisher Scientific Inc., USA) using an isocratic mixture of 0.05% trifluoroacetic acid and methanol at a flow rate of 0.3 mL min^{-1}. The methanol content in the mobile phase was 60 % for MC-RR, -LR and -YR; and 70 % for MC-LF, -LW and -LA. The oxidation products of MC-LR was analyzed by RSLC coupled with a Q Exactive™ Quadrupole-Orbitrap Mass Spectrometer (Thermo Fisher Scientific Inc., USA) (LC/MS). Detailed analytical conditions were the same as those used for the *Identification of MC-LR and its products* in section 2.1.4. CA, *p*CBA and HCHO derivatized by DNPH (HCHO-2,4-DNPH) were also analyzed by RSLC with UV absorbance detection at 280, 230 and 350 nm, respectively. Separation was performed on the same analytic column as mentioned above using an isocratic mixture of 0.1% phosphoric acid and organic solvents (methanol for CA and acetonitrile for *p*CBA and HCHO-2,4-DNPH in a 50:50 ratio at a flow rate of 0.3 mL min^{-1}. The concentrations of Fe(II) and H_2O_2 were measured by the 1,10-phenanthroline method[106] and the titanium sulfate method[107] using a UV/Vis spectrophotometer (S-3100, Sinco Co., Korea). The concentration of dissolved organic carbon (DOC) was measured by TOC analyzer (TOC-V_{CPH}, Shimadzu Co., Japan).

2.3. Oxidation of MC-LR by Fe(IV)-TPP complex

2.3.1. Reagents. All chemicals were of reagent grade and were used without further purification, except for DNPH. DNPH was recrystallized three times using acetonitrile. The chemicals used in this study are as follows: iron(II) sulfate heptahydrate (≥99%, Sigma-Aldrich), EDTA (99.4–100.6%, Sigma-Aldrich), and sodium tetrapolyphosphate (≥98%, International Laboratory Co.). $Fe(ClO_4)_3 \cdot xH_2O$, H_2O_2, NaOH, $HClO_4$, $K_2C_2O_4 \cdot H_2O$, six MCs (MC-RR, -LR, -YR, -LF, -LW, and -LA), 0.1% formic acid (v/v) in water, trifluoroacetic acid, acetonitrile, and methanol were same as that of section 2.1.1. and 2.2.1. All solutions were prepared using deionized (DI) water (>18 MΩ·cm, Millipore Co., USA). The Fe(II) stock solution (10 mM) was prepared immediately prior to the experiments.

2.3.2. Experimental procedure. All experiments for Fe(II)-TPP/O_2 and Fe(II)-TPP/H_2O_2 systems were performed with 20 mL solutions in a 25 mL-beaker open to the atmosphere at room temperature (23 ± 2˚C). Iron chelators such as TPP and/or H_2O_2 were first mixed with a target MC and the pH was then adjusted using 0.1 N $HClO_4$ and 0.1 N NaOH solutions. In the presence of TPP, which also functions as a buffer, the pH of the solution varied by less than 0.2 units for each reaction. The reaction was initiated by adding an aliquot of the Fe(II) stock solution. Samples (1 mL) were withdrawn at predetermined time intervals and were immediately quenched by the addition of 20 μL methanol. The UV/H_2O_2 experiments were performed using a 30-mL quartz reactor placed in a dark chamber equipped with 4W low-pressure mercury lamps (λ_{max} = 254 nm, Philips Co., USA). The incident light intensity of this setup was determined to be 1.27×10^{-6} Einstein/L/s by ferrioxalate actinometry (refer to Figure 2.9).[104] All experiments were conducted at least in duplicate, and the mean values with standard deviations are presented.

2.3.3. Experimental design for response surface methodology. Response surface methodology (RSM) was applied to evaluate the optimal doses of Fe(II), TPP, and H_2O_2 needed to efficiently degrade MC-LR by the Fe(II)-TPP/O_2 and Fe(II)-TPP/H_2O_2 systems. A two-factor and three-level central composite face-centered design (CCFCD) was employed to generate a regression model with a minimum number of experimental trials. The CCFCD matrix consisted of nine experimental points, including a center point that was replicated three times. In this study, two separate models were developed for the respective Fe(II)-TPP/O_2 and Fe(II)-TPP/H_2O_2 systems. Models for efficient degradation of MC-LR were developed using two independent factors (i.e., Fe(II) and TPP concentrations for the Fe(II)-TPP/O_2 system; TPP:Fe(II) molar ratio ([TPP]/[Fe(II)]) and H_2O_2 concentration for the Fe(II)-TPP/H_2O_2 system). The explored ranges (center point ± variance) of Fe(II) concentration (X_1), TPP concentration (X_2), [TPP]/[Fe(II)] (X_3), and H_2O_2 concentration (X_4) were 100 ± 95 μM, 500 ± 490 μM, 5 ± 4.9, and 250 ± 250 μM, respectively (Table 2.4).

Table 2.4. Experimental design for RSM

Trials	Group 1 (Fe(II) vs. TPP)[a]		Group 2 ([TPP]/[Fe(II)] vs. H_2O_2) [b]	
	X_1: Fe(II) (μM)	X_2: TPP (μM)	X_3: [TPP]/[Fe(II)][c]	X_4: H_2O_2 (μM)
1	5	10	0.1	0
2	5	500	0.1	250
3	5	990	0.1	500
4	100	10	5	0
5	100	500	5	250
6	100	990	5	500
7	195	10	9.9	0
8	195	500	9.9	250
9	195	990	9.9	500

[a]Group 1: experimental conditions for Fe(II)-TPP/O_2 system. [b]Group 2: experimental conditions for Fe(II)-TPP/H_2O_2 system. [c]$[Fe(II)]_0$ = 100 μM.

The experimental data were fitted into a quadratic polynomial using the following equation:

$$Y = \beta_0 + \sum_{i=1}^{n} \beta_i X_i + \sum_{i=1}^{n} \beta_{ii} X_i^2 + \sum_{i=1}^{n-1} \sum_{j=i+1}^{n} \beta_{ij} X_i X_j \quad (2.17)$$

Where, Y is the predicted response; n is the number of variables, X_i and X_j refer to the input variables, β_0 is the intercept coefficient, β_i is the linear coefficient, β_{ij} is the interaction coefficient, and β_{ii} is the quadratic coefficient. The adequacy of each developed regression model was evaluated by R^2, p-value, lack-of-fit (*LOF*), adequate precision (*AP*), and the normal probability plot of residuals. The analysis of variances (ANOVA) was carried out using the Design-Expert 7.1.6 software (Stat-Ease Inc., USA).

2.3.4. Analytical methods. The measurement of MCs, oxidation products of MC-LR, HCHO, Fe(II), H_2O_2 were same as that of section 2.2.4. The hepatotoxicities of solutions containing MC-LR and its oxidation products were evaluated by the PP2A activity assay using a MicroCystest kit (ZEU Inmunotec, Spain). For the assay, the linear range in which the inhibition of PP2A activity is clearly observed is 0.25-2.5 nM (0.251-2.512 μg/L) as MC-LR. Samples were appropriately diluted to yield readings within this range. The relative inhibition of PP2A activity ([PP2A activity of DI water − PP2A activity of sample] / PP2A activity of DI water × dilution factor) was used as an indicator to represent the hepatotoxicity.

Chapter 3. Results and Discussion

3.1. Oxidation of MCs by Mn(VII)

3.1.1. Kinetics for the reactions of MCs with Mn(VII). $k_{Mn(VII),MC}$ *at neutral conditions.* To estimate the reactivity of the six MCs with Mn(VII), $k_{Mn(VII),MC}$ values were determined at pH 7.2 and 21 ± 1°C (Table 3.1). The $k_{Mn(VII),MC}$ values were calculated from the slope of the linear plot of the pseudo-first-order rate constant (k_{obs}) versus the initial concentration of Mn(VII) (Figure 3.1a); Figure 3.2 presents the time-dependent profiles of $\ln([MC]_0/[MC])$ to determine the k_{obs} values. The determined $k_{Mn(VII),MC}$ values varied from 160.4 to 520.1 $M^{-1} s^{-1}$ with the order MC-RR > -LR ≈ -YR > -LF ≈ -LW > -LA, which exhibited reasonable agreement with the results of previous studies.[30, 42–44] There are two possible explanations on how amino acids in the X and Y positions can affect the reactivity of MCs with Mn(VII). First, the direct reactions of those amino acids in the X and Y positions with Mn(VII) can be considered. However, this possibility is ruled out by the observation that the related amino acids do not significantly react with Mn(VII) (except for Tyr, which possesses a highly Mn(VII)-reactive phenolic group)[72] (refer to Figure 3.3). Second, the amino acids in the X and Y positions can alter the electron density of reaction sites; alkene groups in the Adda and Mdha moieties of MC structure are known to be the primary oxidation sites by Mn(VII) (refer to Figure 3.4).[21, 43, 44, 49] It appears that electron-donating and -withdrawing properties of the amino acids in the X and Y positions change the π-d electron density of the alkenes through electronic (inductive/resonance) effects.[108, 109] This explanation is quite interesting, because the alkene groups are relatively far (four to six bonds distant) from the amino acids in the X and Y positions (refer to Figure 1.3).

Table 3.1. Summary of $k_{Mn(VII),MC}$ and E_a values

	MC-RR	MC-LR	MC-YR	MC-LF	MC-LW	MC-LA	Conditions	References
$k_{Mn(VII),MC}$ (M^{-1} s^{-1})	520.1 ± 8.6	386.2 ± 0.4	382.1 ± 1.2	213.4 ± 0.3	201.7 ± 2.6	160.4 ± 1.3	pH 7.2, 21 ± 1°C	This study
	469.0 ± 37.0						pH 6.7, 25°C	42
	418.0	357.2 ± 12.5	405.9				pH 7.2, 20°C	43
	470	408	396	246	273	170	pH 7.6, 22 ± 1°C	30
		289.9					Neutral pH, 23 ± 2°C	44
E_a (kJ mol^{-1})	20.8 ± 1.6	21.2 ± 0.9	19.4 ± 0.5	19.7 ± 0.6	15.1 ± 0.7	21.5 ± 0.6	pH 7.2, 5−30°C	This study
	18.9						pH 6.7, 15−30°C	42

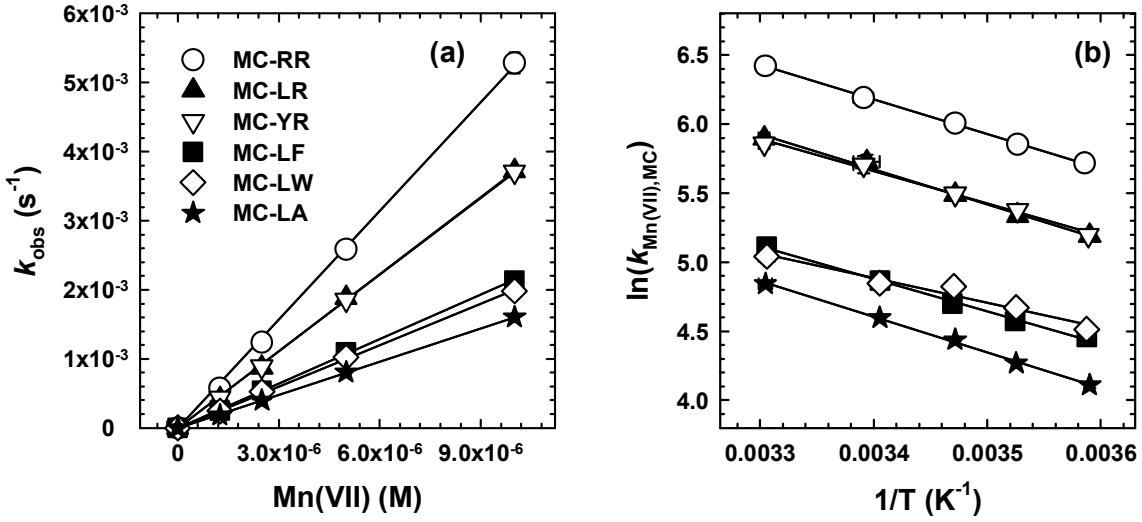

Figure 3.1. (a) Plots of k_{obs} as a function of Mn(VII) concentration, and (b) Arrhenius plots of $k_{Mn(VII),MC}$ ($[MCs]_0$ = 0.1 μM, pH = 7.2 for (a) and (b); temperature = 21 ± 1°C for (a)).

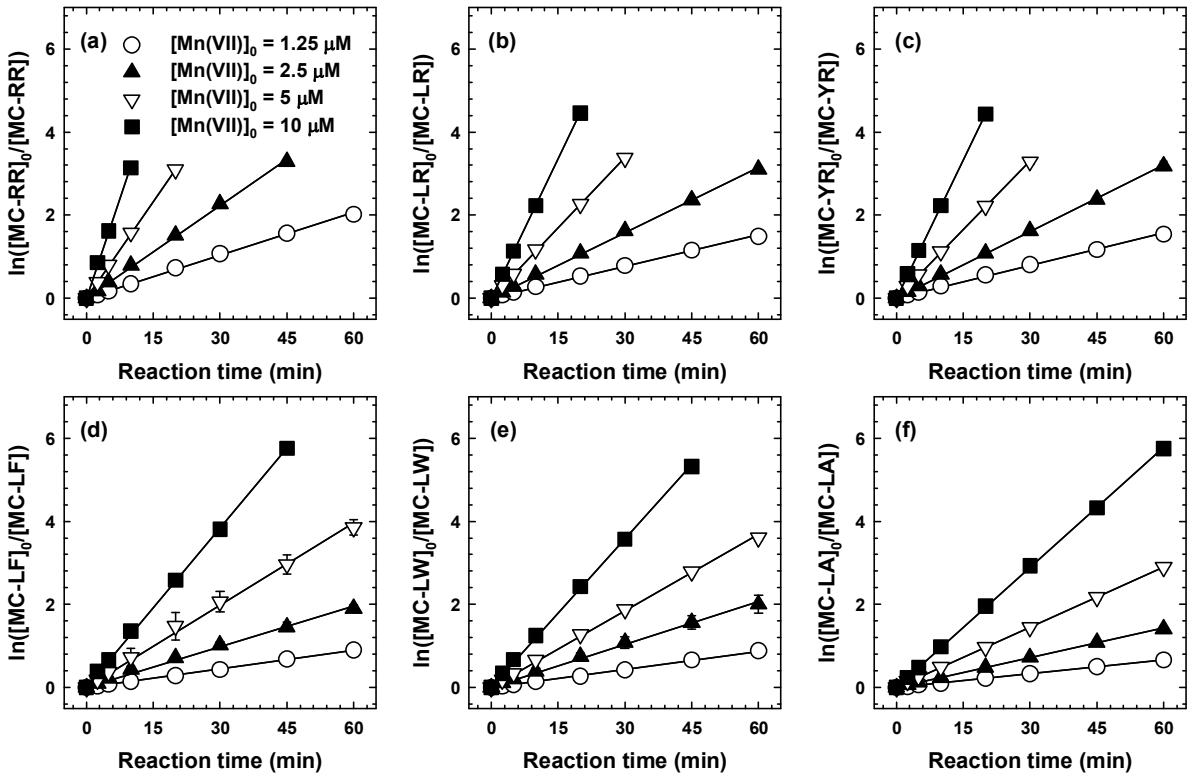

Figure 3.2. Time-dependent profiles of ln($[MC]_0$/[MC]) at different Mn(VII) doses ($[MC\text{-}RR]_0$ = $[MC\text{-}YR]_0$ = $[MC\text{-}LR]_0$ = $[MC\text{-}LW]_0$ = $[MC\text{-}LF]_0$ = $[MC\text{-}LA]_0$ = 0.1 μM, pH 7.2, temperature = 21 ± 1°C).

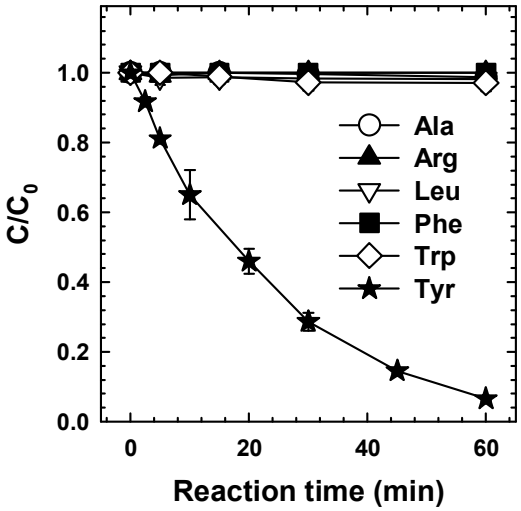

Figure 3.3. Oxidation of L-amino acids by Mn(VII) ([L-Ala]$_0$ = [L-Arg]$_0$ = [L-Leu]$_0$ = [L-Phe]$_0$ = [L-Trp]$_0$ = [L-Tyr]$_0$ = 0.1 μM, [Mn(VII)]$_0$ = 5 μM, pH 7.2, temperature = 21 ± 1°C).

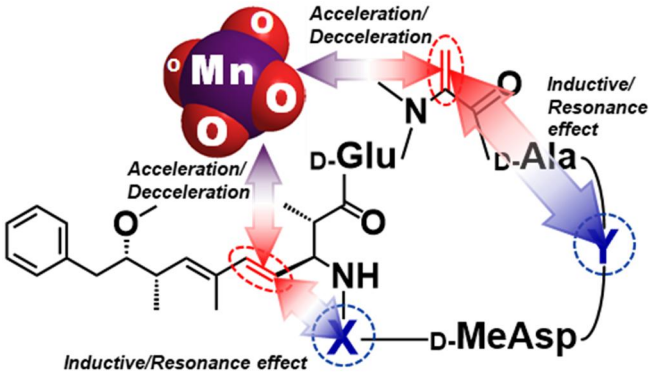

Figure 3.4. Electronic effect of the amino acids located in the X and Y positions in MC structure on the reactivities of alkene groups with Mn(VII).

Effect of temperature on $k_{Mn(VII),MC}$. The temperature-dependency of $k_{Mn(VII),MC}$ was examined with varying temperatures from 5 to 30°C. The E_a values for the reactions of MCs with Mn(VII) were calculated to be 15.1–22.4 kJ mol^{-1} (Table 3.1) from the slope of the Arrhenius plot (ln($k_{Mn(VII),MC}$) versus 1/T) (Figure 3.1b); Figure 3.5 represents the time-dependent profiles of ln([MCs]$_0$/[MC]). The activation parameters (i.e., activation enthalpy ($\Delta H^{\ddagger}$) and activation entropy ($\Delta S^{\ddagger}$)) of each MC were determined by the Erying equation. The $\Delta H^{\ddagger}$ and $\Delta S^{\ddagger}$ values of the six MCs ranged from 12.6 to 19.1 J mol^{-1}, and from −131.3 to −161.2 J K^{-1} mol^{-1}, respectively (Table 3.2). Relatively low $\Delta H^{\ddagger}$ and high negative $\Delta S^{\ddagger}$ values were also reported for the reactions of other alkene compounds with Mn(VII) (Table 3.2).[73, 111–114] On the basis of the determined E_a values, the $k_{Mn(VII),MC}$ values vary by 72.3–745.8 M^{-1} s^{-1} depending on MC in the temperature range of 10.5–37.0°C, at which the blooms of *Microcystis aeruginosa* generally occur.[115, 116] The removal efficiency of MCs by Mn(VII) can change with temperature accordingly.

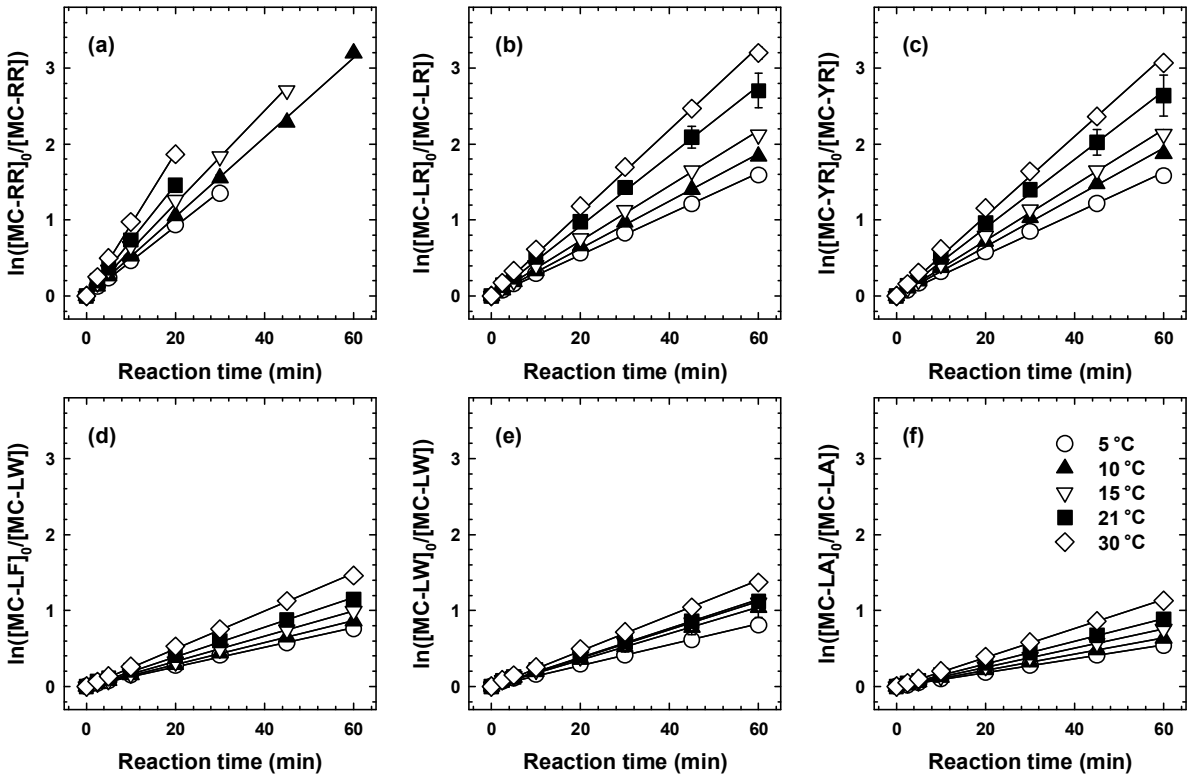

Figure 3.5. Time-dependent profiles of ln([MC]$_0$/[MC]) at different temperatures ([MC-RR]$_0$ = [MC-YR]$_0$ = [MC-LR]$_0$ = [MC-LW]$_0$ = [MC-LF]$_0$ =[MC-LA]$_0$ = 0.1 μM, [Mn(VII)]$_0$ = 2.5 μM, pH 7.2).

Table 3.2. Summary of the activation enthalpy ($\Delta H^{\ddagger}$) and activation entropy ($\Delta S^{\ddagger}$) for the Mn(VII) reactions of different compounds having alkene groups (the values for MCs determined in this study, and those for other compounds reported in the literature)

Substrates	$\Delta H^{\ddagger}$ (J mol^{-1})	$\Delta S^{\ddagger}$ (J K^{-1} mol^{-1})	pH	References
MC-RR	18.3 ± 1.5	-131.3 ± 5.3	7.2	This study
MC-LR	18.7 ± 0.9	-134.1 ± 3.2		
MC-YR	16.9 ± 0.5	-140.3 ± 1.8		
MC-LF	17.2 ± 0.7	-145.8 ± 2.4		
MC-LW	12.6 ± 0.8	-161.2 ± 2.9		
MC-LA	19.1 ± 0.5	-141.7 ± 1.6		
Allyl alcohol	31.4 ± 2.9	-100.4 ± 8.4	6.5-13	110
Acrylate	22.2 ± 2.9	-125.5 ± 8.4		
Crotonate	20.1 ± 2.9	-133.9 ± 8.4		
Vinylacetate	26.8 ± 2.9	-117.2 ± 8.4		
4-Pentenoate	27.6 ± 2.9	-112.9 ± 8.4		
Cinnamate	13.8 ± 2.9	-150.1 ± 8.4		
Maleic acid	12[a]	-140[a]	3.15	111
Fumaric acid	13[a]	-140[a]	5.0	
Methylfumaric acid	17.6[a]	-128[a]	5.42	112
Dimethylmaleic acid	15.5[a]	-148[a]	3.6	
Bromomaleic acid	17.4[a]	-164[a]	4.96	113
Dibromomaleic acid	15.2[a]	-169[a]	4.9	
cis-Dichloroethylene	36.8[a]	-150.6[a]	7	114
1,1-Dichloroethylene	34.7[a]	-129.7[a]		
trans-Dichloroethylene	34.3[a]	-125.5[a]		
Trichloroethylene	26.3[a]	-150.6[a]		
Tetrachloroethylene	21.7[a]	-138.1[a]		
Carbamazepine	19 ± 1	-140 ± 5	7	73

[a]Estimated accuracy ± 10%

Effect of pH on $k_{Mn(VII),MC}$. The effect of pH on $k_{Mn(VII),MC}$ was examined by varing pH 2–11 (Figure 3.6); Figure 3.7 presents the time-dependent profiles of ln([MCs]$_0$/[MC]). The results of Figure 2 show that the species-specific second-order rate constants can be determined using the predicted macroscopic pK_a values of MCs (Table 2.2); the speciation of Mn(VII) is ignorable (pK_a of $HMnO_4$ = –2.25[117]). Considering the pH-dependent species of MCs (e.g., MC_i = MC_1, MC_2, MC_3, etc.), $k_{Mn(VII),MC}$ can be expressed by Equation 3.1:

$$k_{Mn(VII),MC} = \sum_i k_{Mn(VII),MCi}\ \alpha_i \tag{3.1}$$

where, $k_{Mn(VII),MCi}$ and α_i represent the species-specific second-order rate constant and the molar fraction of MC_i, respectively. The $k_{Mn(VII),MCi}$ values were determined by fitting the experimental data of $k_{Mn(VII),MC}$ (Figure 3.6) into Equation 3.1, using the least-squares regression function of Microsoft Excel 2016 software. Table 3.3 summarizes the best-fit values of $k_{Mn(VII),MCi}$ for the six MCs. For all MCs, the species-specific rate constants were in the order $k_{Mn(VII),MC1} > k_{Mn(VII),MC2} > k_{Mn(VII),MC3} \approx k_{Mn(VII),MC4}$, except for MC-YR which showed high $k_{Mn(VII),MC4}$ and $k_{Mn(VII),MC5}$ values.

Figure 3.6 shows that the $k_{Mn(VII),MC}$ values of all MCs decreased with increasing pH from 2 to 5. A similar trend has typically been observed in Mn(VII) reactions of various organic compounds that compose the unsaturated C–C bonds (i.e., alkene and alkyne groups) with low pK_a values.[118–121] Alkene groups in MCs can be more electron-deficient by decreasing pH because of the inductive effect of protonated carboxyl groups,[122] which as a result, facilitates the nucleophilic attack of Mn(VII). It should be noted that Mn(VII) shows both electrophilic and nucleophilic nature for the reactions with alkenes, depending on the electron density of the target alkene group (affected by electron-donating or -withdrawing substituents).[123–126] While the $k_{Mn(VII),MC}$ values generally plateaued over pH 5, only $k_{Mn(VII),MC}$ for MC-YR increased from pH 9 to 11 (Figure 3.6c). This increased reactivity of MC-YR is mainly attributed to the deprotonation of the phenolic group in Tyr ($–C_6H_5OH \rightarrow –C_6H_5O^–$, p$K_a$ = 9.9; refer to Figure 2.4).[127, 128]

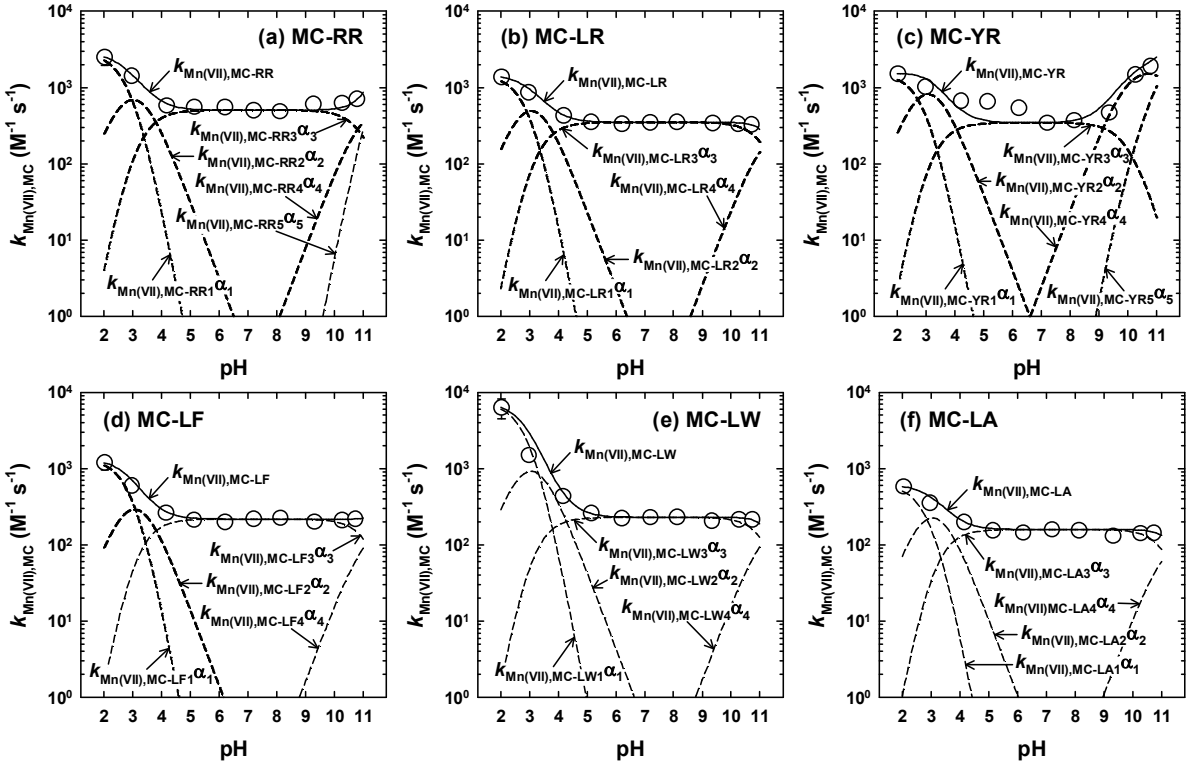

Figure 3.6. Effect of pH on the $k_{Mn(VII),MC}$ values for the six selected MCs. Symbols represent experimental data, and lines represent model predictions of $k_{Mn(VII),MC}$ (solid) and $k_{Mn(VII),MCi}\,\alpha_i$ (dashed) ($[MCs]_0$ = 0.1 μM, $[Mn(VII)]_0$ = 2.5 μM, temperature = 21 ± 1°C).

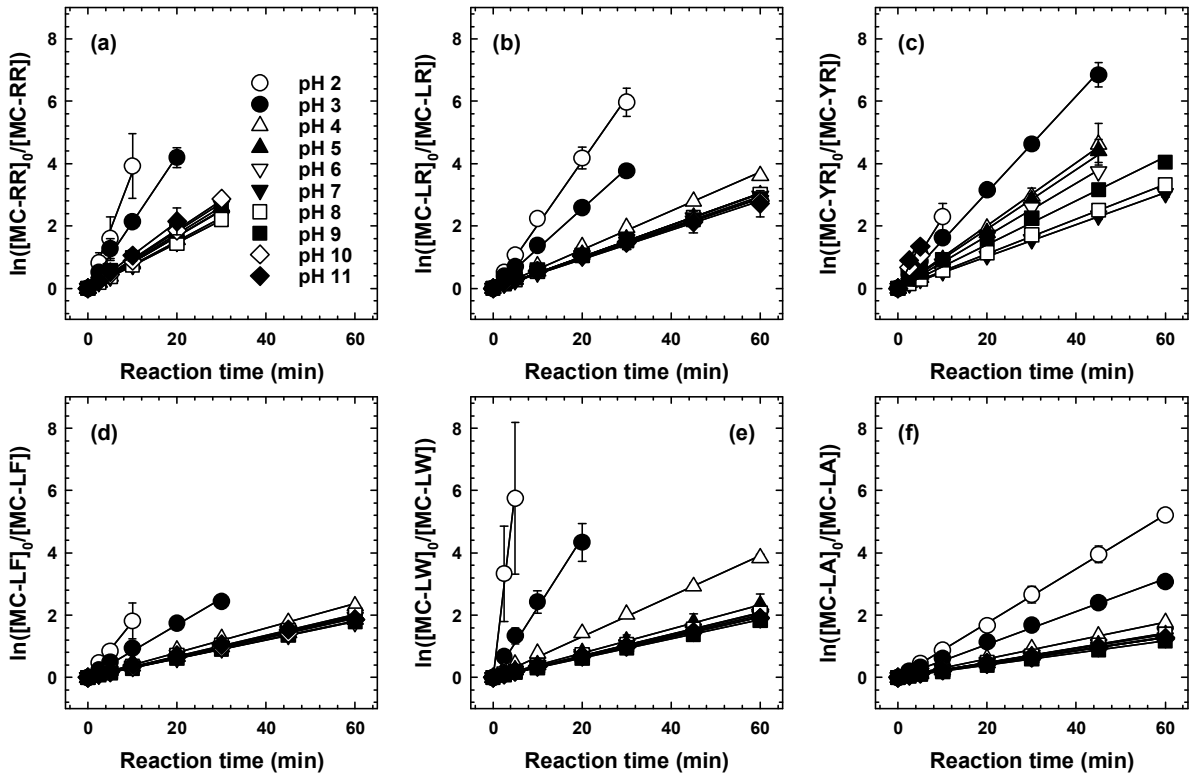

Figure 3.7. Time-dependent profiles of $\ln([MC]_0/[MC])$ at different pH values ($[MC\text{-}RR]_0 = [MC\text{-}YR]_0 = [MC\text{-}LR]_0 = [MC\text{-}LW]_0 = [MC\text{-}LF]_0 = [MC\text{-}LA]_0$ = 0.1 μM, $[Mn(VII)]_0$ = 2.5 μM, temperature = 21 ± 1°C).

Table 3.3. Summary of the species-specific second-order rate constants for the reactions of MCs with Mn(VII) ($k_{Mn(VII),MCi}$, M^{-1} s^{-1}), determined in this study

MCs	$k_{Mn(VII),MC1}$	$k_{Mn(VII),MC2}$	$k_{Mn(VII),MC3}$	$k_{Mn(VII),MC4}$	$k_{Mn(VII),MC5}$
MC-RR	2862 ± 607.3	1241.6 ± 144	505.3 ± 9.3	651.7 ± 20.7	-
MC-LR	1468.9 ± 82	934.6 ± 33.3	350.3 ± 12.3	332.8 ± 14.4	-
MC-YR	1531 ± 167	1548 ± 26.1	345.7 ± 10.7	2002.2 ± 87	4698.7 ± 137
MC-LF	1330.9 ± 301.7	552.8 ± 31	218.1 ± 2.9	209.4 ± 4.4	-
MC-LW	7282.3 ± 2269.5	1746.6 ± 99.1	230.2 ± 4.3	214.2 ± 4.3	-
MC-LA	615.2 ± 8.4	427.6 ± 86.8	159.4 ± 5.3	139.6 ± 0.6	-

$k_{Mn(VII),MCi}$ values ($i > 4$) are not shown because of their high uncertainty (except for $k_{Mn(VII),MC\text{-}YR5}$).

3.1.2. Oxidative degradation of MCs in natural waters. The oxidative degradation of MCs by Mn(VII) was examined in five natural water samples spiked with MCs at trace concentrations (10 nM) (Figure 3.8). The oxidation rates of the MCs in Maegok and Cheonsang waters were lower than those in Hoeya, Gamak, and Taehwa waters, because Maegok and Cheonsang waters commonly include higher contents of DOM. DOM decomposes Mn(VII), thus consuming $\int$[Mn(VII)]dt. Indeed, the $\int$[Mn(VII)]dt values in Maegok and Cheonsang waters were lower than the others; the $\int$[Mn(VII)]dt values in the five natural waters were obtained by monitoring the decomposition of Mn(VI) during the reaction (Figures 3.9 and 3.10). Using the $k_{Mn(VII),MC}$ and $\int$[Mn(VII)]dt values (Figures 3.6 and 3.10), the oxidation of MCs by Mn(VII) in natural waters was modeled by the following equation:

$$[MC]_t = [MC]_0 \exp(-k_{Mn(VII),MC} \int [Mn(VII)]dt) \quad (3.2)$$

In all cases, the model calculations (solid lines in Figures 3.8a–e) fit very well with the experimental data.

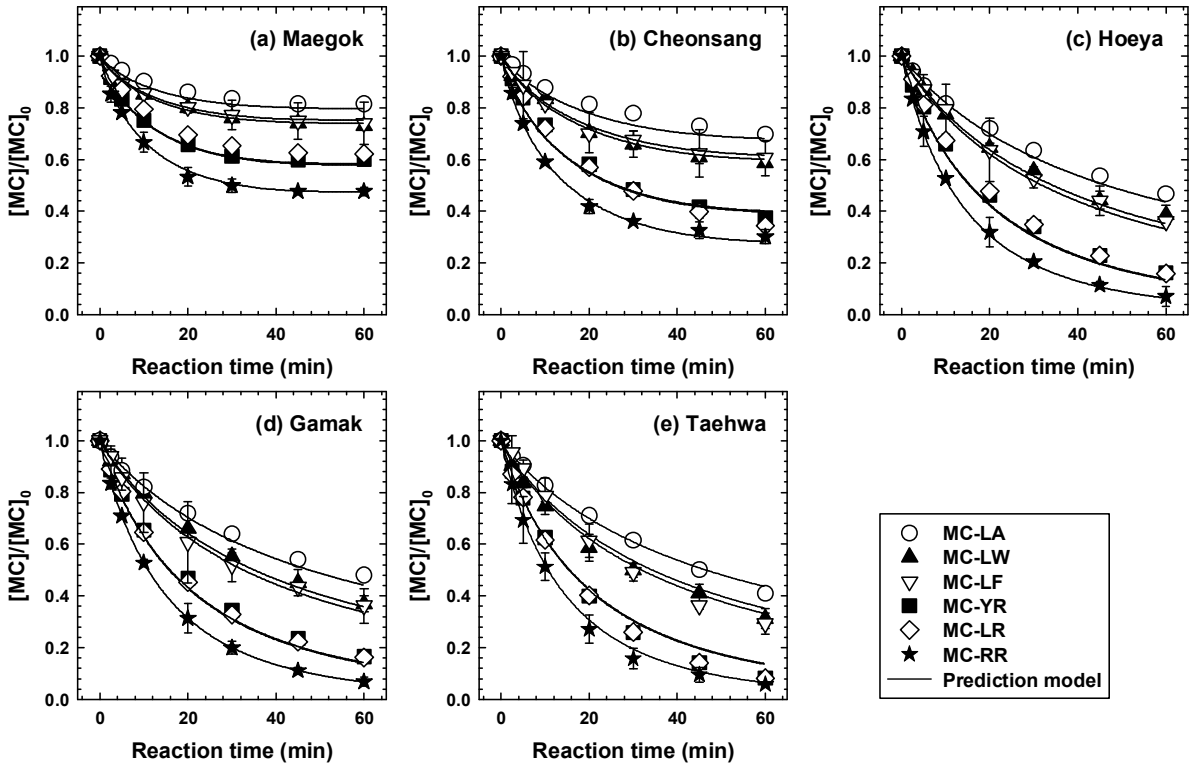

Figure 3.8. Oxidation of MCs in natural waters. Symbols represent experimental data, and solid lines represent model predictions using Equation 3.2 with the measured $\int$[Mn(VII)]dt ([MCs]$_0$ = 10 nM, [Mn(VII)]$_0$ = 2.5 μM, temperature = 21 ± 1°C).

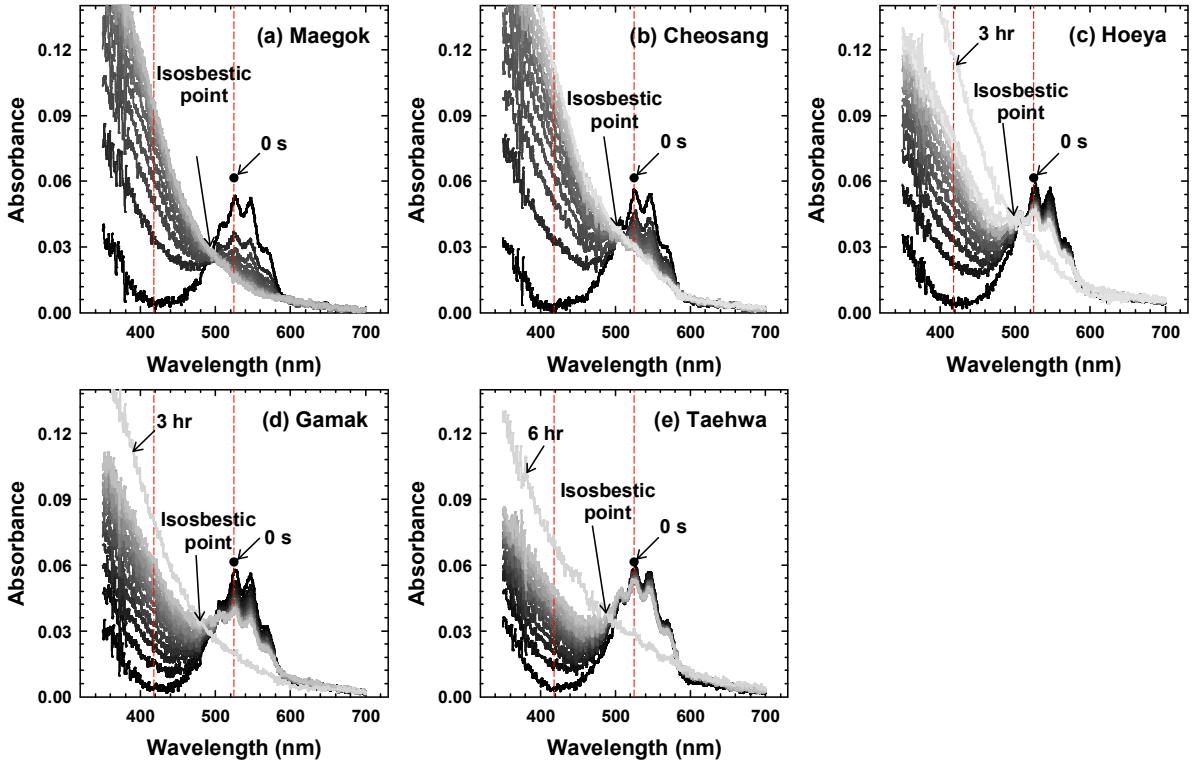

Figure 3.9. Absorbance spectra during the decomposition of Mn(VII) in natural waters. The lightest lines are the final spectra ($[Mn(VII)]_0$ = 2.5 μM, temperature = 21 ± 1°C).

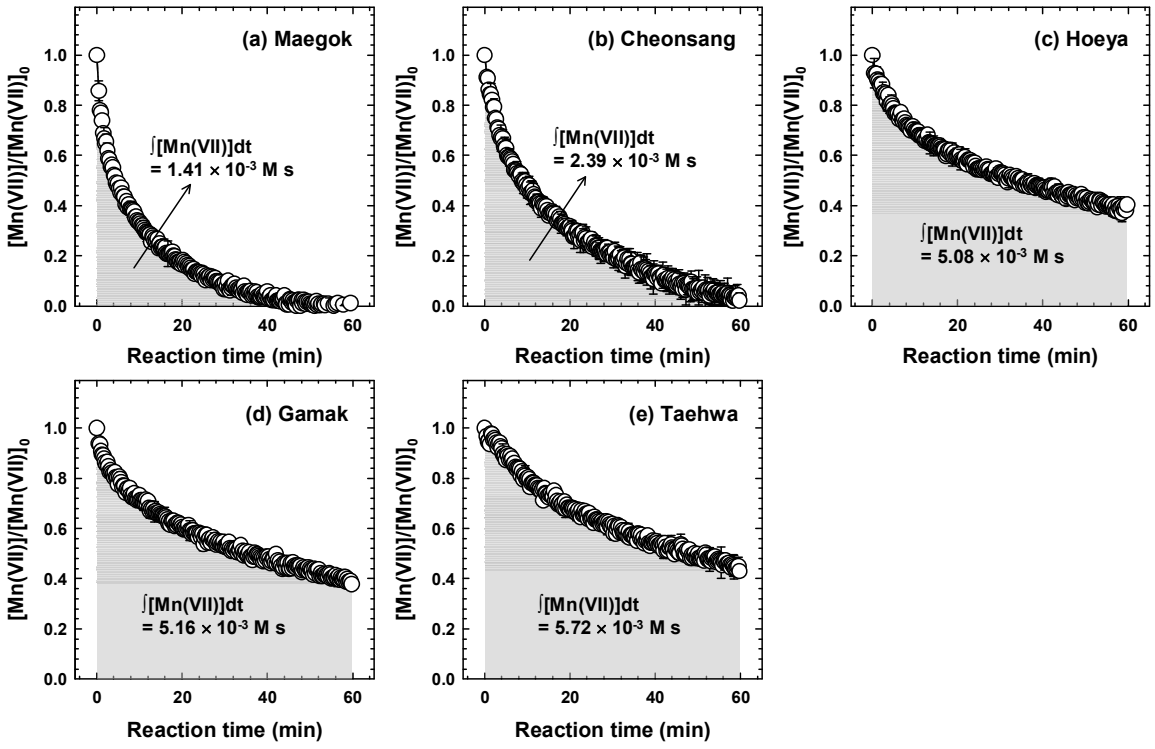

Figure 3.10. Decomposition of Mn(VII) in natural waters. The ∫[Mn(VII)]dt value was calculated for each graph ($[Mn(VII)]_0$ = 2.5 μM, temperature = 21 ± 1°C).

3.1.3. Effects of DOM characteristics on ∫[Mn(VII)]dt. Although the kinetic model (Equation 3.2) demonstrates a high prediction accuracy, its field application is cumbersome, because ∫[Mn(VII)]dt is variable depending on the water quality that can change in real time, and its immediate measurement in the water treatment plant is quite difficult. This limitation can be overcome, provided that ∫[Mn(VII)]dt is quantitatively correlated with water quality parameters that are immediately measurable in the field. The preliminary experiments demonstrated that the most important factors affecting ∫[Mn(VII)]dt were the type and concentration of the DOM; the effects of the other water quality parameters were ignorable. The detailed contents of the preliminary experiments are as follows.

Effects of water quality parameters on the oxidation of MC-LR by Mn(VII). In order to investigate the effects of several water quality parameters on Mn(VII) oxidation, the oxidation of MC-LR by Mn(VII) was examined by varying the input concentration of carbonate alkalinity, cations (K^+, Na^+, Ca^{2+}, NH_4^+, and Mg^{2+}), anions (Cl^-, Br^-, NO_3^-, PO_4^{3-}, and SO_4^{2-}), and DOM fractions (SRHA, SRFA, and NaHA) (Figure 3.11).

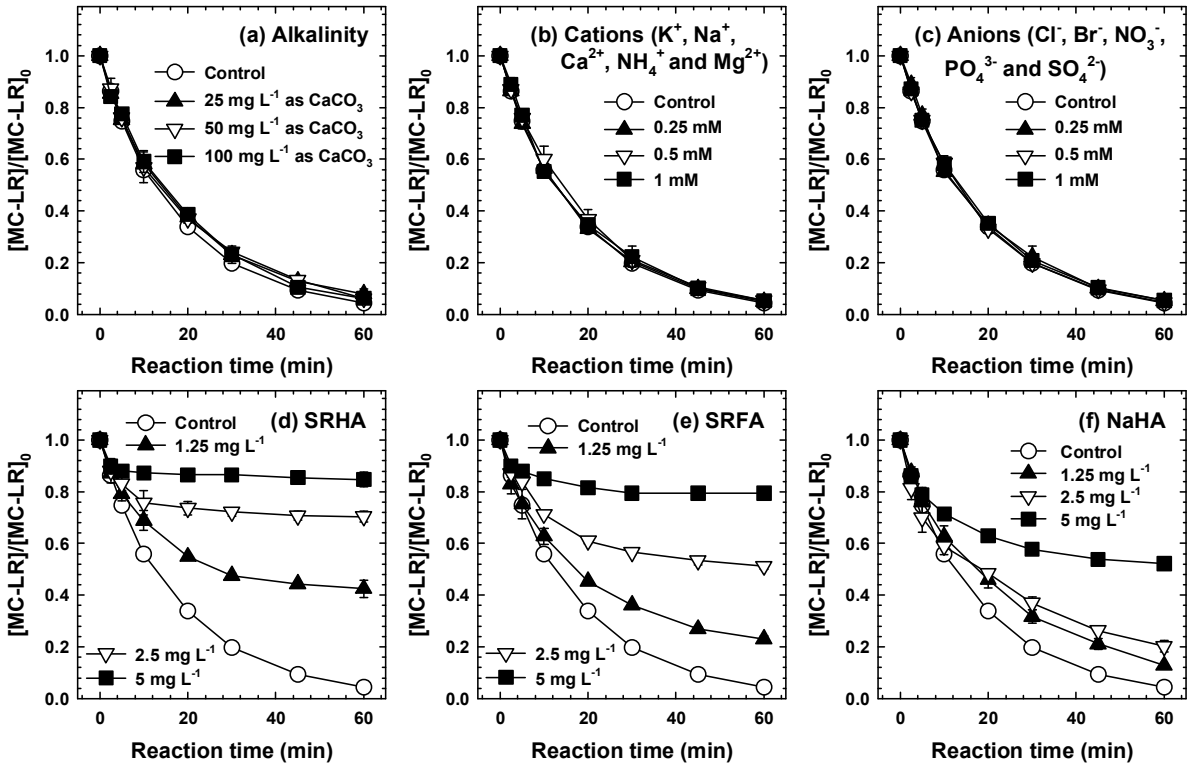

Figure 3.11. Effects of various water quality parameters on the oxidation of MC-LR by Mn(VII) ([MC-LR]$_0$ = 0.1 μM, [Mn(VII)]$_0$ = 2.5 μM, temperature = 21 ± 1°C; (b) counter anion: Cl^-; (c) counter cation: Na^+).

Alkalinity, cations, and anions showed negligible effects on the oxidation rate of MC-LR (Figures 3.11a–c). However, the type and concentration of DOM strongly affected the oxidation of MC-LR by Mn(VII) (Figure 3.11d–f), which is in agreement with the results of previous studies.[27, 44] This inhibitory effect of DOM fractions was in the order SRHA > SRFA > NaHA. This observation was somewhat different from that of a previous study, which showed stronger inhibitory effect of SRFA than SRHA on the MC-LR oxidation.[44] The reactivity of DOM with Mn(VII) is mainly determined by reactive functional groups in the DOM fractions. Figure 3.12 shows the Fourier-transform infrared (FTIR) spectra of SRHA, SRFA, and NaHA. In all spectra, O–H (3328 cm^{-1}), C–H (2923 cm^{-1}), C=O (1707 cm^{-1}), C=C (1606 cm^{-1}) and N–O (1384 cm^{-1}) groups were observed,[129] and their intensity varied according to the type of DOM. Among the functional groups observed, aromatic and olefinic C=C functional groups are known to be reactive with Mn(VII), and their content appears to increase in the order SRHA > SRFA > NaHA.[25, 126] On the other hand, aliphatic C–C functional groups, unreactive with Mn(VII), are found to be abundant in the order of NaHA > SRFA > SRHA.[44] These FTIR results are consistent with the order of inhibitory effects of DOM fractions.

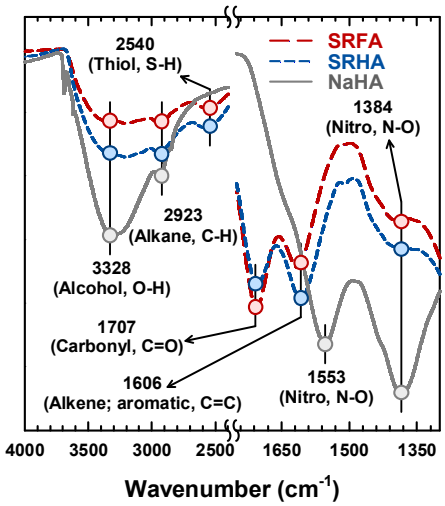

Figure 3.12. FTIR spectra of different DOM fractions.

Therefore, various DOM characteristics (i.e., DOC concentration, UV absorbance at 254 nm (UV_{254}), specific ultraviolet absorbance at 254 nm ($SUVA_{254}$), and fluorescence intensity values from the EEM spectra) of the five natural waters were analyzed for their correlation with ∫[Mn(VII)]dt. To draw DOM characteristics from the EEM fluorescence spectroscopy, the EEM spectra were categorized into four regions (i.e., aromatic protein (Region I), fluvic acid-like (Region II), soluble microbial byproduct-like (Region III), and humic acid-like substances (Region IV), Figure 3.13).[130] Then, the average values of fluorescence intensity in the four individual regions (four) and the values of peak fluorescence intensity in Region II and IV (two) were selected as DOM characteristics (total six); for

the latter two, the peak values were commonly found at Ex-235 nm/Em-426 nm and Ex-315 nm/Em-426 nm, respectively, in all the natural water samples (Figure 3.13).

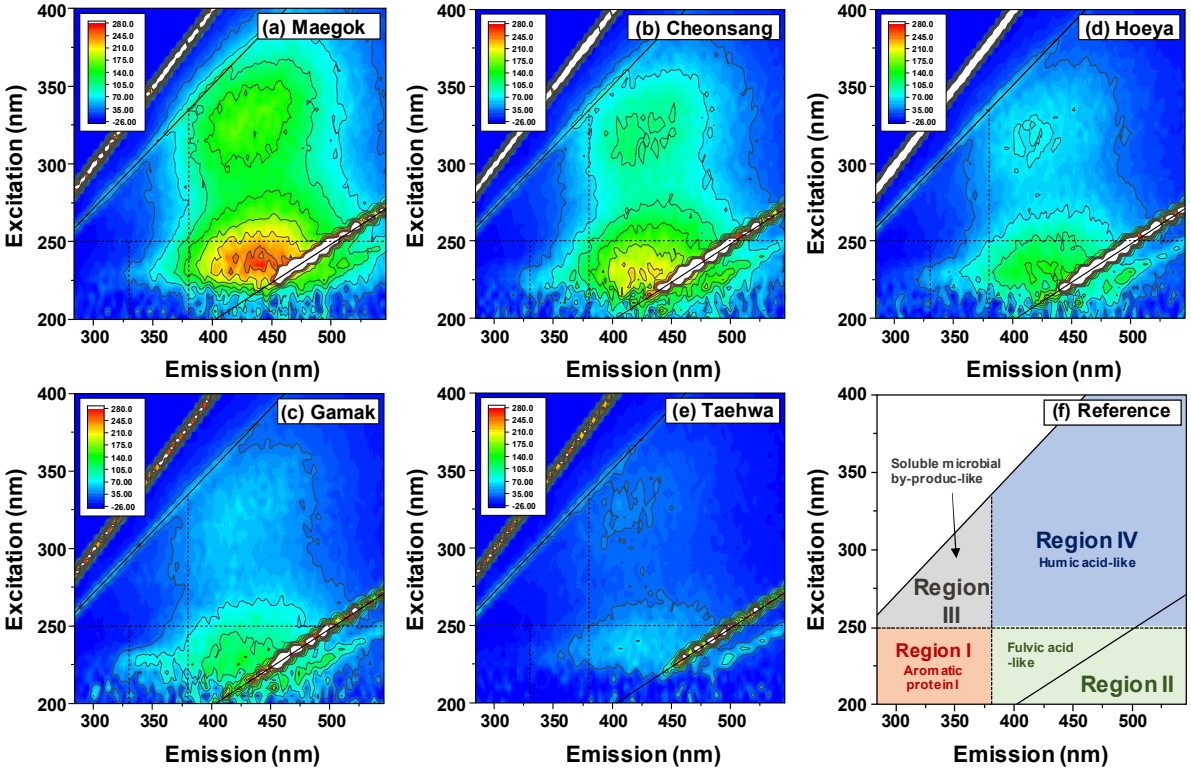

Figure 3.13. (a)–(e) Fluorescence excitation-emission matrix (EEM) spectra measured for the five natural waters, and (f) a reference indicating four regions in the EEM spectra.[130]

A total of nine DOM characteristics of natural waters were correlated with ∫[Mn(VII)]dt (Figure 3.14). As anticipated, ∫[Mn(VII)]dt was negatively correlated with DOC concentration, and exhibited fair linearity (R^2 = 0.84) (Figure 3.14a). UV_{254} and $SUVA_{254}$ were better correlated with ∫[Mn(VII)]dt (R^2 = 0.95 and 0.96) (Figures 3.14b and c), indicating that the aromatic carbon content of DOM mainly contributes to the Mn(VII) consumption. Among the DOM characteristics from EEM analysis (Figures 3.14c–i), the fluorescence intensity values for humic- and fulvic-like substances (Region III and V) were found to be strongly correlated with ∫[Mn(VII)]dt. The average intensity values of Region III and V showed fair linearity with ∫[Mn(VII)]dt (R^2 = 0.89 and 0.94, respectively; Figures 3.14e and g). In particular, the peak intensity values in Region III and V exhibited improved correlation with ∫[Mn(VII)]dt (R^2 = 0.94 and 0.99, respectively; Figure 3.14h and i). It is noteworthy that humic- and fulvic-like matters are composed of linearly condensed aromatic rings and conjugated unsaturated carbon contents, which are believed to be more prone to react with Mn(VII) (refer to Figure 3.12).[131, 132]

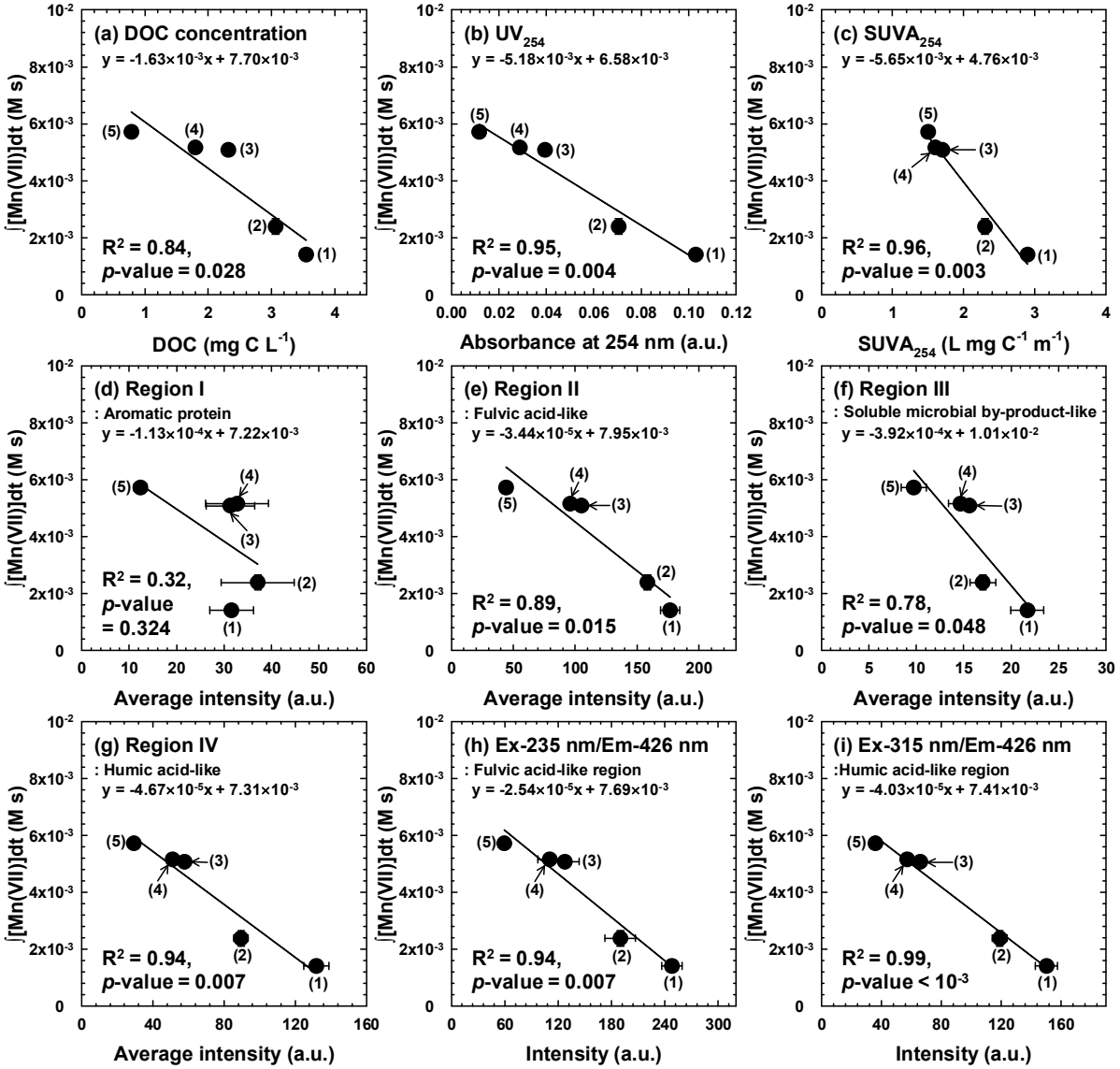

Figure 3.14. Correlation between ∫[Mn(VII)]dt and DOM characteristics ((a) DOM concentration, (b) UV_{254}, (c) $SUVA_{254}$, (d)–(g) average fluorescence intensity in five EEM regions, and (h)–(i) peak fluorescence intensity in Region II and IV) for natural waters ((1) Maegok, (2) Cheonsang, (3) Hoeya, (4) Gamak, and (5) Taehwa) ($[Mn(VII)]_0$ = 2.5 μM, temperature = 21 ± 1°C).

Meanwhile, the intensities in Region I and III, which are related to the protein components,[133, 134] showed relatively poor correlation with ∫[Mn(VII)]dt (R^2 = 0.19, 0.45, and 0.78, respectively; refer to Figures 3.14c, d, and f). These results are consistent with the observation that protein-like DOM fractions have less reactivity with Mn(VII).[44]

Table 3.4 presented the calculated The ∫[Mn(VII)]dt values in the five natural waters based on the correlation equations for the three best-correlated DOM characteristics (i.e., UV_{254} (Figure 3.14b), $SUVA_{254}$ (Figure 3.14c) and fluorescence intensity values at Ex-315 nm/Em-426 nm (Figure 3.14d)).

Table 3.4. Summary of the predicted ∫[Mn(VII)]dt values for natural waters

Natural waters	∫[Mn(VII)]dt[a]	∫[Mn(VII)]dt[b]	∫[Mn(VII)]dt[c]
Maegok	1.24×10^{-3}	1.09×10^{-3}	1.35×10^{-3}
Cheonsang	2.93×10^{-3}	3.00×10^{-3}	2.61×10^{-3}
Hoeya	4.54×10^{-3}	4.90×10^{-3}	4.75×10^{-3}
Gamak	5.09×10^{-3}	5.22×10^{-3}	5.10×10^{-3}
Taehwa	5.97×10^{-3}	5.54×10^{-3}	5.96×10^{-3}
Sample 01[d]	4.78×10^{-3}	5.21×10^{-3}	5.25×10^{-3}
Sample 02[e]	2.98×10^{-3}	3.24×10^{-3}	3.18×10^{-3}
Sample 03[f]	1.69×10^{-3}	1.65×10^{-3}	1.60×10^{-3}

[a, b, c] ∫[Mn(VII)]dt values were calculated from the slope of the linear regression plots of ∫[Mn(VII)]dt versus UV_{254} (Figure 3.14b), $SUVA_{254}$ (Figure 3.14c), and fluorescence intensity at Ex-315 nm/Em-426 nm (Figure 3.14i), respectively. [d, e, f] UV_{254} = 0.034, 0.069 and 0.094. [d, e, f] $SUVA_{254}$ = 1.60, 2.22 and 2.72. [d, e, f] Fluorescence intensity values at Ex-315 nm/Em-426 nm = 53.65, 104.95 and 144.05.

Using the calculated ∫[Mn(VII)]dt values and Equation 3.2, the removal efficiencies of the six MCs in the five natural waters were modeled, and the results were compared with the experimental data (Figure 3.15). The predictions using the calculated ∫[Mn(VII)]dt generally agreed with the experimental data; most of data points were located in the 95% prediction intervals. This model prediction was further verified using three additional natural waters that has not been utilized to draw the correlation equations (Figure 3.16). These results indicate that the DOM characteristic immediately measured by UV and fluorescence spectroscopy can be a useful index to predict the removal of MCs by Mn(VII), and also can be possibly extendable to the oxidation of other organic contaminants.

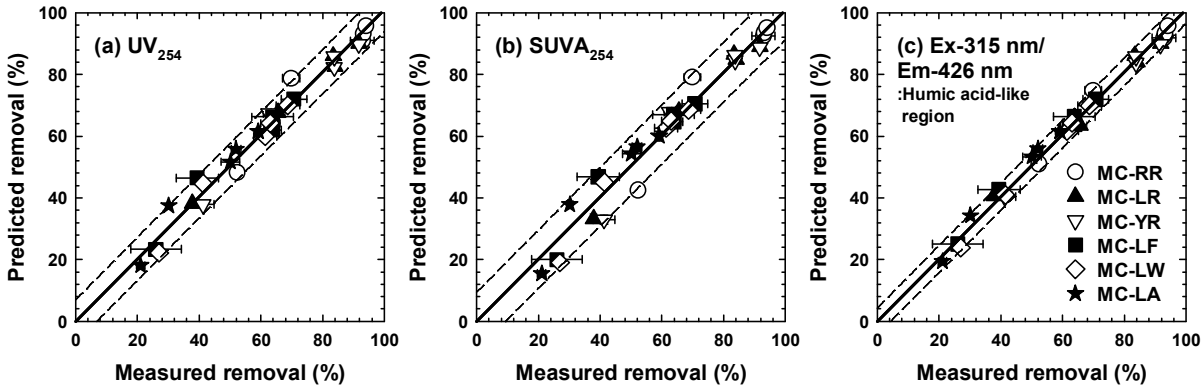

Figure 3.15. Experimental and predicted removal efficiency of MCs in natural waters. Lines represent the obtained linear regression model (solid) and the 95% prediction interval (dashed). ($[MCs]_0$ = 10 nM, $[Mn(VII)]_0$ = 2.5 μM, reaction time = 1 h, temperature = 21 ± 1°C).

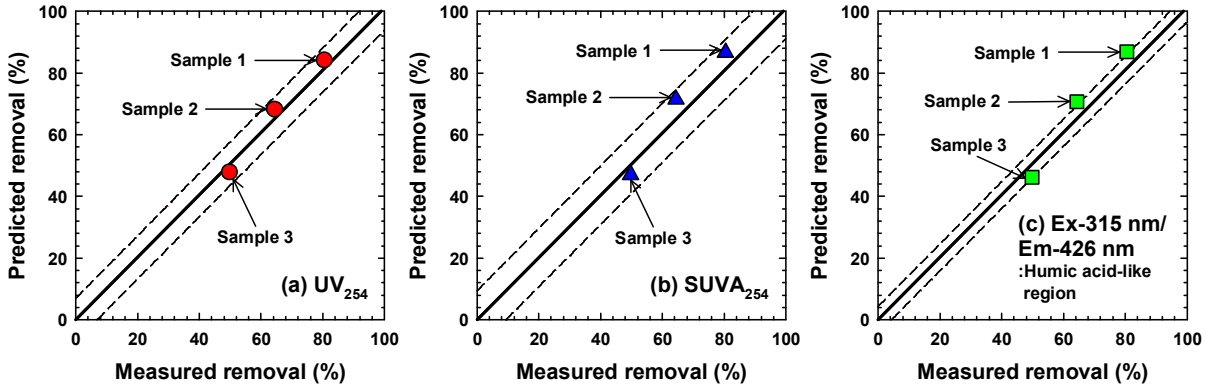

Figure 3.16. Experimental and predicted removal efficiency of MC-LR in three natural water samples (sample 1, 2, and 3) from different sites of the Nakdong river in Korea ($[MC\text{-}LR]_0$ = 10 nM, $[Mn(VII)]_0$ = 2.5 μM, reaction time = 1 h, temperature = 21 ± 1°C).

**These three natural waters are not used to derive the correlation equations in Figure 3.14. The values of UV_{254}, $SUVA_{254}$ and fluorescence intensity at Ex-315 nm/Em-426 nm of the three water samples were measured, and were used for the calculation of the $\int[Mn(VII)]dt$ values (refer to Table 3.4). Using the calculated $\int[Mn(VII)]dt$ values and Equation 3.2, the removal efficiencies of MC-LR in the three natural waters were modeled, and the results were compared with the experimental data. Lines represent the obtained linear regression model (solid) and the 95% prediction interval (dashed) from the data in Figure 3.14b, c and i.*

3.1.4. Oxidation products and pathways. Two previous studies have proposed the oxidation mechanism of MC-LR by Mn(VII) based on the product study using LC/MS.[28, 44] However, a majority of these oxidation pathways appear to be speculative due to the inconsistency with the chemistry generally known for alkene oxidation by Mn(VII) and their lack of mass spectrometric evidences for their conclusions. The detailed limitations of their studies are described as follows.

Limitations of previous product studies on MC-LR oxidation by Mn(VII). The first product study for MC-LR oxidation by Mn(VII) was conducted by Huang et al.[28] In their study, di-hydroxylated MC-LR, which is formed by the dihydroxylation of alkene groups in Adda moiety, was proposed as a primary product. However, the mass spectral evidence of di-hydroxylated MC-LR ($[(MC\text{-}LR+O_2)+H]^+$ = 1029.5621) was not found in their mass spectra. Recently, Jeong et al., which analyzed the oxidation products of MC-LR during the Mn(VII) treatment at a neutral pH conditions using LC/MS, also suggested the production of di-hydroxylated MC-LR as a primary product (Figure 3.17).[44] In addition, a number of oxidized derivatives of di-hydroxylated MC-LR were proposed; the remaining primary oxidation sites of di-hydroxylated MC-LR can be further oxidized to form tetra-hydroxylated and hexa-hydroxylated MC-LR ($[(MC\text{-}LR+2O_2)+H]^+$ = 1063.5676 and $[(MC\text{-}LR+3O_2)+H]^+$ = 1097.5730, respectively) (refer to Figure 3.17a). However, these pathways for the formation of di-hydroxylated MC-LR and its secondary and tertiary oxidation products are unacceptable, because the respective evidence is not clarified or not detected. If the primary production of di-hydroxylated MC-LR is correct, there is no reason for it not to be detected; di-hydroxylated MC-LR has been clearly found after the oxidation of MC-LR by ozone,[41] chlorine dioxide,[31] hydroxy radical,[56] sulfate radical,[59] and ferrate.[135] It should be noted that such diol production from the oxidation alkene by Mn(VII) is known to proceed only under the alkaline pH conditions (Figure 3.18).[75, 76] Apart from the oxidation of alkene groups, Jeong et al. also suggested that Mn(VII) attacks phenyl group of Adda moiety to produce mono-hydroxylation of MC-LR ($[(MC\text{-}LR+O)+H]^+$ = 1011.5515) and its subsequent products, even though the m/z 1011.5515 was not detected (refer to Figure 3.17b); mono-hydroxylated MC-LR has been clearly found after oxidation of MC-LR by ozone,[41] hydroxy radical,[56] sulfate radical,[59] and ferrate.[135] These oxidation products derived from phenyl moiety seem to be misidentified because benzylic compounds are rarely oxidized by Mn(VII) (e.g., second-order rate constants for the reaction of BTEX with Mn(VII) varied from 7×10^{-6} to 1.13×10^{-2} M^{-1} s^{-1} at pH 5−7 and 20−70°C[72]).

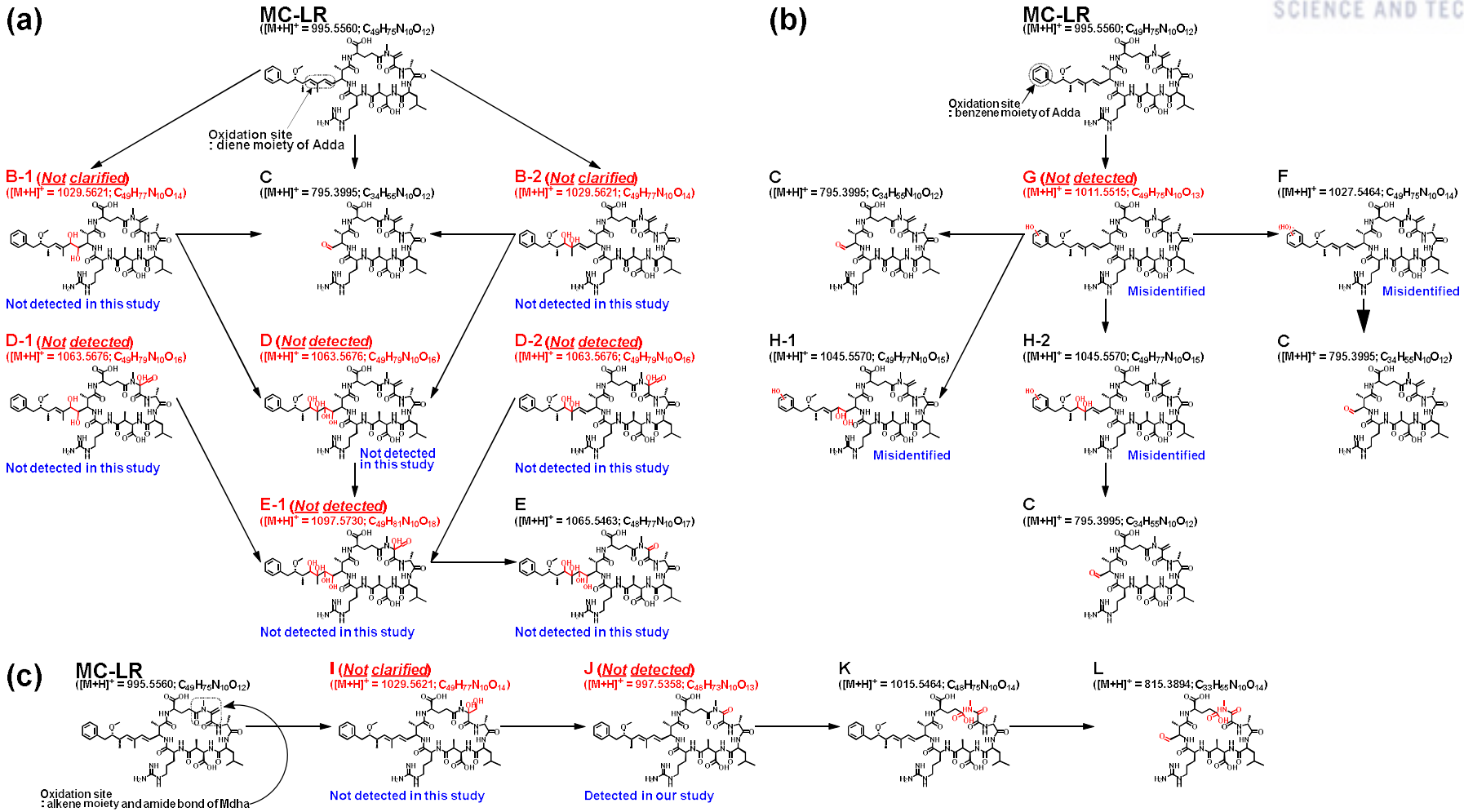

Figure 3.17. Oxidation pathways of MC-LR by Mn(VII) proposed by Jeong et al.[44]: (a) diene oxidation products, (b) aromatic ring oxidation products, and (c) amide bond hydrolysis products. "Not detected" indicates the product noted as not detected by Jeong et al.'s study. "Not clarified" indicates the product of which detection was not clearly stated in Jeong et al.'s study. The comments on each product are in blue text.

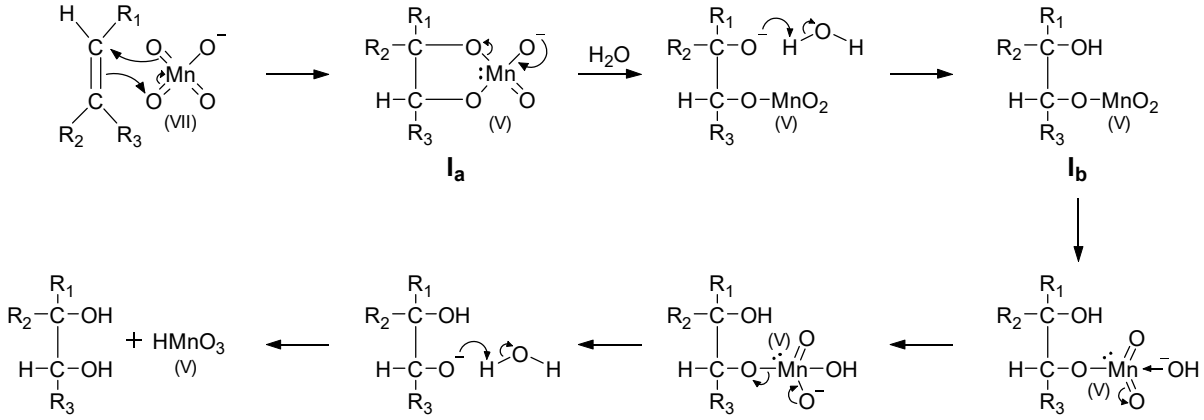

Figure 3.18. Mechanism of alkene oxidation by Mn(VII) at alkaline pH conditions.

In this study, 17 oxidation products were identified by the LC/MS analysis (Table 3.5), and Figures 3.19–3.36 present their chromatograms. The oxidation pathways of MC-LR by Mn(VII) were proposed based on the identified products (Figure 3.37). There are three sites that Mn(VII) is believed to attack in the MC-LR structure (Sites A–C): two alkene groups in Adda (Sites A and B), and an alkene group in Mdha (Site C) (refer to Figures 3.37).

Table 3.5. Oxidation products of MC-LR identified by LC/MS

Products	Chemical formula $[M+H]^+$	Theoretical m/z	△[a] (ppm)	RT (min)	References
MC-LR	$C_{49}H_{75}N_{10}O_{12}$	995.5560	-1.31	26.60	-
P_{795}	$C_{34}H_{55}N_{10}O_{12}$	795.3995	0.63	1.67	40, 41, 44, 47, 51, 53, 56, 66–137
P_{797}	$C_{33}H_{53}N_{10}O_{13}$	797.3788	2.38	2.07	No literature
P_{811}	$C_{34}H_{55}N_{10}O_{13}$	811.3944	2.10	1.78	40, 51
P_{813}	$C_{33}H_{53}N_{10}O_{14}$	813.3737	2.09	2.15	No literature
P_{815}	$C_{33}H_{55}N_{10}O_{14}$	815.3893	-0.12	1.73, 2.05	44, 137
P_{827}	$C_{34}H_{55}N_{10}O_{14}$	827.3893	1.09	1.70	No literature
P_{843}	$C_{34}H_{55}N_{10}O_{15}$	843.3842	0.00	2.43	No literature
P_{845}	$C_{34}H_{57}N_{10}O_{15}$	845.3999	0.24	1.55	No literature
P_{997}	$C_{48}H_{73}N_{10}O_{13}$	997.5353	-3.21	20.20	No literature
P_{1015}	$C_{48}H_{75}N_{10}O_{14}$	1015.5458	3.74	14.60	44, 53
P_{1027}	$C_{49}H_{75}N_{10}O_{14}$	1027.5458	-2.04	2.26, 3.59, 7.73, 8.21, 8.53, 14.64, 20.66, 24.66	44, 47, 53, 56, 59, 135–136
P_{1029}	$C_{48}H_{73}N_{10}O_{15}$	1029.5251	-1.65	12.41, 14.12, 18.65	44
P_{1045}	$C_{49}H_{77}N_{10}O_{15}$	1045.5564	-2.01	5.79, 7.19, 7.68, 9.33, 9.88, 11.27, 11.94	44, 56
P_{1047}	$C_{48}H_{75}N_{10}O_{16}$	1047.5357	-1.91	3.63, 6.00, 12.47, 14.22, 15.18, 22.57, 28.68	No literature
P_{1059}	$C_{49}H_{75}N_{10}O_{16}$	1059.5357	-2.17	6.22, 7.59, 8.20, 8.51, 8.86, 9.28, 10.16, 10.98, 12.37, 12.90, 13.43, 14.98, 15.51, 15.97	No literature
P_{1077}	$C_{49}H_{77}N_{10}O_{17}$	1077.5462	-1.76	4.94, 6.13, 7.10, 8.21, 8.73, 8.96, 9.31, 9.76, 9.80, 10.78, 11.79, 12.97, 14.44, 15.39, 16.69, 18.25, 19.24, 19.92, 21.23, 22.08, 23.59	No literature
P_{1091}	$C_{49}H_{75}N_{10}O_{18}$	1091.5255	-0.82	8.66, 9.51, 10.38, 11.06, 11.77, 14.93, 16.39	No literature

[a]△ represents the mass tolerance (maximal difference between an experimental mass and a theoretical mass, ppm).

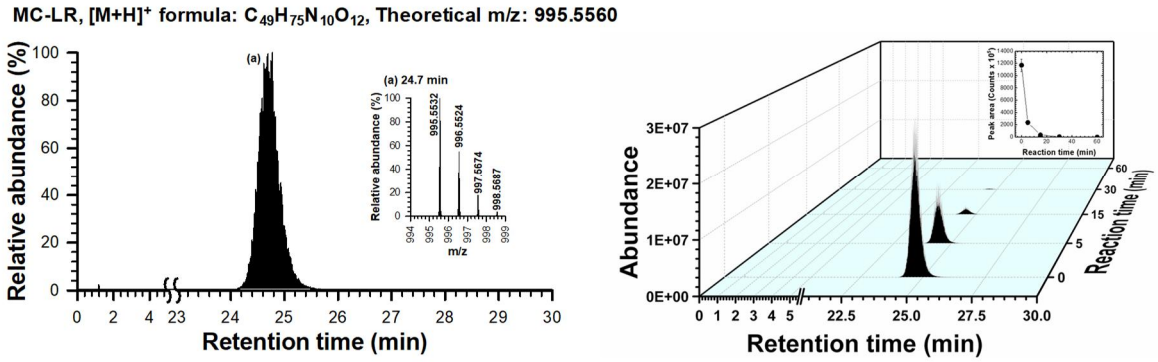

Figure 3.19. LC/MS identification of MC-LR ($[M+H]^+$ = 995.5560). The chromatogram at 0 min with mass spectra (left) and time-dependent chromatograms (right) of MC-LR.

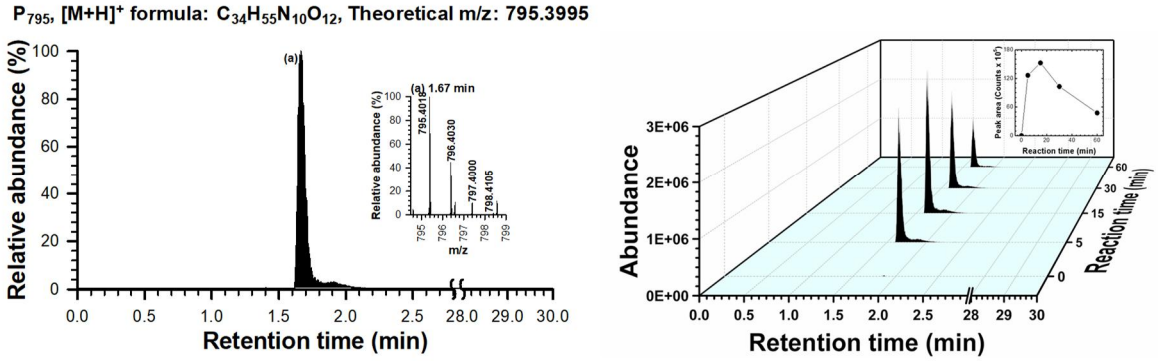

Figure 3.20. LC/MS identification of P_{795} ($[M+H]^+$ = 795.3995). The chromatogram at 15 min with mass spectra (left) and time-dependent chromatograms (right) of P_{795}.

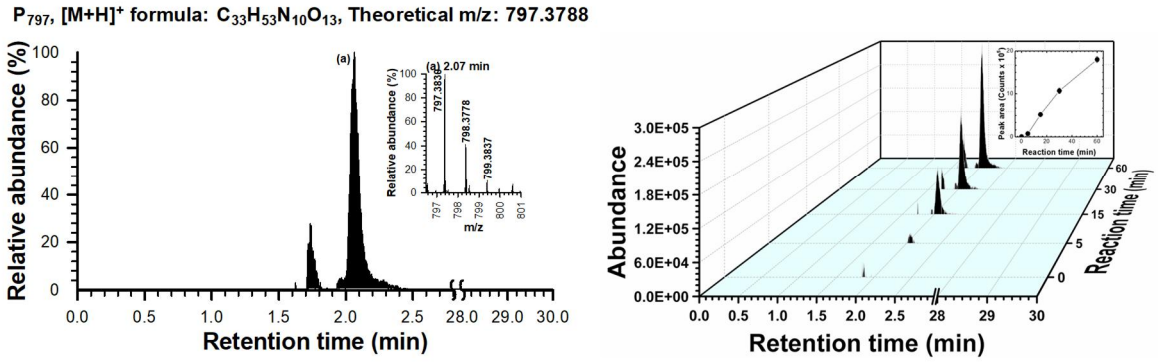

Figure 3.21. LC/MS identification of P_{797} ($[M+H]^+$ = 797.3788). The chromatogram at 60 min with mass spectra (left) and time-dependent chromatograms (right) of P_{797}.

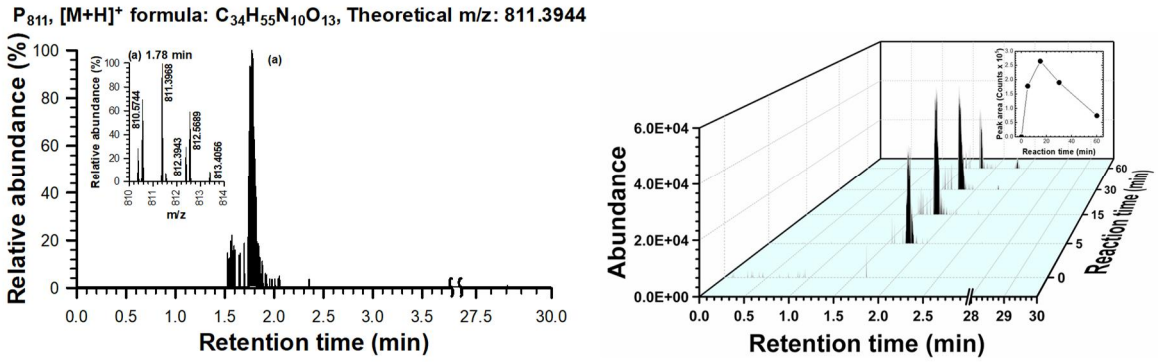

Figure 3.22. LC/MS identification of P_{811} ($[M+H]^+$ = 811.3944). The chromatogram at 15 min with mass spectra (left) and time-dependent chromatograms (right) of P_{811}.

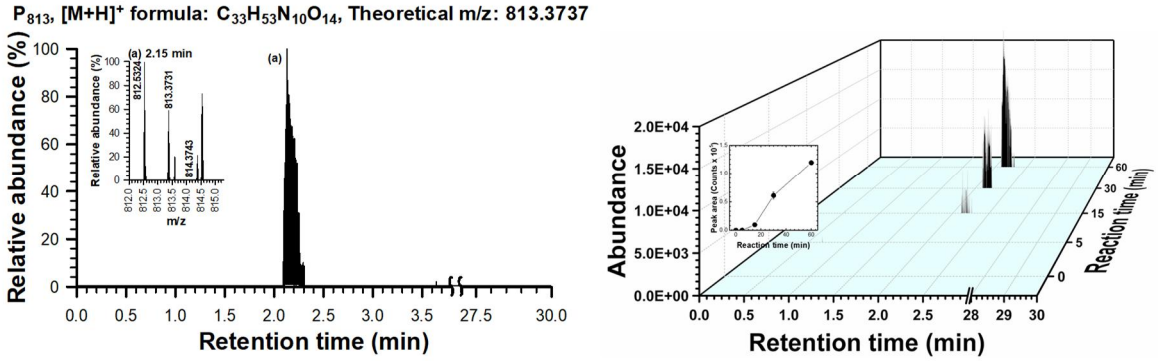

Figure 3.23. LC/MS identification of P_{813} ($[M+H]^+$ = 813.3737). The chromatogram at 60 min with mass spectra (left) and time-dependent chromatograms (right) of P_{813}.

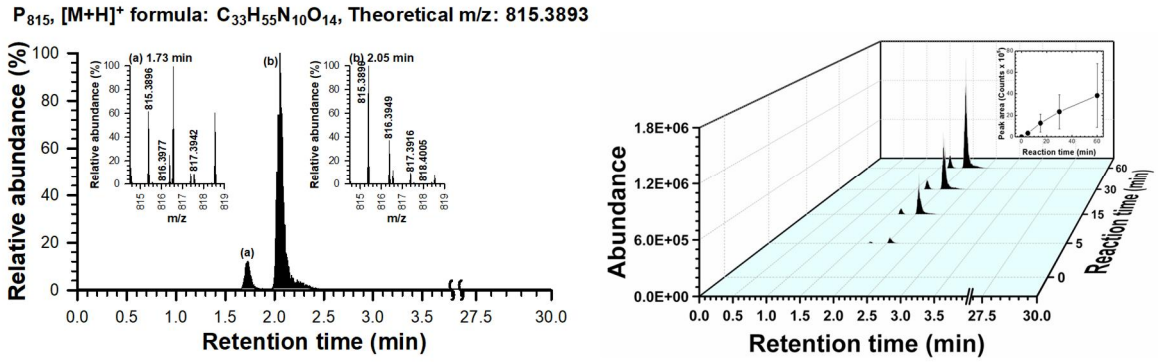

Figure 3.24. LC/MS identification of P_{815} ($[M+H]^+$ = 815.3893). The chromatogram at 60 min with mass spectra (left) and time-dependent chromatograms (right) of P_{815}.

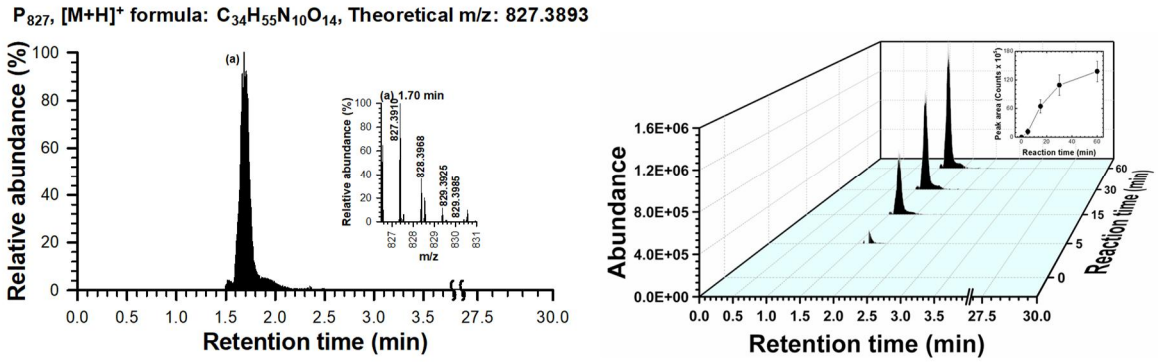

Figure 3.25. LC/MS identification of P_{827} ($[M+H]^+$ = 827.3893). The chromatogram at 60 min with mass spectra (left) and time-dependent chromatograms (right) of P_{827}.

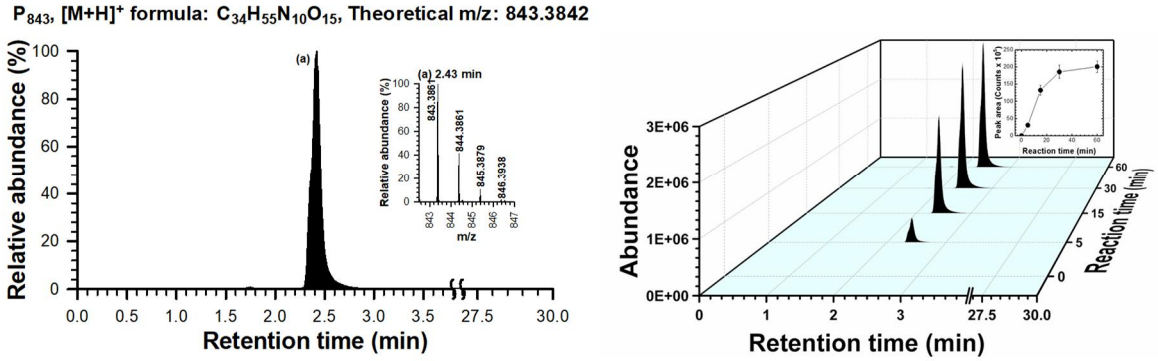

Figure 3.26. LC/MS identification of P_{843} ($[M+H]^+$ = 843.3842). The chromatogram at 60 min with mass spectra (left) and time-dependent chromatograms (right) of P_{843}.

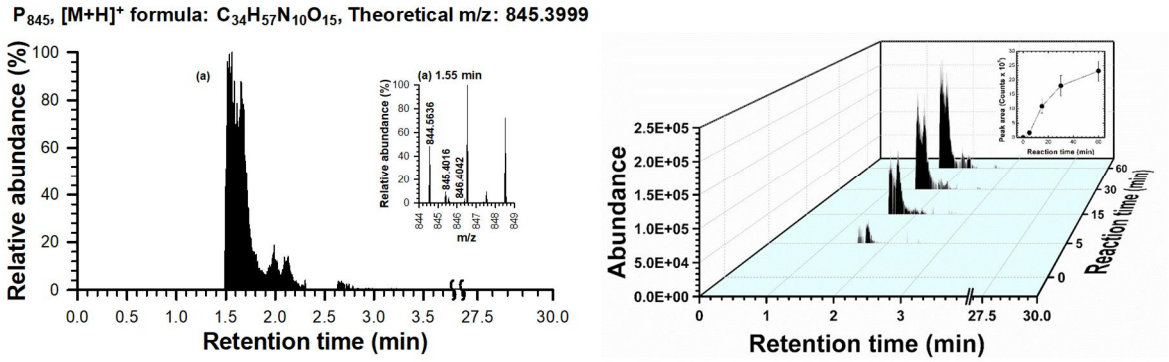

Figure 3.27. LC/MS identification of P_{845} ($[M+H]^+$ = 845.3999). The chromatogram at 60 min with mass spectra (left) and time-dependent chromatograms (right) of P_{845}.

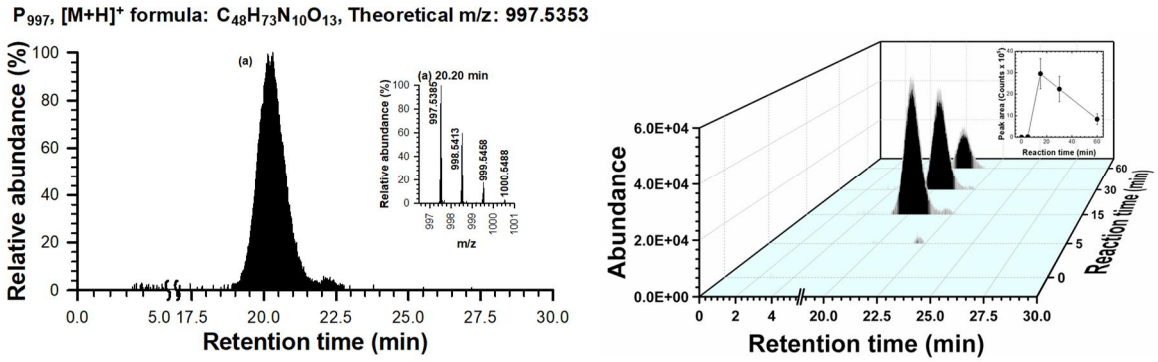

Figure 3.28. LC/MS identification of P_{997} ($[M+H]^+$ = 997.5353). The chromatogram at 15 min with mass spectra (left) and time-dependent chromatograms (right) of P_{997}.

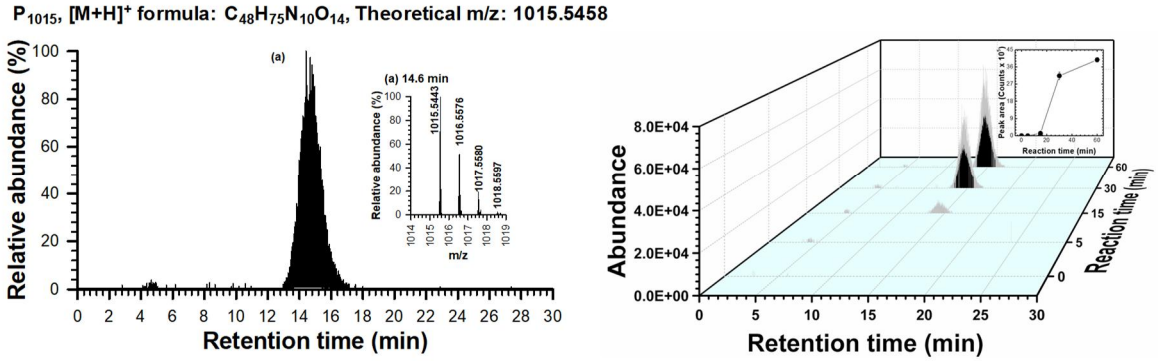

Figure 3.29. LC/MS identification of P_{1015} ($[M+H]^+$ = 1015.5458). The chromatogram at 60 min with mass spectra (left) and time-dependent chromatograms (right) of P_{1015}.

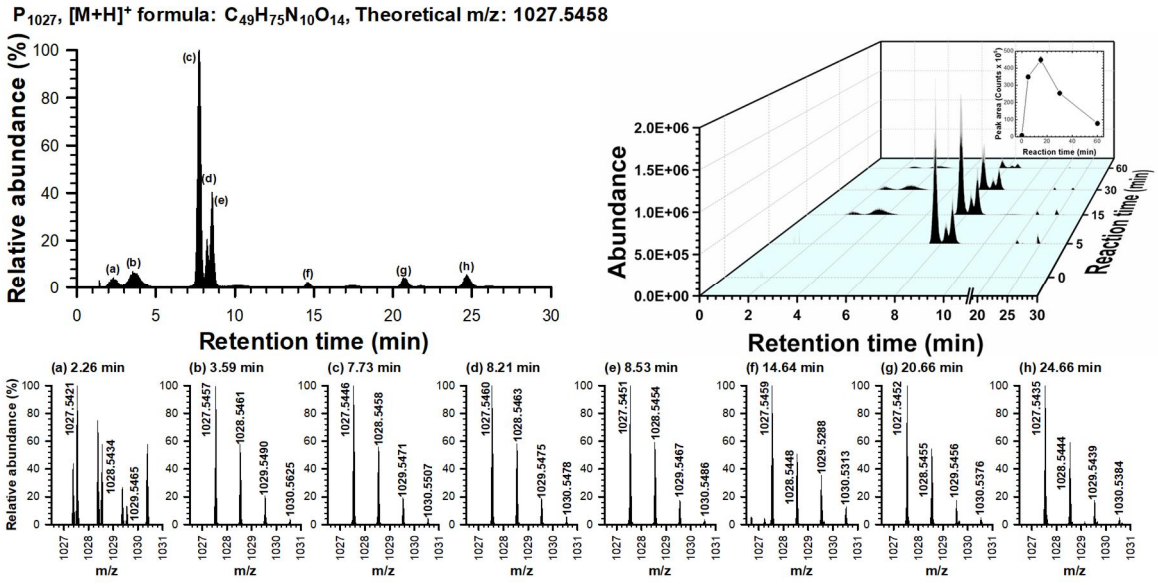

Figure 3.30. LC/MS identification of P_{1027} ($[M+H]^+$ = 1027.5458). The chromatogram at 15 min with mass spectra (left) and time-dependent chromatograms (right) of P_{1027}.

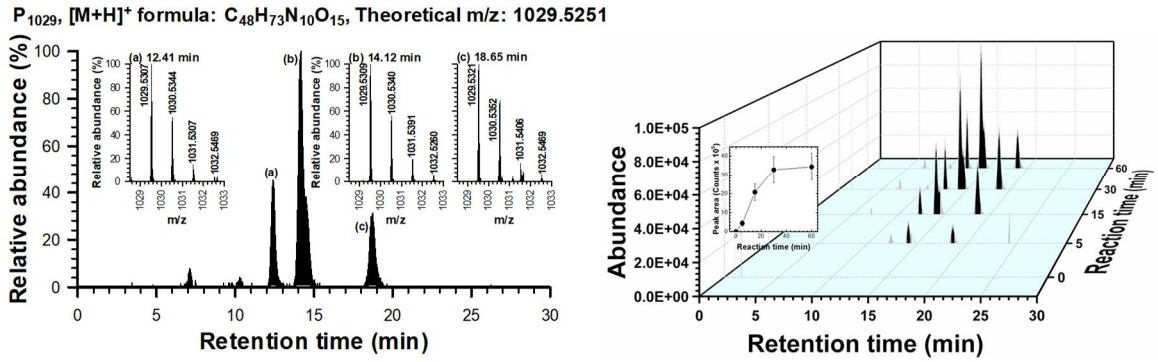

Figure 3.31. LC/MS identification of P_{1029} ($[M+H]^+$ = 1029.5251). The chromatogram at 60 min with mass spectra (left) and time-dependent chromatograms (right) of P_{1029}.

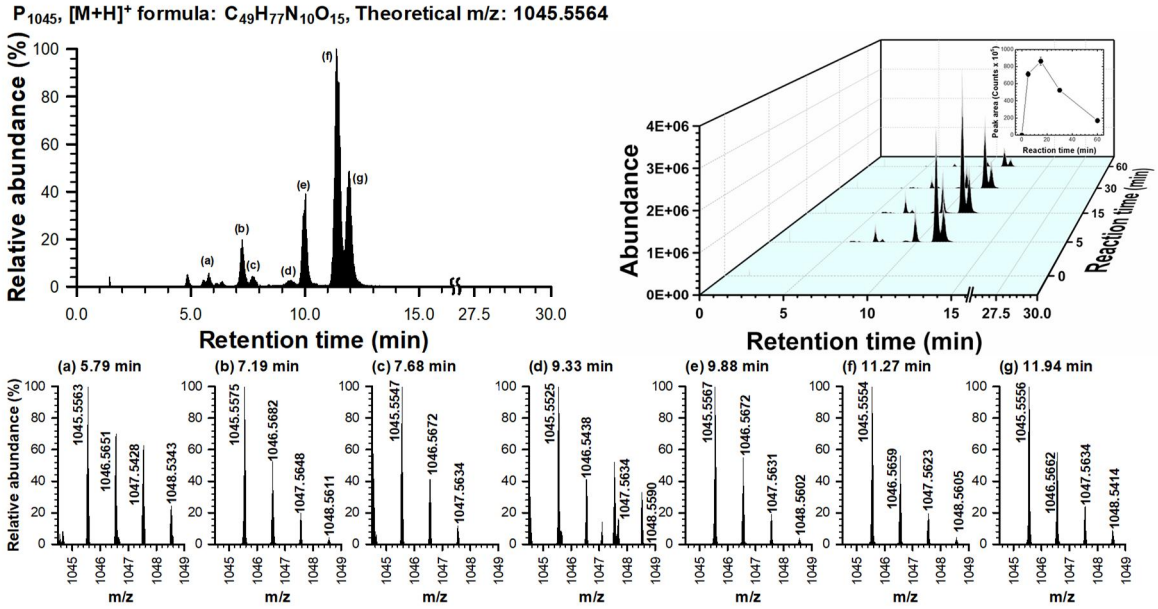

Figure 3.32. LC/MS identification of P_{1045} ($[M+H]^+$ = 1045.5564). The chromatogram at 15 min with mass spectra (left) and time-dependent chromatograms (right) of P_{1045}.

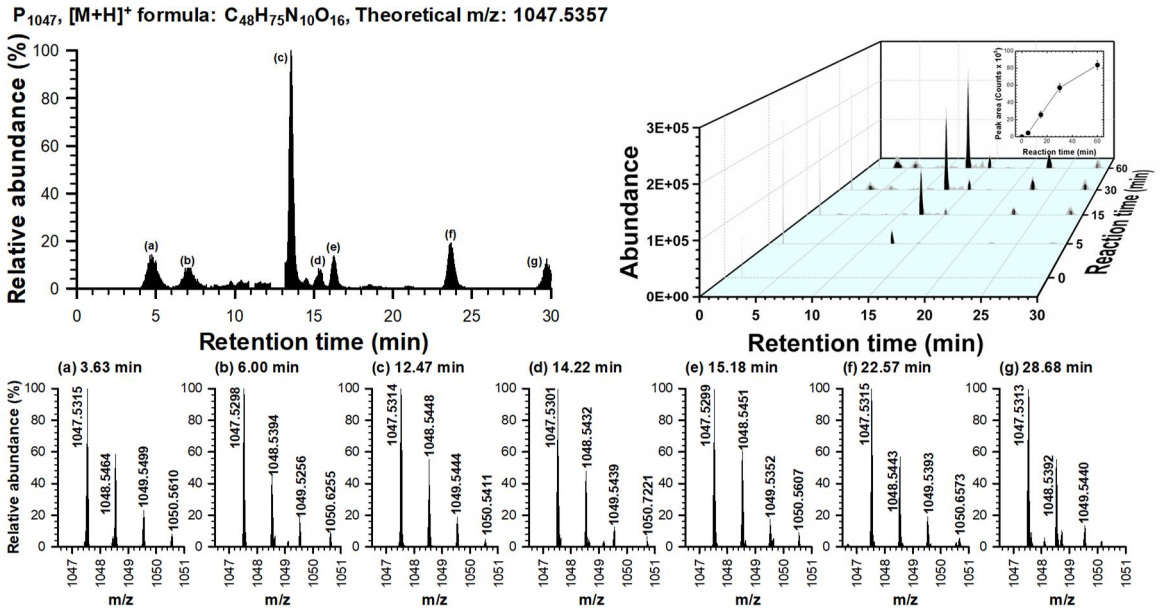

Figure 3.33. LC/MS identification of P_{1047} ($[M+H]^+$ = 1047.5357). The chromatogram at 60 min with mass spectra (left) and time-dependent chromatograms (right) of P_{1047}.

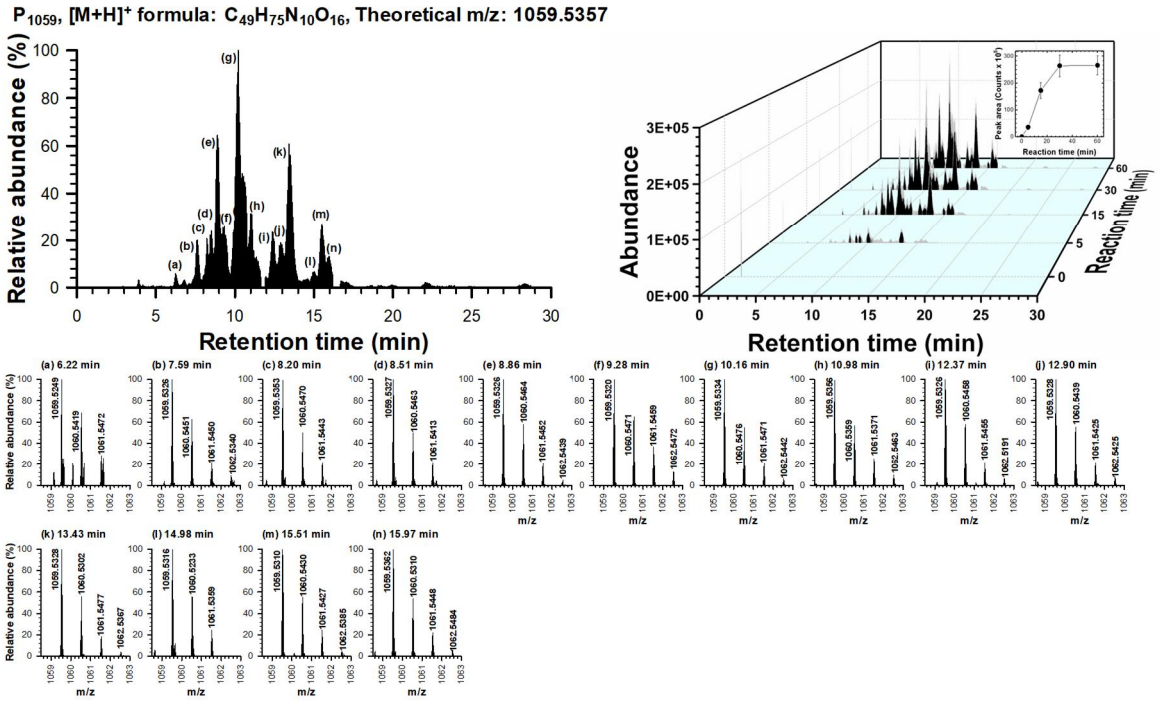

Figure 3.34. LC/MS identification of P_{1059} ($[M+H]^+$ = 1059.5357). The chromatogram at 60 min with mass spectra (left) and time-dependent chromatograms (right) of P_{1059}.

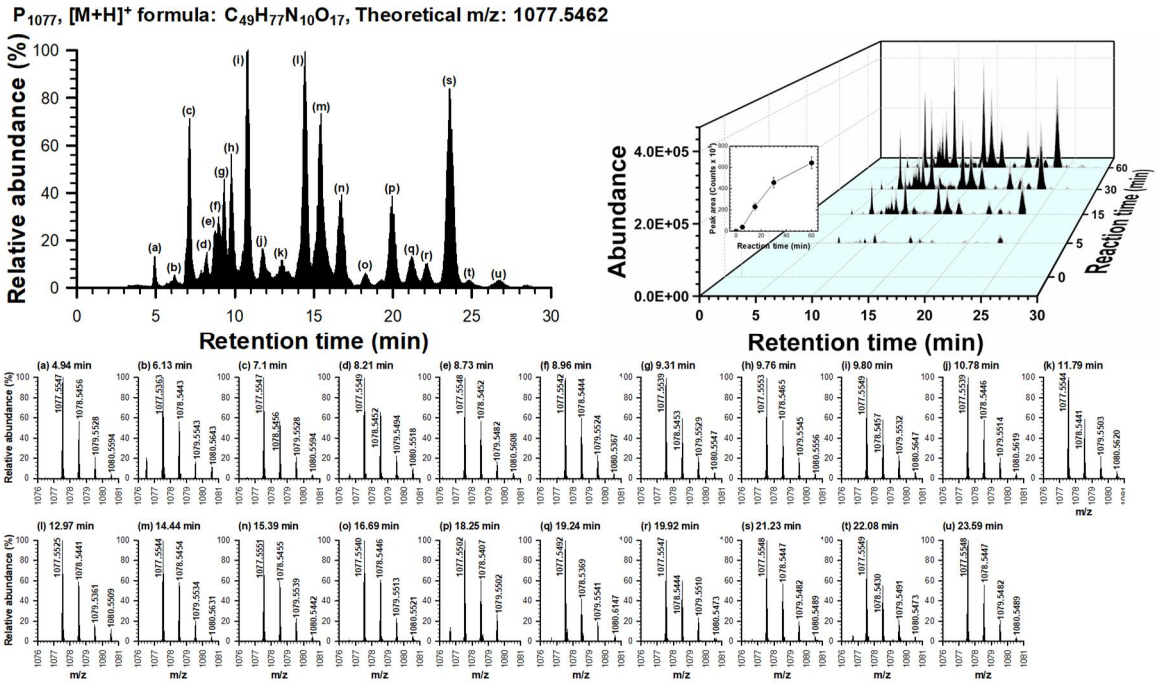

Figure 3.35. LC/MS identification of P_{1077} ($[M+H]^+$ = 1077.5462). The chromatogram at 60 min with mass spectra (left) and time-dependent chromatograms of P_{1077} (right).

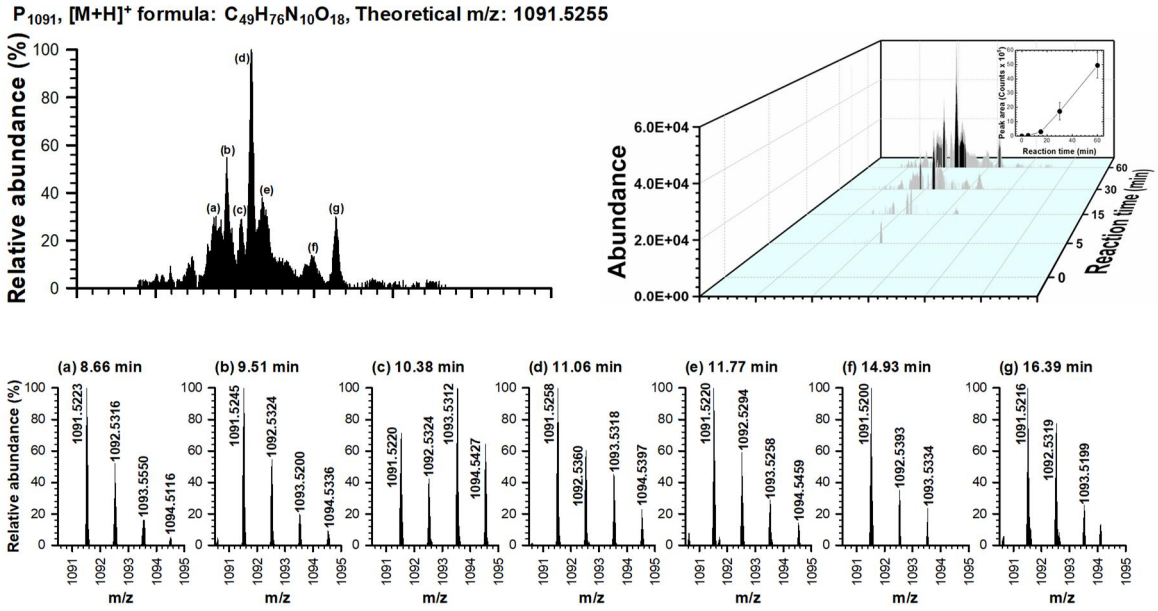

Figure 3.36. LC/MS identification of P_{1091} ($[M+H]^+$ = 1091.5255). The chromatogram at 60 min with mass spectra (left) and time-dependent chromatograms of P_{1091} (right).

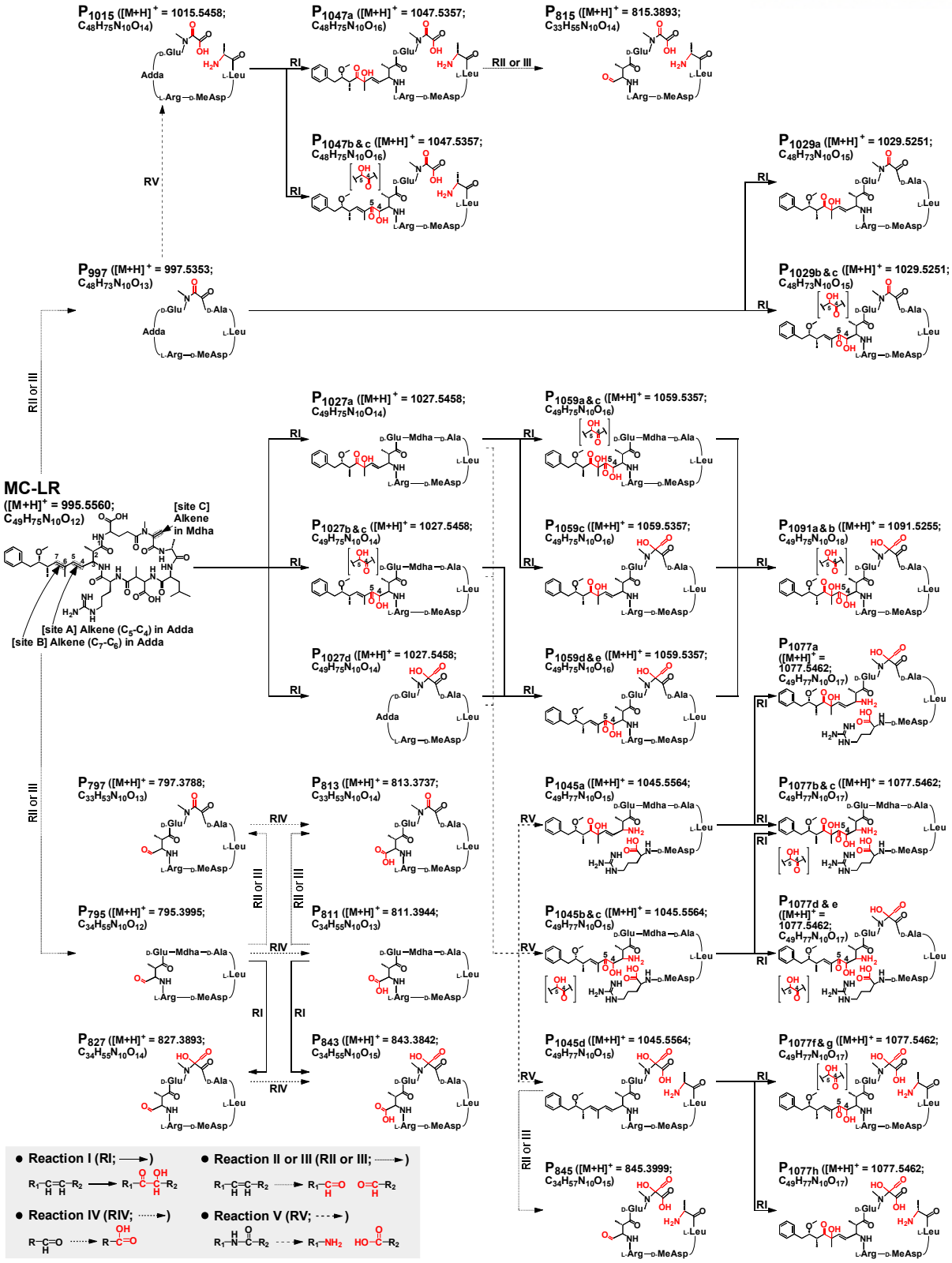

Figure 3.37. Proposed pathways for the oxidation of MC-LR by Mn(VII).

The alkene oxidation by Mn(VII) under the neutral pH conditions begins with forming the cyclic hypomanganate(V) ester as an intermediate (denoted as I_a). The I_a is rapidly transformed into an α-hydroxyketone, or decomposed into an aldehyde and a ketone through three different reaction pathways (refer to Reactions I, II, and III in Figure 3.38a): in Reaction I, I_a undergoes hydrolysis to yield another intermediate (i.e., $R_1–C_1HO–C_2H(OMnO_2)–R_2$, denoted as I_b), which is subsequently transformed into an α-hydroxyketone (i.e., $R_1–C_1HO–C_2(=O)–R_2$) by proton (adjacent to C_2) abstraction; in Reaction II, I_b is cleaved into two aldehydes (i.e., $R_1–C_1HO$ and $R_2–C_2HO$) through proton (adjacent to C_1) abstraction; in Reaction III, I_a is directly oxidized to hypomanganate(VI) ester, subsequently yielding an aldehyde and a ketone.[76] Furthermore, aldehydes can be further oxidized by Mn(VII) to carboxylic acid through the O_2 transfer mechanism (Reaction IV in Figure 3.38b).[138] Meanwhile, amides can be hydrolyzed to yield an amine and a carboxylic acid (Reaction V in Figure 3.38c).

All reaction pathways in the process of MC-LR oxidation by Mn(VII) (Figure 3.37) can be successfully explained by the transformation of Sites A–C via Reactions I–V. The oxidation of alkenes at Sites A–C via Reaction I produced the corresponding α-hydroxyketones ($P_{1027a–d}$), which were further oxidized to secondary and tertiary products ($P_{1059a–e}$ and $P_{1091a\ and\ b}$) in the same manner. The oxidative cleavage of alkenes at Sites B and C via Reaction II (or Reaction III) produced aldehyde (P_{795}) and ketone (P_{997}) products, respectively. The aldehyde product (P_{795}) was further oxidized to the carboxylic acid via Reaction IV. These oxidation products underwent further oxidation via Reactions I–III, yielding a number of daughter products (P_{797}, P_{811}, P_{813}, P_{827}, P_{843}, and $P_{1029a–c}$); note that the high mass tolerance (△ = 35.4 ppm) of mass spectrometry used in this study differentiates P_{1029} (m/z = 1029.5251) from the dihydroxylated product (m/z = 1029.5621).

One of the amide bonds in the primary oxidation products (P_{997} and $P_{1027a–d}$) appears to be hydrolyzed to yield separate amine and carboxylic groups (P_{1015} and $P_{1045a–d}$) via Reaction V. There are seven amide groups in the MC structure, and it is unclear which amide bond preferentially undergoes the hydrolysis. However, it is likely that the amide group in the vicinity of the ketone produced in the former step has been hydrolyzed; the electron-withdrawing property of adjacent ketones may accelerate the nucleophilic attack of a water molecule on the carbonyl carbon in the amide bond. The remaining alkene groups of P_{1015} and $P_{1045a–d}$ were further oxidized to yield P_{815}, P_{845}, $P_{1047a–c}$, and $P_{1077a–h}$ through Reactions I–III.

On the basis of the identified oxidation products, it was demonstrated that the oxidation of MC-LR by Mn(VII) generally proceeded in the direction of destruction of the Adda moiety (which is the functional group responsible for the hepatotoxicity of MCs). Although the two identified products (P_{997} and P_{1015}) include the intact Adda moiety, their production was ignorable (refer to Figures 3.28 and 3.29). In fact, Rodríguez et al. proved that the decrease of the MC-LR concentration synchronized with the reduction of hepatotoxicity during Mn(VII) oxidation.[26]

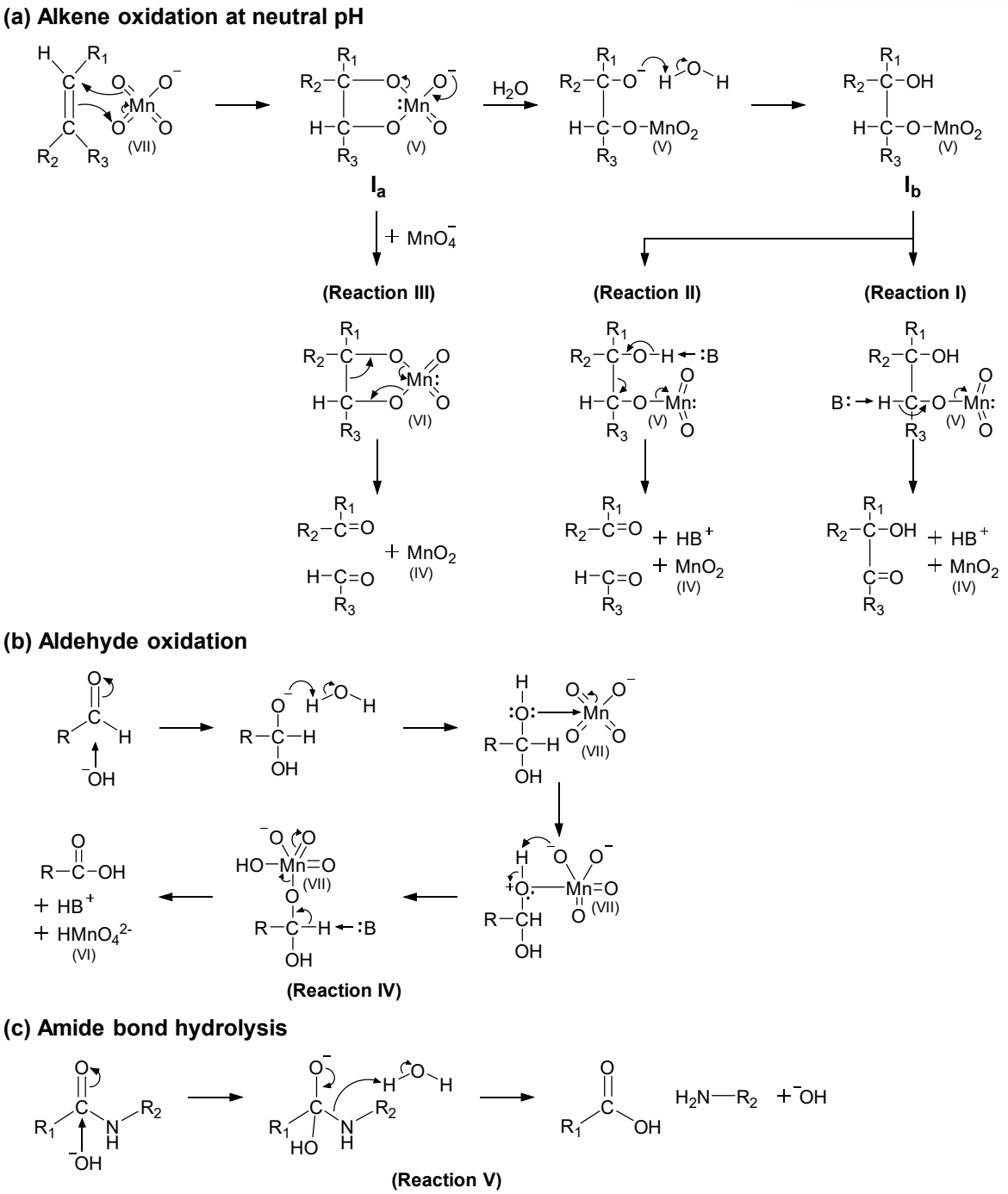

Figure 3.38. Various reaction mechanisms applied in the reaction of MC-LR with Mn(VII). B indicates base.

3.2. Oxidation of MCs by O_3

3.2.1. Kinetics for the reactions of MCs with O_3. To assess the reactivity of the six selected MCs with O_3, $k_{O3,MC}$ values were determined using CK with CA as a competitor at various pH (pH 6.2–9 at 20 ± 1°C) and temperature (4–33°C at pH 7.2) conditions. Depending on the pH and temperature variations, the CK results for six MCs are plotted in Figures 3.39 and 3.40, respectively. All of the results exhibit an excellent linearity ($R^2 > 0.94$).

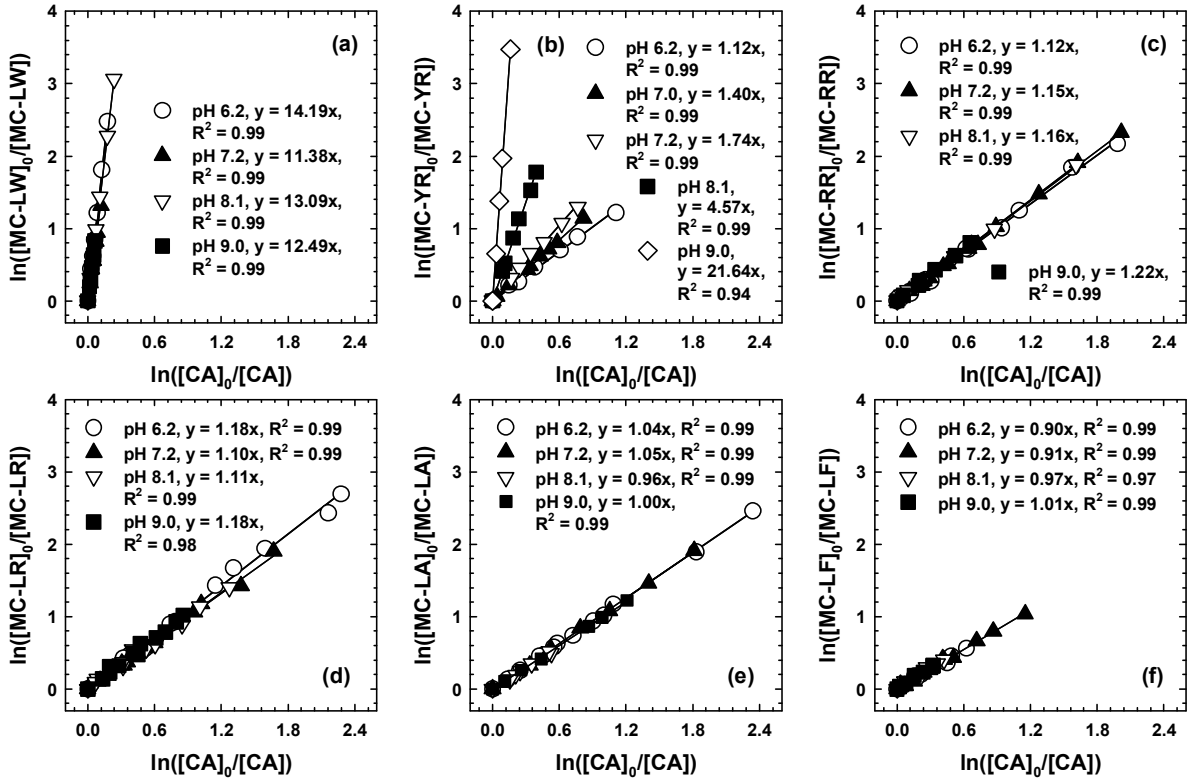

Figure 3.39. Variations of $\ln([MC]_0/[MC])$ as a function of corresponding $\ln([CA]_0/[CA])$ during the ozonation at different pH values ($[MC]_0$ = 0.1 μM, $[CA]_0$ = 0.1 μM, $[O_3]_0$ = 0.025–0.25 μM, $[t\text{-BuOH}]_0$ = 5 mM, temperature = 20 ± 1°C).

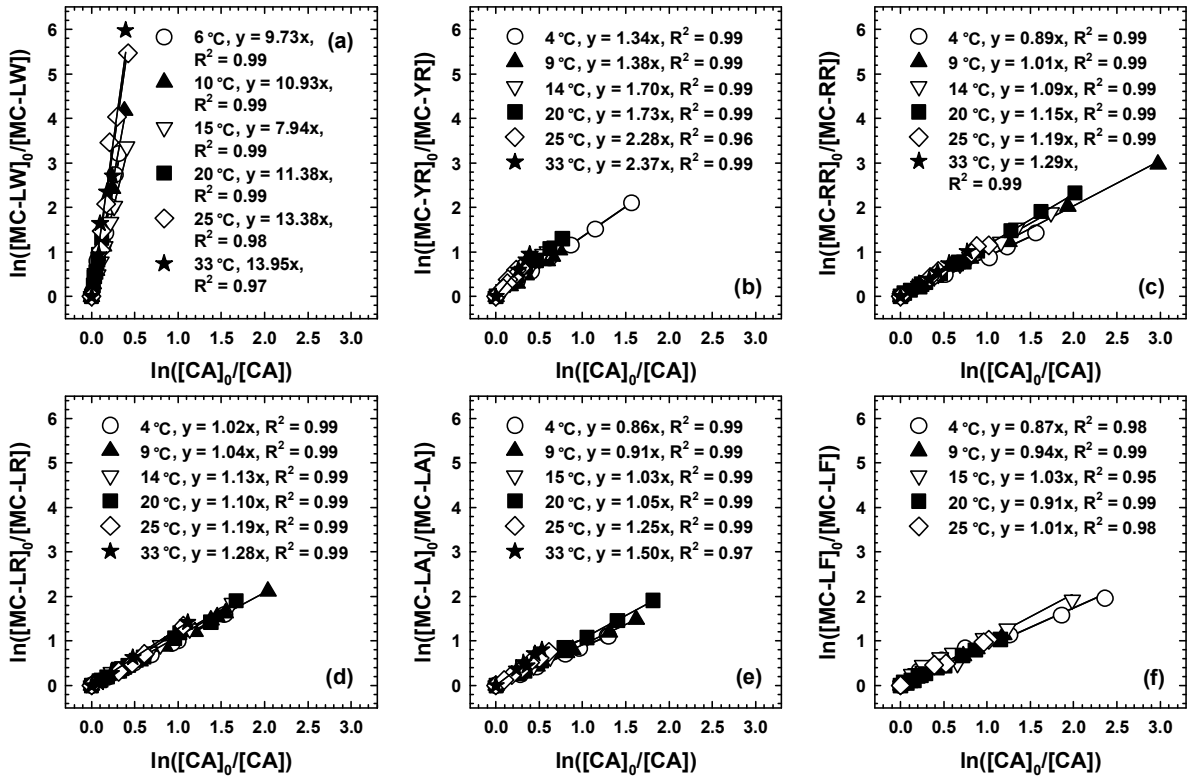

Figure 3.40. Variations of $\ln([MC]_0/[MC])$ as a function of corresponding $\ln([CA]_0/[CA])$ during the ozonation at temperatures ($[MC]_0$ = 0.1 μM, $[CA]_0$ = 0.1 μM, $[O_3]_0$ = 0.025–0.25 μM, $[t\text{-BuOH}]_0$ = 5 mM, pH = 7.2).

Before the calculation of $k_{O3,MC}$ values from the obtained Figures 3.39 and 3.40, it is necessary to prepare an ensured kinetics of CA. In many previous studies, CA is one of the most frequently used competitors for the determination of second-order rate constants for the reaction of various target compounds (including MC-LR) with O_3, because it has an apparent rate constant of a similar magnitude, around 10^5 M^{-1} s^{-1}.[38] However, the reported second-order rate constants for the reaction of CA with O_3 ($k_{O3,CA}$) exhibited a significant difference from 3.8×10^5 to 1.2×10^6 M^{-1} s^{-1}, depending on each study.[139–141] In this situation, the $k_{O3,CA}$ value applied in calculating the $k_{O3,MC}$ values is very important, because a second-order rate constant derived by a certain $k_{O3,CA}$ value could be over- or underestimated. Therefore, to obtain the reliable $k_{O3,MC}$ values using CK, it is necessary to determine an absolute $k_{O3,CA}$. In this study, the $k_{O3,CA}$ values were directly determined by SFS at various pH and temperature conditions. The $k_{O3,CA}$ values were calculated from the slope of the linear plot of the pseudo-first-order rate constant (k_{obs}) versus initial O_3 concentrations using SFS at pH 2.3–9 and 7.5–25°C (Figure 3.41).

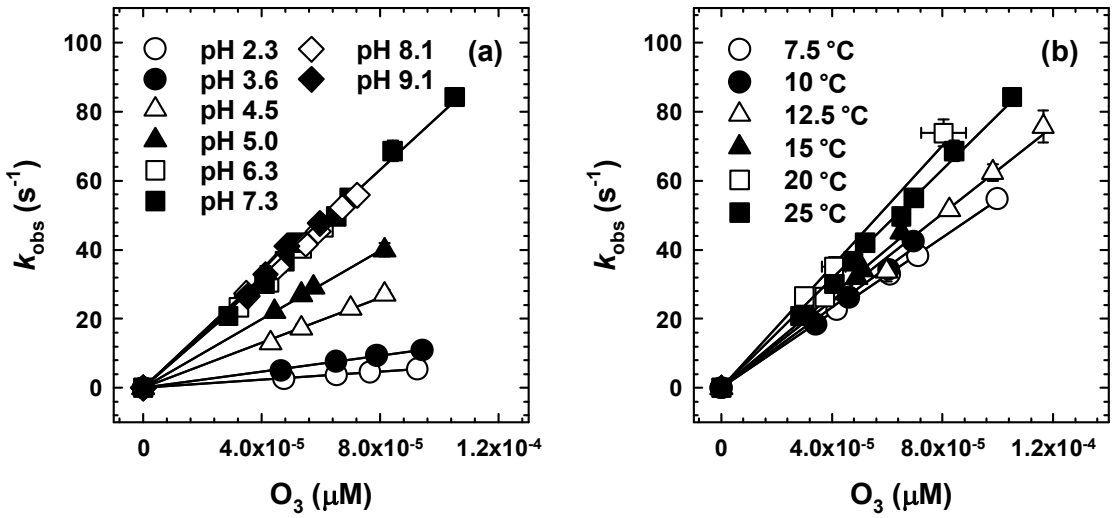

Figure 3.41. Plot of k_{obs} as a function of O_3 concentration at different (a) pH values and (b) temperatures ($[CA]_0$ = 5 μM, $[t\text{-BuOH}]_0$ = 5 mM, temperature = 20 ± 1°C for (a) and (b); temperature = 20 ± 1°C for (a), pH = 7.2 for (b)).

The species-specific second-order rate constants for the reaction of CA with O_3 at 20 ± 1°C were determined by fitting the experimental data (refer to Figures 3.41a) into Equation 2.5 using the least-squares regression function of Microsoft Excel 2016 software, and were calculated to be $5.8 \pm 0.1 \times 10^4$ M^{-1} s^{-1} of $k_{O3,CA1}$ and $7.5 \pm 0.4 \times 10^5$ M^{-1} s^{-1} of $k_{O3,CA2}$, respectively. The $k_{O3,CA2}$ value derived from this study was comparatively close to that reported by Wolf et al. (7.6×10^5 M^{-1} s^{-1} [141]) who also directly determined $k_{O3,CA}$ using SFS, and was almost two times lower or higher compared with other $k_{O3,CA}$ values.[139, 140]

The E_a value for the reaction of CA with O_3 at pH 7.2 was calculated to be 19.1 ± 1.2 kJ mol^{-1} from the slope of the Arrhenius plot (Figures 3.41b and 3.42b), and was also comparable to that found by Wolf et al. (21.2 kJ mol^{-1} [141]).

On the basis of the obtained pH- and temperature-dependent $k_{O3,CA}$ values, and the results of Figures 3.39 and 3.40, pH- and temperature-dependent $k_{O3,MC}$ values were calculated using Equation 2.1, and were summarized and plotted in Table 3.6 and Figure 3.43.

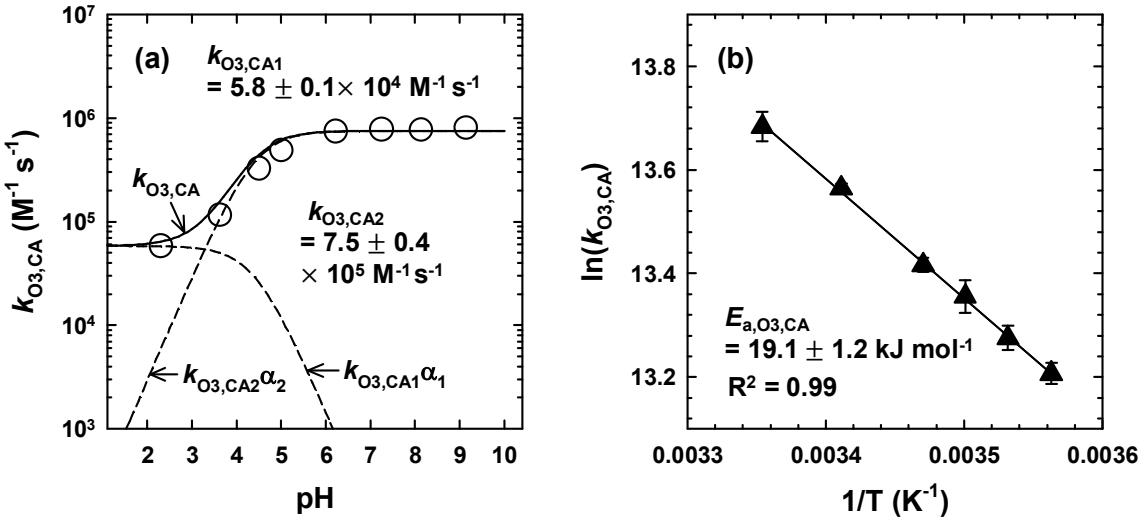

Figure 3.42. (a) pH-dependence of $k_{O3,CA}$, and (b) Arrhenius plot of $k_{O3,CA}$. Symbols and lines in (a) represent experimental data, model prediction of $k_{O3,CA}$ (solid) and $k_{O3,CAi}\alpha_i$ (dashed), respectively ($[CA]_0$ = 5 μM, $[O_3]_0$ = 28.7–118.4 μM, $[t\text{-BuOH}]_0$ = 5 mM for (a) and (b); temperature = 20 ± 1°C for (a), pH = 7.2 for (b)).

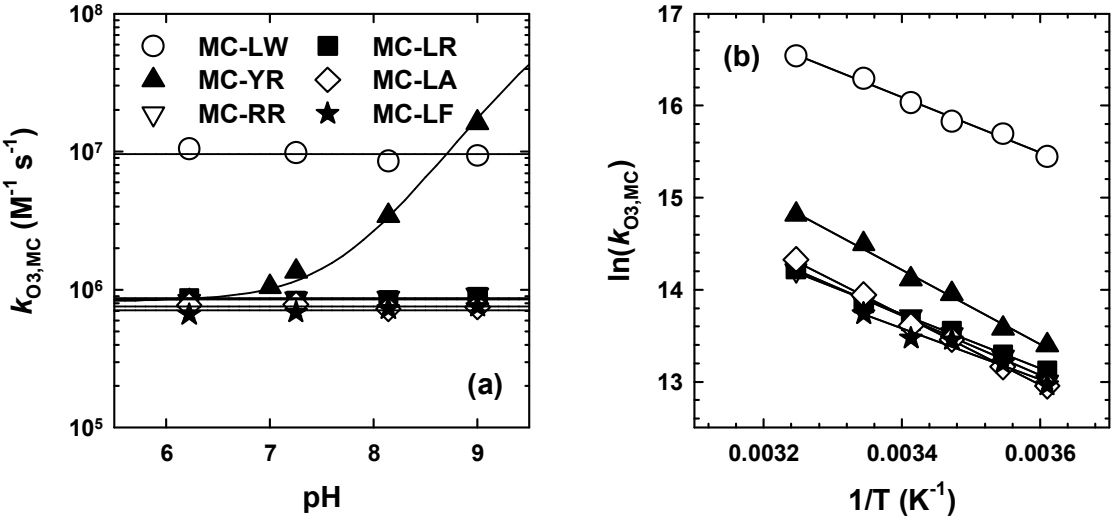

Figure 3.43. (a) pH-dependence of $k_{O3,MC}$ and (b) Arrhenius plots of $k_{O3,MC}$ (temperature = 20 ± 1°C for (a), pH = 7.2 for (b)).

Table 3.6. Summary of $k_{O3,MC}$ and $k_{\bullet OH,MC}$, and their temperature dependencies

	LW	YR	RR	LR	LA	LF	Conditions	References
$k_{O3,MC}$				3.4×10^4			pH 7, 20°C, and no scavenger	36
				$4.1 \pm 0.1 \times 10^5$			pH 8, $[t\text{-BuOH}]_0$ = 50 mM	38
			2.45×10^4	6.79×10^4			pH 7, 20°C, and no scavenger	39
	$6.27 \pm 0.96 \times 10^6$	$8.64 \pm 0.14 \times 10^{5a}$ 1.49×10^{8b}	$8.97 \pm 0.33 \times 10^5$	$8.79 \pm 0.31 \times 10^5$	$7.79 \pm 0.27 \times 10^5$	$7.30 \pm 0.39 \times 10^5$	pH 6.2–9.1, 20 ± 1°C, $[t\text{-BuOH}]_0$ = 5 mM	This study
E_a (O_3)				12.3			pH 7, 10–30°C, no scavenger	36
	29.0 ± 0.9	34.5 ± 0.5	27.5 ± 0.1	24.7 ± 0.7	32.9 ± 1.4	21.6 ± 0.2	pH 7.2, 4–38.3°C, $[t\text{-BuOH}]_0$ = 5 mM	This study
$k_{\bullet OH,MC}$				$1.1 \pm 0.01 \times 10^{10}$			pH 8	38
				$2.3 \pm 0.1 \times 10^{10}$			pH 7, room temperature	64
		1.6×10^{10}	1.5×10^{10}	1.1×10^{10}	1.1×10^{10}		pH 7.4, room temperature	47
	$1.64 \pm 0.18 \times 10^{10}$	$1.41 \pm 0.19 \times 10^{10a, b}$	$1.45 \pm 0.03 \times 10^{10}$	$1.20 \pm 0.09 \times 10^{10}$	$1.16 \pm 0.04 \times 10^{10}$	$1.35 \pm 0.12 \times 10^{10}$	pH 6.2–9.1, 20 ± 1°C	This study
E_a (•OH)	35.1 ± 0.2	35.7 ± 0.3	35.5 ± 0.8	35.1 ± 0.7	36.0 ± 0.1	36.7 ± 0.5	pH 7.2, 4–38.3°C	his study

[a] $k_{O3,MC\text{-}YR3}$, and $k_{\bullet OH,MC\text{-}YR3}$. [b] $k_{O3,MC\text{-}YR4}$ and $k_{\bullet OH,MC\text{-}YR4}$.

At the neutral condition (pH 7.2 and 20 ± 1°C), the determined $k_{O3,MC}$ values varied from 9.6 ± 0.5 × 10^6 to 7.1 ± 0.4 × 10^5 with the order MC-LW > -YR > -RR ≈ -LR ≈ -LA ≈ -LF, which exhibited much higher values compared with the results of $k_{O3,MC\text{-}RR}$ and $k_{O3,MC\text{-}LR}$; in the previous studies (refer to Table 3.6). The first report of $k_{O3,MC\text{-}LR}$ was performed by Shawwa and Smith using SFS.[36] However, their experiments seem to have some problems, such as no use of *t*-BuOH as an •OH scavenger and the absence of compensation for background UV absorbance derived by excess O_3 (in this case, rate constant values can be dramatically underestimated; refer to *Determination of* $k_{O3,CA}$ in section 2.2.2 and Figure 2.6). The other study performed by Al Momani and Jarrah[39] also used SFS for the determination of $k_{O3,MC\text{-}RR}$ and $k_{O3,MC\text{-}LR}$, and seems to have made the same mistakes (no use of *t*-BuOH and missing of background subtraction) as in the previous study[36]. Furthermore, the $k_{O3,MC\text{-}RR}$ and $k_{O3,MC\text{-}LR}$ values from Al Momani and Jarrah[39] exhibit significant variation depending on the initial concentration of MCs. Onstad et al. strictly determined the $k_{O3,MC\text{-}LR}$ values in the same manner as in this study using CK with CA as a competitor.[38] Despite following the same procedure, the reason that their $k_{O3,MC\text{-}LR}$ value is about two times lower than in this study is due to the different rate constants of the applied competitor; indeed, the slopes of the CK plot for MC-LR from Onstad et al. (i.e., $y = 1.06x$[38]) exactly matches that of the present study (refer to Figure 3.39d).

All of the $k_{O3,MC}$ values, expect for $k_{O3,MC\text{-}LW}$, show similar values to $k_{O3,CA}$ (refer to the slopes in Figures 3.39b–f), indicating that the dominant oxidation mechanism of MCs by O_3 is alkene oxidation. MC-LW exhibit the highest reactivity with O_3, which is mainly attributable to the direct reactions of Try (which is located in the X position of MC-LW; refer to Figure 1.3) with O_3 (second-order rate constant of Try with O_3, $k_{O3,Try} = 7 \times 10^6$ M^{-1} s^{-1} [142]).

Figure 3.43a shows the variation of $k_{O3,MC}$ values as a function of pH (from 6.2 to 9). Because five MCs (MC-LW, -RR, -LR, -LA and -LF) has no speciation in that pH range, their $k_{O3,MC}$ values exhibit a plateau. However, $k_{O3,MC\text{-}YR}$ values exhibit a rapid increase, and this increased reactivity of MC-YR toward O_3 is attributed to the deprotonation of the phenolic group in Tyr ($-C_6H_5OH \rightarrow -C_6H_5O^-$, pK_a = 9.9; refer to Figure 2.4c); the second-order rate constant for the reaction of phenolate with O_3 is much higher than that of phenol ($k_{O3,phenolate} = 1.4 \times 10^9$ M^{-1} s^{-1} > $k_{O3,phenol} = 1.3 \times 10^6$ M^{-1} s^{-1} [143]). In other words, as the pH increases, the dominant oxidation mechanism of MC-YR by O_3 is converted from alkene oxidation to phenolate oxidation.

The E_a values for the reactions of MCs with O_3 were calculated to be 22.6–31.9 kJ mol^{-1} from the slope of the Arrhenius plot (Figure 3.43b). On the basis of the determined activation energies, $k_{O3,MC}$ values vary by $5.6 \times 10^5 - 1.8 \times 10^7$ M^{-1} s^{-1} depending on MC in the temperature range of 10.5–37.0°C, at which the bloom of *Microcystis aeruginosa* are generally found.[115, 116]

3.2.2. Kinetics for the reactions of MCs with •OH. To assess the reactivity of the six selected MCs with •OH, $k_{\bullet OH,MC}$ values were determined using CK with *p*CBA as a competitor at various pH (pH 6.2–9 at 20 ± 1°C) and temperature (5.2–27.0°C at pH 7.2) conditions. Depending on the pH and temperature variations, the CK results for six MCs are plotted in Figures 3.44 and 3.45, respectively. All of results exhibit an excellent linearity ($R^2 > 0.95$).

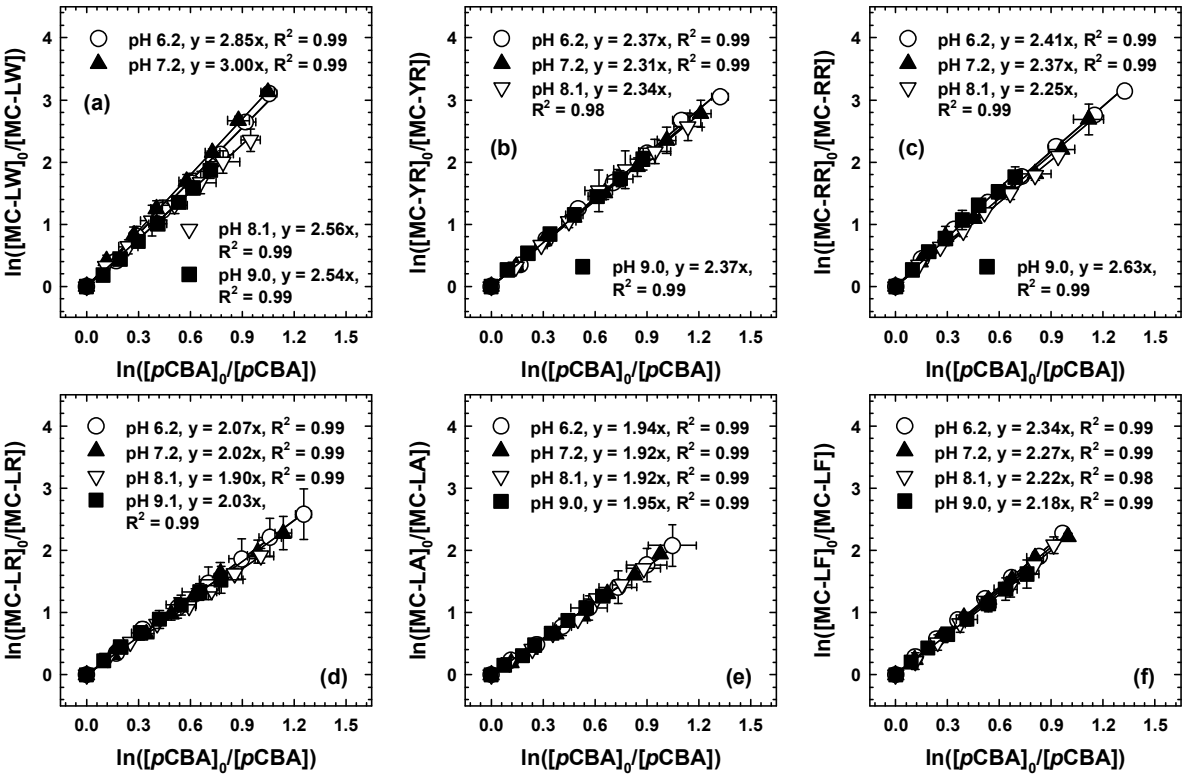

Figure 3.44. Variations of $\ln([MC]_0/[MC])$ as a function of corresponding $\ln([pCBA]_0/[pCBA])$ during the oxidation reaction in UV/H_2O_2 system at different pH values ($[MC]_0$ = 0.1 μM, $[CA]_0$ = 0.1 μM, $[H_2O_2]_0$ = 1 mM, temperature = 20 ± 1°C).

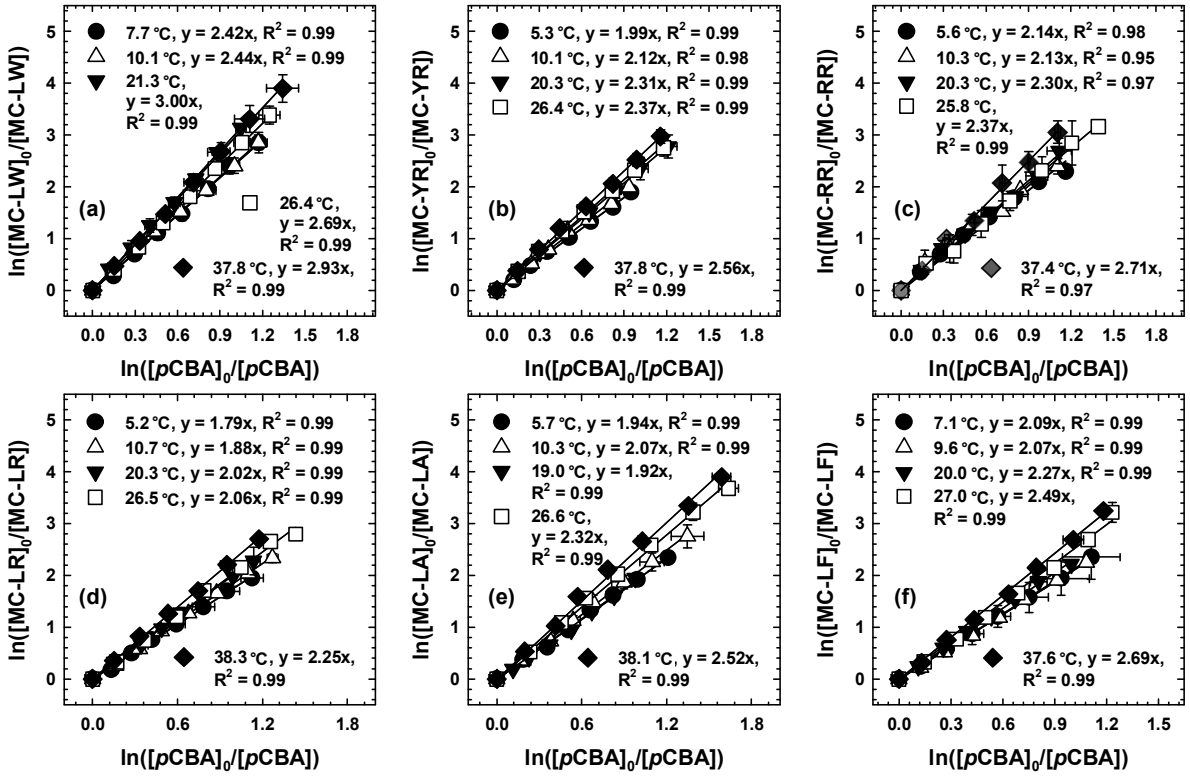

Figure 3.45. Variations of $\ln([MC]_0/[MC])$ as a function of corresponding $\ln([p\text{CBA}]_0/[p\text{CBA}])$ during the oxidation reaction in UV/H_2O_2 system at different temperatures ($[MC]_0$ = 0.1 μM, $[CA]_0$ = 0.1 μM, $[H_2O_2]_0$ = 1 mM, temperature = 20 ± 1°C).

For the calculation of $k_{\bullet OH,MC}$ values from the obtained Figures 3.44 and 3.45, the temperature-dependent $k_{\bullet OH,p\text{CBA}}$ values are required. Although the original report that first investigated rate constants for the reaction of various aromatic compounds with •OH provided the $k_{\bullet OH,p\text{CBA}}$ as 5.0×10^9 M^{-1} s^{-1} at pH 6–9.4,[103] no information is given about either the reaction temperature or the E_a for the reaction of *p*CBA with •OH ($E_{a,\bullet OH,p\text{CBA}}$). Therefore, in this study, the $E_{a,\bullet OH,p\text{CBA}}$ value was determined using the CK method with HCHO as a competitor whose second-rate constant for HCHO with •OH ($k_{\bullet OH,HCHO}$) and its temperature dependency were estimated to be 3.9×10^8 M^{-1} s^{-1} at 25°C and 13 kJ mol^{-1}, respectively. The $k_{\bullet OH,p\text{CBA}}$ values at various temperature conditions (3.7–37.8°C) were determined from the slope of the CK plot (Figure 3.46a), and the obtained $k_{\bullet OH,p\text{CBA}}$ value of $6.0 \pm 0.4 \times 10^9$ M^{-1} s^{-1} at 20°C was comparable to the 5.0×10^9 M^{-1} s^{-1} found in the literature[103]. Using the results shown in Figure 3.46a, $E_{a,\bullet OH,p\text{CBA}}$ at pH 7.2 was calculated to be 30.2 ± 1.9 kJ mol^{-1} from the slope of the Arrhenius plot (Figure 3.46b).

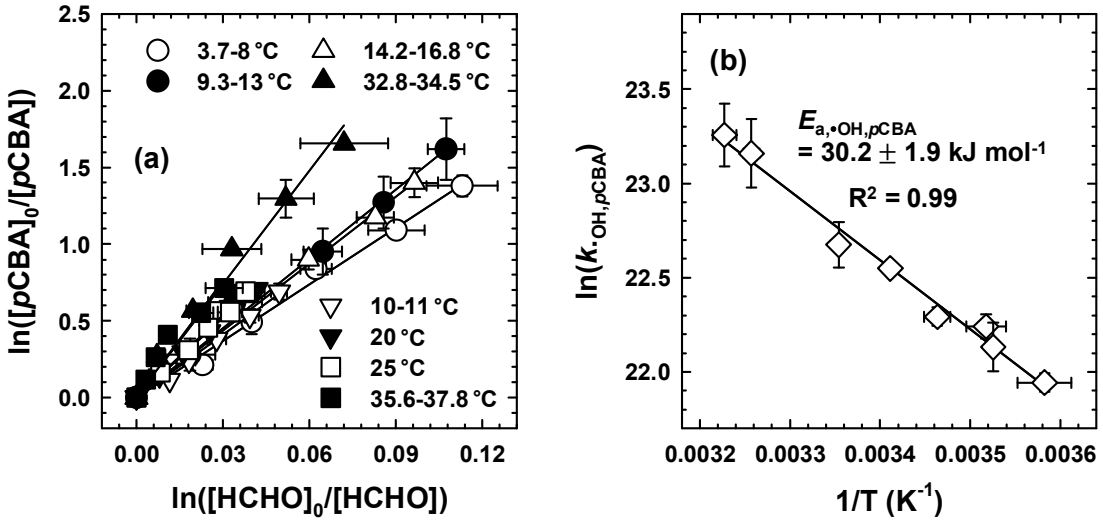

Figure 3.46. (a) Variations of ln([*p*CBA]$_0$/[*p*CBA]) as a function of corresponding ln([HCHO]$_0$/[HCHO]) during the oxidation reaction in UV/H_2O_2 system at different temperatures, and (b) Arrhenius plot of $k_{\bullet OH,pCBA}$ ([HCHO]$_0$ = 10 μM, [*p*CBA]$_0$ = 0.1 μM, pH = 7.2, [H_2O_2]$_0$ = 1 mM).

On the basis of the obtained $k_{\bullet OH,pCBA}$ and $E_{a,\bullet OH,pCBA}$ values, and the results of Figure 3.44 and 3.45, pH- and temperature-dependent $k_{\bullet OH,MC}$ values were calculated using Equation 2.1, and are summarized and plotted in Table 3.6 and Figure 3.47.

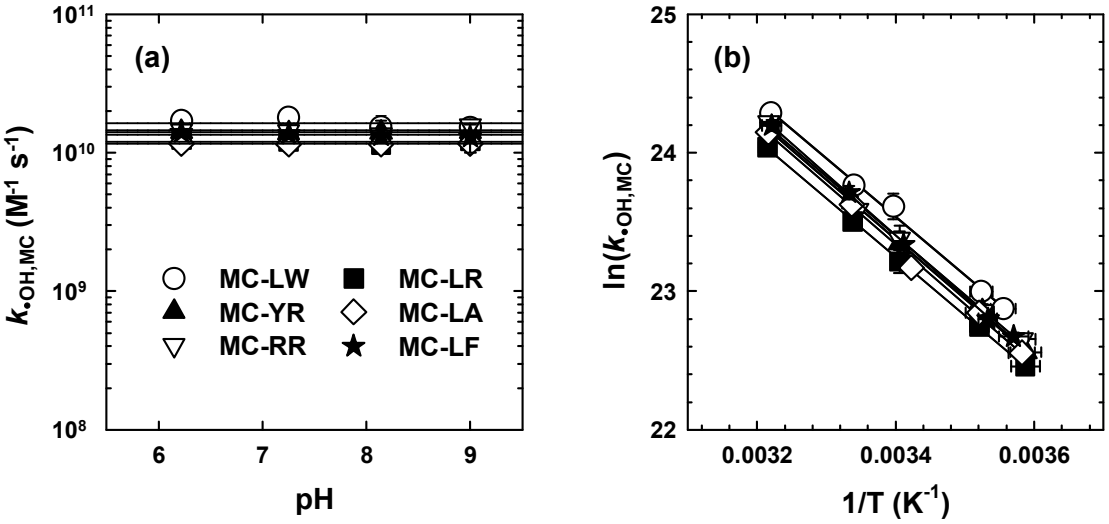

Figure 3.47. (a) pH-dependence of $k_{\bullet OH,MC}$ and (b) Arrhenius plots of $k_{\bullet OH,MC}$ (temperature = 20 ± 1°C for (a), pH = 7.2 for (b)).

As shown in Figure 3.47a, All of the $k_{\bullet OH,MC}$ values were very similar to each other, ranging from 1.2×10^{10} to 1.6×10^{10} M^{-1} s^{-1} regardless of either the effect of pH or the sort of MC, which is in good agreement with previous investigations. The estimated E_a values for the reaction of MCs with •OH values were also very similar to each other, and ranged from 35.1 to 36.7 kJ mol^{-1} (Figure 3.47b). These similar reactivities of MCs toward •OH can be elucidated by the highly reactive and nonselective nature of •OH.

3.2.3. Oxidation of MCs by O_3 in natural waters. In order to verify the validity of the determined $k_{O3,MC}$ and $k_{\bullet OH,MC}$ values, The oxidative degradation of MCs by various O_3 doses was examined in five natural water samples spiked with 0.1 μM of MCs (Figure 3.48).

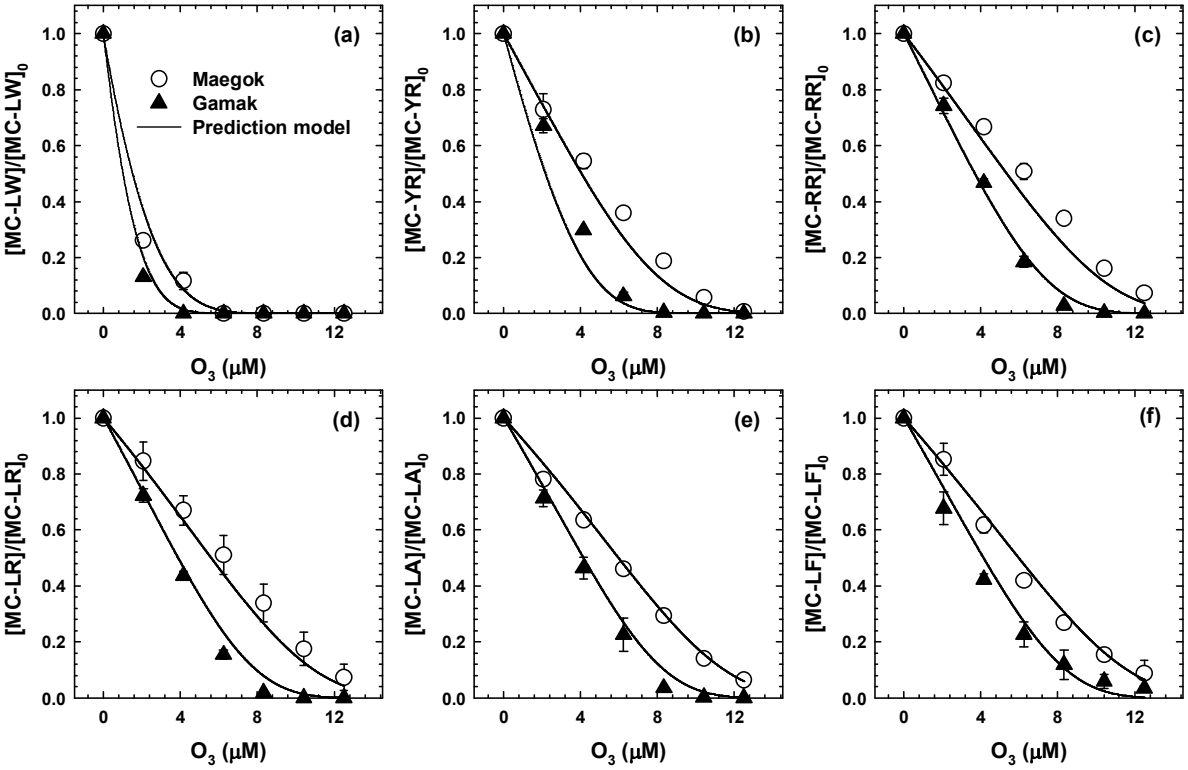

Figure 3.48. Oxidation of MCs as a function of O_3 concentration in Maegok and Gamak natural waters. Symbols and lines represent experimental data and prediction model using Equation 3.3 ($[MCs]_0$ = 0.1 μM, temperature = 20 ± 1°C).

The oxidation efficiency of the MCs in Maegok water was lower than those in Gamak water, because Maegok water contains higher concentrations of DOM. To predict the removal efficiency of MCs by various O_3 in the two natural waters, oxidant exposure values (i.e., $\int[O_3]dt$ and $\int[\bullet OH]dt$) were obtained by monitoring the rapid decomposition of O_3 using SFS and the use of a low concentration of •OH probe compound (0.1 μM of *p*CBA), respectively, at various O_3 doses (Figure 3.49).

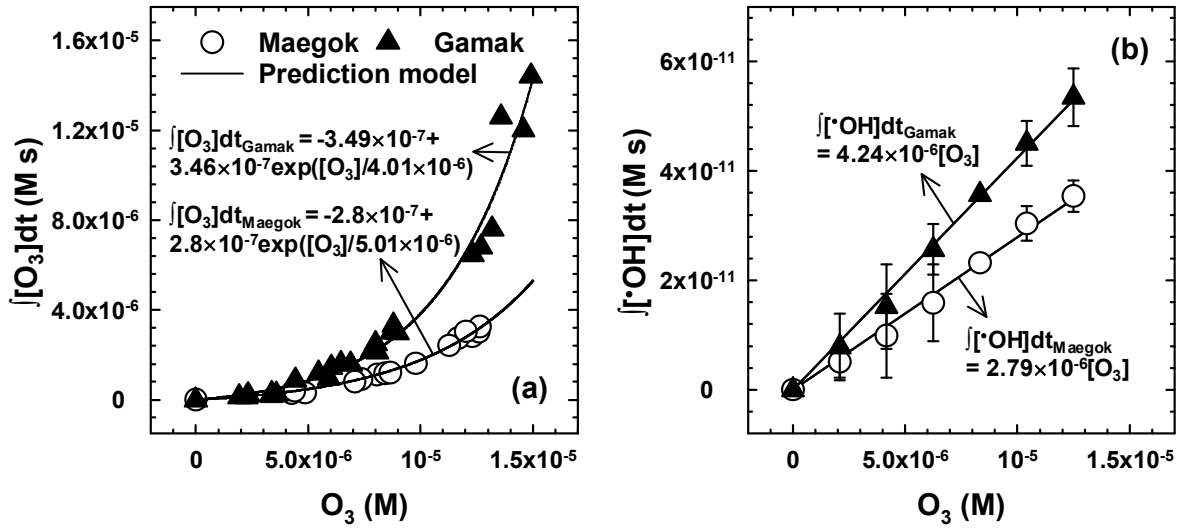

Figure 3.49. ∫[O_3]dt and (b) ∫[•OH]dt as a function of O_3 concentration. Symbols and lines represent experimental data and prediction model, respectively.

The values of ∫[O_3]dt and ∫[•OH]dt in each water sample were fitted into exponential and linear equations, respectively. Based on the equations in Figure 3.49, both ∫[O_3]dt and ∫[•OH]dt values at various initial O_3 concentrations (within 0.7 mg L^{-1}) can be calculated. Using the $k_{O3,MC}$, $k_{•OH,MC}$, ∫[O_3]dt, and ∫[Mn(VII)]dt values (Table 3.6 and Figure 3.49), the oxidative removal of MCs by O_3 in natural waters was modeled by the following equation:

$$[MC]_t = [MC]_0 \exp(-k_{O3,MC} \int[O_3]dt - k_{•OH,MC} \int[•OH]dt) \quad (3.3)$$

In all cases, the model calculations (solid lines in Figures 3.48a–e) fit well with the experimental data, confirming the validity of the $k_{O3,MC}$ and $k_{•OH,MC}$ values determined in this study. The $k_{O3,MC}$ and $k_{•OH,MC}$ values in the literature have not been validated by modeling MC removal by ozonation in natural water samples.

3.3. Oxidation of MC-LR by Fe(IV)-TPP complex

3.3.1. MC-LR degradation by the Fe(II)/O_2 and Fe(II)/H_2O_2 systems in the presence of ligands. Oxidative degradation of MC-LR by Fe(II)/O_2 and Fe(II)/H_2O_2 systems was examined in the absence and presence of iron-chelating agents (ligands: EDTA, oxalate, and TPP) at neutral pH (Figure 3.50).

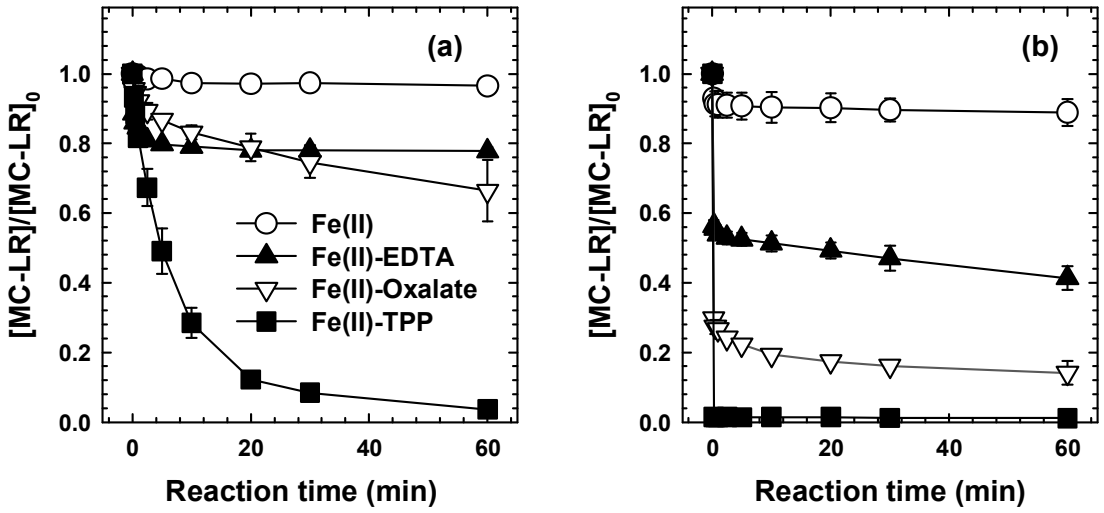

Figure 3.50. Degradation of MC-LR by (a) Fe(II)/O_2 and (b) Fe(II)/H_2O_2 systems with various ligands ($[MC\text{-}LR]_0$ = 0.2 μM, $[Fe(II)]_0$ = 100 μM, $[EDTA]_0$ = $[Oxalate]_0$ = $[TPP]_0$ = 500 μM, $[H_2O_2]_0$ = 250 μM, pH = 7).

The degradation of MC-LR in the absence of ligands was minor for both the Fe(II)/O_2 and Fe(II)/H_2O_2 systems. However, the addition of ligands significantly enhanced the degradation of MC-LR; TPP led to the highest enhancement. The Fe(II)-ligand/O_2 and Fe(II)-ligand/H_2O_2 systems exhibited different patterns in terms of the kinetics of MC-LR degradation. In the Fe(II)-ligand/O_2 system, MC-LR was gradually degraded over the duration of the reaction (Figure 3.50a), whereas MC-LR degradation by the Fe(II)-ligand/H_2O_2 system proceeded instantaneously in the initial stage of the reaction (Figure 3.50b).

The MC-LR degradation by the Fe(II)-ligand/O_2 systems is mainly attributed to oxidation by Fe(IV) species produced via Reactions 3.4–3.6.[85, 86]

$$\text{Fe(II) (-ligand)} + O_2 \rightarrow \text{Fe(III) (-ligand)} + O_2^{\bullet-} \quad (3.4)$$

$$\text{Fe(II) (-ligand)} + O_2^{\bullet-} \rightarrow \text{Fe(III) (-ligand)} + H_2O_2 \quad (3.5)$$

$$\text{Fe(II) (-ligand)} + H_2O_2 \rightarrow \text{Fe(IV) (-ligand)} + 2OH^- \quad (3.6)$$

In the absence of ligands, Fe(IV) (likely oxo or hydroxo) complexes are produced by the same

mechanism, but the yields and reactivities are very slow, limiting the degradation of organic contaminants (MC-LR in this study) (refer to Kim et al. for the detailed explanation[86]). Evidence from the literature exhibits that the oxidant yields (Δ[Fe(IV)]/Δ[Fe(II)]) reported for Fe(II)-ligand/O_2 systems at pH 7 were : TPP (~70%) > oxalate (~25%) > EDTA (5~15%).[85, 86] These results are consistent with the patterns in MC-LR oxidation found in this study (Figure 3.50).

In the Fe(II)-ligand/O_2 systems, the rate-determining step (RDS) for Fe(IV) production is believed to be the reaction of Fe(II) with O_2 (Reaction 3.4). This result was estimated by extrapolating from the known kinetics of uncomplexed Fe(II) reactions.[82] Therefore, the oxidation rate of MC-LR by Fe(II)-ligand/O_2 systems is predominantly governed by Reaction 3.4. However, when H_2O_2 is externally supplied (the Fe(II)-ligand/H_2O_2 systems), the reaction of Fe(II) with H_2O_2 (Reaction 3.6) becomes the RDS that governs the MC-LR oxidation rate. The faster degradation of MC-LR by the Fe(II)-ligand/H_2O_2 system compared to the Fe(II)-ligand/O_2 systems (Figure 3.50) represents that Reaction 3.6 is faster than Reaction 3.4 in the presence of ligands. This result is also consistent with the kinetics of Fe(II) oxidation without ligands.[82]

3.3.2. Optimization of Fe(II), TPP, and H_2O_2 doses. *Effects of Fe(II) and TPP concentrations on MC-LR degradation by the Fe(II)-TPP/O_2 system.* To find out the optimum doses of Fe(II) and TPP in the Fe(II)-TPP/O_2 system, the oxidation of MC-LR was tested by varying the input concentrations of Fe(II) and TPP (refer to Table 2.4 and Figure 3.51a). The obtained data were evaluated using RSM. Experimental data were fitted to a model equation, and the resultant response surface was described in Figure 3.52a. The developed model produced representative estimates, i.e., R^2 = 0.8939, *p*-value = 0.0442, *p*-value of *LOF* = 0.0607, and *AP* value = 7.6 (refer to Table 3.7). The normal probability plot of the residuals was almost linear (Figure 3.53a), showing that prediction errors are distributed with a constant variance.

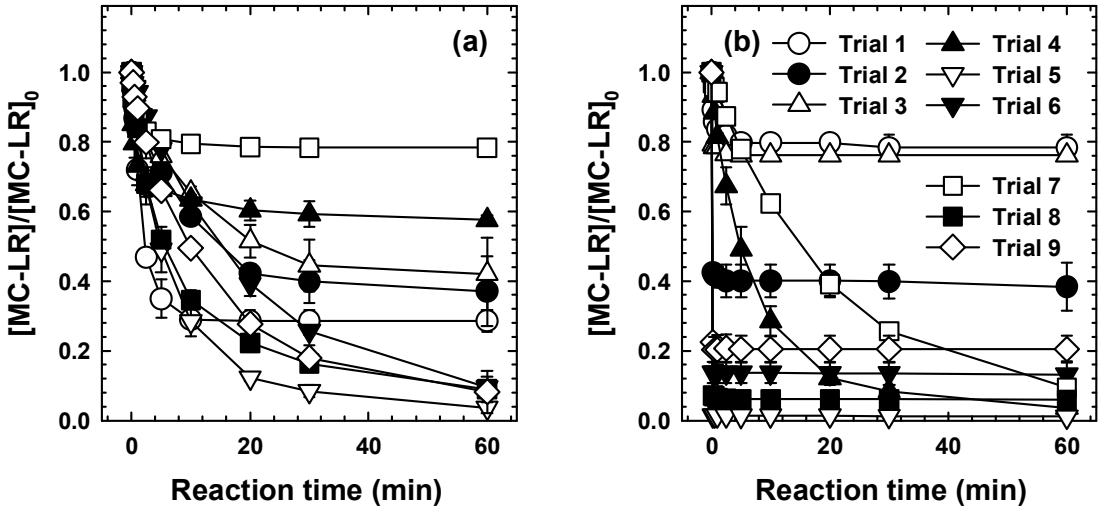

Figure 3.51. (a) Degradation of MC-LR by Fe(II)-TPP/O_2 system with different Fe(II) and TPP concentrations, and (b) degradation of MC-LR by Fe(II)-TPP/H_2O_2 system with different TPP:Fe(II) ratios and H_2O_2 concentration. Refer to Table 2.4 for detailed conditions ($[MC\text{-}LR]_0$ = 0.2 μM, $[Fe(II)]_0$ = 5, 100, 195 μM, $[TPP]_0$ = 10, 500 and 990 μM, $[H_2O_2]_0$ = 0, 250 and 500 μM, pH = 7).

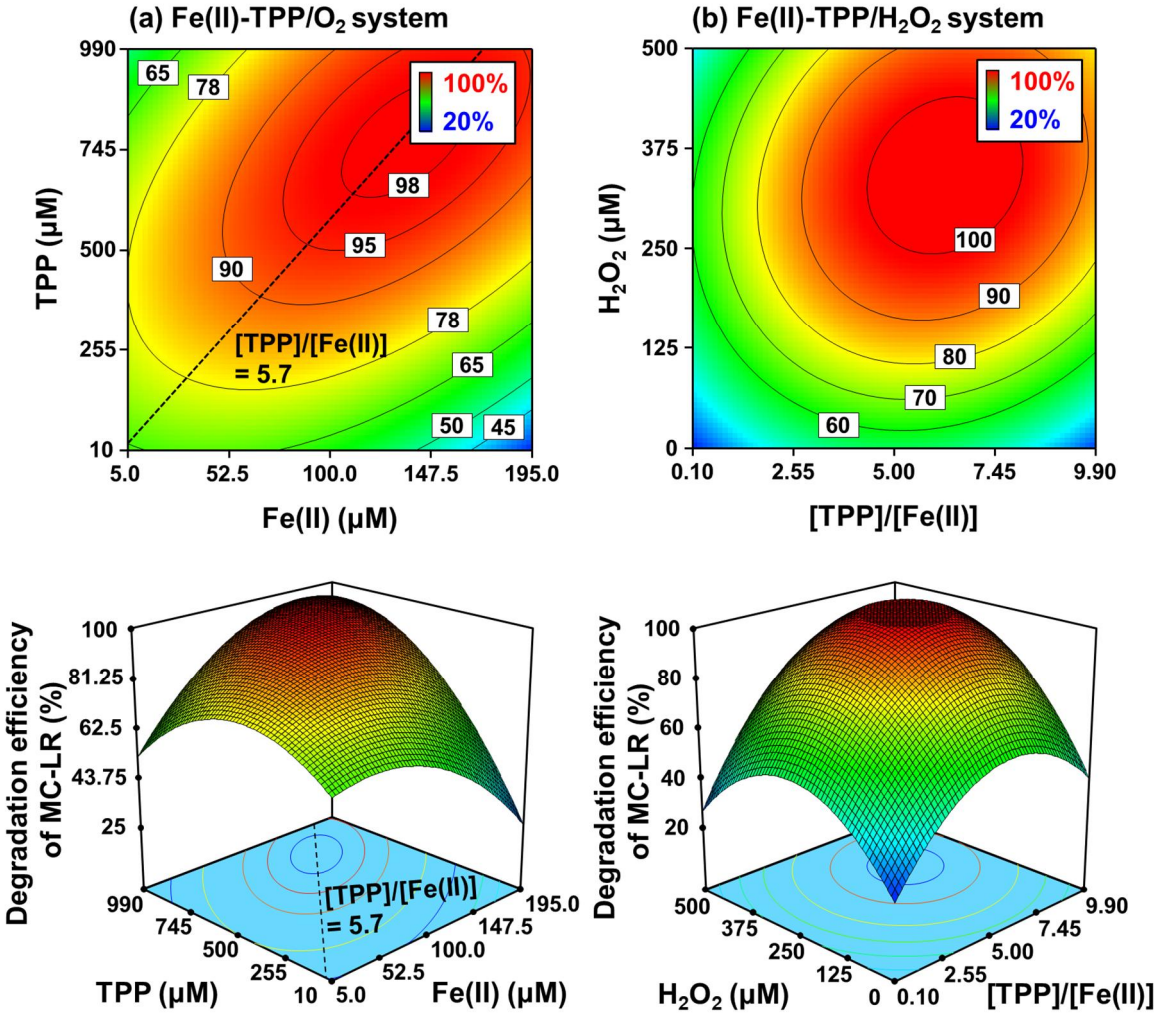

Figure 3.52. Effects of Fe(II), TPP, and H_2O_2 doses on the degradation efficiency of MC-LR by Fe(II)-TPP/O_2 (a) and Fe(II)-TPP/H_2O_2 systems ($[MC\text{-}LR]_0$ = 0.201 mg/L (0.2 μM), pH = 7, $[Fe(II)]_0$ = 100 μM for (b), reaction time = 60 min for (a) and 10 min for (b)).

Table 3.7. ANOVA for the regression model of degradation efficiency of MC-LR (Y_1) as functions of Fe(II) (X_1) and TPP concentrations (X_2) (for Figure 3.52a)

Source	Sum of squares	Degree of freedom	Mean square	*F*-value	*p*-value
Model	4698.55	5	939.71	6.74	0.0442
X_1	7.38	1	7.38	0.053	0.8293
X_2	1211.95	1	1211.95	8.69	0.0421
X_1X_2	1625.06	1	1625.06	11.65	0.0269
X_1^2	624.07	1	624.07	4.47	0.1019
X_2^2	925.28	1	925.28	6.63	0.0616
Residual	557.90	4	139.47		
LOF	556.63	3	185.54	146.31	0.0607
Pure error	1.27	1	1.27		
Correlation total	5256.45	9			

Developed model equation:

$$Y_1 = 62.39 + 0.16X_1 + 0.07X_2 + 4.33 \times 10^{-4}X_1X_2 - 1.81 \times 10^{-3}X_1^2 - 8.29 \times 10^{-5}X_2^2 \quad (R^2 = 0.8939, AP = 7.6) \quad (3.7)$$

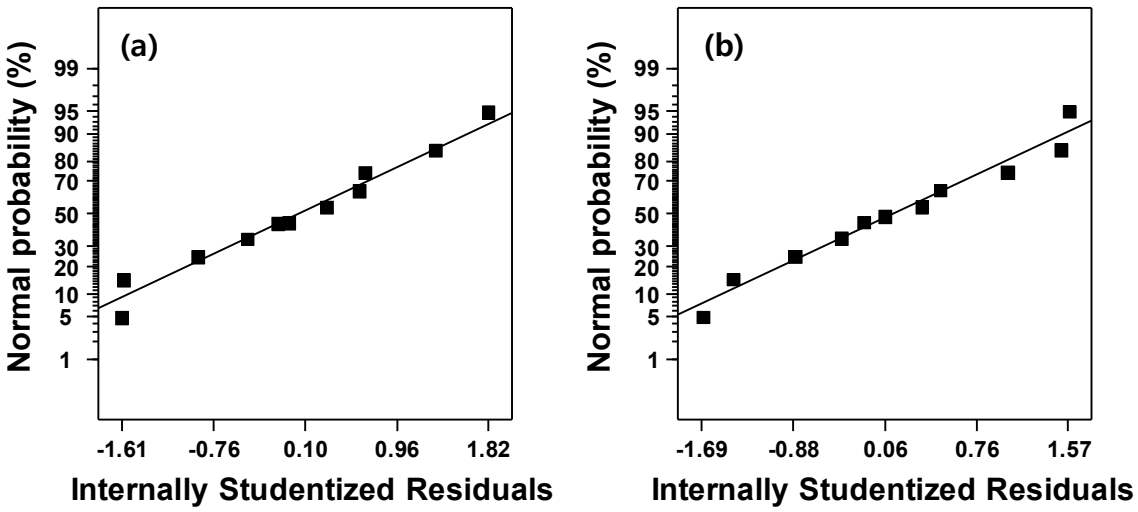

Figure 3.53. Normal probability plot of residuals for the model of MC-LR degradation efficiency by (a) the Fe(II)-TPP/O_2 system and (b) the Fe(II)-TPP/O_2.

The degradation efficiency of MC-LR by the Fe(II)-TPP/O_2 system was optimized at 134.6 μM Fe(II) and 763.8 μM TPP respectively, exhibiting the maximum value of 99.4% (Figure 3.52a). Increasing the Fe(II) concentration increases the oxidant production, as a result enhancing the degradation of MC-LR. However, excessive Fe(II) scavenges the oxidant (Reaction 3.8). These two contrasting factors optimize the Fe(II) concentration for the MC-LR oxidation.

$$\text{Fe(II)-TPP} + \text{Fe(IV)-TPP} \rightarrow 2\text{Fe(III)-TPP} \quad (3.8)$$

The coordination geometry of Fe(II)-TPP complexes affects the reactivity of these complexes with O_2 and subsequently the production of Fe(IV)-TPP complex, as can be seen from the occurrence of an optimum TPP dose. The coordination number intimately influences the reactivity of iron complexes by changing the ligand field strength, bond angles around the iron atom, and the spin-state of complexes.[145] The degradation efficiency of MC-LR tended to exhibit high values according to the line of [TPP]/[Fe(II)] = 5.7 (Figure 3.52a), which may indicate the optimum coordination number of Fe(II)-TPP complexes for oxidant production. However, further study is required to verify the speciation of Fe(II)-TPP complexes. The ratio between Fe(II) and TPP can interactively affect the coordination chemistry of Fe(II)-TPP complexes. This result was reflected in the statistical significance of the interaction term between the two factors; X_1X_2 exhibited the highest significance level with a *p*-value of 0.0269 (Table 3.7).

Meanwhile, previous studies have demonstrated that the high concentration of EDTA inhibited the O_2 activation by Fe(II)-EDTA complexes, suggesting that the presence of excess EDTA may suppress the binding of O_2 to the iron coordination.[146–148] A similar mechanism can also apply for the Fe(II)-TPP complexes.

Effects of TPP:Fe(II) molar ratio and H_2O_2 concentration on MC-LR degradation by the Fe(II)-TPP/H_2O_2 system. The oxidation of MC-LR by the Fe(II)-TPP/H_2O_2 system was tested by changing [TPP]/[Fe(II)] and H_2O_2 does (refer to Table 2.4 and Figure 3.51b). The degradation efficiencies of MC-LR (after 10 min) were fitted to the model equation, and the response surface was depicted (Figure 3.52b). The developed model fitted the data well, as can be seen from the estimates, i.e., R^2 = 0.9768, *p*-value = 0.0004, *p*-value of *LOF* = 0.2202, and *AP* value = 16.194 (refer to Table 3.8). The residual errors of the fitted model were normally distributed, as can be observed from the normal probability plot (Figure 3.53b).

Table 3.8. ANOVA for the regression model of degradation efficiency of MC-LR (Y_2) as functions of [TPP]/[Fe(II)] (X_3) and H_2O_2 concentration (X_4) (for Figure 3.52b)

Source	Sum of squares	Degree of freedom	Mean square	*F*-value	*p*-value
Model	8695.56	5	1739.11	42.08	0.0004
X_3	731.99	1	731.99	17.71	0.0084
X_4	1939.56	1	1939.56	46.93	0.0010
X_3X_4	355.05	1	355.05	8.59	0.0326
X_3^2	2143.65	1	2143.65	51.87	0.0008
X_4^2	2014.01	1	2014.01	48.73	0.0009
Residual	206.64	5	41.33		
LOF	175.07	3	58.36	3.70	0.2202
Pure error	31.57	2	15.78		
Correlation total	8902.20	10			

Developed model equation:

$$Y_2 = 21.92 + 12.45X_3 + 0.26X_4 + 7.69E^{-3}X_3X_4 - 1.21X_3^2 - 4.51E^{-4}X_4^2$$

($R^2 = 0.9768$, $AP = 16.194$) (3.9)

As shown in Figure 3.52b, the response surface exhibiting the degradation efficiency of MC-LR was shaped as a hemispherical dome, showing the complete oxidation of MC-LR in the circular region of [TPP]/[Fe(II)] = 4.32–8.13 and [H_2O_2] = 243–440 μM. Similar to the case of Fe(II), the existence of the optimum H_2O_2 concentration can be explained by two contrasting factors: i) the enhanced oxidant production with increasing H_2O_2 concentration, and ii) the oxidant scavenging by excessive H_2O_2. It has been reported that Fe(IV) can react with H_2O_2 through a series of one-electron transfer reactions (Reactions 3.10 and 3.11 [149]).

$$Fe(IV)=O^{2+} + H_2O_2 \rightarrow Fe(III) + {}^{\bullet}HO_2 + OH^- \quad (3.10)$$

$$Fe(IV)=O^{2+} + {}^{\bullet}HO_2 \rightarrow Fe(III) + O_2 + OH^- \quad (3.11)$$

As was the case for the Fe(II)-TPP/O_2 system, the coordination chemistry of Fe(II)-TPP complexes can determine the optimum [TPP]/[Fe(II)] in the Fe(II)-TPP/H_2O_2 system. The Fe(II)-TPP complexes that exhibited the highest reactivity with H_2O_2 may occur in the range of [TPP]/[Fe(II)] = 4.32–8.13; the range in which the maximum MC-LR degradation was observed; Figure 3.52b). The estimated optimum of [TPP]/[Fe(II)] was 5.9, similar to the value in the Fe(II)-TPP/O_2 system, 5.7.

3.3.3. Effect of pH. The degradation of MC-LR was examined by varying the pH from 3 to 11 in the Fe(II)-TPP/O_2 and Fe(II)-TPP/H_2O_2 systems. The degradation efficiencies of MC-LR were plotted as functions of pH (Figure 3.54); the time-concentration profiles were shown in Figure 3.55.

In the Fe(II)-TPP/O_2 system, the degradation efficiencies of MC-LR had two optima at pH 6–7 and 9 (Figure 3.54a), respectively. The same trends in pH-dependency observed in this study were also reported for the degradation of Reactive Black 5 and carbamazepine in a separate study.[86] The pH-dependent contaminant oxidation by the Fe(II)-TPP/O_2 system was explained by two factors: i) the pH-dependent oxidant yield and ii) the speciation of the reactive oxidant (Fe(IV)-TPP complex).[86] The low degradation efficiencies at acidic pH (e.g., decreasing degradation of MC-LR at pH < 5; Figure 3.54a) are because of the poor oxidant yields. A previous study has demonstrated that the oxidation of Fe(II)-TPP complexes by O_2 decelerates with decreasing of pH, producing decreased amounts of oxidants[86]; note that the oxidation rate of MC-LR decreases with decreasing of pH as exhibited in time-concentration profiles (Figure 3.55a). However, the unique patterns of pH-dependency in neutral and alkaline pH ranges (showing two optimum points) are mainly attributed to the pH-dependent speciation of Fe(IV)-TPP complexes that show different reactivities; note that the oxidant production by the Fe(II)-TPP/O_2 system continuously improves with increasing pH over the entire pH range. [86]

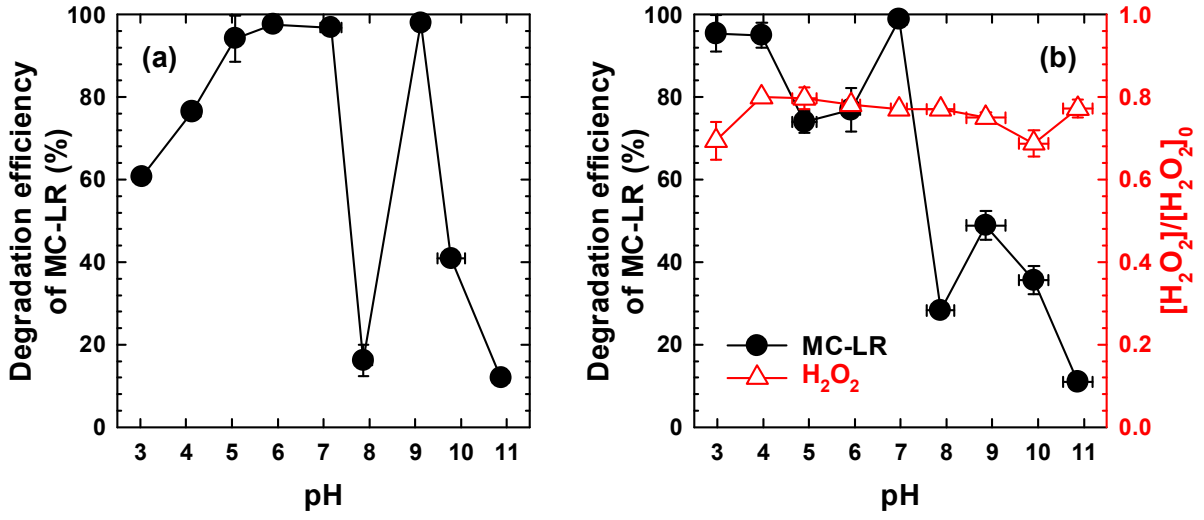

Figure 3.54. Degradation efficiency of MC-LR by (a) Fe(II)-TPP/O_2 and (b)Fe(II)-TPP/H_2O_2 systems as a function of pH. Red open circles in (b) represent the fraction of residual H_2O_2 ($[MC\text{-}LR]_0$ = 0.2 μM, $[Fe(II)]_0$ = 100 μM, $[TPP]_0$ = 500 μM, $[H_2O_2]_0$ = 250 μM for (b), reaction time = 60 min).

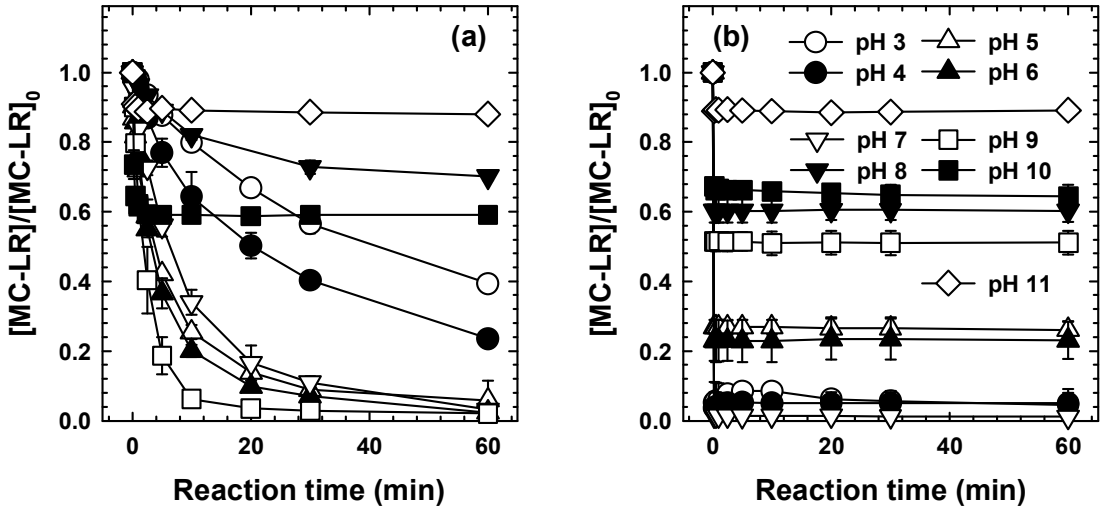

Figure 3.55. Degradation of MC-LR by Fe(II)-TPP/O_2 (a) and Fe(II)-TPP/H_2O_2 (b) systems at different pH values ($[MC\text{-}LR]_0$ = 0.201 mg/L (0.2 μM); $[Fe(II)]_0$ = 100 μM; $[TPP]_0$ = 500 μM; $[H_2O_2]_0$ = 250 μM).

The Fe(II)-TPP/H_2O_2 system exhibited peak values of MC-LR degradation efficiency at pH 3–4, 7 and 9 (Figure 3.54b). In contrast to the reaction with O_2, the oxidation of Fe(II)-TPP complexes by H_2O_2 is fast, regardless of pH; note that the MC-LR degradation by the Fe(II)-TPP/H_2O_2 system proceeded instantaneously at all pH values (Figure 3.55b), and the H_2O_2 decomposition did not yield many variants over the entire pH range (Figure 3.54b). Therefore, the pH-dependent MC-LR oxidation by the Fe(II)-TPP/H_2O_2 system solely results from the speciation of Fe(IV)-TPP complexes with different reactivities.

On the basis of the aforementioned explanations with respect to the Fe(IV)-TPP speciation, it is postulated that the Fe(IV)-TPP species produced at pH 7 (where the MC-LR oxidation is maximized in both the Fe(II)-TPP/O_2 and Fe(II)-TPP/H_2O_2 systems) has a higher reactivity than the species produced at pH 8 (where the MC-LR degradation is minimized in both the systems). Since an oxidant with high reactivity generally shows poor selectivity, the Fe(IV)-TPP species at pH 7 should be less selective than the one at pH 8. In order to verify this postulate, the degradation efficiencies of six different MCs (i.e., MC-LR, -YR, -RR, -LA, -LF, and -LW) were compared at two pH values (i.e., pH 7 and 8) in the Fe(II)-TPP/O_2 system (Figure 3.56) (refer to Figure 1.3 for chemical structures of MC congeners).

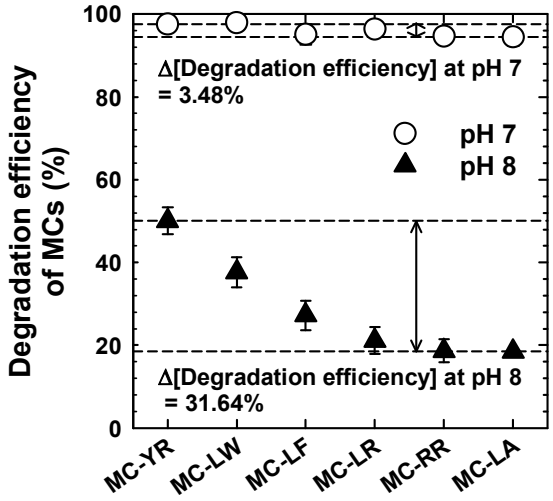

Figure 3.56. Degradation efficiency of different MC congeners by the Fe(II)-TPP/O_2 system ([MC-LF]$_0$ = [MC-YR]$_0$ = [MC-LW]$_0$ = [MC-LR]$_0$ = [MC-RR]$_0$ = [MC-LA]$_0$ = 0.2 μM, [Fe(II)]$_0$ = 100 μM, [TPP]$_0$ = 500 μM, pH = 7, reaction time = 60 min).

The results in Figure 3.56 clearly exhibit that the variation in degradation efficiencies of different MCs was much less at pH 7 (3.48%) than at pH 8 (31.64%), proving that the oxidant produced at pH 7 is less selective than that at pH 8 (also refer to the time-concentration profiles of the six MCs during their oxidation, Figure 3.57).

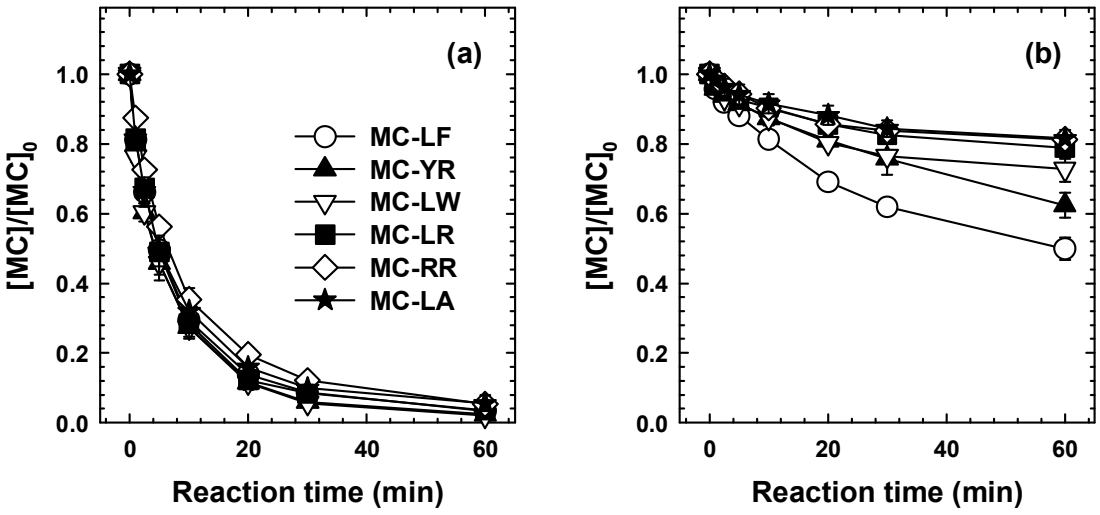

Figure 3.57. Degradation of six MC congeners by Fe(II)-TPP/O_2 system at pH (a) 7 and (b) 8 ([MC-LF]$_0$ = [MC-YR]$_0$ = [MC-LW]$_0$ = [MC-LR]$_0$ = [MC-RR]$_0$ = [MC-LA]$_0$ = 0.2 μM, [Fe(II)]$_0$ = 100 μM, [TPP]$_0$ = 500 μM).

At pH 8, the degradation efficiencies of MCs were of the order of MC-YR > MC-LW > MC-LF > MC-LR ≈ MC-RR ≈ MC-LA (Figure 3.56), suggesting that the reactivity of amino acids with the oxidant is of the order of L-Tyr > L-Trp > L-Phe > L-Leu ≈ L-Ala ≈ L-Arg (refer to amino acids in X^2 and Y^4 positions of the MC structure for each congener, Figure 1.3). A similar pattern has been reported for the reactivity of Fe(IV) chelated by *N*,*N*-bis(2-pyridylmethyl)-*N*-bis(2-pyridyl)-methylamine (denoted as $[Fe^{IV}(O)N4Py]^{2+}$) with amino acids[150]; Tyr and Trp were found to significantly react with $[Fe^{IV}(O)N4Py]^{2+}$, whereas Phe, Arg, Ala, and Leu were unreactive.

3.3.4. Oxidation products and pathways. In order to gain an insight into the oxidation mechanism of MC-LR by the Fe(IV)-TPP complex, the oxidation products formed during MC-LR degradation by the Fe(II)-TPP/O_2 system were analyzed. The analysis using LC/MS identified 22 oxidation products (summarized in Table 3.9); also refer to chromatograms for the identified products (Figures 3.58–3.80).

Table 3.9. Oxidation products of MC-LR identified by LC/MS

Products	Chemical formula $[M+H]^+$	Theoretical m/z	△[a] (ppm)	RT (min)	References
MC-LR	$C_{49}H_{75}N_{10}O_{12}$	995.5560	-2.11	26.60	-
P_{783}	$C_{33}H_{55}N_{10}O_{12}$	783.3995	-3.19	1.69, 1.83	46, 53, 68
P_{785}	$C_{32}H_{53}N_{10}O_{13}$	785.3788	-2.55	1.74, 2.23	No literature
P_{795}	$C_{34}H_{55}N_{10}O_{12}$	795.3995	-0.75	1.69	40, 41, 46, 47, 51, 53, 66, 151, 68
P_{797}	$C_{33}H_{53}N_{10}O_{13}$	797.3788	4.01	1.76, 2.17	No literature
P_{811}	$C_{34}H_{55}N_{10}O_{13}$	811.3944	-1.97	1.80	40, 51
P_{813}	$C_{33}H_{53}N_{10}O_{14}$	813.374	-1.23	2.27	No literature
P_{835}	$C_{37}H_{59}N_{10}O_{12}$	835.4308	-4.55	1.87	40, 41, 46, 47, 51, 53, 66, 68, 151
P_{837}	$C_{36}H_{57}N_{10}O_{13}$	837.4101	2.99	1.76, 2.45	No literature
P_{851}	$C_{37}H_{59}N_{10}O_{13}$	851.4257	-3.64	1.78	68
P_{853}	$C_{36}H_{57}N_{10}O_{14}$	853.4050	2.70	2.33, 2.47	No literature
P_{855}	$C_{36}H_{59}N_{10}O_{14}$	855.4206	0.47	2.77	No literature
P_{997}	$C_{48}H_{73}N_{10}O_{13}$	997.5353	2.71	23.94	No literature
P_{1009}	$C_{49}H_{73}N_{10}O_{13}$	1009.5353	4.06	19.35	53, 66
P_{1011}	$C_{49}H_{75}N_{10}O_{13}$	1011.5509	0.30	6.25, 7.42, 11.11	31, 46, 47, 53, 59, 135, 66, 151
P_{1013}	$C_{48}H_{73}N_{10}O_{14}$	1013.5302	-6.02	10.48, 11.76, 12.69, 13.99, 21.06	No literature
P_{1015}	$C_{48}H_{75}N_{10}O_{14}$	1015.5458	1.58	15.43	53
P_{1027}	$C_{49}H_{75}N_{10}O_{14}$	1027.5458	-3.21	2.68, 3.03, 3.92, 5.81, 6.40	47, 53, 59, 135, 66, 151
P_{1029}	$C_{48}H_{73}N_{10}O_{15}$	1029.5251	8.16	3.24, 4.29, 4.86, 6.78, 7.34, 9.60	No literature
P_{1031}	$C_{48}H_{75}N_{10}O_{15}$	1031.5408	1.65	12.13, 13.96, 17.31, 20.41	No literature
P_{1043}	$C_{49}H_{75}N_{10}O_{15}$	1043.5408	-0.10	3.15, 3.87	59; 135
P_{1045}	$C_{48}H_{73}N_{10}O_{16}$	1045.5200	6.31	3.58, 3.87	No literature
P_{1047}	$C_{48}H_{75}N_{10}O_{16}$	1047.5357	-2.29	4.07,7.97,7.00	No literature

[a]△ represents the mass tolerance (maximal difference between an experimental mass and a theoretical mass, ppm).

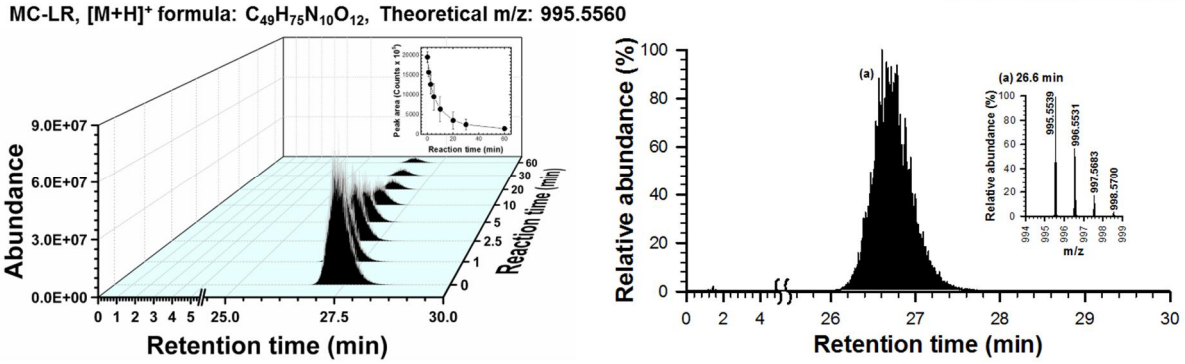

Figure 3.58. LC/MS identification of MC-LR ($[M+H]^+$ = 995.5560). The chromatogram at 20 min with mass spectra (left) and time-dependent chromatograms of MC-LR (right).

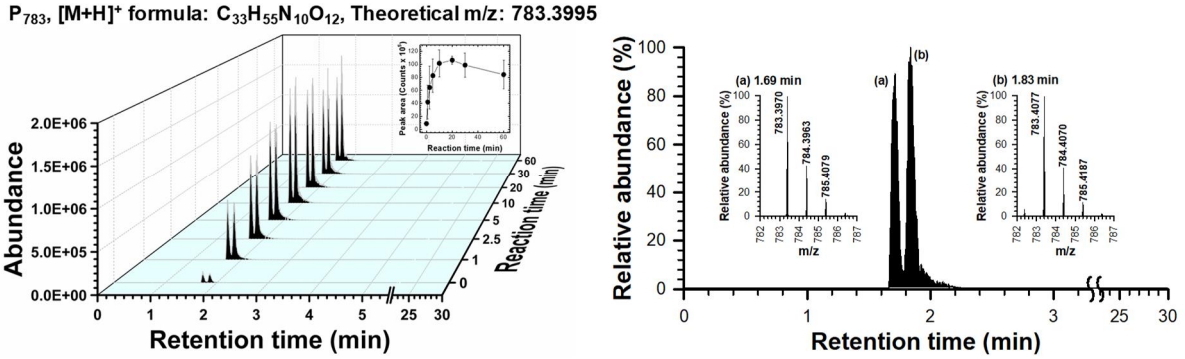

Figure 3.59. LC/MS identification of P_{783} ($[M+H]^+$ = 783.3995). The chromatogram at 20 min with mass spectra (left) and time-dependent chromatograms of P_{783} (right).

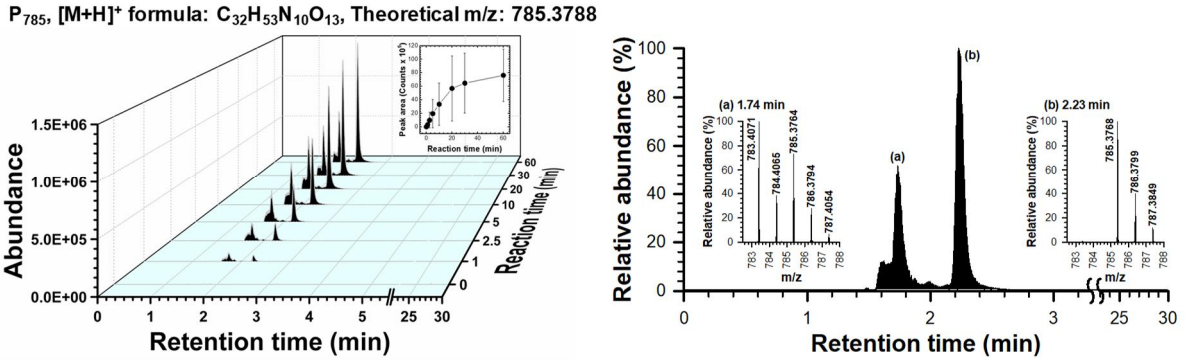

Figure 3.60. LC/MS identification of P_{785} ($[M+H]^+$ = 785.3788). The chromatogram at 20 min with mass spectra (left) and time-dependent chromatograms of P_{785} (right).

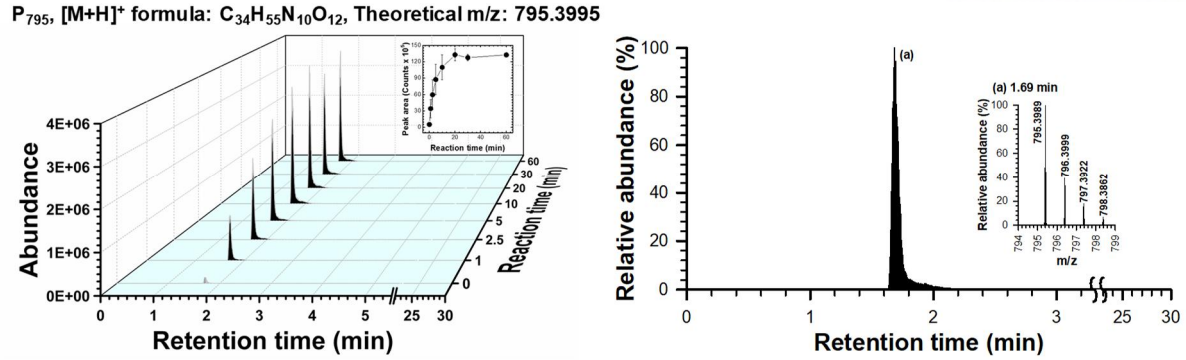

Figure 3.61. LC/MS identification of P_{795} ($[M+H]^+$ = 795.3788). The chromatogram at 20 min with mass spectra (left) and time-dependent chromatograms of P795.3788 (right).

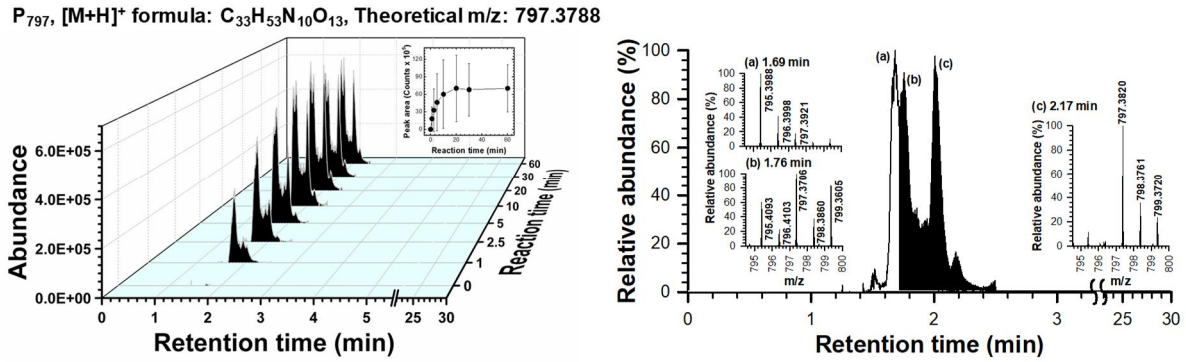

Figure 3.62. LC/MS identification of P_{797} ($[M+H]^+$ = 797.3788). The chromatogram at 20 min with mass spectra (left) and time-dependent chromatograms of P_{797} (right). **Note: The peak filled in white was excluded because it overlapped with P_{795}.*

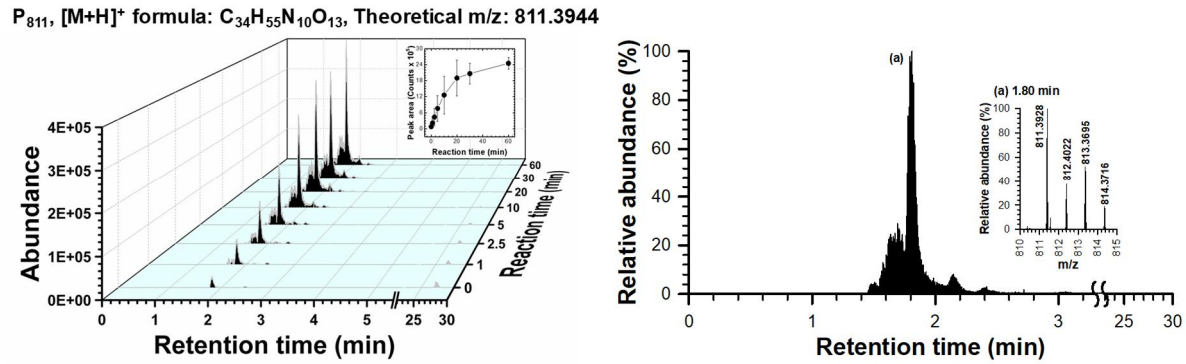

Figure 3.63. LC/MS identification of P_{811} ($[M+H]^+$ = 811.3944). The chromatogram at 20 min with mass spectra (left) and time-dependent chromatograms of P_{811} (right).

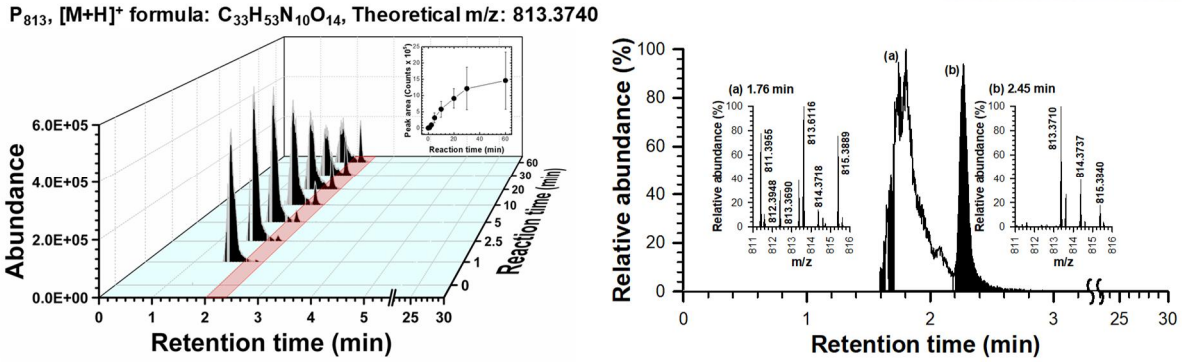

Figure 3.64. LC/MS identification of P_{813} ($[M+H]^+$ = 813.3740). The chromatogram at 20 min with mass spectra (left) and time-dependent chromatograms of P_{813} (right). **Note: The peak filled in white was excluded because it overlapped with P_{811}.*

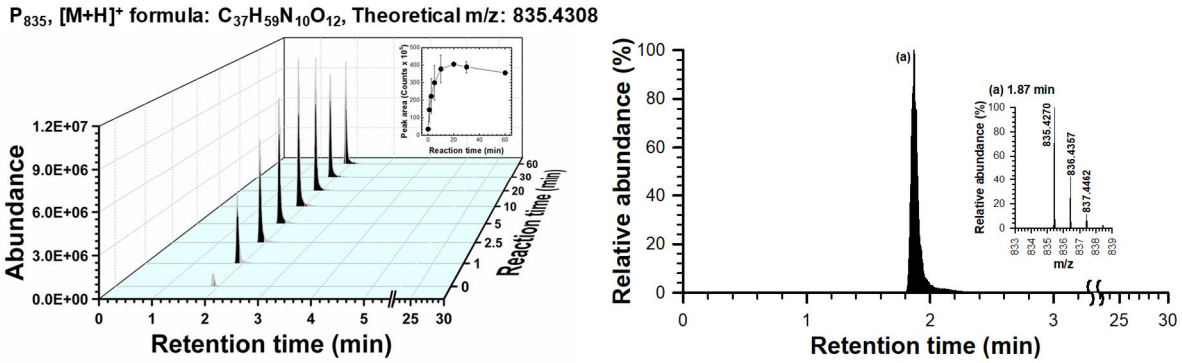

Figure 3.65. LC/MS identification of P_{835} ($[M+H]^+$ = 835.4308). The chromatogram at 20 min with mass spectra (left) and time-dependent chromatograms of P_{835} (right).

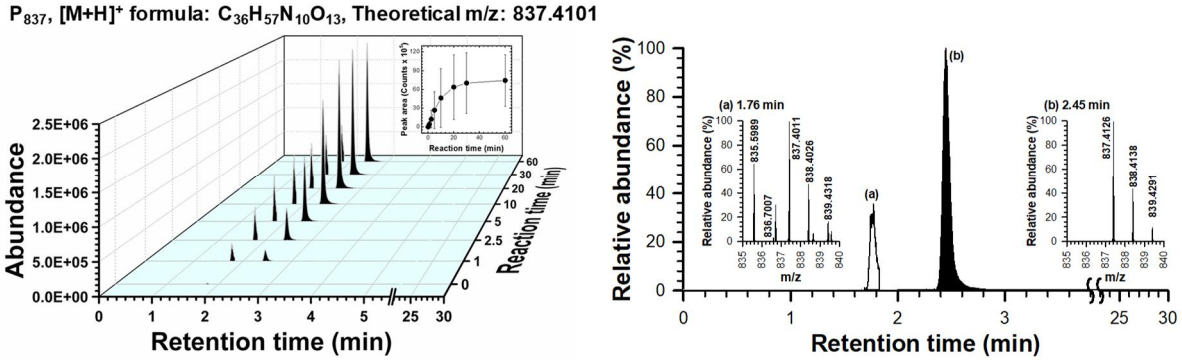

Figure 3.66. LC/MS identification of P_{837} ($[M+H]^+$ = 837.4101). The chromatogram at 20 min with mass spectra (left) and time-dependent chromatograms of P_{837} (right).

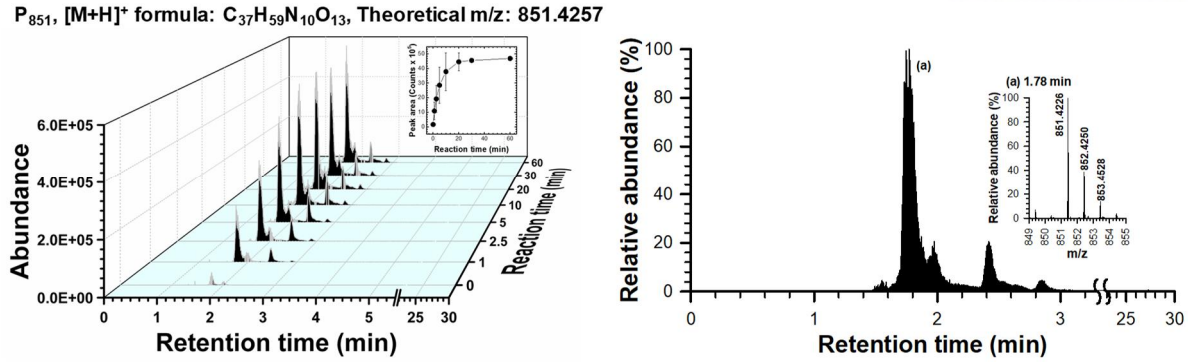

Figure 3.67. LC/MS identification of P_{851} ($[M+H]^+$ = 851.4257). The chromatogram at 20 min with mass spectra (left) and time-dependent chromatograms of P_{851} (right).

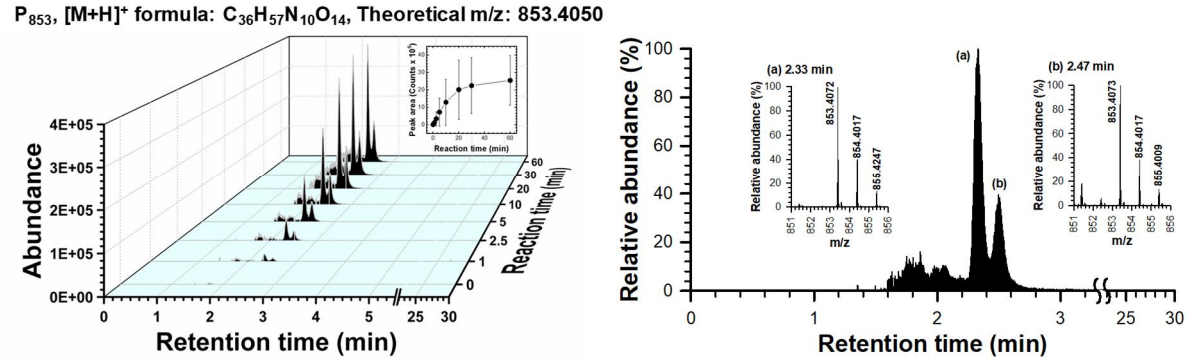

Figure 3.68. LC/MS identification of P_{853} ($[M+H]^+$ = 853.4050). The chromatogram at 20 min with mass spectra (left) and time-dependent chromatograms of P_{853} (right).

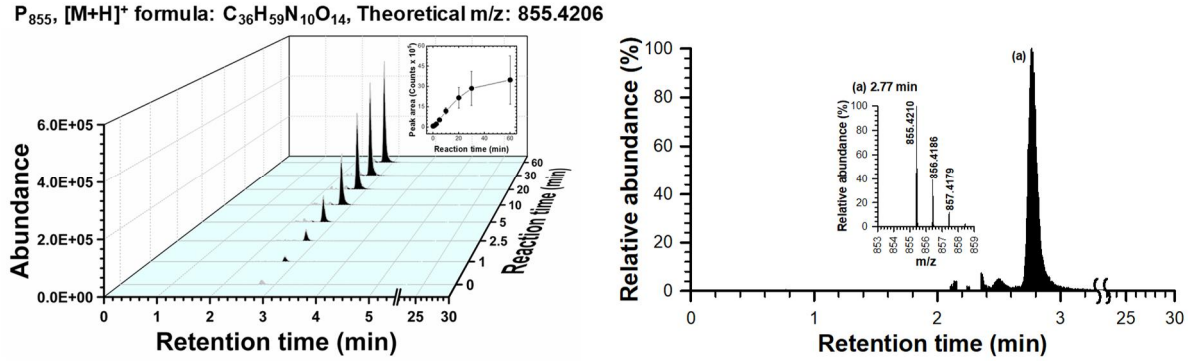

Figure 3.69. LC/MS identification of P_{855} ($[M+H]^+$ = 855.4206). The chromatogram at 20 min with mass spectra (left) and time-dependent chromatograms of P_{855} (right).

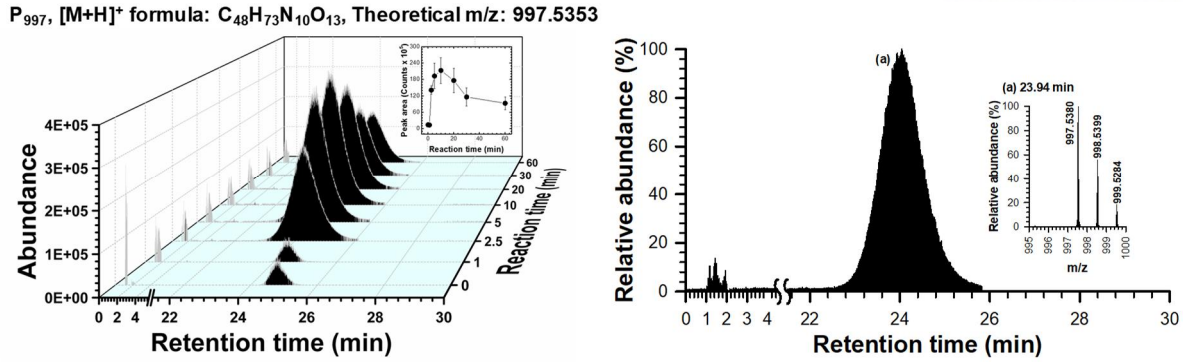

Figure 3.70. LC/MS identification of P_{997} ($[M+H]^+$ = 997.5353). The chromatogram at 20 min with mass spectra (left) and time-dependent chromatograms of P_{997} (right).

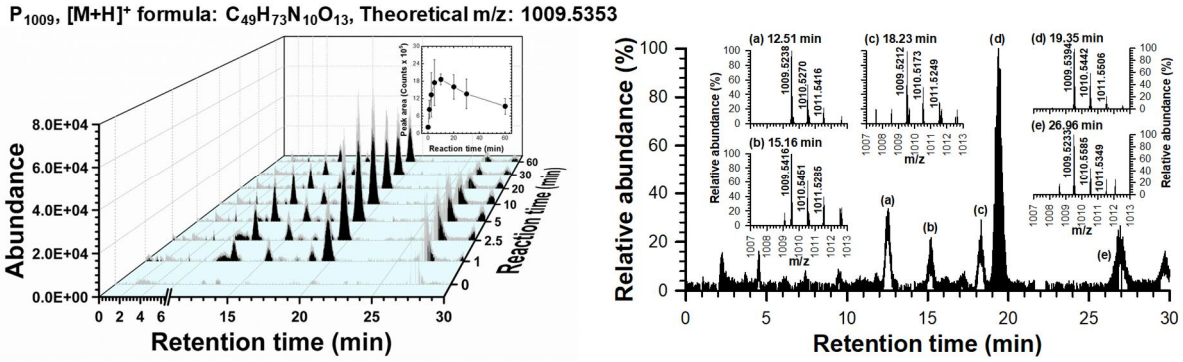

Figure 3.71. LC/MS identification of P_{1009} ($[M+H]^+$ = 1009.5353). The chromatogram at 20 min with mass spectra (left) and time-dependent chromatograms of P_{1009} (right). **Note: The white peaks were excluded because the mass tolerances (for the monoisotopic mass) were over 10 ppm.*

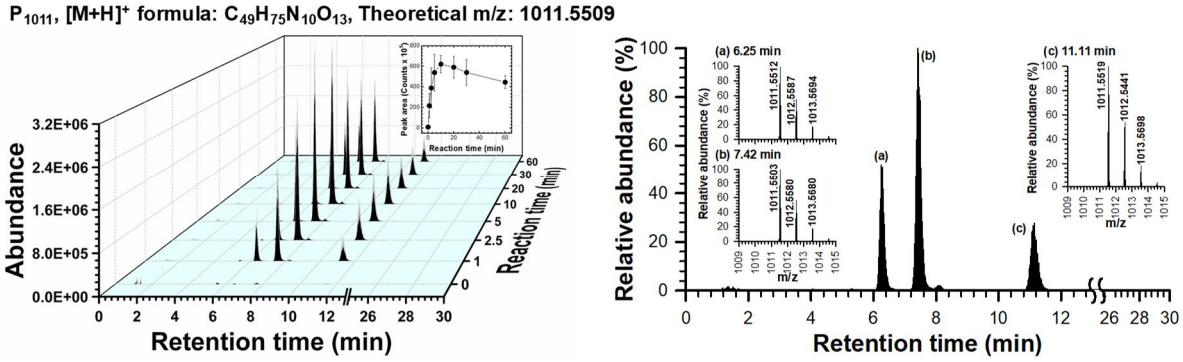

Figure 3.72. LC/MS identification of P_{1011} ($[M+H]^+$ = 1011.5509). The chromatogram at 20 min with mass spectra (left) and time-dependent chromatograms of P_{1011} (right).

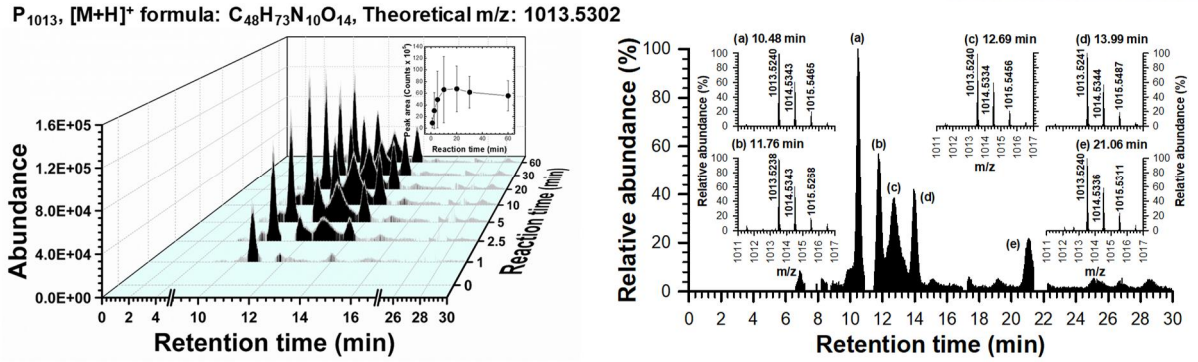

Figure 3.73. LC/MS identification of P_{855} ($[M+H]^+$ = 1013.5302). The chromatogram at 20 min with mass spectra (left) and time-dependent chromatograms of P_{1013} (right).

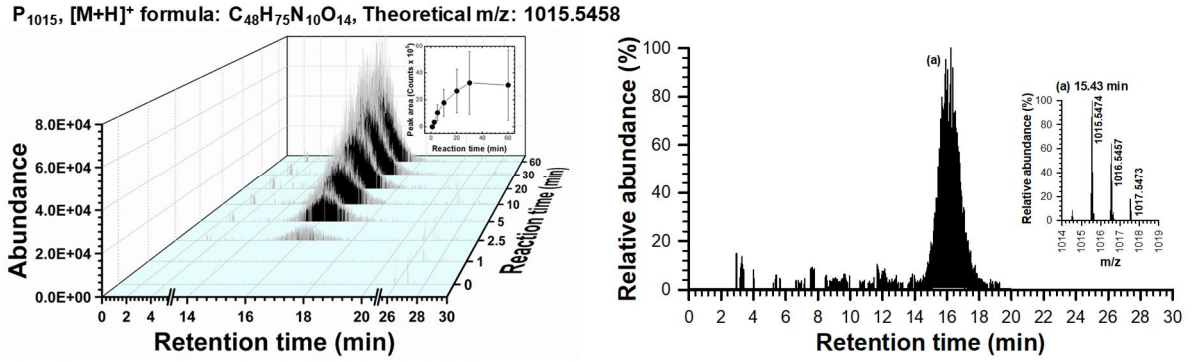

Figure 3.74. LC/MS identification of P_{1015} ($[M+H]^+$ = 1015.5458). The chromatogram at 20 min with mass spectra (left) and time-dependent chromatograms of P_{1015} (right).

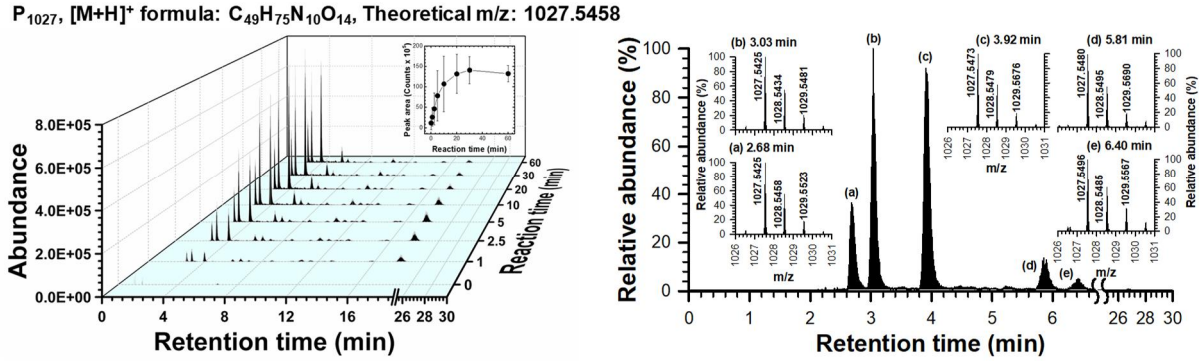

Figure 3.75. LC/MS identification of P_{1027} ($[M+H]^+$ = 1027.5458). The chromatogram at 20 min with mass spectra (left) and time-dependent chromatograms of P_{1027} (right).

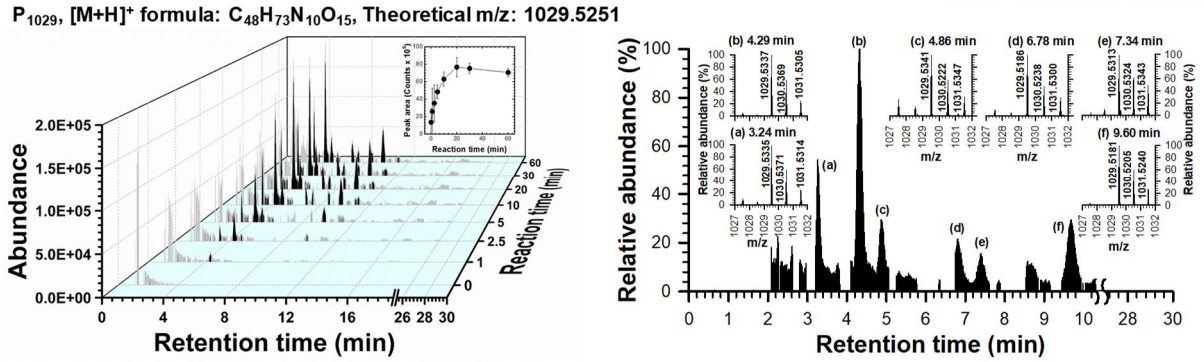

Figure 3.76. LC/MS identification of P_{1029} ($[M+H]^+$ = 1029.5251). The chromatogram at 20 min with mass spectra (left) and time-dependent chromatograms of P_{1029} (right).

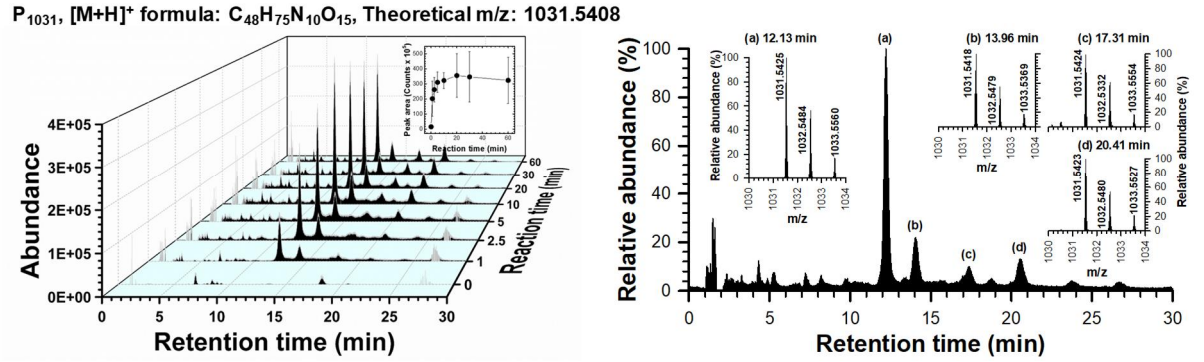

Figure 3.77. LC/MS identification of P_{1031} ($[M+H]^+$ = 1031.5408). The chromatogram at 20 min with mass spectra (left) and time-dependent chromatograms of P_{855} (right).

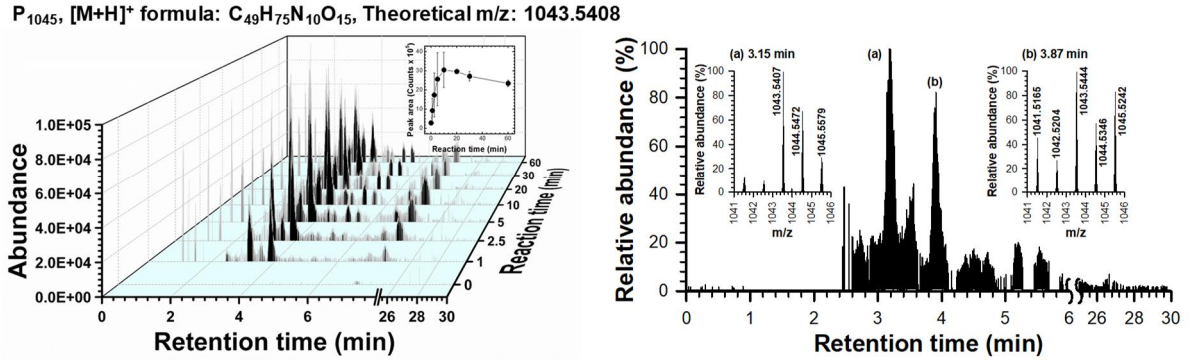

Figure 3.78. LC/MS identification of P_{1043} ($[M+H]^+$ = 1043.5308). The chromatogram at 20 min with mass spectra (left) and time-dependent chromatograms of P_{1043} (right).

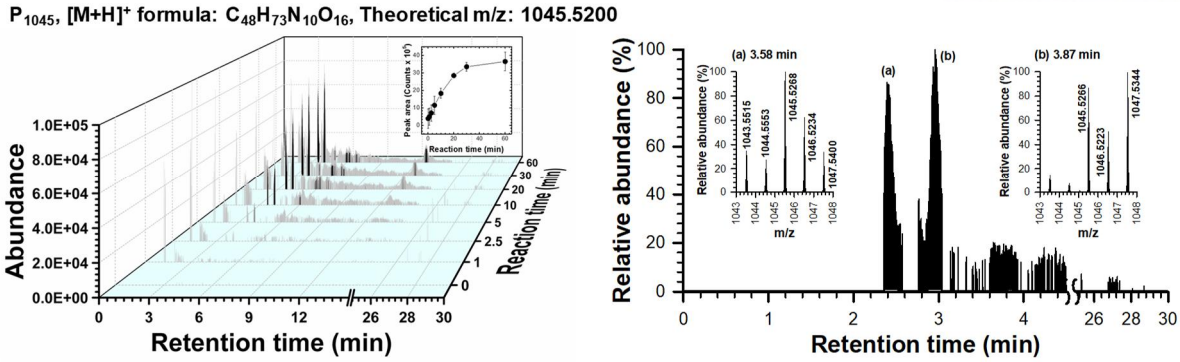

Figure 3.79. LC/MS identification of P_{1045} ($[M+H]^+$ = 1045.5200). The chromatogram at 20 min with mass spectra (left) and time-dependent chromatograms of P_{1045} (right).

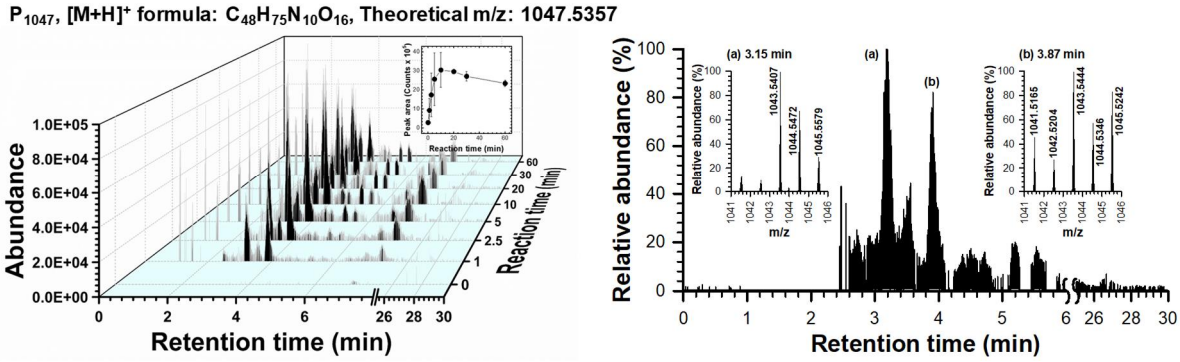

Figure 3.80. LC/MS identification of P_{1047} ($[M+H]^+$ = 1047.5357). The chromatogram at 20 min with mass spectra (left) and time-dependent chromatograms of P_{1047} (right).

Four reactive sites in MC-LR (i.e., phenyl, methoxy, and three alkene groups of Adda and Mdha moieties, Sites A–D in Figure 3.81) have been proposed as preferred positions that undergo primary oxidation.[53]

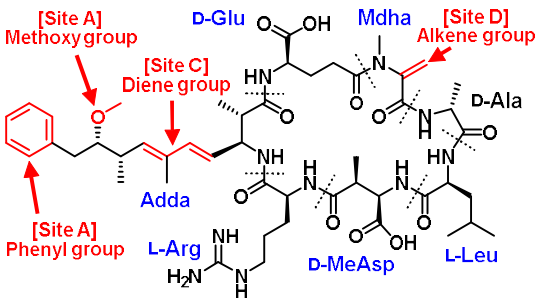

Figure 3.81. The structure of MC-LR and its primary oxidation sites (A–D).

The degradation pathways of MC-LR were postulated along the four sites and the identified oxidation products (Figure 3.82). Hydroxylation of the phenyl moiety of Adda (Site A) produced P_{1011a}, P_{1027a}, and P_{1043} (mono-, di-, and tri-hydroxyphenyl compounds, respectively). These hydroxylated products have also been observed after oxidation of MC-LR by $SO_4^{\bullet-}$,[59] TiO_2 photocatalysis,[151] and ferrate[135]. P_{1009} was produced by the carbonylation of methoxy carbon (Site B). Degradation of MC-LR by oxidation with either $SO_4^{\bullet-}$ or TiO_2 photocatalysis also produced this product.[53, 66] The two alkene groups of Adda moiety (Site C) are believed to be the most vulnerable site to oxidation. These alkene groups were firstly hydroxylated (P_{1011b} and P_{1027b}), and the carbon chain was broken via further oxidation, forming a number of subsequent daughter products (P_{783}, P_{795}, P_{811}, P_{835}, and P_{851}). These products have been observed in oxidation by O_3,[40, 41, 51] TiO_2 photocatalysis,[53, 66, 151] $SO_4^{\bullet-}$,[59] and UV/H_2O_2 system[45, 46]. P_{1011c} and P_{1015} were produced by oxidation of the alkene group of Mdha moiety (Site D). Other studies have also found P_{1015} after photocatalytic oxidation of MC-LR.[53]

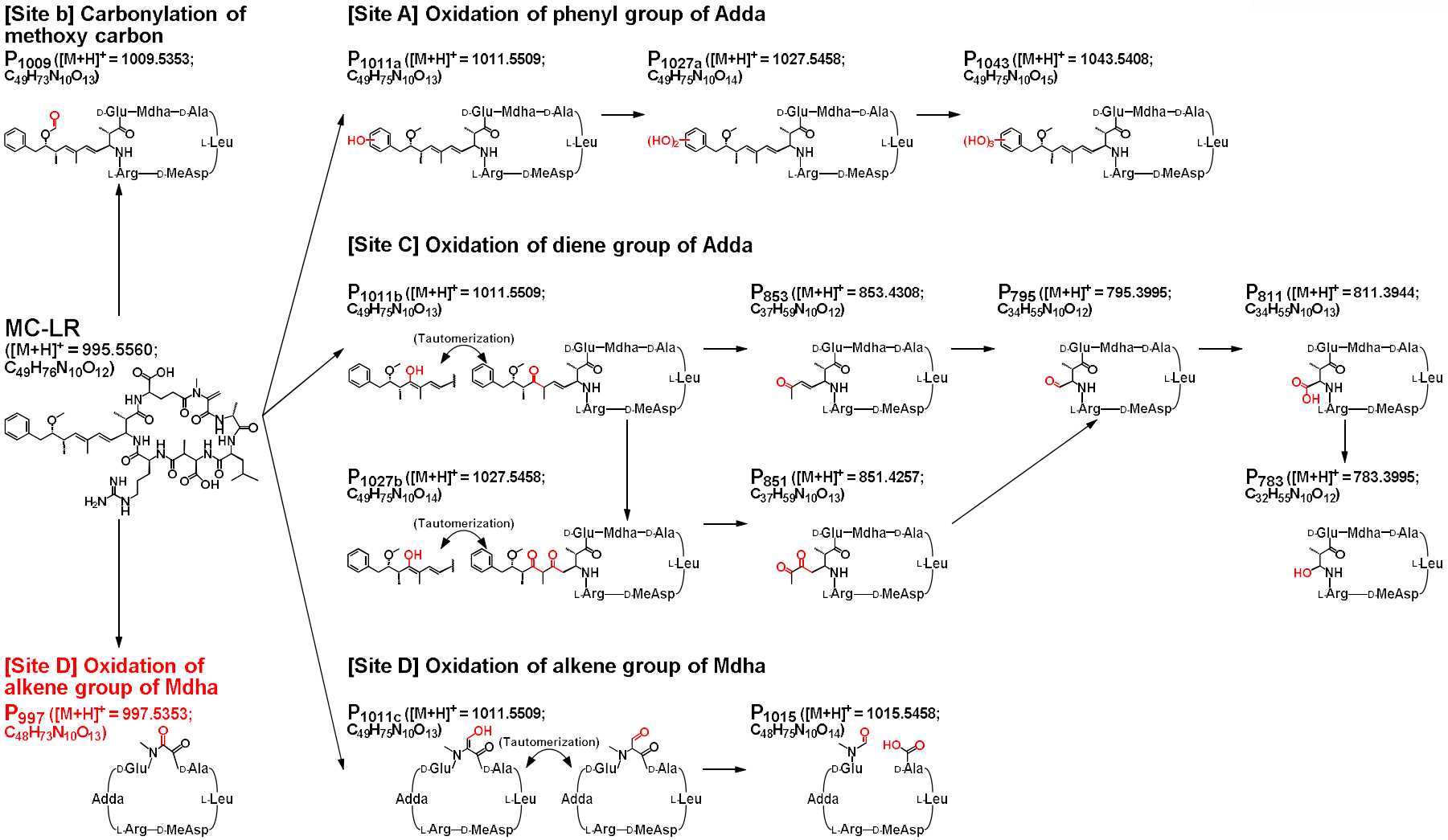

Figure 3.82. Proposed pathways for oxidative degradation of MC-LR by the Fe(II)-TPP/O_2 system.

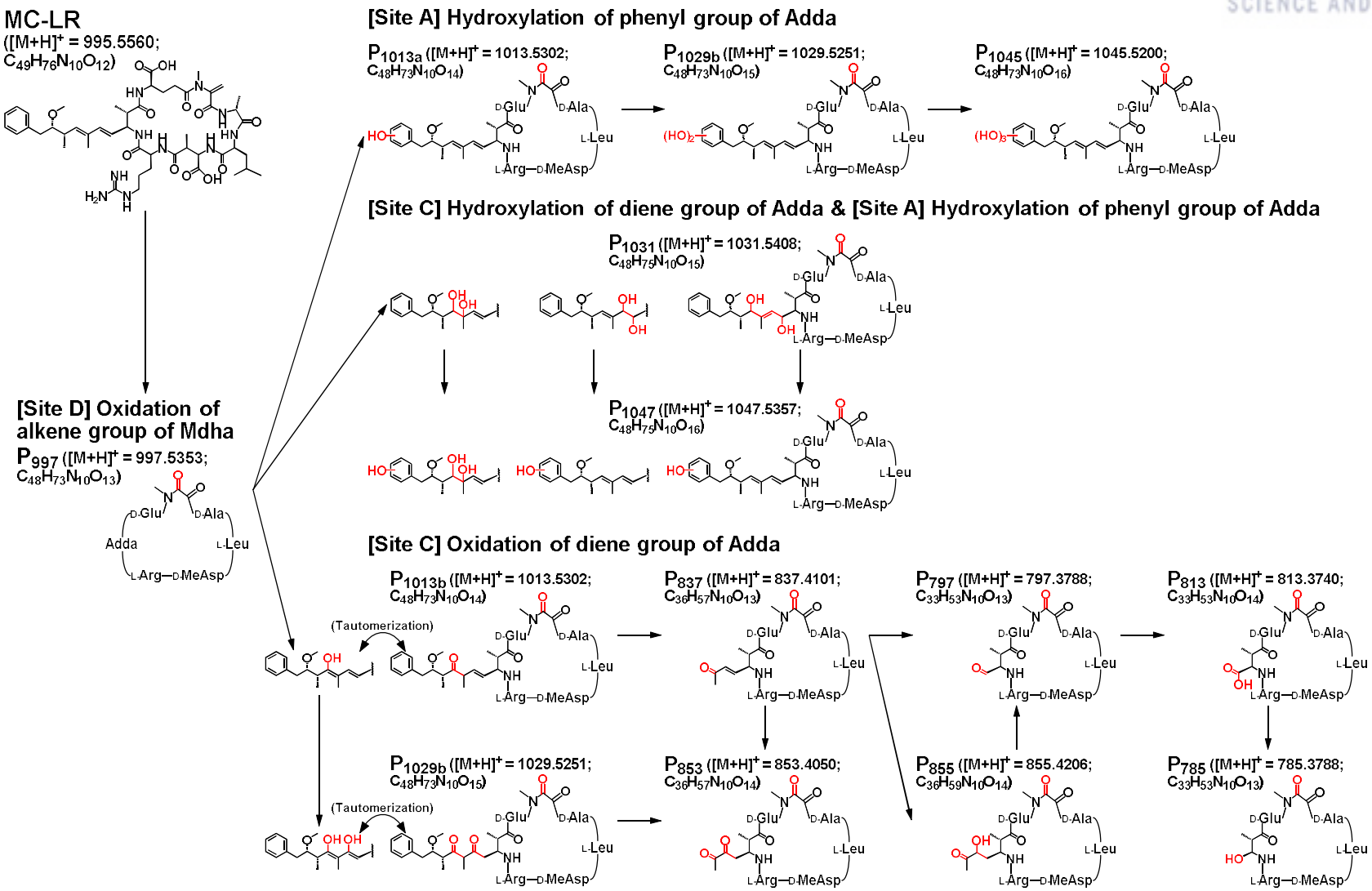

Figure 3.83. Proposed pathways for oxidative degradation of P_{997} by the Fe(II)-TPP/O_2 system.

It is should be note that P_{997} is firstly discovered as a new primary product which is not observed in the literature. P_{997} is believed to result from the transformation of the alkene group of Mdha moiety (Site D) into a carbonyl group (i.e., R_2-C=CH_2 → R_2-C=O). The LC/MS chromatogram of P_{997} (Figure 3.70) showed a single peak, exhibiting that there are no stereoisomers and structural isomers. Moreover, a number of oxidized derivatives of P_{997} were observed (refer to oxidation pathways of P_{997}, Figure 3.83); the remaining primary oxidation sites of P_{997} were oxidized to produce P_{1013a}, P_{1029a}, P_{1045} (Site A), P_{785}, P_{797}, P_{813}, P_{837}, P_{853}, P_{855}, P_{1013b}, P_{1029b} (Site C), and P_{1031}, P_{1047} (Site C and A). The production of P_{997} and its oxidized derivatives has not previously been reported in the literature with respect to the MC-LR oxidation by other oxidants, including •OH. These results propose that P_{997} may be produced through a unique oxidation mechanism containing Fe(IV)-TPP complex. A possible pathway of MC-LR oxidation to P_{997} has been proposed as shown in Figure 3.84.

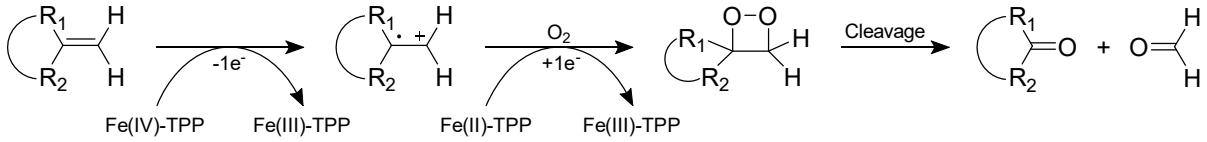

Figure 3.84. Proposed reaction pathway for the production of P_{997}.

The oxidation reaction is initiated by one-electron transfer from the π-bond of the alkene group to Fe(IV)-TPP complex. The resultant carbon-centered radical immediately reacts with O_2 to produce a dioxetane, which subsequently goes through the cleavage of C-C bond, producing P_{997} and HCHO.

To verify whether •OH can cause MC-LR oxidation through a pathway analogous to the one proposed in Figure 3.84, the UV/H_2O_2 system was applied to oxidize MC-LR, for monitoring the oxidation products. The abundance ratio of P_{997} to P_{1011} (which is the most abundant primary product) was plotted as a function of the MC-LR oxidation degree in the Fe(II)-TPP/O_2 and UV/H_2O_2 systems (Figure 3.85a); the time peak area profiles of P_{997} and P_{1011} in the two systems are shown in Figures 3.58, 3.70, 3.72, 3.86, 3.87 and 3.88.

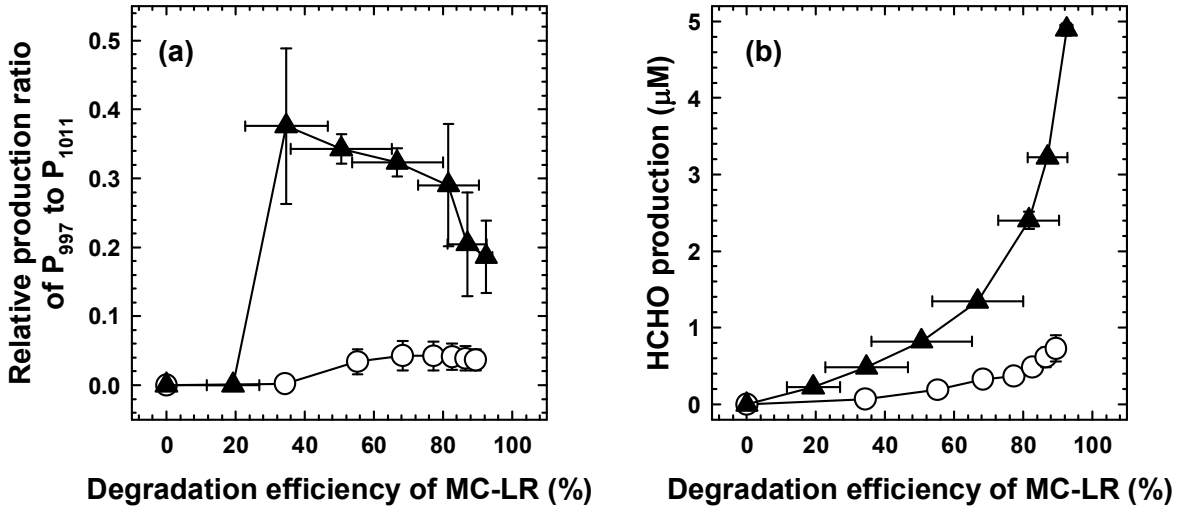

Figure 3.85. Production of (a) P_{997} (relative to P_{1011}) and (b) HCHO during the MC-LR degradation by Fe(II)-TPP/O_2 and UV/H_2O_2 systems ([MC-LR]$_0$ = 2 μM, pH = 7, [Fe(II)]$_0$ = 100 μM and [TPP]$_0$ = 500 μM for the Fe(II)-TPP/O_2 system, [H_2O_2]$_0$ = 250 μM).

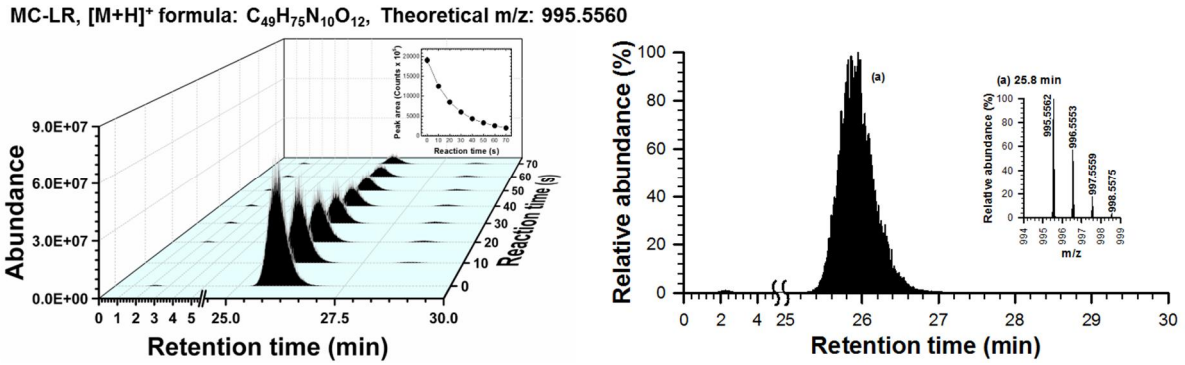

Figure 3.86. LC/MS identification of MC-LR ([M+H]$^+$ = 995.5560). The chromatogram at 20 min with mass spectra (left) and time-dependent chromatograms of MC-LR (right).

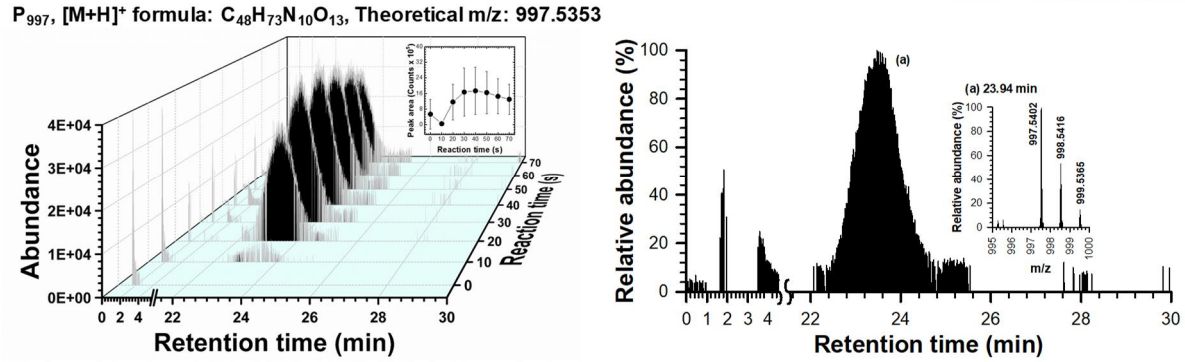

Figure 3.87. LC/MS identification of P_{997} ($[M+H]^+$ = 997.5353). The chromatogram at 20 min with mass spectra (left) and time-dependent chromatograms of P_{997} (right).

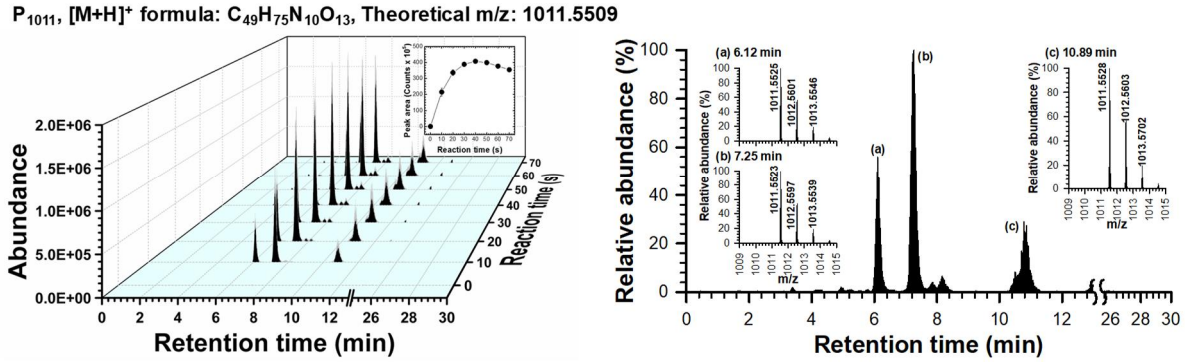

Figure 3.88. LC/MS identification of P_{1011} ($[M+H]^+$ = 1011.5509). The chromatogram at 20 min with mass spectra (left) and time-dependent chromatograms of P_{1011} (right).

As shown in Figure 3.85a, the Fe(II)-TPP/O_2 system generated a much higher fraction of P_{997} compared to the UV/H_2O_2 system, exhibiting that the production pathway of P_{997} proceeds favorably by Fe(IV)-TPP complex rather than $^{\bullet}$OH; the abundance ratio of P_{997} to P_{1011} in the Fe(II)-TPP/O_2 system was 180-fold higher than that in the UV/H_2O_2 system.

In the suggested pathway in Figure 3.84, HCHO is formed together with P_{997}. Thus, the HCHO production during MC-LR degradation was compared in the Fe(II)-TPP/O_2 and UV/H_2O_2 systems; the time-concentration profiles of HCHO are provided in Figures 3.89 and 3.90. As shown Figure 3.85b, the Fe(II)-TPP/O_2 system generated a greater amount of HCHO than the UV/H_2O_2 system, resulting that the suggested pathway by Fe(IV)-TPP complex may contribute to HCHO production.

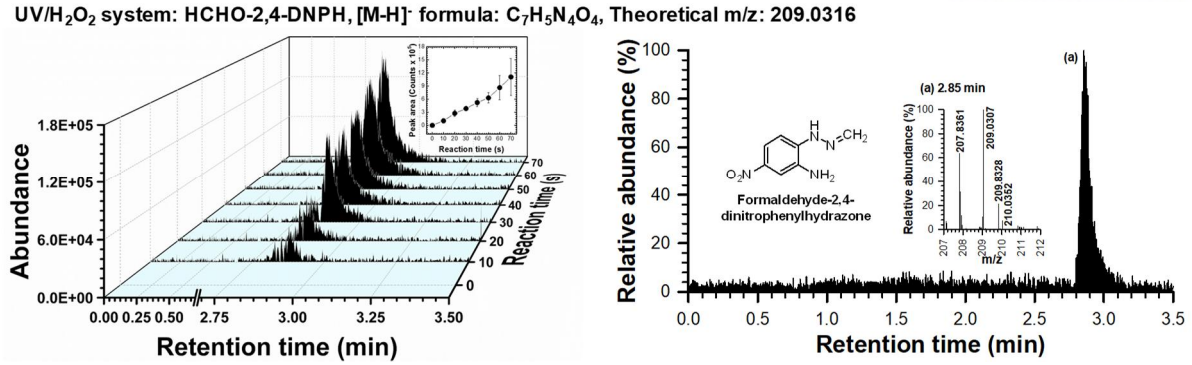

Figure 3.89. LC/MS identification of DNPH-derivatized HCHO (HCHO-2,4-DNPH; $[M-H]^-$ = 209.0316) produced from MC-LR oxidation by the Fe(II)-TPP/O_2 system: time-dependent chromatograms of HCHO-2,4-DNPH (left) and the chromatogram at 20 min with mass spectra (right).

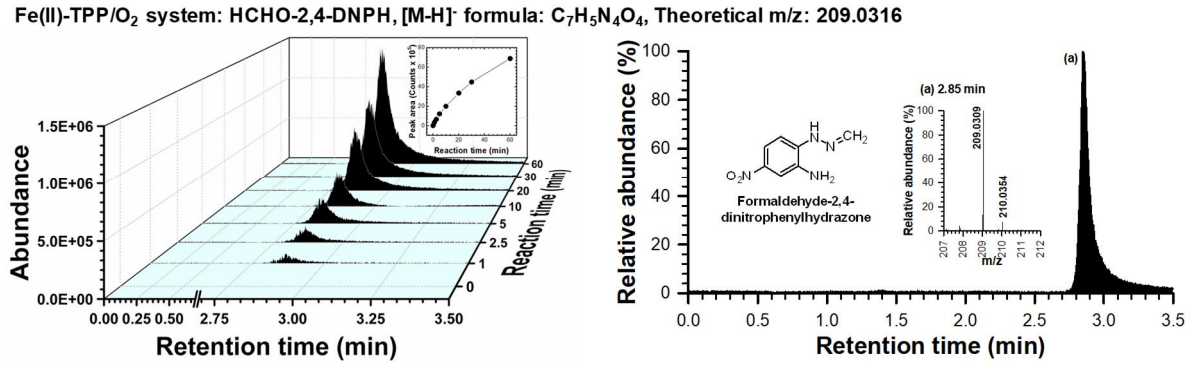

Figure 3.90. LC/MS identification of DNPH-derivatized HCHO (HCHO-2,4-DNPH; $[M-H]^-$ = 209.0316) produced from MC-LR oxidation by the UV/H_2O_2 system: time-dependent chromatograms of HCHO-2,4-DNPH (left) and the chromatogram at 20 min with mass spectra (right).

3.3.5. Hepatotoxicity test. The hepatotoxicity (expressed as relative inhibition of PP2A activity) of the reaction solution was monitored during MC-LR oxidation by the Fe(II)-TPP/O_2 system, and plotted together with the MC-LR concentration (Figure 3.91). The reduction of hepatotoxicity synchronized with a decrease of the MC-LR concentration, exhibiting that a majority of the oxidation products of MC-LR are not hepatotoxins. This observation is well agreed with the oxidation pathways of MC-LR (Figure 3.82 and 3.83) in which the Adda side chain (known to be mainly responsible for the hepatotoxicity of MC-LR[5]) is mostly transformed.

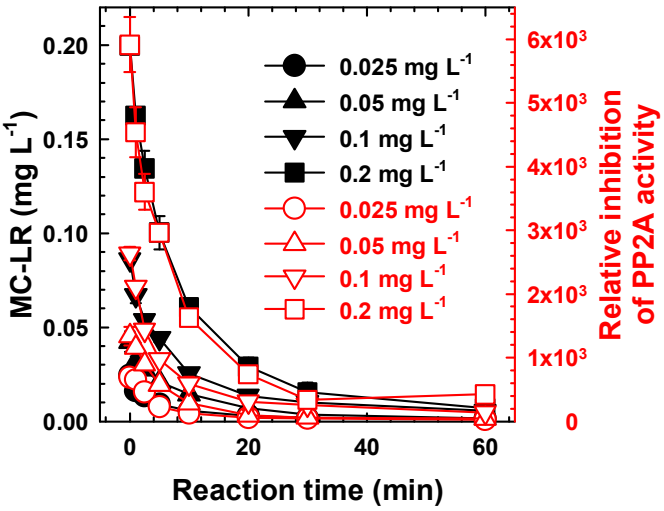

Figure 3.91. Variations of MC-LR concentration and hepatotoxicity during the degradation of MC-LR at different initial concentrations by the Fe(II)-TPP/O_2 system ($[Fe(II)]_0$ = 100 μM; $[TPP]_0$ = 500 μM; pH = 7).

Chapter 4. Conclusions

This study investigated the oxidation of common MCs by two conventional oxidants (i.e., Mn(VII) and O_3) and a promising oxidation system (i.e., Fe(II)-TPP/O_2) in terms of the kinetics and oxidation mechanism. The results from this study provide the following: a comprehensive and reliable kinetic database for the reactions of six MCs with Mn(VII), O_3, and $^{\bullet}OH$; suggest a new approach for the improvement of their field applicability, and also demonstrate the potential of Fe(IV) for the effective control of MC-LR. The major conclusions and the environmental implications for each topic are presented as follows.

The $k_{Mn(VII),MC}$ values were determined to be 160.4–520.1 $M^{-1} s^{-1}$ (MC-RR > -LR ≈ -YR > -LF ≈ -LW > -LA) at pH 7.2 and 21°C. The $k_{Mn(VII),MC}$ values indicated similar temperature-dependencies, with E_a values ranging from 15.1 to 22.4 kJ mol^{-1}. With increasing pH increasing from 2 to 11, the $k_{Mn(VII),MC}$ values decreased until pH 5, and plateaued over the pH range of 5–11, except for that of MC-YR (which increased at pH > 8). Species-specific second-order rate constants were calculated using computationally predicted pK_a values of MCs. The oxidation of MCs in natural waters was accurately predicted by the kinetic model using $k_{Mn(VII),MC}$ and ∫[Mn(VII)]dt values. A kinetic model using the determined rate constants and ∫[Mn(VII)]dt accurately predicted the Mn(VII)-oxidation of MCs in natural waters, proving the validity of those rate constants. Among different characteristics of DOM in natural waters, UV_{254}, $SUVA_{254}$, and the abundance of humic-like substances characterized by fluorescence spectroscopy exhibited good correlation with ∫[Mn(VII)]dt ($R^2 > 0.95$). This quantitative correlation between the DOM characteristics and ∫[Mn(VII)]dt showed the promise of developing a kinetic model that can be promptly applied in the field. A kinetic model using temperature-dependent rate constants and measured ∫[Mn(VII)]dt will the prediction of MC oxidation at different seasonal temperatures. However, to develop a temperature-dependent kinetic model using DOM characteristics, the temperature-dependent quantitative correlation between the DOM characteristics and ∫[Mn(VII)]dt is needed, which warrants further study. In addition, the product research conducted in this study broadens our understanding of the oxidation mechanism of MCs by Mn(VII), and corrects the existing misinformation about the oxidation pathways. It also indicates that major oxidation products do not possess the toxic Adda moiety.

As the competitors for the oxidation of six MCs by O_3 and $^{\bullet}OH$ in the CK experiments, the pH- and temperature-dependent kinetics of CA and *p*CBA were determined as follows: i) CA: $k_{O3,CA2} = 7.5 \pm 0.4 \times 10^5$ $M^{-1} s^{-1}$, $E_a = 19.1 \pm 1.2$ kJ mol^{-1}; ii) *p*CBA: $k_{\bullet OH,pCBA} = 6.0 \pm 0.4 \times 10^5$ $M^{-1} s^{-1}$, $E_a = 30.2 \pm 1.9$ kJ mol^{-1}. Using the obtained $k_{O3,CA}$, the $k_{O3,MC}$ values were determined to be $7.1 \times 10^5 – 9.6 \times 10^6$ $M^{-1} s^{-1}$ (MC-LW > -YR > -RR ≈ -LR ≈ -LA ≈ -LF) at pH 7.2 and 21°C. The $k_{O3,MC}$ values from the literature ($2.58 \times 10^3 – 4.1 \times 10^5$ $M^{-1} s^{-1}$) were found to be underestimated compared to the results from this study.

The $k_{O3,MC}$ values exhibited similar temperature-dependencies, with E_a values ranging from 22.6 to 31.9 kJ mol^{-1}. Using the obtained $k_{\bullet OH,pCBA}$, the $k_{\bullet OH,MC}$ values were determined to be $1.2 \times 10^{10} – 1.6 \times 10^{10}$ M^{-1} s^{-1} at pH 7.2 and 21°C, which is comparable to the $k_{\bullet OH,MC}$ values from the literature ($1.1 \times 10^{10} – 2.3 \times 10^{10}$ M^{-1} s^{-1}). The $k_{O3,MC}$ values exhibited similar temperature-dependencies, with E_a values ranging from 35.1 to 36.7 kJ mol^{-1}. A kinetic model using the determined rate constants and $\int[O_3]dt$ and $\int[^{\bullet}OH]dt$ accurately predicted the O_3 oxidation of MCs in natural waters, proving the validity of those rate constants. This study is the first to verify the $k_{O3,MC}$ and $k_{\bullet OH,MC}$ values by the kinetic model. To expand the availability of the kinetic model, a similar strategy to that described in the previous chapter is required; one which can predict the oxidant exposure values based on their quantitative correlation with various water quality parameters. Since O_3 and $^{\bullet}OH$ are nonselective oxidants compared to Mn(VII), the effects of the more various water quality parameters of the oxidant consumption should be considered in a further study.

The Fe(II)-TPP/O_2 and Fe(II)-TPP/H_2O_2 systems effectively degraded MC-LR under neutral pH conditions. Because of the different kinetics of RDS for oxidant production, MC-LR degradation by the Fe(II)-TPP/H_2O_2 system was much faster (occurred instantaneously) than degradation by the Fe(II)-TPP/O_2 system. The RSM analysis found similar ranges of optimum [TPP]/[Fe(II)] values in the two systems (5.7–5.9). In the Fe(II)-TPP/H_2O_2 system, an excess amount of H_2O_2 inhibited the MC-LR degradation due to oxidant scavenging. The oxidation of MC-LR by the Fe(II)-TPP/O_2 and Fe(II)-TPP/H_2O_2 systems was strongly dependent on pH. This pH-dependency can mainly be explained by the pH-dependent speciation of reactive oxidants, Fe(IV)-TPP complexes. The characteristics of Fe(IV)-TPP complex with a high selectivity can be advantageous to intensively decompose the target organic pollutants without being consumed by the background matrix of DOM in natural water, and this potential should be confirmed in a further study. In addition, the drastically decrease of oxidative performance of Fe(IV)-TPP complex at pH 8 also has to be complemented for application in the field. The LC/MS analysis identified 22 oxidation products of MC-LR, including a new primary product that is rarely found in other oxidative treatments. This product is suggested to be produced by one-electron oxidation of the alkene moiety of the Mdha group and is believed to reflect a unique reaction pathway of Fe(IV)-TPP complex. During the degradation of MC-LR, the hepatotoxicity of the reaction solution showed the same reduced trend as the concentration of MC-LR, indicating that most of the oxidation products of MC-LR do not cause hepatotoxicity.

References

1. Wells, M. L.; Trainer, V. L.; Smayda, T. J.; Karlson, B. S. O.; Trick, C. G.; Kudela, R. M.; Ishikawa, A.; Bernard, S.; Wulff, A.; Anderson, D. M.; Cochlan, W. P. Harmful algal blooms and climate change: Learning from the past and present to forecast the future. *Harmful Algae* **2015**, 49, 68–93.
2. Codd, G. A.; Morrison, L. F.; Metcalf, J. S. Cyanobacterial toxins: Risk management for health protection. *Toxicol. Appl. Pharm.* **2005**, 203 (3), 264–272.
3. Antoniou, M. G.; de la Cruz, A. A.; Dionysiou, D. D. Cyanotoxins: New generation of water contaminants. *J. Environ. Eng.* **2005**, 131 (9), 1239–1243.
4. Qin, B.; Zhu, G.; Gao, G.; Zhang, Y.; Li, W.; Paerl, H. W.; Carmichael, W. W. A drinking water crisis in Lake Taihu, China: Linkage to climatic variability and lake management. *Environ. Manage.* **2010**, 45 (1), 105–112.
5. Dawson, R. M. The toxicology of microcystins. *Toxicon* **1998**, 36 (7), 953–962.
6. Yoshizawa, S.; Matsushima, R.; Watanabe, M. F.; Harada, K. -I.; Ichihara, A.; Carmichael, W. W.; Fujiki, H. Inhibition of protein phosphatases by microcystins and nodularin associated with hepatotoxicity. *J. Cancer Res. Clin. Oncol.* **1990**, 116 (6), 609–614.
7. Vasconcelos, V. M.; Sivonen, K.; Evans, W. R.; Carmichael, W. W.; Namikoshi, M. Hepatotoxic microcystin diversity in cyanobacterial blooms collected in Portuguese freshwaters. *Water Res.* **1996**, 30 (10), 2377–2384.
8. Sivonen, K.; Jones, G., Cyanobacterial toxins. In *Toxic Cyanobacteria in Water: A Guide to their Public Health Consequences, Monitoring and Management*, Chorus, I., Bartram, J., Eds.; E&FN Spon: London, 1999; pp. 55–124.
9. Parveen, G.; Khan, M. F.; Ali, H.; Ibrahim, T.; Shah, R. Determination of lethal dose (LD_{50}) of venom of four different poisonous snakes found in Pakistan. *Biochem. Mol. Biol. J.* **2017**, 3 (3), 1–4.
10. Teixeira, M. G. L. C.; Costa, M. C. N.; Carvalho, V. L. P.; Pereira, M. S.; Hage, E. Gastroenteritis epidemic in the area of the Itaparica Dam, Bahia, Brazil. *Bull. Pan Am. Health Organ.* **1993**, 27 (3), 244–253.
11. Jochimsen, E. M.; Carmichael, W. W.; An, J. S.; Cardo, D. M.; Cookson, S. T.; Holmes, C. E.; Antunes, M. B.; de Melo Filho D. A.; Lyra, T. M.; Barreto, V. S.; Azevedo, S. M.; Jarvis, W. R. Liver failure and death after exposure to microcystins at a hemodialysis center in *Brazil. New Engl. J. Med.* **1998**, 338 (13), 873–878.
12. Pouria, S.; de Andrade, A.; Barbosa, J.; Cavalcanti, R. L.; Barreto, V. T.; Ward, C. J.; Preiser, W.; Poon, G. K.; Neild, G. H.; Codd, G. A. Fatal microcystin intoxication in haemodialysis unit in Caruaru, Brazil. *Lancet* **1998**, 352 (9121), 21–26.

13. World Health Organization. *Guidelines for Drinking-Water Quality*, 4th ed.; World Health Organization: Geneva, 2011.
14. Wang, J.; Xie, P.; Guo, N. Effects of nonylphenol on the growth and microcystin production of *Microcystis* strains, *Environ. Res.* **2007**, 103 (1), 70–78.
15. Hoeger, S. J.; Shaw, G.; Hitzfeld, B. C.; Dietrich, D. R. Occurrence and elimination of cyanobacterial toxins in two Australian drinking water treatment plants. *Toxicon* **2004**, 43 (6), 639–649.
16. Hoeger, S. J.; Hitzfeld, B. C.; Dietrich, D. R. Occurrence and elimination of cyanobacterial toxins in drinking water treatment plants. *Toxicol. Appl. Pharm.* **2005**, 203 (3), 231–242.
17. Jurczak, T.; Tarczynska, M.; izydorczyk, K.; Mankiewicz, J.; Zalewski, M.; Meriluoto, J. Elimination of microcystins by water treatment processes–examples from Sulejow Reservoir, Poland. *Water Res.* **2005**, 39 (11), 2394–2406.
18. Chow, C. W. K.; Drikas, M.; House, J.; Burch, M. D.; Velzeboer, R. M. A. The impact of conventional water treatment processes on cells of the cyanobacterium. *Microcystis aeruginosa*. *Water Res.* **1999**, 33 (15), 3253–3262.
19. Keijola, A. M.; Himberg, K.; Esala, A. L.; Sivonen, K.; Hiis-Virta, L. Removal of cyanobacterial toxins in water treatment processes: Laboratory and pilot-scale experiments. *Toxic. Assess.* **1988**, 3 (5), 643–656.
20. Svrcek, C.; Smith, D. W. Cyanobacteria toxins and the current state of knowledge on water treatment options: A review. *J. Environ. Eng. Sci.* **2004**, 3 (3), 155–185.
21. Sharma, V. K.; Triantis, T. M.; Antoniou, M. G.; He. X.; Pelaez, M.; Han, C.; Song, W.; O'Shea, K. E.; de la Cruz, A. A.; Kaloudis, T.; Hiskia, A.; Dionisiou, D. D. Destruction of microcystins by conventional and advanced oxidation processes: A review. *Sep. Purif. Technol.* **2012**, 91, 3–17.
22. Tsuji, K.; Watanuki, T.; Kondo, F.; Watanabe, M. F.; Nakazawa, H.; Suzuki, M.; Uchida, H.; Harada, K. -I. Stability of microcystins from cyanobacteria–IV. Effect of chlorination on decomposition. *Toxicon* **1997**, 35 (7), 1033–1041.
23. Acero, J. L.; Rodriguez, E.; Meriluoto, J. Kinetics of reactions between chlorine and the cyanobacterial toxins microcystins. *Water Res.* **2005**, 39 (8), 1628–1638.
24. Ho, L.; Onstad, G.; von Gunten, U.; Rinck-Pfeiffer, S.; Craig, K.; Newcombe, G. Different in the chlorine reactivity of four microcystin analogues. *Water Res.* **2006**, 40 (6), 1200–1209.
25. Rodríguez, E.; Onstad, G. D.; Jull, T. P. J.; Metcalf, Acero, J. L.; von Gunten, U. Oxidative elimination of cyanotoxins: Comparison of ozone, chlorine, chlorine dioxide and permanganate. *Water Res.* **2007**, 41 (15), 3381–3393.
26. Rodríguez, E. M.; Acero, J. L.; Spoof, L.; Meriluoto, J. Oxidation of MC-LR and -RR with chlorine and potassium permanganate: Toxicity of the reaction products. *Water Res*. **2008**, 42 (6–7), 1744–1752.

27. Acero, J. L.; Rodríguez, E.; Majado, M. E.; Sordo, A.; Meriluoto, J. Oxidation of microcystin-LR with chlorine and permanganate during drinking water treatment. *J. Water Supply Res. Technol.* **2008**, 57 (6), 371–380.
28. Huang, T. -L.; Zhao, J. -W.; Chai, B. -B. Mechanism studies on chlorine and potassium permanganate degradation of microcystin-LR in water using high-performance liquid chromatography tandem mass spectrometry. *Water Sci. Technol.* **2008**, 58 (5), 1079–1084.
29. Merel, S.; LeBot, B.; Clément, M.; Seux, R.; Thomas, O. Ms identification of microcystin-LR chlorination by-products. *Chemosphere* **2009**, 74 (6), 832–839.
30. Ding, J.; Shi, H.; Timmons, T.; Adams, C. Release and removal of microcystins from *Microcystis* during oxidative-, physical-, and UV-based disinfection. *J. Environ. Eng.* **2010**, 136 (1), 2–11.
31. Kull, T. P. J.; Backlund, P. H.; Karlsson, K. M.; Meriluoto, J. A. O. Oxidation of the cyanobacterial hepatotoxin microcystin-LR by chlorine dioxide: Reaction kinetics, characterization, and toxicity of reaction products. *Environ. Sci. Technol*. **2004**, 38 (22), 6025–6031.
32. Kull, T. P. J.; Sjövall, Q. T.; Tammenkoski, M. K.; Backlund, P. H.; Meriluoto, J. A. O. Oxidation of the cyanobacterial hepatotoxin microcystin-LR by chlorine dioxide: Influence of natural organic matter. *Environ. Sci. Technol*. **2006**, 40 (5), 1504–1510.
33. Ji, Y.; Huang, J. -L.; Fu, J.; Wu, M. -S.; Cui, C. -W. Degradation of microcystin-RR in water by chlorine dioxide. *J. China Univ. Mining & Technol.* **2008**, 18 (4), 623–628.
34. Rositano, J.; Nicholson, B. C.; Pieronne, P. Destruction of cyanobacterial toxins by ozone. *Ozone Sci. Eng.* **1998**, 20 (3), 223–238.
35. Rositano, J.; Newcombe, G.; Nicholson, B.; Sztajnbok, P. Ozonation of NOM and algal toxins in four treated waters. *Water Res.* **2001**, 35 (1), 23–32.
36. Shawwa, A. R.; Smith, D. W. Kinetics of microcystin-LR oxidation by ozone. *Ozone Sci. Technol.* **2001**, 23 (2), 161–170.
37. Brooke, S.; Newcombe, G.; Nicholson, B.; Klass, G. Decrease in toxicity of microcystins LA and LR in drinking water by ozonation. *Toxicon* **2006**, 48 (8), 1054–1059.
38. Onstad, G. D.; Strauch, S.; Meriluoto, J.; Codd, G. A.; von Gunten, U. Selective oxidation of key functional groups in cyanotoxins during drinking water ozonation. *Environ. Sci. Technol.* **2007**, 41 (12), 4397–4404.
39. Al Momani, F. A.; Jarrah, N. Treatment and kinetic study of cyanobacterial toxin by ozone, *J. Environ. Sci. Health A* **2010**, 45 (6), 719–731.
40. Miao, H. -F.; Qin, F.; Tao, G. -J.; Tao, W. -Y.; Ruan, W. -Q. Detoxification and degradation of microcystin-LR and -RR by ozonation. *Chemosphere* **2010**, 79 (4), 355–361.
41. Chang, J.; Chen, Z. -L.; Wang, Z.; Shen, J. -M.; Chen, Q.; Kang, J.; Yang, L.; Liu, X. -W.; Nie, C. -X. Ozonation degradation of microcystin-LR in aqueous solution: Intermediates, byproducts and pathways. *Water Res.* **2014**, 63, 52–61.

42. Chen, X.; Xiao, B.; Liu, J.; Fang, T.; Xu, X. Kinetics of the oxidation of MCRR by potassium permanganate. *Toxicon* **2005**, 45 (7), 911–917.
43. Rodríguez, E.; Majado, M. E.; Meriluoto, J.; Acero, J. L. Oxidation of microcystins by potassium permanganate: Reaction kinetics and implications for water treatment. *Water Res.* **2007**, 41 (1), 102–110.
44. Jeong, B.; Oh, M. -S.; Park, H. -M.; Park, C.; Kim, E. -J.; Hong, S. W. Elimination of microcystin-LR and residual Mn species using permanganate and powdered activated carbon: Oxidation products and pathways. *Water Res.* **2017**, 114, 189–199.
45. He, X.; Pelaez, M.; Westrick, J. A.; O'Shea, K. E.; Hiskia, A.; Triantis, T.; Kaloudis, T.; Stefan, M. I.; de la Cruz, A. A.; Dionysiou, D. D. Efficient removal of microcystin-LR by UV/H_2O_2 in synthetic and natural water samples. *Water Res.* **2012**, 46 (5), 1501–1510.
46. Zong, W.; Sun, F.; Sun, X. Oxidation by-products formation of microcystin-LR exposed to UV/H_2O_2: Toward the generative mechanism and biological toxicity. *Water Res.* **2013**, 47 (9), 3211–3219.
47. He, X.; de la Cruz, A. A.; Hiskia, A.; Kaloudis, T.; O'Shea, K.; Dionysiou, D. D. Destruction of microcystins (cyanotoxins) by UV-254 nm-based direct photolysis and advanced oxidation processes (AOPs): Influence of variable amino acids on the degradation kinetics and reaction mechanisms. *Water Res.* **2015**, 74, 227–238.
48. Robertson, P. K. J.; Lawton, L. A.; Cornish, B. J. P. A.; Jaspars, M. Processes influencing the destruction of microcystin-LR by TiO_2 photocatalysis. *J. Photoch. Photobio. A* **1998**, 116 (3), 215–219.
49. Lawton, L. A.; Robertson, P. K. J.; Cornish, B. J. P. A.; Jaspars, M. Detoxification of microcystions (cyanobacterial hepatotoxins) using TiO_2 photocatalytic oxidation. *Environ. Sci. Technol.* **1999**, 33 (5), 771–775.
50. Feitz, A. J.; Waite, D. Kinetic modeling of TiO_2-catalyzed photodegradation of trace levels of microcystin-LR. *Environ. Sci. Technol*. **2003**, 37 (3), 561–568.
51. Liu, I., Lawton, L. A., Robertson, P. K. J. Mechanistic studies of the photocatalytic oxidation of microcystin-LR: An investigation of byproducts of the decomposition process. *Environ. Sci. Technol.* **2003**, 37 (14), 3214–3219.
52. Antoniou, M. G.; Shoemaker, J. A.; de la Cruz, A. A.; Dionysiou, D. D. LC/MS/MS structure elucidation of reaction intermediates formed during the TiO_2 photocatalysis of microcystin-LR. *Toxicon* **2008**, 51 (6), 1103–1118.
53. Antoniou, M. G.; Shoemaker, J. A.; de la Cruz, A. A.; Dionysiou, D. D. Unveiling new degradation intermediates/pathways from the photocatalytic degradation of microcystin-LR. *Environ. Sci. Technol.* **2008**, 42 (23), 8877–8883.
54. Gajdek, P.; Lechowski, Z.; Bochnia, T.; Kępczyński, M. Decomposition of microcystin-LR by Fenton oxidation. *Toxicon* **2001**, 39 (10), 1575–1578.

55. Bandala, E. R.; Martínez, D.; Martínez, E.; Dionysiou, D. D. Degradation of microcystin-LR toxin by Fenton and photo-Fenton processes. *Toxicon* **2004**, 43 (7), 829–832.
56. Zhong, Y.; Jin, X.; Qiao, R.; Qi, X.; Zhuang, Y. Destruction of microcystin-RR by Fenton oxidation. *J. Hazard. Mater.* **2009**, 167 (1–3), 1114–1118.
57. Park, J. -A.; Yang, B.; Park, C.; Choi, J. -W.; van Genuchten, C. M.; Lee, S. -H. Oxidation of microcystin-LR by the Fenton process: Kinetics, degradation intermediates, water quality and toxicity assessment. *Chem. Eng. J.* **2017**, 309, 339–348.
58. Antoniou, M. G.; de la Cruz, A. A.; Dionysiou, D. D. Degradation of microcystin-LR using sulfate radicals generated through photolysis, thermolysis and e^- transfer mechanisms. *Appl. Catal. B: Environ.* **2010**, 96 (3–4), 290–298.
59. Antoniou, M. G.; de la Cruz, A. A.; Dionysiou, D. D. Intermediates and reaction pathways from the degradation of microcystin-LR with sulfate radicals. *Environ. Sci. Technol.* **2010**, 44 (19), 7238−7244.
60. Carmichael, W. W.; Beasley, V.; Bunner, D. L.; Eloff, J. N.; Falconer, I.; Gorham, P.; Harada, K. -I.; Krishnamurthy, T.; Min-Juan, Y.; Moore, R. E.; Rinehart, K.; Runnegar, M.; Skulberg, O. M.; Watanabe, M. Naming of cyclic heptapeptide toxins of cyanobacteria (blue-green algae). *Toxicon* **1988**, 26 (11), 971–973.
61. Rinehart, K. L.; Namikoshi, M.; Choi, B. W. Structure and biosynthesis of toxins from blue-green algae (cyanobacteria). *J. Appl. Phycol.* **1994**, 6 (2), 159–176.
62. Puddick, J.; Prinsep, M. R.; Wood, S. A.; Kaufononga, S. A. F.; Cary, S. C.; Hamilton, D. P. High levels of structural diversity observed in microcystins from *Microcystis* CAWBG11 and characterization of six new microcystin congeners. *Mar. Drugs* **2014**, 12 (11), 5372–5395.
63. Graham, J. L.; Loftin, K. A.; Meyer, M. T.; Ziegler, A. C. Cyanotoxin mixtures and taste-and-odor compounds in cyanobacterial blooms from the Midwestern United States. *Environ. Sci. Technol.* **2010**, 44 (19), 7361–7368.
64. Song, W.; Xu, T.; Cooper, W. J.; Dionysiou, D. D.; de la Cruz, A. A.; O'Shea, K. E. Radiolysis studies on the destruction of microcystin-LR in aqueous solution by hydroxyl radicals. *Environ. Sci. Technol.* **2009**, 43 (5), 1487–1492.
65. Pelaez, M.; de la Cruz, A. A.; Stathatos, E.; Falaras, P.; Dionysiou, D. D. Visible light-activated N-F-codoped TiO_2 nanoparticles for the photocatalytic degradation of microcystin-LR in water. *Catal. Today* **2009**, 144 (1–2), 19–25.
66. Fang, Y.; Huang, Y.; Yang, J.; Wang, P.; Cheng, G. Unique ability of BiOBr to decarboxylate D-Glu and D-MeAsp in the photocatalytic degradation of microcystin-LR in water. *Environ. Sci. Technol.* **2011**, 45 (4), 1593–1600.
67. Fotiou, T.; Triantis, T. M.; Kaloudis, T.; Pastrana-Martínez, L. M.; Likodimos, V.; Falaras, P.; Silva, A. M. T.; Hiskia, A. Photocatalytic degradation of microcystin-LR and off-odor compounds in water

under UV-A and solar light with a nanostructured photocatalyst based on reduced graphene oxide-TiO_2 composite. Identification of intermediate products. *Ind. Eng. Chem. Res.* **2013**, 52 (39), 13991–14000.

68. Fang, Y.; Zhang, Y.; Ma, W.; Johnson, D. M.; Huang, Y. -P. Degradation of microcystin-LR in water: Hydrolysis of peptide bonds catalyzed by maghemite under visible light. *Appl. Catal., B.* **2014**, 160–161, 597–605.
69. Sampaio, M. J.; Pastrana-Martínez, L. M.; Silva, A. M. T.; Buijnsters, J. G.; Han, C.; Silva, C. G.; Carabineiro, S. A. C.; Dionysiou, D. D.; Faria, J. L. Nanodiamond-TiO_2 composites for photocatalytic degradation of microcystin-LA in aqueous solutions under simulated solar light. *RSC Adv.* **2015**, 5, 58363–58370.
70. Yoo, H. -Y.; Yan, S.; Ra, J. W.; Jeon, D.; Goh, B.; Kim, T. -Y.; Mackeyev, Y.; Ahn, Y. -Y.; Kim, H. -J.; Wilson, L. J.; Alvarez, P. J. J.; Lee, Y.; Song, W.; Hong, S. W.; Kim, J.; Lee, J. Tin porphyrin immobilization significantly enhances visible-light-photosensitized degradation of microcystins: Mechanistic implications. *Appl. Catal., B.* **2016**, 199, 33–44.
71. Wang, L.; Wang, F.; Li, P.; Zhang, L. Ferrous-tetrapolyphosphate complex induced dioxygen activation for toxic organic pollutants degradation. *Sep. Purif. Technol.* **2013**, 120, 148–155.
72. Waldemer, R. H.; Tratnyek, P. G. Kinetics of contaminant degradation by permanganate. *Environ. Sci. Technol.* **2006**, 40 (3), 1055–1061.
73. Hu, L.; Martin, H. M.; Strathmann, T. J. Oxidation kinetics of antibiotics during water treatment with potassium permanganate. *Environ. Sci. Technol.* **2010**, 44 (16), 6416–6422.
74. Lawton, L. A.; Robertson, P. K. J. Physico-chemical treatment methods for the removal of microcystins (cyanobacterial hepatotoxins) from potable waters. *Chem. Soc. Rev.* **1999**, 28, 217–224.
75. Lemieux, R. U.; von Rudloff, E. Periodate-permanganate oxidations: I. Oxidation of olefins. *Can. J. Chem.* **1955**, 33 (11), 1701–1709.
76. Wiberg, K. B.; Saegebarth, K. A. The mechanisms of permanganate oxidation. IV. hydroxylation of olefins and related reactions. *J. Am. Chem. Soc.* **1957**, 79 (11), 2822–2824.
77. Dash, S.; Patel, S.; Mishra, B. K. Oxidation by permanganate: Synthetic and mechanistic aspects. *Tetrahedron* **2009**, 65 (4), 707–739.
78. Bard, A. J.; Parsons, R.; Jordan, J. *Standard Potentials in Aqueous Solution*; Marcel Dekker: New York, 1985.
79. von Gunten, U. Ozonation of drinking water: Part I. Oxidation kinetics and product formation. *Water Res*. **2003**, 37 (7), 1443–1467.
80. Lee, Y.; von Gunten, U. Quantitative structure-activity relationships (QSARs) for the transformation of organic micropollutants during oxidative water treatment. *Water Res.* **2012**, 46 (19), 6177–6195.

81. Syche, A. Y.; Isak, V. G. Iron compounds and the mechanisms of the homogeneous catalysis of the activation of O_2 and H_2O_2 and of the oxidation of organic substrates. *Russ. Chem. Rev.* **1995**, 64 (12), 1105–1129.
82. King, D. W.; Lounsbury, H. A.; Millero, F. J. Rates and Mechanism of Fe(II) oxidation at nanomolar total iron concentrations. *Environ. Sci. Technol.* **1995**, 29 (3), 818–824.
83. Keenan, C. R.; Sedlak, D. L. Factors affecting the yield of oxidants from the reaction of nanoparticulate zero-valent iron and oxygen. *Environ. Sci. Technol.* **2008**, 42 (4), 1262–1267.
84. Seibig, S.; van Eldik, R. Kinetics of [Fe-II(edta)] oxidation by molecular oxygen revisited. New evidence for a multistep mechanism. *Environ. Sci. Technol.* **1997**, 36 (18), 4115−4120.
85. Keenan, C. R.; Sedlak, D. L. Ligand-enhanced reactive oxidant generation by nanoparticulate zero-valent iron and oxygen. *Environ. Sci. Technol.* **2008**, 42 (18), 6936−6941.
86. Kim, H. -H.; Lee, H.; Kim, H. -E.; Seo, J.; Hong, S. W.; Lee, J. -Y.; Lee, C. Polyphosphate-enhanced production of reactive oxidants by nanoparticulate zero-valent iron and ferrous ion in the presence of oxygen: Yield and nature of oxidants. *Water Res.* **2015**, 86, 66−73.
87. Wang, L.; Cao, M.; Ai, Z.; Zhang, L. Dramatically enhanced aerobic atrazine degradation with Fe@Fe_2O_3 core−shell nanowires by tetrapolyphosphate. *Environ. Sci. Technol.* **2014**, 48 (6), 3354−3362.
88. Wang, L.; Cao, M.; Ai, Z.; Zhang, L. Design of a highly efficient and wide pH electro-Fenton oxidation system with molecular oxygen activated by ferrous-tetrapolyphosphate complex. *Environ. Sci. Technol.* **2015**, 49 (5), 3032−3039.
89. Hou, X.; Shen, W.; Huang, X.; Ai, Z.; Zhang, L. Ascorbic acid enhanced activation of oxygen by ferrous iron: A case of aerobic degradation of rhodamine B. *J. Hazard. Mater.* **2016**, 308 (5), 67−74.
90. Lee, D. G.; Perez-Benito, J. F. Oxidation of hydrocarbons. 14. Autocatalysis during the oxidation of 1-tetradecene by methyltributylammonium permanganate. *Can. J. Chem.* **1985**, 63 (6), 1275–1279.
91. Schothorst, R. C.; Boef, G. D. The application of strongly oxidizing agents in flow injection analysis. *Anal. Chim. Acta* **1985**, 169, 99–107.
92. Mata-Perez, F.; Perez-Benito, J. F. Identification of the product from the reduction of permanganate ion by trimethylamine in aqueous phosphate buffers. *Can. J. Chem.* **1985**, 63 (4), 988–992.
93. Crimi, M.; Ko, S. Control of manganese dioxide particles resulting from in situ chemical oxidation using permanganate. *Chemosphere* **2009**, 74 (6), 847–853.
94. Rivasseau, C.; Martins, S.; Hennion, M. -C. Determination of some physicochemical parameters of microcystins (cyanobacterial toxins) and trace level analysis in environmental samples using liquid chromatography. *J. Hazard. Mater.* **1998**, 799 (1–2), 155–169.
95. Cookson, R. F. The determination of acidity constants. *Chem. Rev.* **1974**, 74 (1), 5–28.

96. Meloun, M.; Bordovská, S. Benchmarking and validating algorithms that estimate pK_a values of drugs based on their molecular structures. *Anal. Bioanal. Chem.* **2007**, 389 (4), 1267–1281.

97. Liao, C.; Nicklaus, M. C. Comparison of nine programs predicting pK_a values of pharmaceutical substances. *J. Chem. Inf. Model.* **2009**, 49 (12), 2801–2812.

98. ACD/Percepta, version 2017.1.1; Advanced Chemistry Development Inc.: Toronto, ON, Canada, 2017; www.acdlabs.com.

99. Blom, J. F.; Robinson, J. A.; Jüttner, F. High grazer toxicity of [D-Asp^3,(*E*)-Dhb^7]microcystin-RR of *Planktothrix rubescens* as compared to different microcystins. *Toxicon* **2001**, 39 (12), 1923–1932.

100. Moffitt, M. C.; Louie, G. V.; Bowman, M. E.; Pence, J.; Noel, J. P.; Moore, B. S. Discovery of two cyanobacterial phenylalanine ammonia lyases: Kinetic and structure characterization. *Biochem.* **2007**, 46 (4), 1004–1012.

101. Elovitz, M. S.; von Gunten, U. Hydroxyl radical/ozone ratios during ozonation processes. I. The R_{ct} concept. *Ozone Sci. Eng.* **1999**, 21 (3), 239–260.

102. Jia, Z.; Ramstad, T.; Zhong, M. Medium-throughput pKa screening of pharmaceuticals by pressure-assisted capillary electrophoresis. *Electrophoresis* **2001**, 22 (6), 1112–1118.

103. Neta, P.; Dorfman, L. M. Pulse radiolysis sduties. XIII. Rate constants for the reaction of hydroxyl radicals with aromatic compounds in aqueous solutions. In *Advances in Chemistry, Radiation Chemistry*; American Chemical Society, 1968; Vol. *81*, pp 222–230.

104. Hatchard, C. G.; Parker, C. A. A new sensitive chemical actinometer. II. Potassium ferrioxalate as a standard chemical actinometer. *Proc. Roy. Soc. Lond. Ser. Math. Phys. Sci.* **1956**, 235 (1203), 518–536.

105. Banxendale, J.; Wilson, J. The photolysis of hydrogen peroxide at high light intensities. *Trans. Faraday Soc.* **1957**, 53, 344–356.

106. Tamura, H.; Goto, K.; Yotsuyanagi, T.; Nagayama, M. Spectrometric determination of iron(III) with 1,10-phonanthroline in the presence of large amounts of iron(III). *Talanta* **1974**, 21, 314–318.

107. Eisenberg, G. Colorimetric determination of hydrogen peroxide. *Ind. Eng. Chem., Anal. Ed.* **1943**, 15 (5), 327–328.

108. Freeman, F.; Kappos, J. C. Permanganate ion oxidation. 16. Substituent effects on the rate of oxidation of α,β-unsaturated carboxylate ions. *J. Org. Chem.* **1986**, 51 (10), 1654–1657.

109. Nelson, D. J.; Henley, R. L. Relative rates of permanganate oxidation of functionalized alkenes and the correlation with the ionization potentials of those alkenes. *Tetrahedron Lett.* **1995**, 36 (36), 6375–6378.

110. Wiberg, K.; Geer, R. D. The kinetics of the permanganate oxidation of alkenes. *J. Am. Chem. Soc.* **1966**, 88 (24), 5827–5832.

111. Simándi, L. I.; Jáky, M. Mechanism of the permanganate oxidation of unsaturated compounds. Part IV. Kinetics investigation of the oxidation of maleic and fumaric acids. *J. Chem. Soc. Perkin Trans. II* **1973**, 1856–1860.

112. Jáky, M.; Simándi, L. I. Mechanism of the permanganate oxidation of unsaturated compounds. Part VI. Kinetics investigation of the oxidation of methylmaleic acid, methylfumaric acid, and dimethylmaleic acid. *J. Chem. Soc. Perkin Trans. II* **1976**, 939–943.

113. Simándi, L. I.; Jáky, M.; Son, N. T.; Hegedüs-Vajda, J. Mechanism of the permanganate oxidation of unsaturated compounds. Part 8. Kinetics investigation of the oxidation of halogenomaleic acid. *J. Chem. Soc. Perkin Trans. II* **1977**, 1794–1798.

114. Huang, K. -C.; Hoang, G. E.; Chheda, P.; Woody, B. A.; Dobbs, G. M. Oxidation of chlorinated ethenes by potassium permanganate: A kinetics study. *J. Hazard. Mater.* **2001**, 87 (1–3), 155–169.

115. Konopka, A.; Brock, T. D. Effect of temperature on blue-green algae (cyanobacteria) in lake Mendota. *Appl. Environ. Microbiol.* **1978**, 36 (4), 572–576.

116. Robarts, R. D.; Zohary, T. Temperature effects on photosynthetic capacity respiration, and growth rates of bloom-forming cyanobacteria. *New Zeal. J. Mar. Fresh. Res.* **1987**, 21 (3), 391–399.

117. Bailey, N.; Carrington, A.; Lott, T. A.; Symons, M. C. R. Structure and reactivity of the oxyanions of transition metals. Part VIII. Acidities and spectra of protonated oxyanions. *J. Chem. Soc.* **1960**, 290–296.

118. Simándi, L. I.; Jáky, M. Kinetics and mechanism of the permanganate oxidation of acetylenedicarboxylic acid. *Tetrahedron Lett.* **1970**, 11 (40), 3489–3492.

119. Simándi, L. I.; Jáky, M. Kinetics and mechanism of the permanganate oxidation of fumaric acid. Evidence for short-lived intermediates. *Inorg. Nucl. Chem. Lett.* **1971**, 7 (7), 605–609.

120. Jáky, M.; Simándi, L. I. Kinetics and mechanism of the permanganate oxidation of diethyl maleate and diethyl fumarate. *React. Kinet. Catal. Lett.* **1975**, 3 (4), 397–404.

121. Simándi, L. I.; Jáky, M. Mechanism of the permanganate oxidation of unsaturated compounds. Part 7. Kinetics of the oxidation of propiolic and phenylpropiolic acids. *J. Chem. Soc. Perkin Trans. II* **1977**, 630–633.

122. Ingold, H. *Structure and mechanism in organic chemistry*; Cornell University Press: 1953.

123. Toyoshima, K.; Okuyama, T.; Fueno, T. Structure and reactivity of α,β-unsaturated ethers. 17. Oxidations by permanganate and osmium tetraoxide. *J. Org. Chem.* **1980**, 45 (9), 1600–1604.

124. Freeman, F.; Kappos, J. C. Permanganate ion oxidation. 15. Additional evidence for formation of soluble (colloidal) manganese dioxide during the permanganate ion oxidation of carbon-carbon double bonds in phosphate-buffered solutions. *J. Org. Chem*. **1985**, 107 (23), 6628–6633.

125. Freeman, F.; Kappos, J. C. Permanganate ion oxidation. 19. Hexadecyltrimethylammonium permanganate oxidation of cycloalkenes. *J. Org. Chem*. **1989**, 54 (11), 2730–2734.

126. Stewart, R. The mechanisms of permanganate oxidation. III. The oxidation of benzhydrol. *J. Am. Chem. Soc.* **1957**, 79 (12), 3057–3061.

127. Jiang, J.; Pang, S. -Y.; Ma, J.; Liu, H. Oxidation of phenolic endocrine disrupting chemicals by potassium permanganate in synthetic and real waters. *Environ. Sci. Technol.* **2012**, 46 (3), 1774–1781.

128. Du, J.; Sun, B.; Zhang, J.; Guan, X. Parabolic-like shaped pH-rate profile for phenols oxidation by aqueous permanganate. *Environ. Sci. Technol.* **2012**, 46 (16), 8860–8867.

129. Francioso, O.; Sanchez-Cortes, S.; Tugnoli, V.; Ciavatta, V.; Sitti, L.; Gessa, C. Infrared, Raman, and nuclear magnetic resonance (^{1}H, ^{13}C, and ^{31}P) spectroscopy in the study of fractions of peat humic acids. *Appl. Spectrosc.* **1996**, 50 (9), 1165–1174.

130. Chen, W.; Westerhoff, P.; Leenheer, J. A.; Booksh, K. Fluorescence exitation–emission matrix regional integration to quantify spectra for dissolved organic matter. *Environ. Sci. Technol.* **2003**, 37 (24), 5701–5710.

131. Świetlik, J.; Sikorska, E. Application of fluorescence spectroscopy in the studies of natural organic matter fractions reactivity with chlorine dioxide and ozone. *Water Res.* **2004**, 38 (17), 3791–3799.

132. He, D.; Guan, X.; Ma, J.; Yu, M. Influence of different nominal molecular weight fractions of humic acids on phenol oxidation by permanganate. *Environ. Sci. Technol.* **2009**, 43 (21), 8332–8337.

133. Determann, S.; Reuter, R.; Wagner, P.; Willkomm, R. Fluorescent matter in the eastern atlantic ocean. Part 1: Method of measurement and near-surface distribution. *Deep–Sea Res., Part I Oceanogr. Res. Pap.* **1994**, 41 (4), 659–675.

134. Coble, P. G. Characterization of marine and terrestrial DOM in seawater using excitation–emission matrix spectroscopy. *Mar. Chem.* **1996**, 51 (4), 325–346.

135. Jiang, W.; Chen, L.; Batchu, S. R.; Gardinali, P. R.; Jasa, L.; Marsalek, B.; Zboril, R.; Dionysiou, D. D.; O'Shea, K. E.; Sharma, V. K. Oxidation of microcystin-LR by ferrate(VI): Kinetics, degradation pathways, and toxicity assessments. *Environ. Sci. Technol.* **2014**, 48 (20), 12164–12172.

136. Andersen, J.; Han, C.; O'Shea, K.; Dionysiou, D. D. Revealing the degradation intermediates and pathways of visible light-induced NF-TiO_2 photocatalysis of microcystin-LR. *Appl. Catal., B.* **2014**, 154–155, 259–266.

137. Zhou, S.; Yu, Y.; Sun, J.; Zhu, S.; Deng, J. Oxidation of microcystin-LR by copper(II) coupled with ascorbic acid: Kinetics modeling towards generation of H_2O_2. *Chem. Eng. J.* **2018**, 333, 443–450.

138. Wiberg, K. B.; Stewart, R. The mechanisms of permanganate oxidation. I. The oxidation of some aromatic aldehydes. *J. Am. Chem. Soc.* **1955**, 77 (7), 1789–1795.

139. Leitzke, A.; Reisz, E.; Flyunt, R.; von Sonntag, C. The reactions of ozone with cinnamic acid: Formation and decay of 2-hydroperoxy-2-hydroxyacetic acid. *J. Chem. Soc., Perkin Trans. 2* **2001**,

5, 793–797.

140. Jans, U. Radikalbildung aus Ozon in atmosphärischen Wassern Einfluss von Licht, gelösten Stoffen and Russpartikeln. Doctoral Thesis, ETH Zurich, 1996.
141. Wolf, C.; von Gunten, U.; Kohn, T. Kinetics of inactivation of waterborne enteric viruses by ozone. *Environ. Sci. Technol.* **2018**, 52 (4), 2170–2177.
142. Pryor, W. A.; Giamalva, D. H.; Church, D. F. Kinetics of ozonation. 2. Amino acids and model compounds in water and comparisons to rates in nonpolar solvents. *J. Am. Chem. Soc.* **1984**, 106 (23), 7094–7100.
143. Hoigné, J.; Bader, H. Rate constants of reactions of ozone with organic and inorganic compounds in water–II. *Water Res.* **1983**, 17 (2), 185–194.
144. Helz, G. R.; Zepp, R. G.; Crosby, D. G. *Aquatic and Surface Photochemistry*; Lewis Publishers: Boca Raton, FL, 1994.
145. Eckert, N. A.; Vaddadi, S.; Stoian, S.; Lachicotte, R. J.; Cundari, T. R.; Holland, P. L. Coordination-number dependence of reactivity in an imidoiron(III) complex. *Angew. Chem. Int. Ed.* **2006**, 118 (41), 7022-7025.
146. Engelmann, M. D.; Bobier, R. T.; Hiatt, T.; Cheng, F. Variability of the Fenton reaction characteristics of the EDTA, DTPA, and citrate complexes of iron. *Biometals* **2003**, 16 (4), 519-527.
147. Noradoun, C. E.; Cheng, I. F. EDTA degradation induced by oxygen activation in a zerovalent iron/air/water system. *Environ. Sci. Technol.* **2005**, 39 (18), 7158-7163.
148. Laine, D. F.; Blumenfeld, A.; Cheng, F. Mechanistic study of the ZEA organic pollutant degradation system: Evidence for H_2O_2, HO•, and the homogeneous activation of O_2 by Fe^{II}EDTA. *Ind. Eng. Chem. Res.* **2008**, 47 (17), 6502-6508.
149. Løgager, T.; Holcman, J.; Sehested, K.; Pedersen, T. Oxidation of ferrous ions by ozone in acidic solutions. *Inorg. Chem.* **1992**, 31 (17), 3523-3529.
150. Abouelatta, A. I.; Campanali, A. A.; Ekkati, A. R.; Shamoun, M.; Kalapugama, S.; Kodanok, J. J. Oxidation of the natural amino acids by a ferryl complex: Kinetics and mechanistic studies with peptide model compounds. *Inorg. Chem.* **2009**, 48 (16), 7729-7739.
151. Andersen, J.; Han, C.; O'Shea, K.; Dionysiou, D. D. Revealing the degradation intermediates and pathways of visible light-induced NF-TiO_2 photocatalysis of microcystin-LR. *Appl. Catal., B.* **2014**, 154-155, 259-266.

감사의 글

2011년 겨울, UNIST 이창하 교수님 연구실에 처음 문을 두드렸던 기억이 아직도 생생합니다. 당시 영어성적미달로 학부졸업이 취소되는 바람에 대학원 입학까지 취소되어 심히 좌절하며 괴로워하던 때가 바로 엊그제 같습니다. 병역미필, 유부남, 사상 초유의 졸업실패 등의 스펙(?)으로 무장한 정체불명이었던 저에게 제 2의 기회를 주실 뿐만 아니라 식지 않는 열정적 가르침과 아낌없는 지원으로 여기까지 이끌어 주신 지도교수님 이창하 교수님께 진심으로 감사드립니다. 지난날 되돌아보면 항상 2% 이상의 부족함으로 지도교수님의 걱정과 근심이 되었던 것 같아 죄송스럽지만, 이후로는 스승의 기쁨이 될 수 있는 든든한 제자가 될 수 있도록 더욱 정진하도록 하겠습니다.

저의 학위논문심사를 위해 귀한 시간을 내주시고 여러 좋은 조언을 아끼지 않으신 포항공과대학교 조강우 교수님, 고려대학교 이재상 교수님, 그리고 울산과학기술원의 권영남 교수님과 조재원 교수님께 깊은 감사를 드립니다. 또한, 학위기간 동안 콘크리트 미세구조의 세계를 맛보게 해 주신 오재은 교수님, 혐기성소화 및 데이터 분석 기법에 대해 지도해주신 이창수 교수님, 샘플링과 기기 분석에 대한 이해를 넓혀 주신 최성득 교수님께도 감사드립니다.

부족한 제가 길고도 험난했던 학위기간을 이겨낼 수 있도록 전후좌우에서 늘 도움과 힘을 주었던 선배님들, 후배님들, 그리고 동료들에게도 감사의 마음을 전합니다. 연구를 위해 태어난 것만 같은 이홍신 박사님, ART lab 소독계의 대모 김형은 박사님, 캐나다를 접수한 풀편딩 포닥 이혜진 박사님, 베트남 걸크러쉬 Thuy 누님과 Pham 박사님, ART lab 음주계의 지킬&하이드 쉰슨생님, 유일했던 동갑내기이자 유부남으로 거듭난 준영, Nature 및 Sicence의 잠재적 제 1저자 지원, 이미 만물박사학위 소지자 학현, 아마도 LV-223에서 파견되어 지금까지 적응중인 리기명, ART lab의 브루스 웨인 타이완, ART lab의 기럭지 대표 형진, A.K.A. 조퀸 지윤, 연차로는 석사 뺨치는 귀염둥이 크롱 재민과 ART lab 음주계의 신성 지혜, 대학원에 도전하는 해병 형석, 환골탈태 중훈, ART lab의 진정한 위너 동현, 또한, 같은 연구실은 아니었지만 곁에서 힘이 되어 주었던 병문, 상균, 민규형님, 그리고 훈련소 동기이자 이제는 박사님이 된 응진과 영욱에게도 감사의 마음을 전합니다. 평생 한 번의 대학원 생활을 여러분들과 함께하여 저에게 큰 영광이었습니다.

환경에 대해 완전히 무지했던 제가 대학원의 포부를 갖도록 지도해주시고 격려해주신 한국외국어대학교 학부시절의 지도교수님이셨던 폐기물 및 오폐수처리 연구실 강구영 교수님께도 깊은 감사를 드립니다. 무기력했던 저의 학부시절 할 수 있다는 열정을 늘 불어넣어 주셨습니다. 학부시절 개념 없는 철부지였던 저를 사랑과 인내로 아껴 주셨던 폐방 선배님들께도 감사의 마음을 전합니다. 폐방의 아버지 진수형님, 폐방의 어머니 택준형님, 항상 든든한 쌍두마차 현진형님과 종욱형님. 인생의 고비 때마다 이겨낼 수 있는 저력과 잊지 못할 소중한 추억들을 만들어 주셔서 감사합니다.

또한, 같은 공간에서 함께하지 않았지만 먼 거리서 응원과 기도로 함께하였던 지인들에게도 고마움을 전합니다. 서울역 태생으로 훗날 도스토옙스키를 뛰어넘을 지음 해성, 아닌척하지만 마음씨가 따뜻한 오천이, 이제는 주를 위해 스텝을 밟는 Boxer 용익, 신학교를 때려치우고 목수가 되어버린 장선생님, 네오에게 찾아온 모피어스 같이 종로에 와 주셨던 영주누님, 한국의 사도 바울 이천수 목사님, 칠흑 같은 마음속 북극성을 달아 주신 박지웅 목사님, 목이 곧은 못된 양인 저를 포기하지 않고 목양해주신 황준호 목사님과 이방인 같았던 저를 이해해주시고 사랑으로 품어 주신 울산사랑의 교회 성도님들께도 고마움을 전합니다.

울산생활의 시작은 저에게 학위기간의 시작이었던 동시에 한 가정의 시작이었습니다. 무조건적인 사랑과 인내로 지원을 아끼지 않은 가족 분들께 깊이 감사드립니다. 나이도 어렸지만 나이보다 더 미성숙했던 김서방을 그저 지지해주시고 기도해주신 장인어른, 장모님 그리고 동명형님 가정에 깊은 감사를 드립니다. 타지였던 울산이란 곳에서 가정을 꾸리며 학업을 병행할 수 있었던 것은 장인어른과 장모님의 헌신이 아니었다면 불가능했을 것입니다. 무엇보다 저를 낳아 주시고 키워 주실 뿐만 아니라 항상 철없는 아들의 무리한 요청에도 늘 희생으로 묵묵히 응답해 주셨던 사랑하는 아버지와 어머니께 진심으로 감사드립니다. 나날이 넘쳐만 가는 사랑과 은혜의 빚 속에서 조금이나마 보은할 수 있는 자랑스런 아들이 될 수 있도록 노력하겠습니다. 또한 이런저런 핑계로 소식 한번 제대로 전하지 않았던 태영누나에게도 동생의 고마움을 전합니다.

0이라기 보다 오히려 마이너스였던, 내세울 것 하나 없는 저를 있는 모습 그대로 사랑해주며 험난했던 길 위를 항상 함께 걸어주었던 사랑하는 아내 장미(藏美) 아람에게 감사의 마음을 전합니다. 또한, 학위기간의 여정 속에서 가족의 인연으로 한 팀이 된 사랑스런 짱이(藏怡), 도희 그리고 한결에게도 미안함과 감사의 마음을 전합니다.

마지막으로 말씀으로 세상과 사람을 창조하신 하나님 아버지와 죄의 삯인 사망으로부터 사람을 구하기위해 십자가에서 죽으실 뿐 아니라 부활하신 구주 예수님과 그 사랑을 깨닫게 하시고 영광의 빛으로 carry하시는 성령님께 영광과 감사를 드립니다.

2018년 6월 ART lab에서